Analyse de la modélisation turbulente en écoulements tourbillonnaires

Jean-François Monier

Numéro d'ordre: 2018LYSEC015

THÈSE DE DOCTORAT DE L'UNIVERSITÉ DE LYON

opérée au sein de

l'École Centrale de Lyon

École Doctorale 162 : Mécanique, Énergétique, Génie Civil et Acoustique

Spécialité : Mécanique des fluides

Soutenue publiquement le 02/07/2018, par :

Jean-François MONIER

Analyse de la modélisation turbulente en écoulements tourbillonnaires

---

Devant le jury composé de :

Paola CINNELLA	Professeur, ENSAM, DynFluid	*Présidente*
Éric LAMBALLAIS	Professeur, Université de Poitiers, UFR SFA	*Rapporteur*
Guillaume BALARAC	Maître de conférences, Grenoble INP, LEGI	*Rapporteur*
Lipeng LU	Professeur, Beihang University, Fluid Machinery dpmt.	*Examinateur*
Liang SHAO	Directeur de recherche CNRS, LMFA	*Directeur de thèse*
Jérôme BOUDET	Maître de conférences, École Centrale de Lyon, LMFA	*Co-directeur de thèse*
Éric LIPPINOIS	Ingénieur Safran Aircraft Engines	*Invité*

When you are studying any matter, or considering any philosophy, ask yourself only what are the facts and what is the truth that the facts bear out. Never let yourself be diverted either by what you wish to believe, or by what you think would have beneficent social effects if it were believed.

Bertrand Russell, *What is it worth telling the future generations?*, BBC interview (1959)

Lorsque vous étudiez quoi que ce soit, ou considérez n'importe quelle philosophie, demandez-vous uniquement quels sont les faits et quelle vérité ces faits viennent confirmer. Ne vous laissez jamais détourner de cela par ce que vous voudriez croire ou par ce que vous imaginez avoir des effets bénéfiques sur la société si cela était cru.

Bertrand Russell, *Quel message voudriez-vous transmettre aux générations futures ?*, BBC interview (1959)

Acknowledgements

I thank the jury for judging my work, and particularly Éric Lamballais and Guillaume Balarac for reviewing my manuscript.

I thank my advisers, Éric Lippinois for Safran Aircraft Engines, Liang Shao and Jérôme Boudet for LMFA. I particularly thank Jérôme for all the time spent and all the corrections and advice that helped me to progress.

I thank all my companions in PhD, Emmanuel, Johannes, Gherardo, Étienne, Zlatko, Quentin, Gille-Alexis, Annabelle, Saira, Giullia, Victor, Julissa, Thomas, Martin, Ludovic, Valdo, Anne-Lise, Pierre, Jiang, and all those that I may be forgetting.

I thank Feng for his help and remarks on the work we shared, and Nicolas for allowing me to experience a great first time as a student project adviser.

I thank all the members of the turbomachinery group, and more specially among them Alexis Giauque and Stéphane Aubert, for the numerous useful discussions that we had.

I thank Christian Nicot and Mathieu Creyssels for the morning discussions around a coffee, that I will miss deeply.

I thank my lifetime friends, Éva, Pierre, Marine, Thomas, Jules and Valentin.

I thank, obviously, my brother, parents and grand-parents, for everything, from my first day to today.

I thank my wife, Élodie, for everything her support and for everything we did together since we first met, whose most important is certainly our wonderful son, Maximilien.

Maximilien, if one day you read these words, know that I thank you deeply for being the wonderful child that you are. For my other children, not yet born, this work is also for you. I am eager to meet you as soon as possible.

Remerciements

Je remercie tous les membres du jury d'avoir accepté d'évaluer mes travaux, et particulièrement Éric Lamballais et Guillaume Balarac d'avoir été rapporteurs.

Je remercie mes encadrants, Éric Lippinois côté Safran Aircraft Engines, Liang Shao et Jérôme Boudet côté LMFA. Je remercie particulièrement ce dernier pour son encadrement. Il a su trouver la bonne distance entre directivité et laisser faire pour que je prenne plaisir à explorer de nouvelles pistes, sans jamais que je ne me sente laissé pour compte. Les discussions que nous avons eu, ses conseils et ses corrections ont été, et sont encore, extrêmement précieux à mes yeux.

Je veux saluer ici tous mes compagnons de galère, qui adoucirent largement l'âpreté des jours sans, ces jours ou rien ne fonctionne et où la seule alternative au fatalisme est d'en faire la catharsis dans le bureau du bout du couloir. Je veux donc remercier tous ceux avec qui j'ai passé de longues minutes (quelqu'un a dit heures ?) à discuter de tout, de rien, et de philosophie, Emmanuel, Johannes, Gherardo, Étienne, Zlatko, Quentin, Gille-Alexis, Annabelle, Wiebke, Saira, Giullia, Victor, Julissa, Thomas, Martin, Ludovic, Valdo, Anne-Lise, Pierre, Jiang, et tous ceux que j'oublie. Il n'y eu guère de temps plus utile que ce temps perdu. Je les remercie aussi pour tout ce qu'ils m'ont appris. Je souhaite d'ailleurs à ceux qui n'ont pas terminé, au moment ou j'écris ces lignes, d'avoir toute confiance en leur réussite. En tout cas, je crois en vous.

Merci à Feng d'avoir toujours été d'un grand répondant dans nos collaborations, et à Nicolas pour m'avoir permis d'avoir une excellente première expérience d'encadrement.

Je veux plus largement remercier tous les membres du groupe Turbomachines pour leur bonne accueil et pour m'avoir fait me sentir à ma place avant même la thèse, dès mon premier jour de stage de TFE, il y a déjà quatre ans. Parmi eux, je tiens particulièrement à remercier Alexis Giauque, pour ne jamais s'être satisfait d'un résidu d'explication et m'avoir obligé à blinder mon discours pour qu'il résiste à toutes les occasions, et Stéphane Aubert, pour ce qu'il m'aura appris sur le Code avec un grand "C", le code de calcul, et en général pour les discussions enrichissantes que nous avons eu et qui m'ont permises de trouver de nouvelles idées.

Je remercie aussi Christian Nicot, avec qui j'ai partagé bien plus qu'un bureau et des cafés. Sans lui, les longues journées de travail devant un écran auraient été bien ternes. Je n'oublie pas Mathieu Creyssels, dont les diatribes flamboyantes contre l'ordre établi ajoutaient juste ce qu'il fallait de subversion au café du matin.

Je tiens aussi à remercier mes amis de très longue date, Éva, Pierre, Marine, et particulièrement Thomas, Jules et Valentin, avec qui je suis sûr nous arriverons un jour à fonder notre ferme collective utopique. Si possible près d'un lac à l'eau turquoise, sur lequel se laisse bercer nonchalamment un pédalo dont la ligne de flottaison ne dessine pas vraiment une ligne d'horizon, et dont les profondeurs sont habitées par un unique

poisson au régime alimentaire plus que spécial. Je ne perd pas non plus espoir qu'un jour ils m'écoutent parler de physique !

Je remercie, car si cela va sans dire, cela va mieux en le disant, mon frère, mes parents et mes grands-parents. C'est beaucoup grâce à vous que j'en suis là aujourd'hui. Je vous aime, vous le savez, et sachez que je ne doute pas de la réciproque.

Parce que la thèse n'est pas une parenthèse dans la vie, je veux remercier Élodie, ma femme, a qui je dois beaucoup. Merci de m'avoir emmené à Bayonne et à l'autre bout du monde. Merci d'avoir organisé le plus incroyable des mariages. Merci d'avoir géré une immense partie de la logistique du quotidien pendant la fin de la thèse. Merci de ton soutien du début à la fin de cette thèse. Merci surtout d'être la meilleure des mamans pour notre (nos) magnifique(s) petit(s) humain(s). Merci d'avoir eu le courage, et l'audace (voir l'inconscience), de te lancer dans tout cela avec moi. Je t'aime BIEN !

Enfin, Maximilien, si un jour tu lis ces lignes, sache que je te remercie d'avoir été un enfant aussi merveilleux pendant cette dernière année de thèse, et de l'avoir rendue à la fois merveilleuse et épique. Tu es le meilleur. Je t'aime. A mes autres enfants, pas encore avec nous, sachez que cette thèse vous est aussi dédiée, et que je vous aime aussi. J'ai hâte de vous connaître, et je ne doute pas que vous soyez aussi les meilleurs.

Abstract

The present study aims at analysing turbulence modelling in Reynolds-averaged Navier-Stokes (RANS) simulations, in the context of turbomachinery flows, using large-eddy simulations (LES) as references. Two test cases are considered: a corner separation (CS) flow in a linear compressor cascade, and a tip-leakage (TL) flow of a single blade in a jet. Two constitutive relations, the Boussinesq constitutive relation and the quadratic constitutive relation (QCR), are investigated, with two versions of Wilcox's $k-\omega$ turbulence model.

The studied constitutive relations rely on two hypotheses: an alignment hypothesis between the Reynolds stress tensor and a mean flow tensor, and an hypothesis on the turbulent viscosity. The alignment hypothesis is investigated using LES, where both the tensors are known independently, with an indicator built on the inner product of the tensors. The results are presented as probability density functions of the indicator value for the entire domain first, and then for three specific areas of interest: the inlet area, similar to a boundary-layer flow, an area of strong interaction between the flow and the walls (CS: passage area, TL: tip clearance) and an area of highly vortical flow (CS: separation wake, TL: tip-leakage vortex). The alignment hypothesis is rarely verified in any area for the Boussinesq constitutive relation. For the QCR, the results are improved for the inlet areas compared to the Boussinesq constitutive relation, but no significant improvement is found in the highly vortical regions. An improvement of the constitutive relation is needed in order to improve the RANS turbulence modelling. In contrast, the use of the turbulent kinetic energy and the specific dissipation rate appears quite correct to estimate the turbulent viscosity.

The modelling of the RANS turbulent kinetic energy (TKE) budget equation is investigated through a term to term comparison with the resolved LES TKE budget equation. The LES presents a turbulence that is not at equilibrium, with the production and the dissipation not superimposed, and an important amount of transport. This differs from the RANS models, at equilibrium: the production and the dissipation are superimposed, with a small amount of transport. The development of a non-equilibrium turbulence model for RANS simulations could improve this aspect of turbulence modelling.

Finally, a new hybrid RANS-LES formulation, based on the wall distance in wall units, is also proposed. It is validated on a bi-periodical channel flow, and a first attempt is made on the corner separation case, but further investigations are still needed for the model to be fully operational.

Keywords : large-eddy simulation; Reynolds-averaged Navier-Stokes; turbulence modelling; constitutive relation; TKE budget; corner separation; tip-leakage; hybrid RANS-LES

Résumé

L'objectif de la présente étude est d'analyser la modélisation de la turbulence de simulations en moyenne de Reynolds (RANS) dans le cadre d'écoulements de type turbomachines, en utilisant des simulations aux grandes échelles (SGE) comme référence. L'étude porte sur deux cas test: un décollement de coin dans une grille d'aubes rectiligne, et un écoulement de jeu pour un aubage isolé dans un jet. Deux lois de comportement, la loi de comportement de Boussinesq et la loi de comportement quadratique (*quadratic constitutive relation* ou QCR), sont analysées, avec deux versions du modèle de turbulence $k-\omega$ de Wilcox.

Les lois de comportement étudiées reposent sur deux hypothèses: une hypothèse d'alignement entre le tenseur de Reynolds et un tenseur construit à partir de l'écoulement moyen, et une hypothèse sur la viscosité turbulente. L'hypothèse d'alignement est étudiée à partir de la SGE, pour laquelle les deux tenseurs sont indépendamment connus, en utilisant un indicateur construit sur le produit scalaire des tenseurs. Les résultats sont présentés sous forme d'une fonction de répartition de la valeur de l'indicateur pour le domaine complet, puis pour trois sous-domaines d'intérêt: l'entrée, une région où l'écoulement interagit fortement avec les parois, et une région où l'écoulement est fortement tourbillonnaire. L'hypothèse d'alignement n'est que rarement valide pour la loi de comportement de Boussinesq. Pour la QCR, les résultats sont meilleurs en entrée, comparé à la loi de Boussinesq. Il ne sont cependant pas meilleurs pour les régions où l'écoulement est plus tourbillonnaire. Une amélioration de la loi de comportement est nécessaire pour pouvoir faire progresser la modélisation turbulente en RANS. En revanche, l'utilisation de l'énergie cinétique turbulente et du taux de dissipation spécifique semble correcte pour estimer la valeur de la viscosité turbulente.

L'analyse de la modélisation de l'équation d'énergie cinétique turbulente (ECT) est réalisée au travers d'une comparaison terme à terme avec l'équation d'ECT résolue par la SGE. Les résultats SGE présentent une turbulence qui n'est pas à l'équilibre : la production et la dissipation ne sont pas superposées, et le terme de transport est important. Pour le RANS, la turbulence est à l'équilibre : la production et la dissipation sont superposées, et le terme de transport est de faible intensité. Un modèle de turbulence qui prend en compte le déséquilibre est nécessaire pour améliorer ce point.

En dernier lieu, une nouvelle formulation hybride RANS/SGE est proposée, fondée sur la distance à la paroi en unités de paroi. La formulation est validée dans un canal bi-périodique et un premier essai est réalisé sur le cas de décollement de coin, mais d'autres analyses sont nécessaires avant que cette formulation ne soit fonctionnelle.

Mot clefs : simulation aux grandes échelles (SGE); simulation en moyenne de Reynolds (RANS); modélisation de la turbulence; loi de comportement; bilan d'énergie cinétique turbulente; décollement de coin; écoulement de jeu; hybride RANS/SGE

Contents

List of Figures

List of Tables

Nomenclature

NB : First order tensors (vectors) are underlined and second order tensors (matrix) are underlined twice. Einstein summation notation is used all over the manuscript, in order to simplify formula writing.

Latin characters

c	[m]	Chord length
C_1	[−]	Kok et al. (2004) hybrid model constant
c_a	[m]	Chord length projection on the x_1 direction
c_{b1}	[−]	Spalart and Allmaras (1994) model constant
c_{b2}	[−]	Spalart and Allmaras (1994) model constant
C_{DES}	[−]	DES model constant (Spalart et al., 1997)
c_{exp}	[−]	Exponentially weighted moving average constant (Cahuzac et al., 2010)
C_f	[−]	Friction coefficient
c_k	[−]	Wilcox (1988) turbulence model constant
c_l	[−]	IDDES model constant (Shur et al., 2008)
C_μ	[−]	Turbulence model constant
c_μ	[−]	Wilcox (1988) turbulence model constant
$c_{\omega 1}$	[−]	Wilcox (1988) turbulence model constant
$c_{\omega 2}$	[−]	Wilcox (1988) turbulence model constant
c_p	[J.K^{-1}.kg^{-1}]	Constant pressure heat capacity
C_p	[−]	Static pressure coefficient
C_{p_t}	[−]	Total pressure loss coefficient
c_{QCR}	[−]	QCR constant
C_s	[−]	Smagorinsky (1963) constant
c_t	[−]	IDDES model constant (Shur et al., 2008)
c_{t3}	[−]	Spalart and Allmaras (1994) model constant
c_{t4}	[−]	Spalart and Allmaras (1994) model constant
c_v	[J.K^{-1}.kg^{-1}]	Constant volume heat capacity
c_{v1}	[−]	Spalart and Allmaras (1994) model constant
c_{w1}	[−]	Spalart and Allmaras (1994) model constant
c_{w2}	[−]	Spalart and Allmaras (1994) model constant
c_{w3}	[−]	Spalart and Allmaras (1994) model constant
C_W	[−]	IDDES model constant (Shur et al., 2008)
d	[m]	Wall distance
$\hat{d}$	[m]	Wall distance for the DES (Spalart et al., 1997)
D	[−]	Lieblein (1959) diffusion factor
d_I	[m]	ZDES wall distance for mode I (Deck, 2012)

d_{II}	[m]	ZDES wall distance for mode II (Deck, 2012)
d_{III}	[m]	ZDES wall distance for mode III (Deck, 2012)
d_{μ}^{+}	[−]	Center of the hybrid transition area
e	[$m^2.s^{-2}$]	Internal energy
e_t	[$m^2.s^{-2}$]	Total energy
$\mathbf{f}$	[−]	Tucker et al. (2012a) model function
f_c	[s^{-1}]	Characteristic frequency of the SISM
f_d	[−]	DDES hybridisation function (Spalart et al., 2006)
f_{d0}	[−]	ZDES model constant (Deck, 2012)
f_e	[−]	IDDES model function (Shur et al., 2008)
f_{e1}	[−]	IDDES model function (Shur et al., 2008)
f_{e2}	[−]	IDDES model function (Shur et al., 2008)
f_{hyb}	[−]	IDDES hybridisation function (Shur et al., 2008)
f_{hyb}	[−]	Proposed hybrid model hybridisation function
f_l	[−]	IDDES model function (Shur et al., 2008)
f_{μ}	[−]	Proposed hybrid model function
f_{r1}	[−]	Modified Wilcox model function (Liu et al., 2016)
f_{step}	[−]	IDDES model function (Shur et al., 2008)
f_t	[−]	IDDES model function (Shur et al., 2008)
f_{t2}	[−]	Spalart and Allmaras (1994) model function
f_{v1}	[−]	Spalart and Allmaras (1994) model function
f_{v2}	[−]	Spalart and Allmaras (1994) model function
f_w	[−]	Spalart and Allmaras (1994) model function
g	[−]	Spalart and Allmaras (1994) model function
$\mathbf{g}$	[−]	Tucker et al. (2012a) model function
h	[m]	Span length for the CS configuration
h	[m]	Clearance height for the TL configuration
H	[m]	ZDES separation height (Deck, 2012)
H_{12}	[−]	Shape factor
$\underline{\underline{I_3}}$	[−]	Identity tensor
I, J, K	[−]	Mesh points indexes
$ides$	[−]	ZDES constant (Deck, 2012)
$imode$	[−]	ZDES constant (Deck, 2012)
k	[$m^2.s^{-2}$]	Turbulent kinetic energy
$\hat{l}$	[m]	Kok et al. (2004) turbulent length-scale
L	[m]	Distance from the wall to the LES area in Tucker et al. (2012a) hybrid model
L_{hyb}	[−]	Hybrid transition length (wall units)
$L_{x_1}, L_{x_2}, L_{x_3}$	[m]	Flat-plate dimensions
M	[−]	Mach number
N_k	[−]	Kinematic vorticity
Nn	[s^{-1}]	Compressor rotation speed
$\underline{\underline{O}}$	[−]	Normalised rotation tensor
p	[$kg.m^{-1}.s^{-2}$]	Static pressure
p_e	[$kg.m^{-1}.s^{-2}$]	Inflow static pressure
P_k	[$kg.m^{-1}.s^{-3}$]	TKE production term
Pr	[−]	Prandtl number

Pr_{SGS}	[−]	SGS Prandtl number
Pr_t	[−]	Turbulent Prandtl number
p_t	[kg.m^{-1}.s^{-2}]	Total pressure
p_{te}	[kg.m^{-1}.s^{-2}]	Inflow total pressure
$\underline{q}$	[kg.s^{-3}]	Heat flux
Q	[s^{-2}]	Local balance between the strain rate and the vorticity magnitude
r	[−]	Spalart and Allmaras (1994) model function
$\underline{\underline{R}}$	[m^2.s^{-2}]	Spatial correlations matrix
r_{air}	[J.K^{-1}.kg^{-1}]	Specific gas constant
r_d	[−]	DDES model function (Spalart et al., 2006)
r_{dl}	[−]	IDDES model function (Shur et al., 2008)
Re	[−]	Reynolds number
R_j	[m^3]	Square root of the Jacobian
s	[m]	Pitch length for the CS configuration
S	[−]	corner separation criterion (Lei et al., 2008)
$\underline{\underline{S}}$	[s^{-1}]	Strain rate tensor
$\tilde{S}$	[s^{-1}]	Spalart and Allmaras (1994) model function
t	[s]	Time
t_{start}	[s]	Beginning time for the average
T	[K]	Static temperature
$\underline{u}$	[m.s^{-1}]	Velocity vector
u_e	[m.s^{-1}]	Free-stream velocity
u_τ	[m.s^{-1}]	Friction velocity
V	[m^3]	Volume of an integration cell
$\underline{x}$	[m]	Position vector

Greek characters

β	[−]	ZLES model function (Boudet et al., 2015a)
γ	[−]	Specific heat ratio
γ	[−]	Stagger angle for the CS configuration
$\underline{\gamma}$	[m^{-1}]	Third vector of the contravariant basis
Γ_1, Γ_2	[−]	Functions for the center and extent of a vortex
δ	[m]	Boundary-layer thickness
Δ	[m]	Grid spacing for the SISM (Lévêque et al., 2007)
Δ	[m]	DES sub-grid scale (Spalart et al., 1997)
$\delta_{1/2}$	[m]	Bi-periodical channel half-height
δ_1	[m]	Displacement thickness
δ_2	[m]	Momentum thickness
δ_{ij}	[−]	Kronecker's delta
$\Delta_{\max}$	[m]	Maximal cell dimension: $\max(\Delta_x, \Delta_y, \Delta_z)$
Δt	[s]	Time step for the average
Δ_{vol}	[m]	Cell dimension based on the cubic root of the volume
Δ_{vort}	[m]	Cell dimension based on the vorticity
Δ_{wn}	[m]	Cell dimension in the wall-normal direction
$\underline{\Delta x}$	[m]	Cell sizes at the wall
ε	[m^2.s^{-3}]	Turbulence dissipation rate

ϵ_0	$[-]$	Tucker et al. (2012a) model constant
ϵ_1	$[-]$	Tucker et al. (2012a) model constant
$\underline{\eta}$	$[\mathrm{m}^{-1}]$	Second vector of the contravariant basis
$\underline{\Theta}$	$[\mathrm{kg.s}^{-3}]$	SGS heat flux
κ	$[-]$	Von Kármán constant for the Spalart and Allmaras (1994) model
κ	$[\mathrm{kg.m.s}^{-3}.\mathrm{K}^{-1}]$	Thermal conductivity
κ_{SGS}	$[\mathrm{kg.m.s}^{-3}.\mathrm{K}^{-1}]$	SGS thermal conductivity
κ_t	$[\mathrm{kg.m.s}^{-3}.\mathrm{K}^{-1}]$	Turbulent thermal conductivity
Λ	$[\mathrm{kg.m}^{-1}.\mathrm{s}^{-3}]$	k-production limiter
μ	$[\mathrm{kg.m}^{-1}.\mathrm{s}^{-1}]$	Dynamic viscosity
μ_{hyb}	$[\mathrm{kg.m}^{-1}.\mathrm{s}^{-1}]$	Hybrid viscosity
μ_{mod}	$[\mathrm{kg.m}^{-1}.\mathrm{s}^{-1}]$	Hybrid turbulent/SGS viscosity (Boudet et al., 2015a)
μ_{SGS}	$[\mathrm{kg.m}^{-1}.\mathrm{s}^{-1}]$	SGS viscosity
μ_t	$[\mathrm{kg.m}^{-1}.\mathrm{s}^{-1}]$	Turbulent viscosity (also called eddy-viscosity)
$\mu_t^{(0)}$	$[\mathrm{kg.m}^{-1}.\mathrm{s}^{-1}]$	Turbulent viscosity estimated as ratio of tensor norms
$\mu_t^{(0)QCR}$	$[\mathrm{kg.m}^{-1}.\mathrm{s}^{-1}]$	Turbulent viscosity estimated as ratio of tensor norms
$\mu_t^{(1)}$	$[\mathrm{kg.m}^{-1}.\mathrm{s}^{-1}]$	Turbulent viscosity estimated with LES ρ, k and ω
ν	$[\mathrm{m}^2.\mathrm{s}^{-1}]$	Kinematic viscosity
$\hat{\nu}$	$[\mathrm{m}^2.\mathrm{s}^{-1}]$	Kinematic viscosity for Spalart and Allmaras (1994) model
$\underline{\xi}$	$[-]$	Cartesian mesh coordinates
$\underline{\Xi}$	$[\mathrm{kg.m}^{-1}.\mathrm{s}^{-3}]$	Numerical residual
$\underline{\underline{\Pi}}$	$[\mathrm{kg.m}^{-1}.\mathrm{s}^{-2}]$	SGS stress tensor
$\underline{\underline{\Pi}}^D$	$[\mathrm{kg.m}^{-1}.\mathrm{s}^{-2}]$	Deviatoric part of the SGS stress tensor
$\underline{\underline{\Pi}}^I$	$[\mathrm{kg.m}^{-1}.\mathrm{s}^{-2}]$	Isotropic part of the SGS stress tensor
ρ	$[\mathrm{kg.m}^{-3}]$	Density
ρ_e	$[\mathrm{kg.m}^{-3}]$	Free-stream density
$\underline{\varsigma}$	$[\mathrm{m}^{-1}]$	First vector of the contravariant basis
$\underline{\underline{\varsigma}}$	$[-]$	Arbitrary quantity
σ	$[-]$	Spalart and Allmaras (1994) model constant
$\underline{\underline{\sigma}}$	$[\mathrm{s}^{-1}]$	Zero-trace strain rate tensor
$\underline{\underline{\sigma}}^{QCR*}$	$[\mathrm{s}^{-1}]$	Zero-trace strain rate tensor with QCR modifications
σ_k	$[-]$	Wilcox (1988) turbulence model constant
σ_ω	$[-]$	Wilcox (1988) turbulence model constant
$\underline{\underline{\tau}}$	$[\mathrm{kg.m}^{-1}.\mathrm{s}^{-2}]$	Viscous stress tensor
$\underline{\underline{\tau_t}}$	$[\mathrm{kg.m}^{-1}.\mathrm{s}^{-2}]$	Reynolds stress tensor
$\underline{\underline{\tau_t}}^*$	$[\mathrm{kg.m}^{-1}.\mathrm{s}^{-2}]$	Reynolds stress tensor modelled with the Boussinesq constitutive relation
$\underline{\underline{\tau_t^{**}}}$	$[\mathrm{kg.m}^{-1}.\mathrm{s}^{-2}]$	Unmodelled zero-trace Reynolds stress tensor
$\underline{\underline{\tau_t}}^{QCR}$	$[\mathrm{kg.m}^{-1}.\mathrm{s}^{-2}]$	Reynolds stress tensor modelled with the QCR
τ_w	$[\mathrm{kg.m}^{-1}.\mathrm{s}^{-2}]$	Wall shear stress
Υ	$[-]$	Alignment indicator for the Boussinesq constitutive relation
Υ^{QCR}	$[-]$	Alignment indicator for the QCR
$\Upsilon_{\mathrm{Schmitt}}$	$[-]$	Schmitt (2007) indicator

$\Upsilon^{QCR}_{\text{Schmitt}}$	$[-]$	Schmitt indicator adapted for the QCR
φ	$[-]$	Arbitrary quantity
χ	$[-]$	Spalart and Allmaras (1994) model kinematic viscosity ratio
ψ	$[-]$	Low Reynolds number DES correction (Spalart et al., 2006)
ω	$[\text{s}^{-1}]$	Specific turbulence dissipation rate
$\underline{\Omega}$	$[\text{s}^{-1}]$	Vorticity
$\underline{\underline{\Omega}}$	$[\text{s}^{-1}]$	Vorticity tensor

Superscripts

φ^+ Quantity in wall units

Subscripts

$i,\ j,\ k$ Subscripts used for Einstein's summation

Abbreviations and names

ACARE	Advisory Council for Aeronautics Research in Europe
AR	Aspect ratio
BUAA	Beijing University of Aeronautics and Astronautics
CDF	Cumulative distribution function
CFD	Computational fluid dynamics
CFL	Courant–Friedrichs–Lewy condition
CPU	Central processing unit
CRV	Counter-rotating vortex
CS	Corner separation
DDES	Delayed detached-eddy simulation
DES	Detached-eddy simulation
DLR	*Deutsches Zentrum für Luft- und Raumfahrt*
ECT	*Énergie cinétique turbulente*
FWH	*Ffowcs Williams Hawkings*
GIS	Grid-induced separation
HPC	High performance computing
IATA	International Air Transport Association
IDDES	Improved delayed detached-eddy simulation
LE	Leading edge
LES	Large-eddy simulation
LMFA	*Laboratoire de Mécanique des Fluides et d'Acoustique*
MSD	Modelled stress depletion
NLES	Numerical LES
PDF	Probability density functions
PIV	Particle image velocimetry
POD	Proper orthogonal decomposition
PS	Pressure side

QCR	Quadratic constitutive relation
RANS	Reynolds-Averaged Navier-Stokes
SGE	*Simulation aux grandes échelles*
SGS	Sub-grid scale
SISM	Shear-improved Smagorinsky model
SS	Suction side
TE	Trailing edge
TL	Tip-leakage
TLV	Tip-leakage vortex
TSV	Tip-separation vortex
TKE	Turbulent Kinetic Energy
Turb'Flow	LMFA in-house CFD solver
VortexFlowCFD	International project of the present thesis
WALE	Wall-adapting local eddy-viscosity model
ZDES	Zonal detached-eddy simulation
ZLES	Zonal large-eddy simulation

Miscellaneous characters

$\underline{\varphi}$	Vector's notation
$\underline{\underline{\varphi}}$	Tensor's notation
$\langle\varphi\rangle$	Ensemble mean estimated as temporal mean
φ'	Ensemble fluctuation estimated as temporal fluctuation ($\varphi = \langle\varphi\rangle + \varphi'$)
$[\varphi]$	Favre ensemble mean estimated as temporal mean ($[\varphi] = \langle\rho\varphi\rangle \,/\, \langle\varphi\rangle$)
φ''	Favre ensemble mean fluctuation ($\varphi = [\varphi] + \varphi''$)
$\overline{\varphi}$	Low frequency filter
$\varphi`$	High frequency filter ($\varphi = \overline{\varphi} + \varphi`$)
$\widetilde{\varphi}$	Favre low frequency filter ($\widetilde{\varphi} = \overline{\rho\varphi}/\overline{\rho}$)
$\varphi``$	Favre high frequency filter ($\varphi = \widetilde{\varphi} + \varphi``$)
φ'	Ensemble mean fluctuating part for low frequency filtered quantity ($\overline{\varphi} = \langle\overline{\varphi}\rangle + \varphi'$)
φ''	Favre ensemble mean fluctuating part for Favre low frequency filtered quantity ($\widetilde{\varphi} = [\widetilde{\varphi}] + \varphi''$)

Introduction

Context

Never in the history of mankind it has been easier to travel around the world. Exchange abroad has never been this ordinary for the students, almost anyone can go as far as the other side of the world, to discover different cultures or make affairs. It is partly due to the development of civil aviation. Not only it is one of the fastest, surest means of transport, it also became incredibly affordable. The IATA gives a record numbers of 3.7 billions aerial passenger in 2016, a growth of 6.3% compared with 2015. This trend is expected to continue and accelerate, since the world aircraft fleet is expected to double within the next thirty years (Tucker, 2013).

This state of affairs suppose incredible challenges. A plane consume kerosene to fly, and release chemical and acoustic pollution in the atmosphere. Due to the deteriorating ecological situation of the world and the rarefaction of fossil fuel, these are burning issues. A global effort to reduce the pollutants emissions of all kind, along with the fuel consumption, is needed. In this context, the ACARE (Advisory Council for Aeronautics Research in Europe) proposed drastic objectives by 2020, with no less than a reduction of the specific fuel consumption by 20%, a CO_2 emissions reduction of 50%, a nitrogen oxide (NO_x) emissions reduction of 80%, and a perceived noise reduction of 50% for the planes compared to the one produced in 2000.

Consequently improvements are required in all the domains of aviation, from the plane conception to the air traffic. Among all the parameters, two key parameters are the engine efficiency and size. The size reduction leads to a mass reduction, thus a consumption reduction. With 40% to 50% of the weight, the gas turbine is an heavy part of the engine. Its mass reduction can be realised with a decrease of the number of its compressor stages. However, nowadays, with the high by-pass ratio and ultra-high by-pass ratio engines, the size reduction and decrease of the number of compressor stages is not the major issue for industrials. The increasing of the by-pass ratio leads to a more important improvement in term of efficiency. One point of compressor efficiency increase can be directly linked with a decrease in the specific fuel consumption between 0.5% and 0.8% (Courtiade, 2012). The problem boils down to a gas turbine compressor conception problem.

A major problem encountered during the conception phase, occurring even without reducing the number of compressor stages and increasing the loading, is the occurrence of three-dimensional, highly vortical secondary flows, such as corner separation or tip-leakage. The corner separation occurs at the junction between the suction side and the hub for a compressor rotor (suction side and casing for a compressor stator). It is the resultant of the end-wall boundary-layer and blade boundary-layer interaction. The tip-leakage flow is induced by the pressure difference between the pressure side

and the suction side of the blade, and the relative motion of the blade tip and the casing. It tends to develop as a large vortex and secondary vortices. These flow disturb the performances of the compressor. They have to be at least controlled, and when possible avoided.

Yet, even their characterisation during the conception phase is difficult. Industrial conception relies highly on numerical simulations. In a given time-span and at a reasonable cost, it allows to optimize configurations. However, industrial solver usually rely on Reynolds-averaged Navier-Stokes (RANS) modelling for computing cost reasons and represent imperfectly such flows. With the development of high performance computing (HPC), large-eddy simulations (LES) became tractable for simulating accurately the secondary flows, in a context of research. Conception improvements may be achieved by a better understanding of the RANS simulations capacity and limitations, to have in mind the bias it infers when it deals with secondary flows. Another possibility is to couple the RANS approach and the LES approach, in order to have an accurate description far from the walls with the LES, with less computational resources thanks to the use of RANS close to the walls. This last approach keeps being more expensive, computationally speaking, than RANS simulations, but can be coupled with it to have a multi-fidelity approach.

Objectives

This thesis is part of the project VortexFlowCFD, an international project that regroups academic structures, LMFA (Laboratoire de Mécanique des Fluides et d'Acoustique) in France and BUAA (Beijing University of Aeronautics and Astronautics) in China, and an industrial company, Safran Aircraft Engines. The objective of the project is to identify improvements in CFD (Computational fluid dynamics) codes with popular turbulence model used in industrial conception, in order to get a better description of highly turbulent, strongly rotating flows within a reasonable time-span.

The present work focuses on the characterisation of turbulence modelling in RANS simulations of rotating flows. These simulations relies on strong hypotheses, such as the Boussinesq hypothesis, and a complete modelling of the turbulent kinetic energy budget equation. Large-eddy simulation, which provides a detailed description of the largest turbulent eddies, is used as reference to evaluate the validity of the Boussinesq hypothesis, through a local criterion, and the turbulent kinetic energy budget equation modelling, through a local term to term comparison. These comparisons are done in three-dimensional, highly vortical flows, a corner separation flow in a linear compressor cascade, and a tip-leakage flow of a single blade in the potential core of a jet.

Furthermore an hybrid RANS-LES formulation is proposed. This formulation is inspired from Tucker's formulation (Tucker et al., 2012a), and presents the advantage to be adaptable to any couple of RANS-LES models that relies on an eddy-viscosity. The hybrid RANS-LES method is tested on the corner separation flow previously mentioned.

Outlines

Part I presents the state of the art.

- Chapter 1 gives a short introduction on turbomachinery and reviews previous works on corner separations and tip-leakage flows.
- Chapter 2 presents the governing equations of the flows and details the large-eddy simulations approximations, models, and formulation, along with the approximations, models, and formulation of Reynolds-averaged Navier-Stokes simulations.
- Chapter 3 reviews the existing hybrid RANS-LES models and discuses their advantages and limitations.

Part II presents the methods used in this thesis.

- Chapter 4 details the implementation of the LES turbulent kinetic energy budget extraction. The implementation is validated on a flat-plate boundary-layer test-case against direct numerical simulation results.
- Chapter 5 details the proposed hybrid RANS-LES method and its validation on a bi-periodical channel, against direct numerical simulation results.
- Chapter 6 details the simulation protocols used for the corner separation simulations and the tip-leakage simulations.

Part III presents the results.

- Chapter 7 concerns the mean flow and the Reynolds stress analysis on the corner separation case. The Reynolds stresses are compared between LES results and RANS results.
- Chapter 8 presents the constitutive relation validity analysis on the corner separation case.
- Chapter 9 is about the turbulent kinetic energy budget comparison on the corner separation case.
- Chapter 10 details the results of an hybrid RANS-LES simulation of the corner separation, compared with the LES results and the RANS results.
- Chapter 11 concerns the mean flow and the Reynolds stress analysis on the tip-leakage case.
- Chapter 12 presents the constitutive relation validity analysis on the tip-leakage case.
- Chapter 13 is about the turbulent kinetic energy budget comparison on the tip-leakage case.

Part I

State of the art

Chapter 1

Secondary flows in axial turbomachineries

Sections

Jet engines were a revolution for aircraft propulsion. Originally imagined in parallel by Frank Whittle and Hans von Ohain as a device able to produce an important amount of thrust for long periods with an affordable mass for aircrafts, the technology has evolved a lot to become the aircraft engines known today.

1.1 Axial turbomachinery generalities

In order to generate thrust, an aircraft engine needs to accelerate the ambient air. This creates a reciprocal force from the fluid on the plane, as stipulated by Newton's third law. This is done in modern aircraft engines by exploiting the Brayton thermodynamic cycle: air is breathed at the inlet of the engine, compressed, a mix of air-fuel is burnt in the combustion chamber, goes through a turbine and is accelerated in a nozzle. The compression is necessary to the cycle. The turbine extracts from the exhaust gas the amount of energy necessary to power the compressor. Finally, the nozzle accelerates the fluid, by changing a part of the remaining fluid thermal energy into kinetic energy, to maximise the thrust, proportional to the mass flow rate times the velocity.

Modern designs rely generally on two-flux turbofans. The primary flux ensures the Brayton cycle while the secondary flux increases the mass flow rate, in order to increase

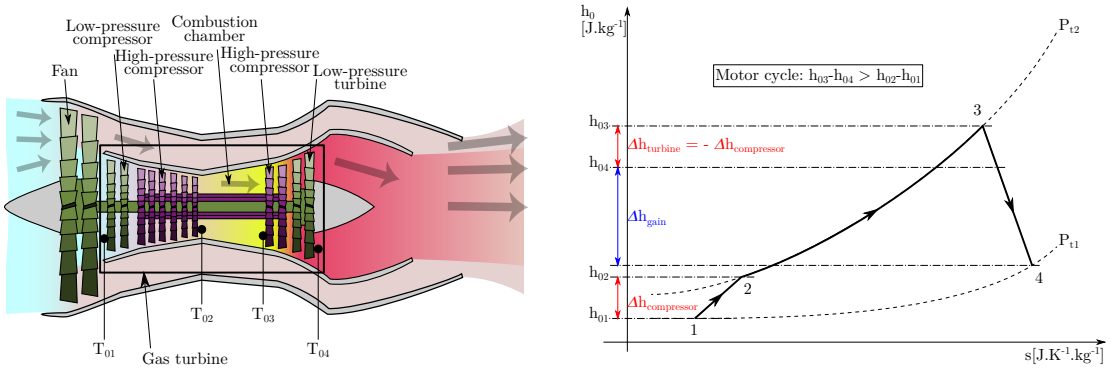

(a) Turbofan sketch (b) Brayton cycle

Figure 1.1: Generic modern turbofan sketch (a) (modified from "Turbofan operation" by K. Aainsqatsi - Own work. Licensed under Creative Commons Attribution 2.5 via Wikimedia Commons.) and its associated Brayton cycle (b).

the thrust. A generic turbofan sketch and its associated Brayton cycle is presented in figure 1.1. The primary flux produces around 20% of the thrust while the secondary flux produces around 80% of the thrust.

The compressor of the axial gas turbine is made of successive stages. Each stage presents a rotor, a row of blades in rotation, upstream a stator, a row of fixed vanes. The rotor aims at increasing the total temperature and pressure, while the stator plays the role of a diffuser that increases the static pressure. The pressure ratio of a stage is defined as the ratio between the outlet pressure and the inlet pressure. The pressure increases along the compressor, so the pressure gradient is adverse to the flow.

Due to the variety of flight phases, the engines are built to operate at various rotation speeds. Considering a given rotation speed, the adverse pressure gradient acts as a throttle. When the pressure ratio increases, the adverse pressure gradient increases and the mass flow rate generally decreases. The evolution of the pressure ratio against the mass flow rate for various rotation speeds are usually represented in a performance characteristic map. A generic performance characteristic map of an axial compressor is presented in Fig. 1.2. For a given rotation speed, if the pressure ratio is too important, *ergo* the mass flow rate too weak to counter the pressure gradient, surge happens. On the other hand, if the the mass flow rate is too important, the flow becomes supersonic and the compressor is choked. The main goal of design is to stay away from these areas, and to place preferably the operating point as close as possible to the maximum of efficiency.

However, even when the operating point is far from the surge line and the choke line, various mechanisms (pressure gradients, trajectory curvature, viscosity,...) lead to what is known as secondary flows. These flows dissipate the energy given to the fluid and can damage the compressor. For this reason, the secondary flows have to be controlled, which requires their correct representation by numerical simulation. An illustration of secondary flows encountered in turbomachinery is given in figure 1.3. Among these secondary flows are the corner separation and the tip-leakage flow, which are studied in this work.

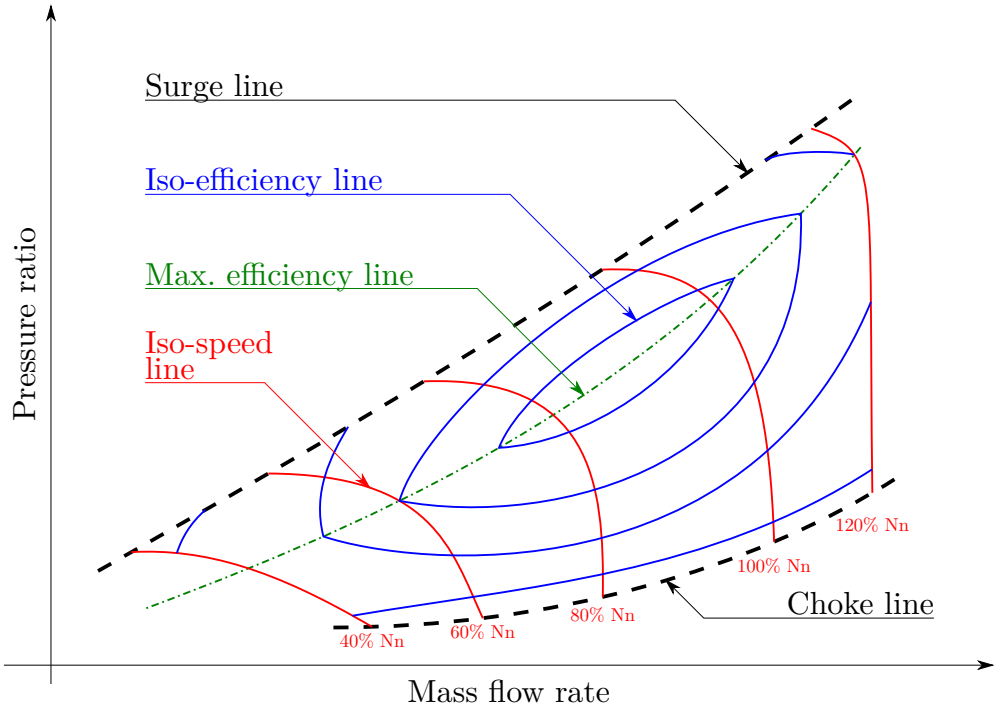

Figure 1.2: Generic performance characteristic map of an axial compressor

1.2 Corner separation

Corner separation is a three-dimensional phenomenon occurring at the junction of two orthogonal boundary layers. In can appear in external flows (Bordji et al., 2015) or in internal flows. This state of the art focuses on internal flows.

In compressors, this can concern the junction between the blade boundary layer and the hub boundary layer for a rotor (or casing boundary layer for a stator). Corner separation can be studied in linear cascades, which present advantages, such as isolation of the phenomenon and easier instrumentation for measurements.

1.2.1 In a rotor

Dring et al. (1982) carried out measurements on an isolated rotor with highly loaded blades. They observed a corner separation on the suction side of the blades. When the loading increases, the separation develops over the entire span of the blade. Conclusions were that corner separation increases losses of the rotor and modifies the wakes generated by the blades, which can impact stages downstream.

Wisler (1985) built a compressor of large dimension in order to make measurements at high Reynolds number with a low velocity flow. He observed a corner separation on the first rotor when the compressor works at full capacity. He considered the corner separation to be one of the most important sources of losses for the compressor.

1.2.2 In a stator

Joslyn and Dring (1985) carried out measurements on the second stage stator of two-stage compressor of large dimension and low rotation speed, which was an upgrade of Dring et al. (1982) experimental set-up. Experiment was made for three working points, the nominal one, a lightly loaded one, and one close to the stall point of the

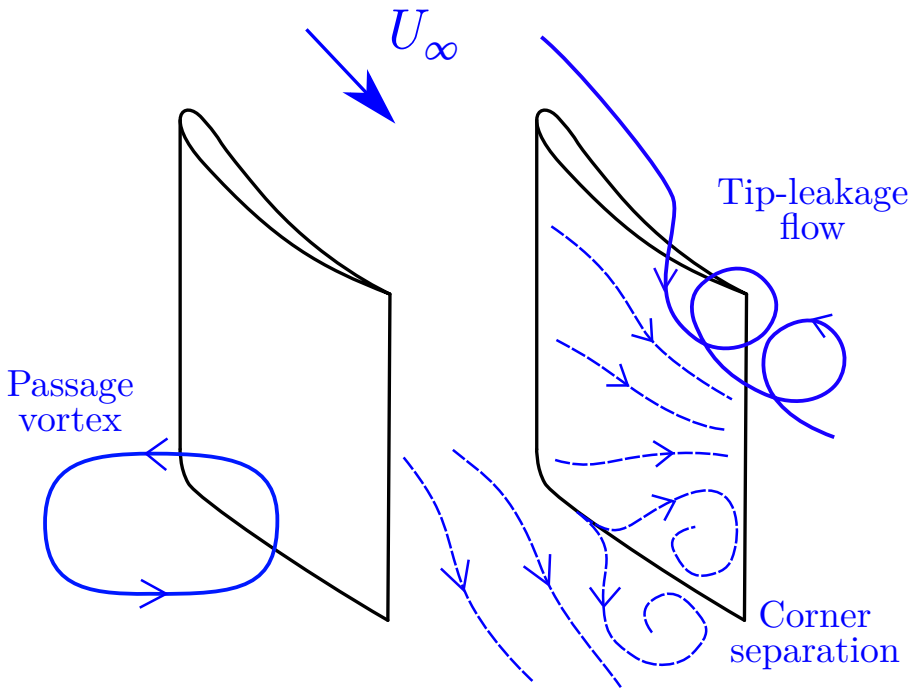

Figure 1.3: Sketch of secondary flows in turbomachinery, modified from Boudet (2014). ——— : stream lines, – – – : friction lines.

blades. Corner separation is observed at each working point, and increases as the loading of the blades increases. Moreover, the majority of losses takes place in the separated regions.

Li et al. (1992) carried out measurements on an annular cascade at low Reynolds number ($\mathrm{Re} < 1.1 \cdot 10^5$) and low Mach number ($M < 0.1$) for four different incidence angles. Flow is directed at the entrance with a distributor. Corner separation is observed through an oil visualisation method and pressure loss measurements. They show that the separation is highly turbulent and can be considered as a "dead zone", not participating to the overall diffusion. They claim that the losses due to corner separation are more important than those due to secondary flows or wake-blade interaction.

Schulz and Gallus (1988) conducted an experimental campaign in order to determine the precise impact of blade loading on three-dimensional flows by varying the incidence angle. The study was done on an annular cascade and the incidence angle variation went from a slightly negative value to a strongly positive value. A corner separation was observed for each incidence at the junction of the hub and the blade. When loading increases, the hub-blade separation tends to increase while the leading edge separation tends to reduce. Besides, a zone of high losses is observed downstream of the separation. Measurements suggest a direct responsibility of the corner separation in those losses.

Hah and Loellbach (1999) lead a study with both experiments and numerical simulations on the aforementioned annular cascade set-up (Schulz and Gallus, 1988). They managed to demonstrate the existence of two counter-rotating vortices using a RANS simulation (Fig. 1.4). One of those vortices originates from the hub, the other from the blade. When they meet, they create a region with strong back-flow that gives birth to corner separation. The experimental results confirm the existence of those

two vortices.

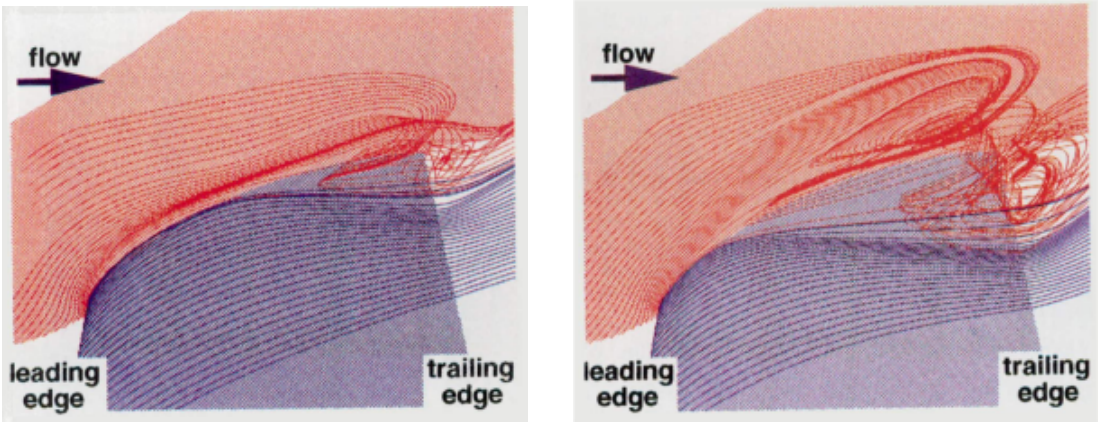

(a) Flow angle : 44.2° (b) Flow angle : 49.2°

Figure 1.4: Visualisation of two counter-rotating vortices for two different incidence angles. At low loading, *i.e.* at low incidence angle, the corner separation is weak (a). When loading increases, corner separation increases in both size and intensity (b). Results from Hah and Loellbach (1999).

Yamada et al. (2016) realised a detached-eddy simulation of the 7th first stages of the test rig used for development of the industrial gas turbine Kawasaki L30A, in order to investigate rotating stall inception. They found a hub corner separation in one passage in the 6th stator stage, whose growth leads to a leading edge separation. This instigates another hub corner separation in a neighbour passage, and evolves into a rotating stall.

1.2.3 In a linear cascade

Yocum and O'Brien (1993a,b) did an experimental study on a linear cascade for various stagger angles. They observed a corner separation and concluded that stagger angle influences strongly its characteristics. Surprisingly, they also concluded that the Reynolds number has little effect on the corner separation characteristics in the range tested $\left(\mathrm{Re} \in \left[5.0 \times 10^4,\ 2.0 \times 10^5\right]\right)$.

Ma et al. (2011, 2013) conducted a series of experiments in order to both understand deeply the physics of corner separation and create a database for LES and RANS calibration. They showed the existence of a bi-modal phenomenon at the interface of the corner separation and the non-separated flow (see fig. 1.5) (Ma et al., 2013). They did not manage to understand clearly the physical origin of such a phenomenon. It is supposed to be due to two aperiodic phenomena appearing alternatively.

Zambonini and Ottavy (2015) realised unsteady pressure measurements on the same linear cascade. In contrast with the velocity measurements, the wall static pressure never presents bimodal probability density functions. However, the second, third and fourth order moments of the unsteady pressure signals show unsteady intermittent behavior of the separation line on the suction surface. Later time-resolved particle imaging velocimetry (PIV) measurements and proper orthogonal decomposition (POD) analysis infer that the bimodal behaviour is an intermittent switch between two sizes of separation, large and almost suppressed (Zambonini, 2016; Zambonini

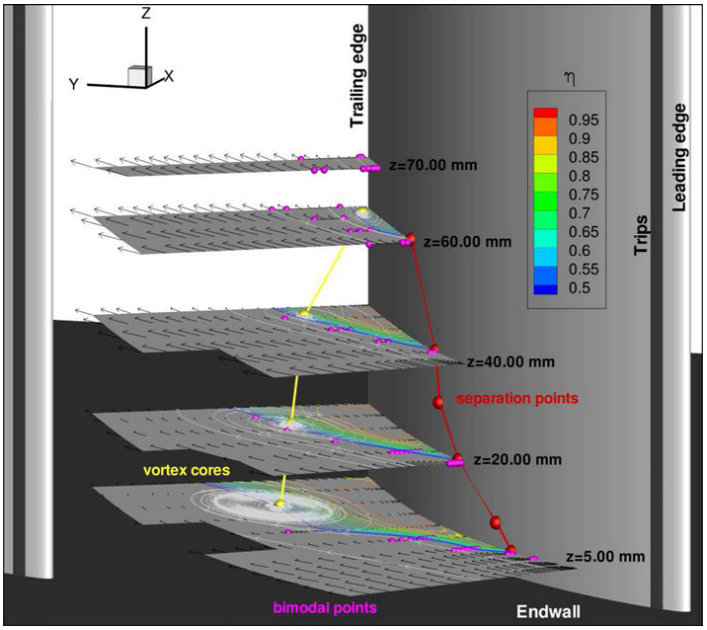

Figure 1.5: Corner separation in a linear cascade, from Ma et al. (2013). Vortex cores, separation border and places where bi-modal phenomena occur are represented.

et al., 2017). The cyclic mechanism begins with the absorption by the separation of fluctuations coming from the leading edge that destabilize it. It provokes a growth of the separation, which increases blockage until its main constituting vortex breaks down and the separation almost vanishes.

Gao et al. (2015a), on the same configuration as Ma et al. (2011), did a numerical study using both LES and RANS simulations. The LES simulation gave results in good agreement with the experimental results. RANS gave poorer results, with a systematic overestimation of the size of the corner separation and the pressure losses. A bi-modal tendency was observed also in the LES simulation (Gao et al., 2015b) but the sampling was not long enough to confirm it. The present work uses the LES results of Gao et al. (2015a) in order to evaluate RANS modelling.

Scillitoe et al. (2017) realised a large-eddy simulation of two linear compressor blade cascades to investigate the effect of various sub-grid scales models on the prediction of corner separation, and the effects of the free-stream turbulence intensity and end-wall boundary-layer state on the corner separation behaviour. They conclude that the usual Smagorinsky SGS model (Smagorinsky, 1963) is not suited for this kind of flow, due to its weak prediction close to the walls. The WALE model (Nicoud and Ducros, 1999) and the σ model (Nicoud et al., 2011) perform better. The state of the end-wall boundary layer is found to be of critical importance for the description of the corner separation. On the other hand, the free-stream turbulence intensity is found to have little effect on the corner separation.

1.2.4 Separation criteria

Lei et al. (2008) did a vast study, experimentally and numerically, on more than hundred different geometries for the numerical part, to find a criterion for the existence of a corner separation and its kind. The criterion is composed of two numbers, S and D, respectively the corner separation criterion and the Lieblein diffusion factor (Lieblein,

1959). Those numbers depend on some global parameters of the flow, such as flow angles, solidity, geometrical characteristics of the blades or boundary-layer thickness for instance. The criterion and its sensitivity is given in figure 1.6. A value $S > 0.12$ indicates a corner separation. A recirculation (much smaller than an actual corner separation) can be found for $S \leqslant 0.12$. Correlation indicates that corner separation appears when $D \geqslant 0.4 \pm 0.05$, but Gao (2014) observed a corner separation for $D = 0.26$ (*cf* fig. 1.7).

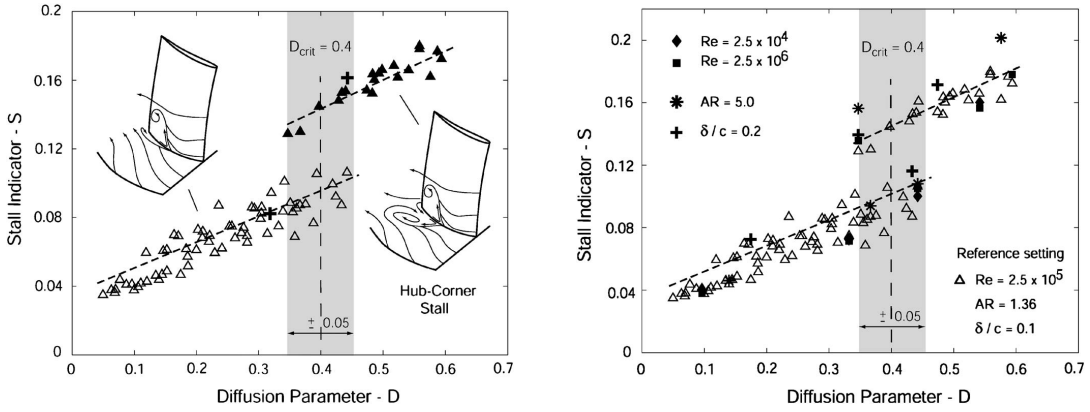

(a) Correlation between S and D

(b) Criterion sensitivity

Figure 1.6: Corner separation criterion from Lei et al. (2008). Sub-figure (a) shows the correlation between the stall criterion S and the Lieblein diffusion factor (D). Sub-figure (b) shows the sensitivity of the criterion to the Reynolds number (Re), the aspect ratio (AR) and the non-dimensional boundary-layer thickness (δ/c).

1.3 Tip-leakage flow

The tip-leakage flow is a three-dimensional, highly vortical flow induced by the pressure difference between the pressure side and the suction side of the blade, and the relative motion of the blade tip and the casing. It is responsible for pressure losses, noise, and influences the stability of the compressor. An intense vortex, referred to as the tip-leakage vortex (TLV), develops from the tip-clearance and can develop natural unsteadinesses.

1.3.1 Topology

Lakshminarayana et al. (1995) realised a detailed measurement, with a rotating five-hole probe, of the flow field in the tip region of an axial flow field compressor rotor. The goal of the study was to obtain the structures of the flow field in the vicinity of the tip gap. They found differences with the flow fields observed in cascades (Storer and Cumpsty, 1991). In their rotor measurements, the leakage jet is present, but does not roll up into a vortex. It mixes with the main flow stream and produces flow separation.

You et al. (2007a) realised a large-eddy simulation of a tip-leakage flow in a turbomachinery cascade with a moving end-wall, in order to understand the viscous loss mechanisms close to the tip gap. The tip-leakage vortex (TLV), tip-separation vortex (TSV) and induced counter-rotating vortex (CRV) were identified (*cf* fig. 1.8).

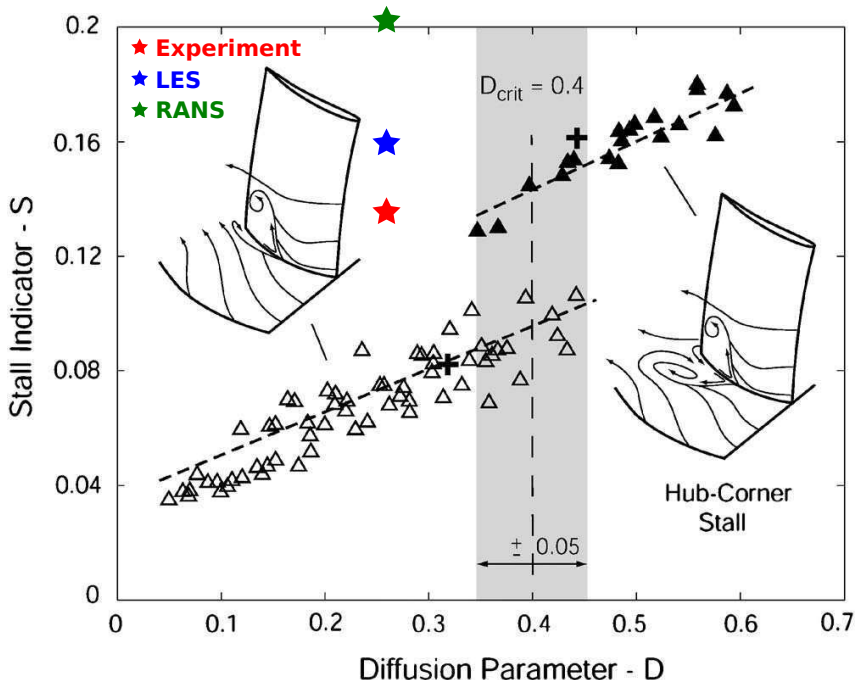

Figure 1.7: Position of Gao (2014) corner separation in Lei's criterion.

The TLV and tip-leakage jet were found to generate strong mean velocity gradients, responsible for the major part of the viscous losses close to the end-wall.

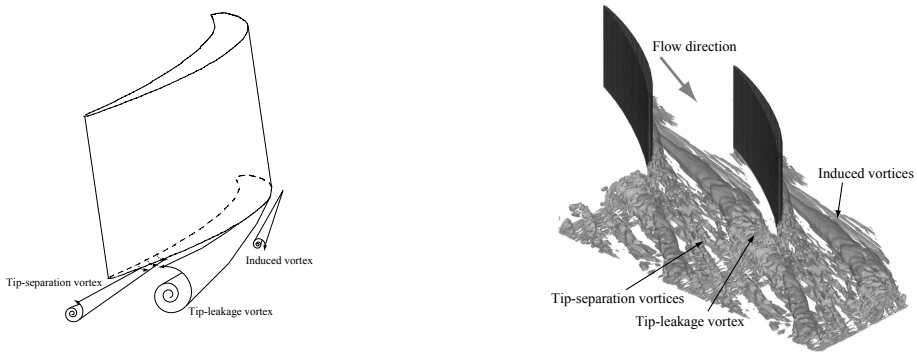

(a) Sketch (b) Visualisation

Figure 1.8: Tip-leakage flow topology from You et al. (2007a). The sketch and visualisation show the tip-separation vortex, the tip-leakage vortex and the induced counter rotating vortex.

1.3.2 Experimental investigations

Devenport research team from Virginia Tech published a series of articles on a linear cascade with a tip gap and a moving endwall (Muthanna and Devenport, 2004; Wang and Devenport, 2004; Devenport et al., 2004). The first article (Muthanna and Devenport, 2004) focuses on the tip-leakage flow mechanisms for a stationary end-wall. The three components of velocity and turbulence quantities were investigated for a

tip gap height equal to 1.6% of the blade chord. Then, the velocities and turbulent quantities were investigated at one station against two tip gap sizes, 0.8% and 3.3% of the blade chord. The structure and topology of the tip-leakage vortex was extensively described. It was found to be similar to the ones in compressor rotors with comparable characteristics. The authors concluded that the characteristics of the tip-leakage flow is essentially controlled by blade loading and geometry. The second article (Wang and Devenport, 2004) focuses on the tip-leakage flow mechanisms for a moving end-wall. The movement has been simulated using a belt moving over a sliding surface under the tips of the blades. The same investigations as for the stationary end-wall were realised. The end-wall motion spread out the vortex center into a ribbon, but the some of the main features, such as the magnitude of the large streamwise mean-velocity deficit at the vortex center and its decay with downstream distance, were unaffected by the end-wall motion. The tip gap size did not influence qualitatively the tip-leakage vortex characteristics, but had a quantitative influence. The third article (Devenport et al., 2004) focuses on the velocity spectra and space-time correlations in the tip-leakage vortex. The velocity spectra levels were high due to the high turbulence levels. However, with the absence of distinct spectral peak, no periodically organised structures were found. The tip-leakage vortex turbulence was found to be highly anisotropic and characterised by inclined elongated eddies (about 30° to the vortex axis).

Tan et al. (2015) realised an experimental investigation of the tip-leakage vortex in subsonic conditions in a compressor-like facility. Thanks to the refraction index of the casing and the blades matching the one of the fluid, unobstructed optic measurements have been achieved. The facility is made to test casing treatments for tip-leakage passive control. The facility is first tested with a smooth casing. The visualisations of the TLV, using the cavitation that it induces, show the trajectories of the vortex in the case of highest flow rate and pre-stall conditions. The time-resolved particle image velocimetry (PIV) measurements show that, for the early phase of the vortex rollup, an area of negative vorticity is present close to the end-wall, as presented in Fig. 1.9 (1). This area represents the interaction of the TLV with the casing boundary-layer, and is responsible of the production for a substantial amount of turbulent kinetic energy.

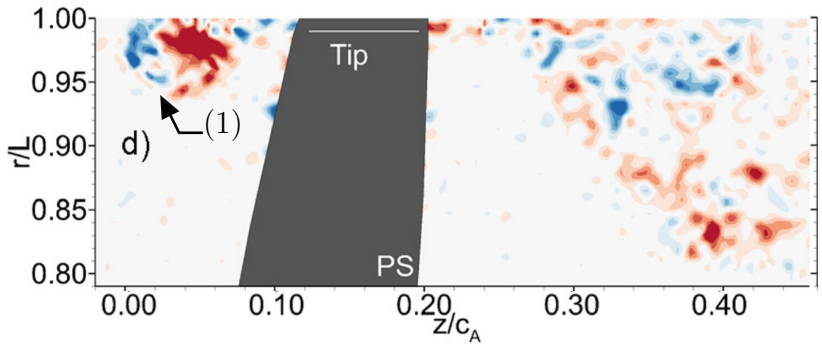

Figure 1.9: Instantaneous PIV of the TLV in a cross section, extracted from Tan et al. (2015). The value plotted is the normalised vorticity.

Li et al. (2017) realised another time-resolved PIV campaign on the same configuration as Tan et al. (2015). The authors analysed the turbulent characteristics in the tip region, with the turbulent kinetic energy, the Reynolds stresses, or the turbulent kinetic energy budget transport terms. As part of the analysis, the authors tested the correlation between the Reynolds stresses and the mean strain-rate. In the tip region,

they are poorly correlated, which means that the Boussinesq hypothesis, commonly used in RANS modelling, is not verified.

Advanced measurements were carried out by Jacob et al. (2016a), on an academic configuration. The experimental set-up is made up with an isolated blade placed between two plates into the potential core of a jet, as presented in Fig 1.10. The blade is attached to the top plate and a clearance is present between the blade tip and the bottom plate. The measurements were realised inside a subsonic anechoic wind tunnel. During the experimental campaign, the unsteady behaviour of the TLV was characterised. A lot of information was gathered, such as the TLV center locations and TLV extent, with respectively the Γ_1 and Γ_2 functions presented in Eq. (1.1) and (1.2), and the Reynolds stresses. The use of time-resolved PIV gave access to a low-frequency oscillation of the TLV, not entirely understood yet. A spectrum hump at medium and high frequencies, in the range [0.7kHz, 7kHz], is also found in the near and far fields.

$$\Gamma_1(P) = \frac{1}{S} \int_{M \in S} \frac{\left(\underline{PM} \wedge \underline{U_M}\right) \cdot \underline{x}}{\| \underline{PM} \| \cdot \| \underline{U_M} \|} \mathrm{d}S \tag{1.1}$$

$$\Gamma_2(P) = \frac{1}{S} \int_{M \in S} \frac{\left[\underline{PM} \wedge \left(\underline{U_M} - \underline{\tilde{U}_P}\right)\right] \cdot \underline{x}}{\| \underline{PM} \| \cdot \| \underline{U_M} - \underline{\tilde{U}_P} \|} \mathrm{d}S \tag{1.2}$$

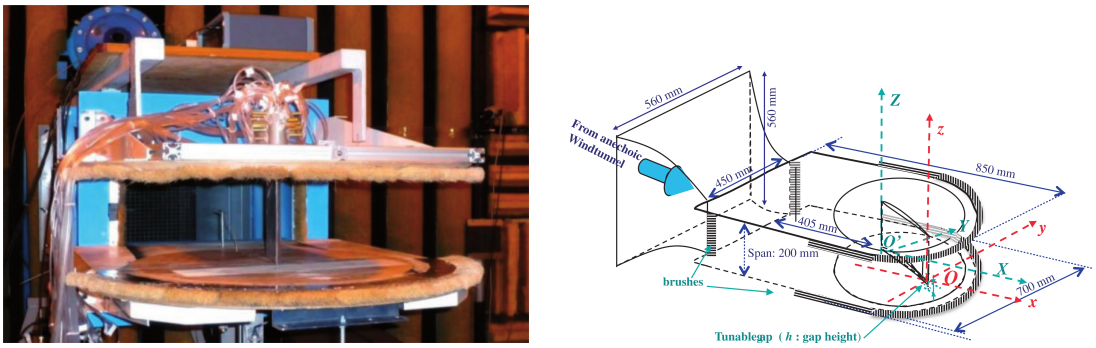

(a) Photo (b) Sketch

Figure 1.10: Experimental set-up from Jacob et al. (2016a). (a) photo of the set-up, (b) sketch of the set-up.

The previous article is completed by a paper (Jacob et al., 2016b), on the same academic case. A ZLES simulation was also performed and presented by Boudet et al. (2016b,a) (*cf* section 1.3.3).

1.3.3 Numerical investigations

Storer and Cumpsty (1991) realised an experimental and numerical study of the tip-leakage flow. The numerical study relies on three-dimensional RANS with the mixing-length turbulence model of Baldwin and Lomax (1978). The experimental results are well represented by the RANS simulation, even though the computation mesh is coarse and the turbulence model unsophisticated. The authors conclude that the mechanism of tip leakage is primarily an inviscid mechanism.

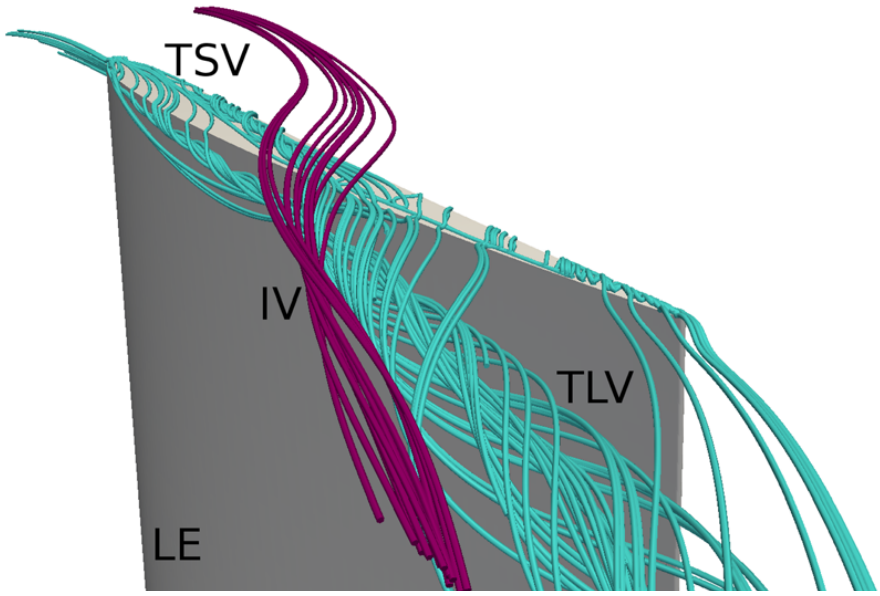

Figure 1.11: Tip-leakage flow topology from Boudet et al. (2015a). The element already found by You et al. (2007a) are present.

Borello et al. (2006) realised a RANS simulation using a second moment closure turbulence model on a 3D linear compressor cascade flow with tip clearance. They conclude that with this modelling, the tip-leakage flow phenomenology description is improved. The pressure distribution and pitch-wise velocity are in better agreement with experimental results than with eddy-viscosity RANS models. Moreover, only the second moment closure simulation seems able to predict the tip-separation vortex.

You et al. (2007b) realised a LES of a linear cascade with a tip gap and a moving end-wall. The analysis focused on the velocity field and low-pressure fluctuations. The tip-leakage vortex was found to be the main vortical structure in the end-wall region. The authors found that the tip-leakage vortex is subject to a pitchwise low frequency wandering motion. This analysis relies on the energy spectra and space-time correlations of the velocity fluctuations. The tip-leakage vortex is found to interact strongly with the induced vortices. The authors believe that the low-pressure fluctuations could be responsible, in hydraulic turbomachineries, for cavitation. These cavitation-inducing low-pressure fluctuations were found to most likely occur in the upstream portion of the tip-leakage vortex and underneath the tip-gap, at around 30-40% axial chord.

Boudet et al. (2015a) realised a numerical investigation of a DLR rotor, using a zonal large-eddy simulation (ZLES) approach. The region of interest at the blade tip is computed with a fully resolved LES, while the others regions rely on RANS simulation with the original Wilcox $k-\omega$ turbulence model (Wilcox, 1988). The classical structures are observed (You et al., 2007a), as presented in figure 1.11. The simulation provides a good description of the flow. An unsteadiness of the TLV has been detected with the analysis of the spectrum, in accordance with the experimental results. The oscillation is believed to be excited by turbulence from the casing boundary-layer or/and the adjacent TLV. It may be a precursor of rotating instability and rotating stall.

Leichtfuß et al. (2013) realised an experimental and numerical investigations of stability-limiting phenomena in the Darmstadt transonic compressor. Counter-rotating

pressure fluctuations were identified in the experimental and numerical results, and linked with the drop in aerodynamic damping. The authors suggested that the tip-leakage flow is fundamental to understand these fluctuations. Later, Möller et al. (2016) realised a numerical investigation of the Darmstadt transonic compressor in order to investigate the tip-clearance flow induced flutter. They found that the flutter vibration pattern happened with a pressure fluctuation pattern of the tip clearance. This pressure fluctuations interacts with the blade motion and caused the instabilities. The interaction happened specifically when the tip clearance flow fluctuation is about 50% of the blade tip speed.

A numerical investigation was lead on the experimental set-up of Jacob et al. (2016a,b). Boudet et al. (2016a,b) realised a ZLES on the configuration. The region of interest at the blade tip is computed with a fully resolved LES, while the other regions rely on RANS with the original Wilcox $k-\omega$ turbulence model (Wilcox, 1988). A special attention is paid to the incoming boundary-layer, as its thickness has a value similar with the tip-clearance height. Some of the flow characteristics, such as mean velocities, Reynolds stresses and spectra, are presented in the papers. A good agreement is found between the experimental and numerical results, on cross stream planes at 80%c and 90%c. The principal results concern the TLV position and swirl velocity, comparable with the free-stream velocity. The position of the TLV center (Fig. 1.13a) and its width were quantified with the Γ_1 and Γ_2 functions. The results are in good agreement with the experiment. The near-field spectral content is also presented, and in good agreement with the experiment, as presented in Fig. 1.13b. The far-field acoustic spectrum is also computed at 2 meters from the blade, using the Ffowcs Williams and Hawkings analogy. A very good agreement is observed in the range of [0.7kHz, 7kHz], as presented in Fig. 1.12. The good agreement between experimental and numerical results serves as a validation of the simulation, in order to use it as a reference for further analysis.

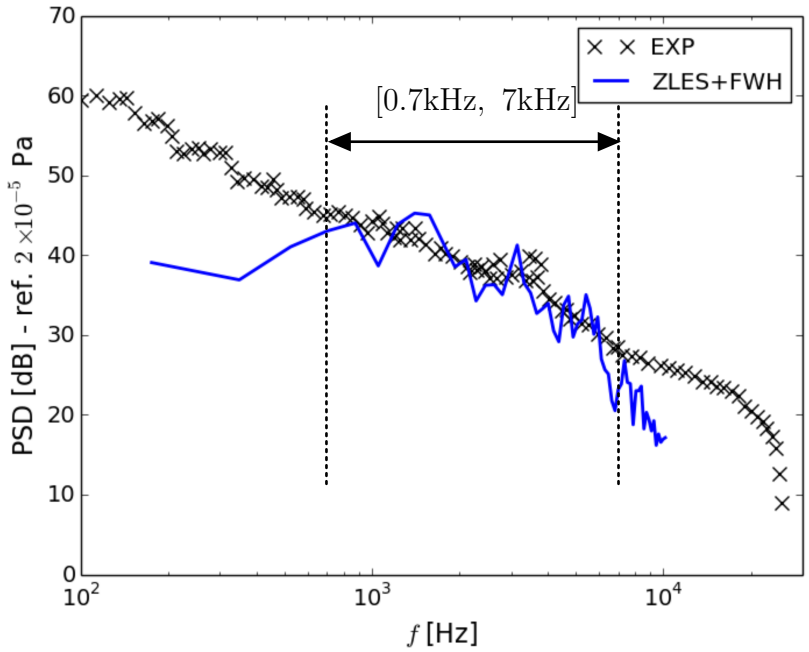

Figure 1.12: Far-field acoustic spectrum at 2m from the blade, extracted from Boudet et al. (2016b). EXP: experiment, ZLES+FWH: Ffowcs Williams Hawkings propagation from the ZLES results.

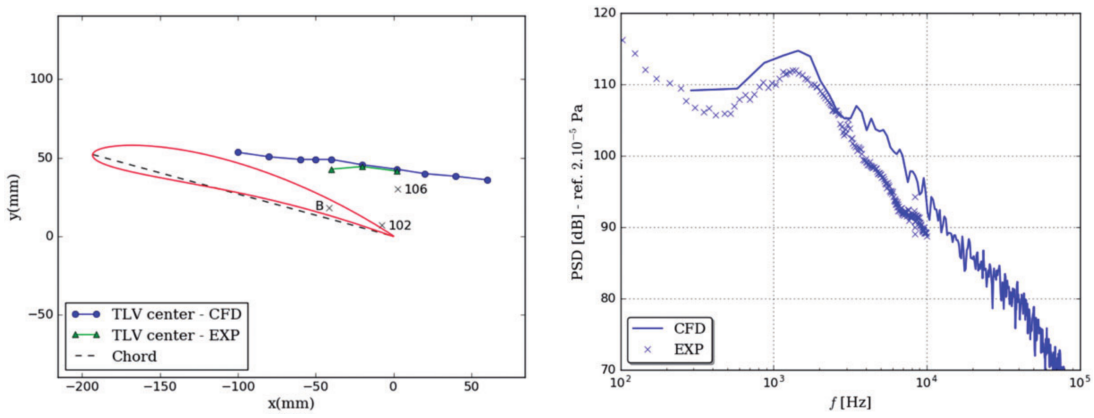

(a) Mean TLV trajectory and probe locations

(b) Pressure spectrum at probe B

Figure 1.13: ZLES results from Boudet et al. (2016a).

Chapter 2

Turbulence modelling

Sections

Given that no exact solution exists for the Navier-Stokes equations in general, the predictions rely on numerical simulations. These simulations necessitate to represent the effects of turbulence in order to be accurate. Turbulence modelling is one of the key aspects of computational fluid dynamics (CFD).

First, the governing equations are detailed. Then, the three main turbulence modelling approaches, direct numerical simulation, large-eddy simulation, and Reynolds-averaged Navier-Stokes are presented. For both large-eddy simulation and Reynolds-averaged Navier-Stokes, the modifications and approximations on the governing equations are detailed, along with the turbulence modelling used and the turbulent kinetic energy budget formulation.

2.1 Governing equations

The present study is dedicated to flow phenomena occurring in aeronautical axial compressor. The fluid considered is air, a Newtonian fluid. Its motion is governed by the compressible Navier-Stokes equations:

$$\frac{\partial \rho}{\partial t} + \frac{\partial \rho u_j}{\partial x_j} = 0 \tag{2.1}$$

$$\forall i \in [\![1 \ ; \ 3]\!], \ \frac{\partial \rho u_i}{\partial t} + \frac{\partial \rho u_i u_j}{\partial x_j} = -\frac{\partial p}{\partial x_i} + \frac{\partial \tau_{ij}}{\partial x_j} \tag{2.2}$$

$$\frac{\partial \rho e_t}{\partial t} + \frac{\partial (\rho e_t + p) u_j}{\partial x_j} = \frac{\partial \tau_{ij} u_i}{\partial x_j} - \frac{\partial q_j}{\partial x_j} \tag{2.3}$$

with ρ the density, t the time, $\underline{u}$ the velocity of the fluid, $\underline{x}$ the position vector, p the static pressure, $\underline{\underline{\tau}}$ the viscous stress tensor, e_t the total energy and $\underline{q}$ the heat flux.

Equation (2.1) expresses the conservation of mass, equation (2.2) expresses the evolution of momentum and equation (2.3) expresses the evolution of energy. Under certain hypotheses, the equations can be expressed using only five conservative variables $(\rho, \rho u_1, \rho u_2, \rho u_3, \rho e_t)$ and constants (Garnier et al., 2009).

The assumption that bulk viscosity can be neglected, known as Stokes hypothesis, allows to write the viscous stress tensor as only dependent on the dynamic viscosity of the fluid μ and the strain rate tensor $\underline{\underline{S}}$:

$$\forall (i,j) \in [\![1 \ ; \ 3]\!]^2, \ \tau_{ij} = \mu \sigma_{ij} \tag{2.4}$$

$$\forall (i,j) \in [\![1 \ ; \ 3]\!]^2, \ \sigma_{ij} = 2 S_{ij} - \frac{2}{3} \delta_{ij} \frac{\partial u_k}{\partial x_k} \tag{2.5}$$

$$\forall (i,j) \in [\![1 \ ; \ 3]\!]^2, \ S_{ij} = \frac{1}{2} \left(\frac{\partial u_i}{\partial x_j} + \frac{\partial u_j}{\partial x_i} \right) \tag{2.6}$$

with δ_{ij} the Kronecker's delta and $\underline{\underline{\sigma}}$ the zero-trace strain rate tensor.

The heat flux $\underline{q}$ can be derived from the law of Fourier under the assumption of negligible energy transport by the molecular diffusion and the radiant transfer:

$$\forall i \in [\![1 \ ; \ 3]\!], \ q_i = -\kappa \frac{\partial T}{\partial x_i} \tag{2.7}$$

with T the static temperature and κ the thermal conductivity.

The thermal conductivity κ can be expressed using the Prandtl number Pr, the dynamic viscosity μ and the constant pressure heat capacity c_p:

$$Pr = \frac{\mu c_p}{\kappa} \tag{2.8}$$

Air is considered to behave as an ideal gas, which means the temperature T can be expressed using the density ρ, the specific gas constant $r_{\text{air}} = 287 \text{J.kg}^{-1}.\text{K}^{-1}$ and the pressure p:

$$p = \rho r_{\text{air}} T \tag{2.9}$$

The specific gas constant r_{air} can be expressed as a function of the constant pressure heat capacity c_p and the constant volume heat capacity c_v, which are linked by the specific heat ratio γ:

$$r_{\text{air}} = c_p - c_v, \ \gamma = \frac{c_p}{c_v} \tag{2.10}$$

Finally, the internal energy e, the total energy e_t, the velocity $\underline{u}$, the pressure p and the density ρ are linked by the relations:

$$e_t = e + \frac{1}{2} u_i u_i \tag{2.11}$$

$$e = c_v T = \frac{1}{\gamma - 1} \frac{p}{\rho} \tag{2.12}$$

For all the flows considered in this study, the Mach number remains under 0.3. The incompressibility hypothesis is valid. This assumption plus the assumptions that the fluid is an ideal gas, that the walls are adiabatic, and that there is no internal energy source, lead to consider the quantities μ, Pr, r_{air}, c_p, c_v and γ are constant. The equations (2.1), (2.2) and (2.3) are finally expressed using only the set of five conservative variables $(\rho, \rho u_1, \rho u_2, \rho u_3, \rho e_t)$ and the constants μ, Pr, r_{air}, c_p, c_v and γ.

Except for some simple cases, such as Couette flow, there is no exact solution to the Navier-Stokes system of equations. Currently, the resolution of the Navier-Stokes equations relies on numerical solvers. The remaining problem is to correctly represent the flow down to the smallest eddy and to take into account the chaotic behaviour of turbulence, with all its aspects. Usually, the simulations are classified in three families (Bailly and Comte-Bellot, 2003), namely the direct numerical simulation (DNS), the more exhaustive, the large-eddy simulation (LES), an intermediate approach, and the Reynolds-averaged Navier-Stokes (RANS) simulation that relies entirely on turbulence modelling.

2.2 Direct numerical simulation

Direct numerical simulation (DNS) is the more natural approach for flow simulations. All the scales of turbulence are directly resolved, down to the smallest eddies. For this reason, this simulation method is the most precise available.

The downside of this approach is its cost. In order to resolve all the scales of turbulence, the grid size must be comparable with the Kolmogorov scale. Due to the necessity of extremely high resolution, the computational cost is important, even with simple, low Reynolds number configurations. In point of fact, the disparity between the turbulent length-scales evolves proportionally to $\text{Re}^{3/4}$, the number of grid points for a three-dimensional case evolves proportionally to $\text{Re}^{9/4}$, so the computational cost evolves as Re^3 (Pope, 2000). For this reason, the DNS approach is used mainly for low or moderate Reynolds number configurations in academic researches, with for instance the work of Jiménez et al. (2010). It can be used to create a database of extremely high fidelity academic cases, for both physical analysis and practical calibration of methods relying on turbulence modelling. However, DNS can not be yet considered for realistic high Reynolds number configurations or for industrial applications, such as turbomachinery.

2.3 Large-eddy simulation

Large-eddy simulation is intended to reduce the simulation cost compared to DNS. The largest, more powerful scales of turbulence (the large eddies) are directly resolved, and the smallest scales (the small eddies) are modelled. The strategy is to filter the

equations, in order to compute the largest scales of turbulence, and to model the remaining part of turbulence using a sub-grid scale (SGS) model (Sagaut, 2006).

With this method, the number of grid points remains important, and so does the computational cost. This makes it impeachable for daily design cycles, but allows detailed investigations on complex, high-Reynolds number configurations (Gao et al., 2015a; Boudet et al., 2016a). In the present work, LES results are used as an high fidelity reference database to analyse physically the turbulence.

The following sub-sections detail the implementation of the LES method in *Turb'Flow* (Boudet et al., 2007), the in-house, compressible, finite volume code used for the present work.

2.3.1 Filtered equations

The filtering of the Navier-Stokes equations can be realised using classical filters such as the box filter or the Gaussian filter (Garnier et al., 2009). In the present work, the filtering is made by the grid, and the influence of the filter characteristics are neglected.

For a given quantity φ, the large-scale filter is represented by the operator $\overline{\varphi}$ and the small-scale residual is represented by the operator $\varphi`$, with the relation $\varphi = \overline{\varphi} + \varphi`$. Due to the fact that the compressible Navier-Stokes equations are considered, the Favre decomposition is used. Considering ρ the density, the Favre large-scale filter is represented by the operator $\widetilde{\varphi} = \overline{\rho\varphi}/\overline{\rho}$, and the Favre small-scale residual is represented by the operator $\varphi``$, with the relation $\varphi = \widetilde{\varphi} + \varphi``$.

The mass conservation equation (2.1) and momentum conservation equation (2.2) are directly filtered, which gives:

$$\frac{\partial \overline{\rho}}{\partial t} + \frac{\partial \overline{\rho}\widetilde{u_j}}{\partial x_j} = 0 \tag{2.13}$$

$$\forall i \in [\![1 \ ; \ 3]\!], \ \frac{\partial \overline{\rho}\widetilde{u_i}}{\partial t} + \frac{\partial \overline{\rho}\widetilde{u_i}\widetilde{u_j}}{\partial x_j} = -\frac{\partial \overline{p}}{\partial x_i} + \frac{\partial \overline{\tau_{ij}}}{\partial x_j} + \frac{\partial \Pi_{ij}}{\partial x_j} \tag{2.14}$$

Π_{ij} is the sub-grid scale (SGS) tensor, defined as:

$$\forall (i,j) \in [\![1 \ ; \ 3]\!]^2, \ \Pi_{ij} = \overline{\rho}\widetilde{u_i}\widetilde{u_j} - \overline{\rho u_i u_j} = -\overline{\rho}\left(\widetilde{u_i u_j} - \widetilde{u_i}\widetilde{u_j}\right) \tag{2.15}$$

Different energy conservation equations can be obtained, depending on the filtering strategy and the approximations realised. For instance, the filtered energy conservation equation can be based on enthalpy, pressure, temperature or entropy (Garnier et al., 2009). In the case of *Turb'Flow*, the total energy equation is directly filtered (Boudet et al., 2007):

$$\frac{\partial \overline{\rho e_t}}{\partial t} + \frac{\partial \overline{(\rho e_t + p)u_j}}{\partial x_j} = \frac{\partial \overline{\tau_{ij} u_i}}{\partial x_j} - \frac{\partial \overline{q_j}}{\partial x_j} \tag{2.16}$$

The filtered viscous stress tensor is approximated by:

$$\forall i \in [\![1 \ ; \ 3]\!], \ \frac{\partial \overline{\tau_{ij}}}{\partial x_j} = \frac{\partial}{\partial x_j}\overline{(\mu\sigma_{ij})} \approx \frac{\partial \overline{\mu}\widetilde{\sigma_{ij}}}{\partial x_j} \tag{2.17}$$

with $\widetilde{\underline{\underline{\sigma}}}$ the Favre filtered zero-trace strain rate tensor:

$$\forall (i,j) \in [\![1 ; 3]\!]^2,\ \widetilde{\sigma_{ij}} = \frac{\partial \widetilde{u_i}}{\partial x_j} + \frac{\partial \widetilde{u_j}}{\partial x_i} - \frac{2}{3}\delta_{ij}\frac{\partial \widetilde{u_k}}{\partial x_k} \tag{2.18}$$

In the original Navier-Stokes equations, the pressure is computed using the total energy as $p = \rho(\gamma - 1)(e_t - 1/2 u_i u_i)$ (see equations (2.11) and (2.12)). The filtered pressure is:

$$\overline{p} = \overline{\rho}\,(\gamma - 1)\left(\widetilde{e_t} - \frac{1}{2}\widetilde{u_i u_i}\right) \approx \overline{\rho}\,(\gamma - 1)\left(\widetilde{e_t} - \frac{1}{2}\widetilde{u_i}\widetilde{u_i}\right) \tag{2.19}$$

because the terms $\widetilde{\tilde{u}_i u_i}^{``}$ and $\widetilde{u_i}^{``}\widetilde{u_i}^{``}$ are neglected in *Turb'Flow*.

The SGS tensor $\underline{\underline{\Pi}}$ needs to be modelled to close the filtered momentum equation (2.14). First, it is decomposed into a deviatoric part $\underline{\underline{\Pi^D}}$ and an isotropic part $\underline{\underline{\Pi^I}}$:

$\forall (i,j) \in [\![1 ; 3]\!]^2$,

$$\Pi_{ij} = \Pi^D_{ij} + \Pi^I_{ij}\ ;\ \Pi^D_{ij} = \Pi_{ij} - \frac{1}{3}\delta_{ij}\Pi_{kk}\ ;\ \Pi^I_{ij} = \frac{1}{3}\delta_{ij}\Pi_{kk} \tag{2.20}$$

The deviatoric part of the SGS tensor is modelled by analogy with the viscous stress tensor, by introducing a sub-grid scale viscosity μ_{SGS}. The isotropic part of the SGS tensor is neglected, considering that the sub-grid scale Mach number remains low (Boudet, 2003):

$$\forall (i,j) \in [\![1 ; 3]\!]^2,\ \Pi_{ij} = \Pi^D_{ij} = \mu_{SGS}\widetilde{\sigma_{ij}} \tag{2.21}$$

The sub-grid scale viscosity μ_{SGS} is computed using a sub-grid scale model, presented in sub-section 2.3.2.

In the filtered energy equation the viscous dissipation term and the pressure velocity term are approximated by:

$$\frac{\partial \overline{\tau_{ij} u_i}}{\partial x_j} \approx \frac{\partial \overline{\tau_{ij}}\widetilde{u_i}}{\partial x_j} \tag{2.22}$$

$$\frac{\partial \overline{u_j p}}{\partial x_j} \approx \frac{\partial \widetilde{u_j}\overline{p}}{\partial x_j} \tag{2.23}$$

The heat flux is approximated by:

$$\forall i \in [\![1 ; 3]\!],\ \overline{q_i} = -\kappa\overline{\frac{\partial T}{\partial x_i}} \approx -\overline{\kappa}\frac{\partial \widetilde{T}}{\partial x_i} \tag{2.24}$$

The remaining term to approximate is the total energy transport term. The total energy is decomposed with the internal energy e:

$$\frac{\partial \overline{\rho e_t u_j}}{\partial x_j} = \frac{\partial \overline{\rho e u_j}}{\partial x_j} + \frac{1}{2}\frac{\partial \overline{\rho u_i u_i u_j}}{\partial x_j} = \frac{\partial \overline{\rho}\widetilde{e}\widetilde{u_j}}{\partial x_j} + \frac{\partial \Theta_j}{\partial x_j} + \frac{1}{2}\frac{\partial \overline{\rho u_i u_i u_j}}{\partial x_j} \tag{2.25}$$

with $\underline{\Theta}$ the sub-grid scale heat flux:

$$\forall i \in [\![1 ; 3]\!],\ \Theta_j = \overline{\rho e u_j} - \overline{\rho}\widetilde{e}\widetilde{u_j} = \overline{\rho} c_v \left(\widetilde{T u_j} - \widetilde{T}\widetilde{u_j}\right) \tag{2.26}$$

The sub-grid scale heat flux $\underline{\Theta}$ is modelled by analogy with the heat flux, with the introduction of a sub-grid scale thermal conductivity κ_{SGS} and a sub-grid scale Prandtl number Pr_{SGS}:

$$\forall i \in [\![1 ; 3]\!],\ \Theta_j = -\kappa_{SGS}\frac{\partial \widetilde{T}}{\partial x_j} = -\frac{\mu_{SGS} c_p}{Pr_{SGS}}\frac{\partial \widetilde{T}}{\partial x_j} \tag{2.27}$$

In this work, the SGS Prandtl number Pr_{SGS} is considered constant, equal to 0.9 (Cahuzac, 2012). The remaining term of the equation (2.25) is modelled as follows:

$$\frac{\partial \overline{\rho u_i u_i u_j}}{\partial x_j} = \frac{\partial \overline{\rho}\widetilde{u_i u_i}\widetilde{u}_j}{\partial x_j} - \frac{\partial \Pi_{ij}\widetilde{u}_j}{\partial x_j} \tag{2.28}$$

Finally, the ideal gas equation is filtered to close the system of equations:

$$\overline{p} = \overline{\rho} r_{\text{air}} \widetilde{T} \tag{2.29}$$

The complete filtered Navier-Stokes system of equations is:

$$\frac{\partial \overline{\rho}}{\partial t} + \frac{\partial \overline{\rho}\widetilde{u}_j}{\partial x_j} = 0 \tag{2.30a}$$

$$\forall i \in [\![1 ; 3]\!],\ \frac{\partial \overline{\rho}\widetilde{u}_i}{\partial t} + \frac{\partial \overline{\rho}\widetilde{u}_i\widetilde{u}_i}{\partial x_j} = -\frac{\partial \overline{p}}{\partial x_i} + \frac{\partial (\overline{\mu} + \mu_{SGS})\widetilde{\sigma_{ij}}}{\partial x_j} \tag{2.30b}$$

$$\frac{\partial \overline{\rho}\widetilde{e_t}}{\partial t} + \frac{\partial (\overline{\rho}\widetilde{e_t} + \overline{p})\widetilde{u}_j}{\partial x_j} = \frac{\partial (\overline{\mu} + \mu_{SGS})\widetilde{\sigma_{ij}}\widetilde{u}_j}{\partial x_j} + \frac{\partial}{\partial x_j}\left((\overline{\kappa} + \kappa_{SGS})\frac{\partial \widetilde{T}}{\partial x_j}\right) \tag{2.30c}$$

2.3.2 Sub-grid scale model

The sub-grid scale model is used to compute μ_{SGS}. The historical model was developed by Smagorinsky (1963). This model is still widely used, but is known to be imprecise close to the walls. The Smagorinsky SGS model is available in *Turb'Flow*. Another classical model available in *Turb'Flow* was developed by Nicoud and Ducros (1999). The model, named wall-adapting local eddy-viscosity model (WALE), was conceived to present a good behaviour close to the walls.

The large-eddy simulations presented in this work were realised with another SGS model, the shear-improved Smagorinsky model (SISM). It is an in-house model developed by Lévêque et al. (2007). The model was conceived to be physically sound and consistent with the scale-by-scale energy budget of locally homogeneous shear turbulence, with a low CPU cost. It demonstrated its capacity to provide good solutions for various academic flow simulations of turbomachinery phenomena (Cahuzac et al., 2011; Gao et al., 2015a; Boudet et al., 2016a).

Formulation

The SISM model is based on the original Smagorinsky model. Following the theoretical developments presented by Lévêque et al. (2007), the Smagorinsky model is modified

by subtracting the magnitude of the mean shear stress $| < \widetilde{\underline{\underline{S}}} > |$ from the magnitude of the resolved instantaneous strain-rate tensor $|\widetilde{\underline{\underline{S}}}|$:

$$\mu_{SGS} = \overline{\rho}\,(C_s\Delta)^2 \left(\left| \widetilde{\underline{\underline{S}}} \right| - \left| \left\langle \widetilde{\underline{\underline{S}}} \right\rangle \right| \right) \tag{2.31}$$

with Δ the grid spacing, computed as the cube root of the cell volume, and $C_s = 0.18$ the Smagorinsky constant. The magnitude of the tensors is calculated as $|\widetilde{\underline{\underline{\varphi}}}| = |\widetilde{\varphi_{ij}}\widetilde{\varphi_{ij}}|$.

The calculation of the SGS viscosity with the SISM model requires the ensemble average of the filtered strain-rate tensor. Practically, this is unknown during the computation. An approximation of the mean flow is necessary.

Mean flow approximation for the SISM

The exponentially weighted moving average approach, implemented and tested by Cahuzac et al. (2010), is used to approximate the mean flow, in order to calculate the mean shear stress. The idea is to update at each time step the mean flow estimate with the new instantaneous field. If we note, φ^n an instantaneous quantity at a given n^{th} time step, φ^{n+1} the instantaneous quantity at the following time step, $< \varphi >^n$ the mean value of the quantity at the n^{th} time step and $< \varphi >^{n+1}$ the mean value at the following time step, the exponentially weighted moving average is calculated as:

$$\langle \varphi \rangle^{n+1} = (1 - c_{exp}) \langle \varphi \rangle^n + c_{exp} \varphi^{n+1} \tag{2.32}$$

where c_{exp} is the smoothing factor, with $(0 < c_{exp} < 1)$.

As a recursive approach, the exponentially weighted moving average needs a first element. The first mean value is chosen equal to the first instantaneous quantity:

$$\langle \varphi \rangle^0 = \varphi^0 \tag{2.33}$$

The approach acts as a low-pass filter on the quantity φ, with a fixed cut-off frequency f_c that can be related to the smoothing factor c_{exp}:

$$c_{exp} \simeq \frac{2\pi f_c \Delta_t}{\sqrt{3}} \tag{2.34}$$

with Δ_t the time step.

With this approach, the samples used to compute the mean quantity are mainly comprised inside a fixed-width temporal window advancing on the time axis at each time step. The width of the window depends on the cut-off frequency f_c, which can be calculated as the ratio between a characteristic velocity and a characteristic length.

An improved version of this averaging has been developed by Cahuzac et al. (2010), as a Kalman filter with a local and instantaneous estimate of the cut-off frequency. However, it is not employed in the present work, for which constant f_c have been determined.

2.3.3 Turbulent kinetic energy budget

A turbulent kinetic energy (TKE) budget, often called turbulence budget, allows to identify the distribution of the TKE transport terms, between production, dissipation

and transport. Such a budget gives valuable insights on the physical behaviour of turbulence at a fine level. However, obtaining such a budget experimentally is quite complicated due to the difficulty to measure the combined statistics. In this regard, DNS and LES offer an interesting alternative for such an in-depth physical analysis of turbulence.

Different works on TKE budget were realised. Lu and Chen (2000) proposed a theoretical framework, based on DNS results, to represent the TKE budget terms computed in the viscous sub-layer with a 3D wave model. Marquillie et al. (2008) extracted TKE budgets from a DNS of a separation after a bump in a tunnel. The configuration reproduces an experiment at École Centrale de Lille. The budget terms are all extracted with great precision. These results constitute a valuable database for comparison on this configuration. Later, Kuban et al. (2012) realised various large-eddy simulations on this configuration in order to test the influence of various SGS models. Bogey and Bailly (2009) simulated a free round jet with LES and extracted the TKE budget on this configuration. Jiménez et al. (2010) extracted TKE budgets from a flat-plate boundary-layer simulation. Finally, Gao (2014) extracted TKE budgets from the LES of a corner separation case, and compared them with RANS results. In the present work, the TKE budget extraction of Gao will be revised and improved, applied to two different configurations, and used to characterise RANS turbulence modelling.

Reynolds stress budget formulation

The filtered momentum equation (2.30b) can be used to obtain the Reynolds stress budget equation (Bogey and Bailly, 2009). Then, the resulting equation is averaged, in order to obtain the ensemble-averaged Reynolds stress budget equation. Four notations are introduced. For a given quantity φ, the ensemble average is represented by $\langle\varphi\rangle$, and the Favre ensemble average is represented by $[\varphi] = \langle\rho\varphi\rangle \,/\, \langle\rho\rangle$. The fluctuating part of the large-scale filtered quantity is noted φ' ($\overline{\varphi} = \langle\overline{\varphi}\rangle + \varphi'$) and the Favre fluctuating part of the Favre large-scale filtered quantity is noted φ'' ($\widetilde{\varphi} = [\widetilde{\varphi}] + \varphi''$).

The detailed procedure to derive the Reynolds stress budget can be found in appendix A. The resulting equations are:

$\forall (i,j) \in [\![\ 1\ ;\ 3\ ]\!]^2$,

$$
\begin{aligned}
\frac{\partial \left\langle \overline{\rho} u_i'' u_j'' \right\rangle}{\partial t} = {} & \underbrace{-\frac{\partial}{\partial x_k}\left(\left\langle \overline{\rho} u_i'' u_j'' \right\rangle \left[\widetilde{u_k} \right] \right)}_{\text{Advection}} \underbrace{- \left\langle \overline{\rho} u_j'' u_k'' \right\rangle \frac{\partial \left[\widetilde{u_i} \right]}{\partial x_k} - \left\langle \overline{\rho} u_i'' u_k'' \right\rangle \frac{\partial \left[\widetilde{u_j} \right]}{\partial x_k}}_{\text{Production}} \\
& \underbrace{-\frac{\partial}{\partial x_k}\left(\left\langle \overline{\rho} u_i'' u_j'' u_k'' \right\rangle \right)}_{\text{Turbulent diffusion}} \underbrace{-\frac{\partial \left\langle u_j'' p' \right\rangle}{\partial x_i} - \frac{\partial \left\langle u_i'' p' \right\rangle}{\partial x_j}}_{\text{Pressure diffusion}} \underbrace{+ \left\langle p' \frac{\partial u_j''}{\partial x_i} \right\rangle + \left\langle p' \frac{\partial u_i''}{\partial x_j} \right\rangle}_{\text{Pressure dilatation}} \\
& - \left\langle u_j'' \right\rangle \frac{\partial \left\langle \overline{p} \right\rangle}{\partial x_i} - \left\langle u_i'' \right\rangle \frac{\partial \left\langle \overline{p} \right\rangle}{\partial x_j} \underbrace{+ \frac{\partial \left\langle \overline{\tau_{ik}} u_j'' \right\rangle}{\partial x_k} + \frac{\partial \left\langle \overline{\tau_{jk}} u_i'' \right\rangle}{\partial x_k}}_{\text{Viscous diffusion}} \underbrace{- \left\langle \overline{\tau_{ik}} \frac{\partial u_j''}{\partial x_k} \right\rangle - \left\langle \overline{\tau_{jk}} \frac{\partial u_i''}{\partial x_k} \right\rangle}_{\text{Viscous dissipation}} \\
& \underbrace{+ \frac{\partial \left\langle \overline{\Pi_{ik}} u_j'' \right\rangle}{\partial x_k} + \frac{\partial \left\langle \overline{\Pi_{jk}} u_i'' \right\rangle}{\partial x_k}}_{\text{SGS diffusion}} \underbrace{- \left\langle \overline{\Pi_{ik}} \frac{\partial u_j''}{\partial x_k} \right\rangle - \left\langle \overline{\Pi_{jk}} \frac{\partial u_i''}{\partial x_k} \right\rangle}_{\text{SGS dissipation}}
\end{aligned}
\tag{2.35}
$$

Turbulent kinetic energy budget formulation

The Favre large-scale filtered part of the turbulent kinetic energy, noted k, is defined as $k = 1/2\ u_i'' u_i''$. The sum of the three ensemble-averaged equations on the Reynolds stress tensor diagonal terms gives the ensemble-averaged turbulent kinetic energy budget equation:

$$
\begin{aligned}
0 = \frac{\partial \langle \overline{\rho} k \rangle}{\partial t} = & \underbrace{-\frac{\partial}{\partial x_k}\left(\langle \overline{\rho} k \rangle \left[\widetilde{u_k}\right]\right)}_{\text{Advection}} \underbrace{-\langle \overline{\rho} u_i'' u_k'' \rangle \frac{\partial \left[\widetilde{u_i}\right]}{\partial x_k}}_{\text{Production}} \underbrace{-\frac{\partial}{\partial x_k}\left(\langle \overline{\rho} k u_k'' \rangle\right)}_{\text{Turbulent diffusion}} \\
& \underbrace{-\frac{\partial \langle u_i'' p' \rangle}{\partial x_i}}_{\text{Pressure Diffusion}} \underbrace{+\left\langle p' \frac{\partial u_i''}{\partial x_i} \right\rangle}_{\text{Pressure dilatation}} - \langle u_i'' \rangle \frac{\partial \langle \overline{p} \rangle}{\partial x_i} \\
& \underbrace{+\frac{\partial \langle \overline{\tau_{ik}} u_i'' \rangle}{\partial x_k}}_{\text{Viscous diffusion}} \underbrace{-\left\langle \overline{\tau_{ik}} \frac{\partial u_i''}{\partial x_k} \right\rangle}_{\text{Viscous dissipation}} \underbrace{+\frac{\partial \langle \overline{\Pi_{ik}} u_i'' \rangle}{\partial x_k}}_{\text{SGS diffusion}} \underbrace{-\left\langle \overline{\Pi_{ik}} \frac{\partial u_i''}{\partial x_k} \right\rangle}_{\text{SGS dissipation}} \underbrace{+\Xi}_{\text{Numerical residual}}
\end{aligned}
\tag{2.36}
$$

In numerical simulations, the TKE budget may not be perfectly balanced, *i.e.* the sum of the terms on the right-hand side may not be exactly zero. Therefore, a numerical residual term, noted Ξ, is added in the budget to close it. This term is computed as minus the sum of all the other spatial terms on the right-hand side.

2.4 Reynolds-averaged Navier-Stokes

The Reynolds-averaged Navier-Stokes (RANS) approach is an alternative to reach an affordable computational cost when considering complex, high Reynolds number configurations. Reynolds (1895) proposed to decompose the flow field into an ensemble-averaged quantity and a fluctuating quantity, or turbulent quantity. The application of such a decomposition to the Navier-Stokes equations generates a tensor, called Reynolds stress tensor, accounting for the effects of turbulence on the mean flow. The computation of only the mean motion of the flow necessitates much less grid points than the computation with LES. The strength of this method is its ability to treat industrial cases in a moderate amount of time. Its weakness is its dependence on the model used to represent turbulence.

The following sub-sections detail the implementation of the RANS method in *Turb'Flow* (Aubert, 1993; Smati, 1997), the in-house, compressible, finite-volume solver used for the present work.

2.4.1 Averaged equations

The averaging is realised with the ensemble average operator. For a given quantity φ, the ensemble average is noted $\langle \varphi \rangle$ and the fluctuating part is noted φ', with the relation $\varphi = \langle \varphi \rangle + \varphi'$. Because the compressible Navier-Stokes equations are considered, the Favre average is used (Favre, 1969). Considering ρ the density, the Favre average is

noted $[\varphi] = \langle\rho\varphi\rangle / \langle\rho\rangle$, and the Favre fluctuating part is noted[1] φ'', with the relation $\varphi = [\varphi] + \varphi''$.

The Navier-Stokes equations are averaged directly:

$$\frac{\partial \langle\rho\rangle}{\partial t} + \frac{\partial \langle\rho\rangle [u_j]}{\partial x_j} = 0 \tag{2.37}$$

$$\forall i \in [\![1 \ ; \ 3]\!], \ \frac{\partial \langle\rho\rangle [u_i]}{\partial t} + \frac{\partial \langle\rho\rangle [u_i] [u_j]}{\partial x_j} = -\frac{\partial \langle p\rangle}{\partial x_i} + \frac{\partial \langle\tau_{ij}\rangle}{\partial x_j} + \frac{\partial \tau_{tij}}{\partial x_j} \tag{2.38}$$

$$\frac{\partial \langle\rho\rangle [e_t]}{\partial t} + \frac{\partial (\langle\rho\rangle [e_t] + \langle p\rangle) [u_j]}{\partial x_j} = -\frac{\partial \left\langle (\rho e_t + p) u_j'' \right\rangle}{\partial x_j} + \frac{\partial \langle\tau_{ij} u_i\rangle}{\partial x_j} - \frac{\partial \langle q_j\rangle}{\partial x_j} \tag{2.39}$$

with $\underline{\underline{\tau_t}}$ the Reynolds stress tensor:

$$\forall (i,j) \in [\![1 \ ; \ 3]\!]^2, \ \tau_{tij} = -\left\langle \rho u_i'' u_j'' \right\rangle \tag{2.40}$$

The averaged viscous stress tensor is approximated by:

$$\forall i \in [\![1 \ ; \ 3]\!], \ \frac{\partial \langle\tau_{ij}\rangle}{\partial x_j} = \frac{\partial \langle\mu\sigma_{ij}\rangle}{\partial x_j} \approx \langle\mu\rangle \frac{\partial [\sigma_{ij}]}{\partial x_j} \tag{2.41}$$

The pressure relation is averaged directly:

$$\langle p\rangle = \langle\rho\rangle (\gamma - 1) \left([e_t] - \frac{1}{2} [u_i] [u_i] - [k] \right) \tag{2.42}$$

with $k = 1/2 \ u_i'' u_i''$ the turbulent kinetic energy.

In order to close the system of equations, the Reynolds stress tensor needs to be modelled. This modelling follows a two-step procedure. First, a constitutive relation is chosen, that introduces a turbulent viscosity (or eddy-viscosity) μ_t. This is detailed in sub-section 2.4.2. Then, the eddy-viscosity is expressed using a turbulence model. In the present case, the original Wilcox $k-\omega$ turbulence model (Wilcox, 1988) is chosen, with ω the specific turbulent dissipation rate. The details of this model are given in sub-section 2.4.3.

The heat flux can be approximated by:

$$\forall i \in [\![1 \ ; \ 3]\!], \ \langle q_i\rangle = -\left\langle \kappa \frac{\partial T}{\partial x_i} \right\rangle \approx -\langle\kappa\rangle \frac{\partial [T]}{\partial x_i} \tag{2.43}$$

with $\langle\kappa\rangle = < \mu > c_p/Pr$.

The viscous transport term is modelled, according to Smati (1997) as:

$$\frac{\partial \langle\tau_{ij} u_i\rangle}{\partial x_j} = \frac{\partial \langle\tau_{ij}\rangle [u_i]}{\partial x_j} + \frac{\partial}{\partial x_j} \left(\langle\mu\rangle \frac{\partial [k]}{\partial x_j} \right) \tag{2.44}$$

The remaining term is modelled as follows:

[1] Note that the same notation φ' is used for the ensemble-averaged fluctuating part and the large-scale filtered fluctuating part. Moreover, the same notation φ'' is used for the Favre averaged fluctuating part and the Favre filtered fluctuating part. This allows common notations for the Reynolds stresses and the turbulent kinetic energy budget between RANS and LES, and aims at simplifying the results presentation.

$$\frac{\partial \left\langle (\rho e_t + p) u_j'' \right\rangle}{\partial x_j} = \frac{\partial c_p \left\langle \rho \right\rangle \left[T u_j'' \right]}{\partial x_j} + \frac{\partial \left\langle \rho u_i'' u_j'' \right\rangle [u_i]}{\partial x_j} + \frac{\partial \left\langle \rho \right\rangle \left[k u_j'' \right]}{\partial x_j} \tag{2.45}$$

The temperature-velocity correlation $[T\underline{u}'']$ is usually expressed in terms of average temperature gradient and turbulent thermal conductivity. A similar approach can be used for the triple correlation $[k\underline{u}'']$. In this case, the correlation is expressed in terms of average turbulent kinetic energy gradient and eddy-viscosity:

$$\frac{\partial \left\langle (\rho e_t + p) u_j'' \right\rangle}{\partial x_j} = -\frac{\partial}{\partial x_j} \left(\kappa_t \frac{\partial [T]}{\partial x_j} \right) - \frac{\partial \tau_{tij} [u_i]}{\partial x_j} - \frac{\partial}{\partial x_j} \left(\frac{\mu_t}{\sigma_k} \frac{\partial [k]}{\partial x_j} \right) \tag{2.46}$$

with $\kappa_t = \mu_t c_p / \mathrm{Pr}_t$, $\mathrm{Pr}_t = 0.9$ the turbulent Prandtl number, and σ_k a constant of the turbulence model.

The previous models are expressed using the Favre averaged temperature. Finally, the the ideal gas equation is averaged to relate the pressure, the density and the temperature and close the system:

$$\langle p \rangle = \langle \rho \rangle \, r_{\mathrm{air}} [T] \tag{2.47}$$

The complete averaged Navier-Stokes system of equations is:

$$\frac{\partial \langle \rho \rangle}{\partial t} + \frac{\partial \langle \rho \rangle [u_j]}{\partial x_j} = 0 \tag{2.48a}$$

$$\forall i \in [\![1 \ ; \ 3]\!], \ \frac{\partial \langle \rho \rangle [u_i]}{\partial t} + \frac{\partial \langle \rho \rangle [u_i] [u_j]}{\partial x_j} = -\frac{\partial \langle p \rangle}{\partial x_i} + \frac{\partial \langle \tau_{ij} \rangle + \tau_{tij}}{\partial x_j} \tag{2.48b}$$

$$\begin{aligned} \frac{\partial \langle \rho \rangle [e_t]}{\partial t} + \frac{\partial (\langle \rho \rangle [e_t] + \langle p \rangle) [u_j]}{\partial x_j} &= \frac{\partial}{\partial x_j} \left((\langle \kappa \rangle + \kappa_t) \frac{\partial [T]}{\partial x_j} \right) \\ &+ \frac{\partial}{\partial x_j} \left((\langle \mu \rangle + \frac{\mu_t}{\sigma_k}) \frac{\partial [k]}{\partial x_j} \right) + \frac{\partial (\langle \tau_{ij} \rangle + \tau_{tij}) [u_i]}{\partial x_j} \end{aligned} \tag{2.48c}$$

2.4.2 Constitutive relations

The Reynolds stress tensor, that represents the impact of turbulence on the mean flow, needs to be modelled. To do it, a constitutive relation, that links the Reynolds stress tensor and the mean flow values, is needed. In the present work, two different constitutive relations are considered. The first one is the classical Boussinesq constitutive relation, that assumes the alignment between the Reynolds stress tensor and the zero-trace strain-rate tensor. The second one is the quadratic constitutive relation (QCR), that adds anisotropy to the Boussinesq constitutive relation.

Boussinesq constitutive relation

The Boussinesq constitutive relation (Boussinesq, 1877) is an analogy with the viscous stress model derived for a Newtonian fluid, and given in equation (2.4). The

Boussinesq relation assumes that the Reynolds stress tensor $\underline{\underline{\tau_t}}$ is proportional to the averaged zero-trace strain-rate tensor $\left[\underline{\underline{\sigma}}\right]$. The Reynolds stress tensor calculated with the Boussinesq constitutive relation is noted $\underline{\underline{\tau_t^*}}$. The proportionality coefficient has the same dimension as a viscosity, therefore this coefficient is named eddy-viscosity μ_t. The eddy-viscosity is calculated with the turbulence model, as presented in subsection 2.4.3. The relation $\underline{\underline{\tau_t}} \approx \underline{\underline{\tau_t^*}} = \mu_t \left[\underline{\underline{\sigma}}\right] - 2/3 < \rho > [k]$, when developed, gives:

$$\forall (i,j) \in [\![\ 1\ ;\ 3\ ]\!]^2,\ \tau_{tij}^* = \mu_t \left(\frac{\partial [u_i]}{\partial x_j} + \frac{\partial [u_j]}{\partial x_i} - \frac{2}{3}\delta_{ij} \frac{\partial [u_k]}{\partial x_k} \right) - \frac{2}{3}\delta_{ij} \langle \rho \rangle [k] \tag{2.49}$$

The hypothesis of alignment between the Reynolds stress tensor and the zero-trace strain-rate tensor is a strong hypothesis. Schmitt (2007) proposed a criterion to analyse its validity, when both tensors are known independently.

This criterion is defined as:

$$\Upsilon_{\text{Schmitt}} = \frac{\left| \underline{\underline{\tau_t^{**}}} : \left[\underline{\underline{\sigma}}\right] \right|}{\left\| \underline{\underline{\tau_t^{**}}} \right\| \left\| \left[\underline{\underline{\sigma}}\right] \right\|} \tag{2.50}$$

with $\left[\underline{\underline{\sigma}}\right]$ the averaged zero-trace strain-rate tensor and $\underline{\underline{\tau_t^{**}}}$ the unmodelled Reynolds stress tensor plus $2k/3$ on the diagonal:

$$\forall (i,j) \in [\![\ 1\ ;\ 3\ ]\!]^2,\ \tau_{tij}^{**} = \tau_{tij} + \frac{2}{3}\delta_{ij} \langle \rho \rangle [k] \tag{2.51}$$

For two tensors $\underline{\underline{\varphi}}$ and $\underline{\underline{\varsigma}}$, the inner product is defined as:

$$\underline{\underline{\varphi}} : \underline{\underline{\varsigma}} = \text{trace}(\underline{\underline{\varphi}}^t \underline{\underline{\varsigma}}) = \varphi_{ij}\varsigma_{ij} \tag{2.52}$$

with the norm associated to this inner product defined as:

$$\|\varphi\| = \varphi : \varphi = \varphi_{ij}^2 \tag{2.53}$$

The indicator[2] $\Upsilon_{\text{Schmitt}}$ is analogous to the cosine of an angle between the tensors. When it is equal to 1, the tensors are aligned, *ergo* proportional, and the Boussinesq hypothesis is valid. When it is equal to 0, the tensors are orthogonal, and the Boussinesq hypothesis is invalid. Schmitt (2007) proposed to consider that the alignment is approximately verified for an indicator value greater than 0.86. With LES, DNS or experimental results, both tensors are known independently, which allows the calculation of the indicator. In this work, LES results are exploited in order to test the Boussinesq constitutive relation hypothesis.

[2]The indicator is named ρ_{RS} in the original paper. In order to avoid confusion, the notation ρ is only used for density related values, and the notation $\Upsilon_{\text{Schmitt}}$ is preferred in this thesis for the Schmitt indicator.

Quadratic constitutive relation

The quadratic constitutive relation (QCR), proposed by Spalart (2000), is a modification of the Boussinesq constitutive relation in order to take into account the important effect of vorticity. The Reynolds stress tensor calculated with the QCR is noted $\underline{\underline{\tau_t^{QCR}}}$. The Reynolds stresses are obtained from:

$$\forall (i,j) \in [\![1 ; 3]\!]^2,\ \tau_{tij}^{QCR} = \tau_{tij}^* - c_{QCR} \left(O_{ik}\tau_{tjk}^* + O_{jk}\tau_{tik}^* \right) \tag{2.54}$$

with $c_{QCR} = 0.3$ a constant, $\underline{\underline{\tau_t^*}}$ the Reynolds stress tensor calculated with the Boussinesq constitutive relation in equation (2.49), and $\underline{\underline{O}}$ the normalised rotation tensor:

$$\forall (i,j) \in [\![1 ; 3]\!]^2,\ O_{ij} = \frac{\frac{\partial [u_i]}{\partial x_j} - \frac{\partial [u_j]}{\partial x_i}}{\sqrt{\frac{\partial [u_k]}{\partial x_l}\frac{\partial [u_k]}{\partial x_l}}} \tag{2.55}$$

The "linear" Reynolds stresses $\underline{\underline{\tau_t^*}}$ are modified by the addition of a term depending on the vorticity divided by the norm of the velocity-gradient tensor. That is why the modification is expected to mainly affect regions where the flow is highly rotational. For example, the flow is highly rotational for corner separation and tip-leakage, thus the QCR is expected to have a non negligible effect. In particular, in the context of external aerodynamics, Bordji et al. (2015) showed a reduction of the size of a corner separation, in better agreement with the experiment. In the context of internal aerodynamics, Scillitoe et al. (2015) obtained an improvement of a corner separation prediction in a numerical simulation with the Spalart and Allmaras (1994) turbulence model and the QCR. Another version of the model exists (Mani et al., 2013), but was not tested during this work.

The Schmitt (2007) indicator previously introduced can be adapted to the QCR as follows:

$$\Upsilon_{\text{Schmitt}}^{QCR} = \frac{\left| \underline{\underline{\tau_t^{**}}} : \left[\underline{\underline{\sigma^{QCR*}}} \right] \right|}{\left\| \underline{\underline{\tau_t^{**}}} \right\| \left\| \left[\underline{\underline{\sigma^{QCR*}}} \right] \right\|} \tag{2.56}$$

with:

$$\forall (i,j) \in [\![1 ; 3]\!]^2,\ \sigma_{ij}^{QCR*} = [\sigma_{ij}] - c_{QCR} \left(O_{ik} [\sigma_{jk}] + O_{jk} [\sigma_{ik}] \right) \tag{2.57}$$

2.4.3 Turbulence models

The only remaining quantity to model, in order to close the problem, is the eddy-viscosity μ_t. Many turbulence models exist to model this quantity. The simplest, and less universals, are the zero equation models (Smith and Cebeci, 1967; Baldwin and Lomax, 1978). They are designed for a given kind of flow, and do not account for the transport effects. The Spalart and Allmaras (1994) one equation model solves the transport of a viscosity-like quantity, used to reconstruct the eddy-viscosity. This model is still widely used, mainly for airfoil conception, but also for internal flow

applications. The next level of complexity is reached with the two equations models. Usually, one equation gives the turbulent kinetic energy k, and the other gives the turbulence dissipation rate ε, or the specific turbulence dissipation rate ω, with $\varepsilon = 0.09k\omega$. Among these models are the Launder and Sharma (1974) $k-\varepsilon$ model, the Wilcox (1988) $k-\omega$ model, the Menter (1994) SST $k-\omega$ model, the Kok (2000) $k-\omega$ model or the Wilcox (2008) $k-\omega$ model.

In this work, three versions derived from the Wilcox $k-\omega$ model of 1988 are considered. The two first versions are the classical model with the Boussinesq constitutive relation and its version with the QCR. The third version uses a modification of the transport equation of ω, in order to present a more realistic behaviour for the corner separation flow. For the naming convention, with the Boussinesq constitutive relation, the model is named the original Wilcox $k-\omega$ model, with the QCR, the model is named the quadratic Wilcox $k-\omega$ model, and the last version is called the modified Wilcox $k-\omega$ model.

Original Wilcox $k-\omega$ model

The original Wilcox $k-\omega$ turbulence model, first mentioned in Wilcox (1988), is a two-equation model for turbulent viscosity modelling. The two model variables, the turbulent kinetic energy k and the specific dissipation rate ω, allow calculating the turbulent viscosity as follows:

$$\mu_t = c_\mu \langle\rho\rangle \frac{[k]}{[\omega]} \tag{2.58}$$

with $c_\mu = 1.0$ a constant of the model.

The two equations of the model are:

$$\frac{\partial \langle\rho\rangle [k]}{\partial t} + \frac{\partial \langle\rho\rangle [k] [u_j]}{\partial x_j} = P_k + \frac{\partial}{\partial x_j}\left(\left(\mu + \frac{\mu_t}{\sigma_k}\right)\frac{\partial [k]}{\partial x_j}\right) - c_k \langle\rho\rangle [k] [\omega] \tag{2.59a}$$

$$\frac{\partial \langle\rho\rangle [\omega]}{\partial t} + \frac{\partial \langle\rho\rangle [\omega] [u_j]}{\partial x_j} = c_{\omega 1}\frac{[\omega]}{[k]}P_k + \frac{\partial}{\partial x_j}\left(\left(\mu + \frac{\mu_t}{\sigma_\omega}\right)\frac{\partial [\omega]}{\partial x_j}\right) - c_{\omega 2}\langle\rho\rangle [\omega]^2 \tag{2.59b}$$

with $c_k = 0.09$, $c_{\omega 1} = 5/9$, $c_{\omega 2} = 3/40$, $\sigma_k = 2.0$, $\sigma_\omega = 2.0$ and P_k the k-production term defined as:

$$P_k = \tau^*_{tij}\frac{\partial [u_i]}{\partial x_j} \tag{2.60}$$

Alternative expressions of the turbulent kinetic energy production term exist, based on the vorticity (Menter, 1992) (eq. (2.61)) or on the product between the vorticity tensor and the strain-rate tensor (Kato, 1993) (eq. (2.62)).

$$P_k = 2\mu_t \Omega_{ij}\Omega_{ij} \tag{2.61}$$

$$P_k = 2\mu_t \sqrt{S_{ij}S_{ij}}\sqrt{\Omega_{ij}\Omega_{ij}} \tag{2.62}$$

In order to keep a coherence between the formulation of the k-production term and the Reynolds tensor modelling, these expressions will not be used in this work.

Quadratic Wilcox $\mathbf{k-\omega}$ model

The quadratic constitutive relation modifies the Reynolds stress tensor. In the transport equations, it has a direct impact only on the k-production term P_k. This modification leads to:

$$P_k = \tau_{tij}^{QCR} \frac{\partial \left[u_i\right]}{\partial x_j} \tag{2.63}$$

Modified Wilcox $\mathbf{k-\omega}$ model

The Wilcox $k-\omega$ model was originally calibrated on flows around simple geometries. The modification, introduced by Liu et al. (2016), impacts the production term in the ω equation. The term is modified using kinematic vorticity, considering that fluid rotation and deformation occur in complex geometries, and calibrated on a low-speed prescribed velocity distribution cascade from Cambridge University (Gbadebo et al., 2004, 2005, 2007).

The ω equation (2.59b) becomes:

$$\frac{\partial \left\langle\rho\right\rangle \left[\omega\right]}{\partial t} + \frac{\partial \left\langle\rho\right\rangle \left[\omega\right] \left[u_j\right]}{\partial x_j} = c_{\omega 1} \frac{\left[\omega\right]}{\left[k\right]} P_k f r_1 + \frac{\partial}{\partial x_j} \left(\left(\mu + \frac{\mu_t}{\sigma_\omega} \right) \frac{\partial \left[\omega\right]}{\partial x_j} \right) - c_{\omega 2} \left\langle\rho\right\rangle \left[\omega\right]^2 \tag{2.64}$$

with the function fr_1 defined as:

$$f_{r1} = -\frac{1}{2\pi} \arctan\left(5(N_k - 1.2)\right) + 0.75 \tag{2.65}$$

$$N_k = \left(1 + \frac{2Q}{\left[S_{ij}\right]\left[S_{ij}\right]} \right)^{1/2} \tag{2.66}$$

$$Q = \frac{1}{2} \left(\left[\Omega_{ij}\right]\left[\Omega_{ij}\right] - \left[S_{ij}\right]\left[S_{ij}\right] \right) \tag{2.67}$$

with N_k the kinematic vorticity, Q the local balance between the strain rate and the vorticity magnitudes, $\left[\underline{\underline{S}}\right]$ the averaged strain rate tensor and $\left[\underline{\underline{\Omega}}\right]$ the averaged rotation tensor defined as:

$$\forall (i,j) \in [\![\ 1\ ;\ 3\ ]\!]^2,\ \left[\Omega_{ij}\right] = \frac{1}{2} \left(\frac{\partial \left[u_i\right]}{\partial x_j} - \frac{\partial \left[u_j\right]}{\partial x_i} \right) \tag{2.68}$$

The modified Wilcox $k-\omega$ model is used with the Boussinesq constitutive relation, *ergo* $P_k = \tau_{t,ij}^* \partial \left[u_i\right] / \partial x_j$.

2.4.4 Turbulent kinetic energy budget

In RANS with the Wilcox $k-\omega$ model, the turbulent kinetic energy budget is essentially given by the equation (2.59a). The Wilcox $k-\omega$ model tends to overpredict k production where anisotropy is important (Strahle, 1985). Consequently, a k-production limiter (Menter, 1994) is implemented in the solver, in the form of a

clipping of the k-production term, when the k-production term is superior to ten times the k-dissipation term. This limiter does not appear in the k equation (2.59a) but is explicitly introduced in the budget, in the form of a dissipative term Λ. Moreover, the TKE budget equation being directly solved, there should be a negligible residual. However, a numerical residual term Ξ is introduced to have a comparable formulation for both RANS and LES budgets. This term is computed as minus the sum of all the other spatial terms. The budget equation is:

$$\frac{\partial \langle\rho\rangle [k]}{\partial t} = \underbrace{P_k}_{\text{Production}} \underbrace{-\frac{\partial \langle\rho\rangle [k] [u_j]}{\partial x_j}}_{\text{Advection}} \underbrace{+\frac{\partial}{\partial x_j}\left(\mu \frac{\partial [k]}{\partial x_j}\right)}_{\substack{\text{Molecular} \\ \text{diffusion}}} \underbrace{+\frac{\partial}{\partial x_j}\left(\frac{\mu_t}{\sigma_k}\frac{\partial [k]}{\partial x_j}\right)}_{\substack{\text{Turbulent transport \&} \\ \text{pressure diffusion}}} \underbrace{-c_k \langle\rho\rangle [k] [\omega]}_{\text{Dissipation}} \underbrace{+\Lambda}_{\substack{k \text{ production} \\ \text{limiter}}} \underbrace{+\Xi}_{\substack{\text{Numerical} \\ \text{residual}}} \tag{2.69}$$

with $P_k = \tau^*_{t,ij} \partial [u_i] / \partial x_j$ for both the original Wilcox model and the modified Wilcox model, and $P_k = \tau^{QCR}_{t,ij} \partial [u_i] / \partial x_j$ for the quadratic Wilcox model.

Chapter 3

Hybrid RANS-LES

Sections

The hybrid RANS-LES approach was born of the will to have a more physical description of the flow than with RANS, but at a lower cost than with the LES approach. The principle of the hybrid RANS-LES modelling is to use RANS modelling close to walls, where the mesh refinement needed with the LES has the highest computational cost, and use the LES approach elsewhere, where the mesh can be coarser. The different methods differ in their way to pass continuously from a model to another. An overview of the "detached-eddy" methods (DES, DDES, IDDES and ZDES) can be found in Spalart (2009).

3.1 DES

The detached eddy simulation formulation is one of the first attempts to hybridise RANS modelling with LES modelling. It was theorised by Spalart et al. (1997) for the Spalart and Allmaras (1992, 1994) turbulence model.

3.1.1 Formulation

The one-equation Spalart and Allmaras (1994) model relies on a wall distance $\hat{d} = d$ in the original RANS formulation:

$$\frac{\partial \hat{\nu}}{\partial t} + u_j \frac{\partial \hat{\nu}}{\partial x_j} = c_{b1}\left(1 - f_{t2}\right)\hat{S}\hat{\nu} - \left(c_{w1} f_w - \frac{c_{b1}}{\kappa^2}\right)\left(\frac{\hat{\nu}}{\hat{d}}\right)^2 + \frac{1}{\sigma}\left[\frac{\partial}{\partial x_j}\left((\nu + \hat{\nu})\frac{\partial \hat{\nu}}{\partial x_j}\right) c_{b2}\frac{\partial \hat{\nu}}{\partial x_i}\frac{\partial \hat{\nu}}{\partial x_i}\right] \tag{3.1}$$

$$\mu_t = \rho \hat{\nu} f_{v1};\ f_{v1} = \frac{\chi^3}{\chi^3 + c_{v1}^3};\ \chi = \frac{\hat{\nu}}{\nu} \tag{3.2}$$

The model introduces some functions in which the wall distance is present. The functions are defined as follows:

$$\hat{S} = \sqrt{\left(\frac{\partial u_i}{\partial x_j} - \frac{\partial u_j}{\partial x_i}\right)\left(\frac{\partial u_i}{\partial x_j} - \frac{\partial u_j}{\partial x_i}\right)} + \frac{\hat{\nu}}{\kappa^2 \hat{d}^2} f_{v2} \tag{3.3}$$

$$f_{v2} = 1 - \frac{\chi}{1 + \chi f_{v1}} \tag{3.4}$$

$$f_w = g\left(\frac{1 + c_{w3}^6}{g^6 + c_{w3}^6}\right)^{1/6} \tag{3.5}$$

$$g = r + c_{w2}\left(r^6 - r\right) \tag{3.6}$$

$$r = \min\left(\frac{\hat{\nu}}{\hat{S}\kappa^2 \hat{d}^2},\ 10\right) \tag{3.7}$$

$$f_{t2} = c_{t3} \exp\left(-c_{t4}\chi^2\right) \tag{3.8}$$

The model constants are $c_{b1} = 0.1355$, $c_{b2} = 0.622$, $\sigma = 2/3$, $\kappa = 0.41$, $c_{v1} = 7.1$, $c_{t3} = 1.2$, $c_{t4} = 0.5$, $c_{w1} = c_{b1}/\kappa + (1 + c_{b2})/\sigma$, $c_{w2} = 0.3$ and $c_{w3} = 2$.

The wall distance $\hat{d}$ is the variable modified in the DES formulation, in order to yield an LES resolution away from the walls:

$$\hat{d} = \min\left(d,\ C_{DES}\Delta\right) \tag{3.9}$$

with $\Delta = \Delta_{\max} = \max(\Delta x,\ \Delta y,\ \Delta z)$ and C_{DES} the Smagorinsky (1963) sub-grid scale model constant.

3.1.2 Alternative formulation

An alternative formulation exists for two-equations models. This formulation, proposed by Kok et al. (2004), relies on the definition of a turbulent length scale $\hat{l}$ for the computation of μ_t:

$$\hat{l} = \min\left(\frac{\sqrt{k}}{\omega},\ C_1\Delta\right);\ \mu_t = \rho\hat{l}\sqrt{k} \tag{3.10}$$

with $C_1 = 0.06$.

Another formulation, presented by Travin et al. (2004), modifies the DES to use the SST model (Menter, 1994; Menter et al., 2003), in order to improve the separation predictions. An hybrid numerical scheme is also presented, with an upwind-biased scheme (order 3 or 5) for the RANS and a fourth-order centred-scheme for the LES.

3.1.3 Low Reynolds number correction

The eddy viscosity μ_t tends to decrease when the Reynolds number decreases, which tends to be considered by the model as a proximity with a wall. In order to correct this behaviour, Spalart et al. (2006) proposed a function $\psi \geqslant 1$ that increases the C_{DES} (or C_1) coefficient:

$$\hat{d} = \min\left(d,\ \psi C_{DES}\Delta\right) \tag{3.11}$$

The correction can be used with the Spalart-Allmaras version of the DES (3.12) or the $k-\omega$ version of the DES (3.13).

$$\psi^2 = \min\left[10^2,\ \frac{1 - \frac{c_{b1}}{c_{w1}\kappa^2 f_w}\left[f_{t2} + (1 - f_{t2})\, f_{v2}\right]}{f_{v1}\max\left(10^{-10},\ 1 - f_{t2}\right)}\right] \tag{3.12}$$

$$\psi = \frac{\beta^*}{C_\mu}\left(\frac{2\alpha}{\alpha^*}\right)^{3/4} \tag{3.13}$$

where the constants of (3.13) can be found in the Wilcox (1988) model definition.

3.1.4 Limitations

The brutal modification of $\hat{d}$, due to the minimum in Eq. (3.9), implies that a careful consideration should be given to the mesh. The variation of Δ must be smooth enough to allow a transition zone (often referred to as the "grey zone") that links correctly the RANS part to the LES part of the simulation.

The model is also known to have troubles to stay in RANS when the boundary-layer is too thick, or if small separations occur (Spalart et al., 2006).

3.2 DDES

The delayed detached-eddy simulation aims at correcting the weakness of the DES for thick boundary-layers.

3.2.1 Formulation

The principle of the correction proposed by Spalart et al. (2006) is to delay the LES activation by using a transition function as follow:

$$\hat{d} = d - f_d \max\left(0,\ d - C_{DES}\Delta\right) \tag{3.14}$$

with :

$$f_d = 1 - \tanh\left(\left[8r_d\right]^8\right) \tag{3.15}$$

$$r_d = \frac{\hat{\nu} + \nu}{\sqrt{\frac{\partial u_i}{\partial x_j}\frac{\partial u_i}{\partial x_j}}\kappa^2 d^2} \tag{3.16}$$

This formulation is less dependant on the mesh and allows three possible states instead of just the two states of the original DES formulation:

- $d \leqslant C_{DES}\Delta$: The RANS model is used and $\hat{d} = d$.
- $d > C_{DES}\Delta,\ r_d \approx 1$: The model makes a transition between RANS and LES, an explicit "grey zone" in which $\hat{d} = (1 - f_d)d + f_d C_{DES}\Delta$.
- $d > C_{DES}\Delta,\ r_d \ll 1$: The LES formulation is used and $\hat{d} = C_{DES}\Delta$.

3.2.2 Alternative formulation

Another formulation, presented by Gritskevich et al. (2012), modifies the DDES to use the $k - \omega$ SST model (Menter, 1994; Menter et al., 2003). The equations are not presented here, but they can be found in the article appendix, along with some of the constants that were re-calibrated.

3.2.3 Low Reynolds number correction

The previous low Reynolds number correction, presented in Eq. (3.12), can be used for the DDES. Another solution is to limit χ before the computation of f_{v1}, f_{v2} and f_{t2}, as follows:

$$\chi = \max\left(\chi,\ 20 f_d\right) \tag{3.17}$$

3.2.4 Limitations

The DDES improves the DES formulation by reducing the mesh dependency. However, some discrepancies remain. The log laws, in the RANS area and in the LES area, do not coincide at the interface for instance (Shur et al., 2008; Spalart, 2009).

3.3 IDDES

The IDDES was presented the first time by Travin et al. (2006), but the final formulation is from the article of Shur et al. (2008). The main goal of the improved delayed detached-eddy simulation is to use the DES formulation to do wall-modelled LES. The limitations of the DES formulation lead to preferably use the concept of the DDES, with an hybridisation function. This aims at correcting the log law discrepancies of the DDES formulation. The IDDES has been successfully used by Greschner and Thiele (2011), with the "Compact Explicit Algebraic Stress Turbulence Model" (Greschner et al., 2010), to simulate the interaction broadband noise in a rotor-stator cascade.

3.3.1 Formulation

First, the sub-grid scale is redefined for the LES part:

$$\Delta = \min\left[\max\left(C_W d,\ C_W \Delta_{\max},\ C_W \Delta_{wn}\right),\ \Delta_{\max}\right] \tag{3.18}$$

with $\Delta_{\max} = \max(\Delta_x,\ \Delta_y,\ \Delta_z)$ the local longest cell dimension, Δ_{wn} the cell dimension in the direction normal to the wall and $C_W = 0.15$ an empirical constant.

Then, the hybridisation function is defined:

$$\hat{d} = f_{hyb}\left(1 + f_e\psi\right) d + \left(1 - f_{hyb}\right) C_{DES}\psi\Delta \tag{3.19}$$

Two new functions, f_{hyb} and f_e, are used in this formulation. f_{hyb} is defined as follows:

$$f_{hyb} = \max\left[\left(1 - f_d,\ f_{step}\right)\right] \tag{3.20}$$

with:

$$f_d = 1 - \tanh\left(\left[8r_d\right]^8\right);\ r_d = \frac{\hat{\nu}}{\kappa^2 d^2}\frac{1}{\max\left(\sqrt{\frac{\partial u_i}{\partial x_j}\frac{\partial u_i}{\partial x_j}}, 10^{-10}\right)} \tag{3.21}$$

and

$$f_{step} = \min\left[2\exp\left(-9\alpha^2\right),\ 1.0\right];\ \alpha = 0.25 - \frac{d}{\Delta_{\max}} \tag{3.22}$$

f_e is defined as follows:

$$f_e = \max\left[\left(f_{e1} - 1\right),\ 0\right]\psi f_{e2} \tag{3.23}$$

with:

$$f_{e1} = \begin{cases} 2\exp\left(-11.09\alpha^2\right) & \text{if} \quad \alpha \geqslant 0 \\ 2\exp\left(-9.0\alpha^2\right) & \text{if} \quad \alpha < 0 \end{cases};\ \alpha = 0.25 - \frac{d}{\Delta_{\max}} \tag{3.24}$$

and:

$$f_{e2} = 1.0 - \max\left(f_t,\ f_l\right) \tag{3.25}$$

$$f_t = \tanh\left[\left(c_t^2 r_d\right)^3\right] \tag{3.26}$$

$$f_l = \tanh\left[\left(c_l^2 r_{dl}\right)^{10}\right];\ r_{dl} = \frac{\nu}{\kappa^2 d^2}\frac{1}{\max\left(\sqrt{\frac{\partial u_i}{\partial x_j}\frac{\partial u_i}{\partial x_j}}, 10^{-10}\right)} \tag{3.27}$$

with the constants $c_t = 1.63$ and $c_l = 3.55$ chosen to have $f_{e2} \approx 0$ for $r_d \approx 1$ and $r_{dl} \approx 1$.

3.3.2 Alternative formulation

Another formulation, presented by Gritskevich et al. (2012), modifies the IDDES to use the $k-\omega$ SST model (Menter, 1994; Menter et al., 2003). The equations are not presented here, but they can be found in the article appendix, along with some of the constants that were re-calibrated.

3.3.3 Low Reynolds number correction

The low Reynolds number correction ψ used in the IDDES is similar to the correction used for the DES, presented in Eq. (3.12), except that instead of using the value of f_w from the Spalart-Allmaras model, $f_w = 0.424$.

3.3.4 Limitations

The IDDES formulation is, by far, the most advanced formulation of the "detached-eddy" method family. Its main limitation comes from its complexity. The model is much more complex than the original DES model, and uses many constants. The correct calibration and validation of such a model necessitate an important amount of efforts. For these reasons, its implementation is quite complicated. The "grey zone" problem is still not completely solved, and the mesh generation keeps being difficult (Spalart, 2009).

3.4 Zonal detached-eddy simulation

The zonal detached-eddy simulation, introduced by Deck (2005), aims at correcting two of the problems present in the "detached-eddy" models. The grid-induced separation (GIS) and the modelled-stress depletion (MSD) are effects of the mesh density variation that affect all the "detached-eddy" models. They occur in the "grey-zone", and create non-physical results in these areas.

The principle of ZDES is to classify the different possible separations occurring in the flow per areas, and use the adapted model from the "detached-eddy" family. Many improvements with respect to the original publication together with advices for implementation and use can be found in Deck (2012).

3.4.1 Formulation

First, the flow has to be classified in order to choose the kind of model to use. The classification of the flows is given in Fig. 3.1.

In the case (I), presented in Fig. 3.1a, the separation is directly imposed by the geometry. The boundary-layer thickness δ is far smaller than the height of the separation H. The place of the separation is well-known *a priori*. The case (II) is different from

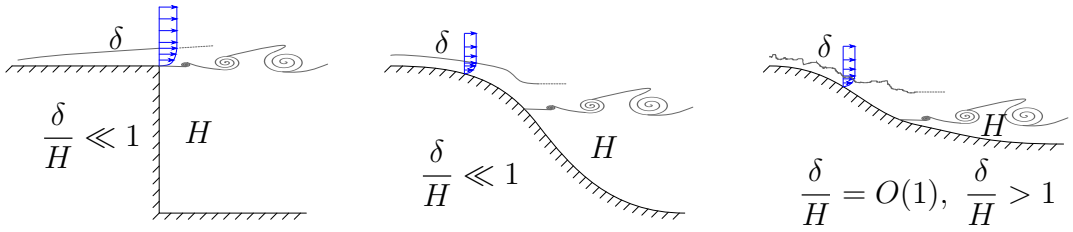

(a) Case (I) (b) Case (II) (c) Case (III)

Figure 3.1: Classification of the flows for the ZDES.

the case (I), as shown in Fig. 3.1b: the separation is induced by an adverse pressure gradient or the curvature of the geometry. If the boundary-layer thickness δ is still far smaller than the height of the separation H, the exact position where the separation occurs is not precisely known. In the case (III), presented in Fig. 3.1c, the main factor influencing the separation is the dynamics of the incoming boundary-layer. In that case, the boundary-layer thickness δ can be approximately equal to the height of the separation H, or bigger.

Secondly, three sub-grid scales are defined, Δ_{vol}, Δ_{vort} and $\Delta_{\max}$:

$$\Delta_{vol} = \left(\Delta_x \Delta_y \Delta_z\right)^{1/3} \tag{3.28}$$

$$\Delta_{vort} = \sqrt{\left(\frac{\Omega_x}{\|\underline{\Omega}\|}\right)^2 \Delta_y \Delta_z + \left(\frac{\Omega_y}{\|\underline{\Omega}\|}\right)^2 \Delta_x \Delta_z + \left(\frac{\Omega_z}{\|\underline{\Omega}\|}\right)^2 \Delta_x \Delta_y} \tag{3.29}$$

$$\Delta_{\max} = \max\left(\Delta_x,\ \Delta_y,\ \Delta_z\right) \tag{3.30}$$

where $\underline{\Omega}$ is the vorticity.

Δ_{vort} can be also calculated as follows:

$$\Delta_{vort} = \sqrt{S_\Omega} \tag{3.31}$$

with S_Ω the cell mean section along the directions normal to $\underline{\Omega}$.

It can be noted that $\Delta_{\max}$ is the usual sub-grid scale for the DES and DDES, and is already present in the computation of the sub-grid scale for the IDDES. The two other sub-grid scales presented in Eq. (3.28) and Eq. (3.29) are newly introduced by the ZDES model.

The ZDES model relies on two variables, *ides* and *imode*, that allow to choose the method. *ides* is the variable to choose if the hybridisation should be activated, while *imode* is the variable to choose the case encountered. If the case studied necessitates pure RANS with no hybridisation, $ides = 0$, thus $\hat{d} = d$. If the case studied is case (I), $ides = 1$, $imode = 1$, and $\hat{d} = d_I$. If the case studied is case (II), $ides = 1$, $imode = 2$, and $\hat{d} = d_{II}$. If the case studied is case (III), $ides = 1$, $imode = 3$, and $\hat{d} = d_{III}$. It is summarised in Tab. 3.1. The definitions of d_I, d_{II} and d_{III} are given in the following sub-sections.

Case (I)

The first case corresponds to a well known and well located separation that does not depend on the state of the incoming boundary-layer, or the pressure gradient. In that

Case	*ides*	*imode*	$\hat{d}$
Pure RANS	0	NA	d
Case (I)	1	1	d_I
Case (II)	1	2	d_{II}
Case (III)	1	3	d_{III}

Table 3.1: ZDES selection variables function of the case studied.

case, the model used is the classical DES model, with a modification of the sub-grid scale:

$$d_I = \min\left(d,\ C_{DES}\Delta\right);\ \Delta = \Delta_{vol} \text{ or } \Delta = \Delta_{vort} \tag{3.32}$$

Case (II)

The second case corresponds to a separation induced by an adverse pressure gradient or the curvature of the geometry. The separation does not take place at a prescribed position as in the first case, but the area of separation is quite correctly bounded. In that case, the model used is preferably the DDES, with a modified sub-grid scale:

$$d_{II} = d - f_d \max\left(0,\ d - C_{DES}\Delta\right) \tag{3.33}$$

with f_d the DDES function defined in Eq. (3.15), and Δ defined as:

$$\Delta = \left[0.5 + \mathbf{sign}\left(0.5,\ f_d - f_{d0}\right)\right]\left(\Delta_{\max} + \{\Delta_{vol} \text{ or } \Delta_{vort}\}\right) \tag{3.34}$$

with $f_{d0} = 0.8$.

The function **sign** is defined as the Fortran function $\mathbf{sign}\,(a, b)$, returning a if $b \geqslant 0$ and $-a$ if $b < 0$. The case (II) can be viewed as a DDES with two conditions. The first one is the criterion on the wall-distance, driven by f_d, as in the classical DDES, and a second one is the criterion on $f_d - f_{d0}$. If $f_d < f_{d0}$, $\Delta = 0$ and $d_{II} = d$.

Case (III)

The last case is the most complex, and relies on a user-defined wall-distance d_{user} to choose the place of transition between RANS and LES:

$$d_{III} = \begin{cases} d & \text{if} \quad d < d_{user} \\ d_I & \text{if} \quad d \geqslant d_{user} \end{cases} \tag{3.35}$$

The hybrid part relies on the case (I) formulation.

3.4.2 Limitations

The ZDES is very interesting and promising, but it relies on a fine knowledge of the flow studied, given that the user have to choose both the areas where the transition between RANS and LES occurs, and the kind of mode to use. In term of complexity, it simplifies the mesh generation since it relies on DDES and IDDES. However, it adds the difficulty of choosing the right case to have the best results. Another good point is that it allows pure zonal simulations, with mode 0 for pure RANS and mode 3 with $d_{user} = 0$ for pure LES (Bordji et al., 2015). The ZDES was described by Spalart (2009) as more powerful and less auto-sufficient at the same time.

3.5 Tucker's formulation

The main goal of Tucker et al. (2012a,b) formulation is to link the RANS zone and the LES zone of the DES through a non-abrupt interface. The model aims at keeping the LES quite close to the wall too. For these reasons, the solution chosen is to use a Hamilton-Jacobi differential equation on $\hat{d}$.

3.5.1 Formulation

The Hamilton-Jacobi equation is written as follows:

$$\left|\nabla\hat{d}\right| = 1 + \mathbf{f}\left(\hat{d}\right)\nabla^2\hat{d} + \mathbf{g}\left(d\right) \tag{3.36}$$

The functions $\mathbf{f}$ and $\mathbf{g}$ are defined as follows:

$$\mathbf{f}\left(\hat{d}\right) = \epsilon_0\hat{d} \tag{3.37}$$

$$\mathbf{g}\left(d\right) = \epsilon_1\left(\frac{d}{L}\right)^n \tag{3.38}$$

with ϵ_0 and ϵ_1 two constants to calibrate, L the distance between the wall and the LES zone, and n an integer to calibrate.

If the model was first designed to be used with the Spalart and Allmaras (1994) turbulence model, it can theoretically be used with any model relying on a turbulence length-scale. The induced modifications are of the same kind of the modifications of the DES, DDES or IDDES alternatives formulations.

3.5.2 Limitations

The model presents the advantage of simplicity, with only three calibration parameters. However, the value for $\hat{d}$ is 0 at the wall and is 0 in the LES zone too, as presented in Fig. 3.2. This means that the MILES model (Boris et al., 1992) is intended to be used in the LES zones (which means, practically, no sub-grid scale model), leading to what is known as numerical LES (NLES). This obligation to do LES without a sub-grid scale model is a major drawback of the model.

Another limitation comes from the resolution of the Hamilton-Jacobi equation. The resolution must be propagated from the nearest wall to the NLES zone. This solution needs a solver compatible with this kind of propagation.

3.6 Zonal large-eddy simulation

Zonal large-eddy simulation (ZLES) was introduced to let the user define where to use LES and where to use RANS. LES can be applied to a specific region of interest, down to the wall, while peripheral regions are described by RANS. However, if RANS is specified in the near wall region, an hybrid RANS-LES formulation is obtained. Any kind of RANS and LES models relying on an eddy viscosity can be used. The transition is continuous, with a parametrised polynomial function, and is made on the eddy viscosity, instead of $\hat{d}$. The model presented was used by Boudet et al. (2015a, 2016a,b) on a tip-clearance flow case, with the original Wilcox model for

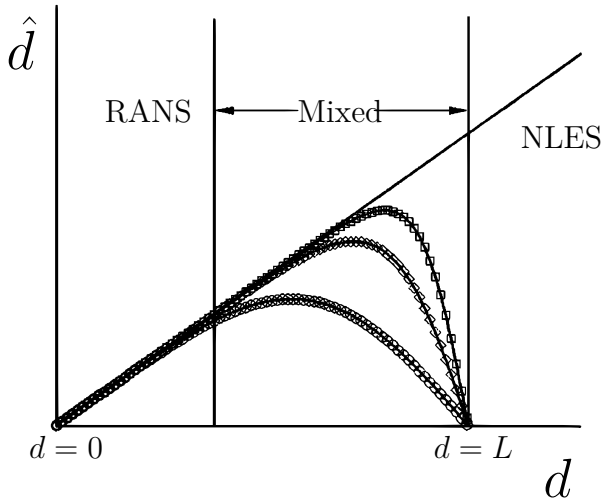

Figure 3.2: Hybridisation function from Tucker et al. (2012a,b) for different ϵ_0 and ϵ_1, and $n = 1$. The central curve is for $\epsilon_0 = 0.2$ and $\epsilon_1 = 1.5$.

RANS (Wilcox, 1988) and the shear-improved Smagorinsky model (SISM) for LES (Lévêque et al., 2007).

3.6.1 Formulation

The formulation given here relies on an hybridisation of the turbulent and SGS viscosities:

$$\mu_{mod} = (1 - \beta(\underline{x}))\,\mu_{SGS} + \beta(\underline{x})\,\mu_t \tag{3.39}$$

with μ_{mod} the hybrid viscosity, μ_{SGS} the sub-grid scale viscosity (LES) and μ_t the turbulent viscosity (RANS).

The β function is a user-defined smooth function (e.g. polynomial).

3.6.2 Limitations

The function $\beta(\underline{x})$ has to be defined by the user, which can be a complex task when dealing with three-dimensional geometries. Moreover, in the version presented by Boudet et al. (2015b), no synthetic fluctuation is imposed at the interface between the RANS and LES zones. For this reason, the $\beta = 0.5$ surface is preferably set tangent to the mean flow, or cross-stream if the flow is oriented from a LES zone towards a RANS zone.

Part II

Methods

Chapter 4

Turbulent kinetic energy budget extraction

Sections

One of the main goals of this work is to compare how turbulent models manage to represent the behaviour of a complex turbulent flow. In order to do this, the turbulent kinetic energy budget is extracted and a term-to-term comparison is done between simulations using RANS modelling and simulations using LES modelling, considered as reference. For RANS simulations, the operation is straightforward. The two-equation models provide one equation on the turbulent kinetic energy. For LES, the operation is more complex. The entire Reynolds stress budget is extracted, and not only the symmetrical terms. The budget relies on many gradients. The ensemble average is practically computed as a time-average, and the acquisition of the data regularly spaced in time is done on the fly. The details of the implementation is presented in this chapter.

4.1 Gradients computation

The turbulent kinetic energy budget presented in equation (2.36) relies on many gradients. These gradients are not directly computed in the flow computation, and have

to be generated *via* a chosen discretisation. The budget gradients are computed using the internal metrics of *Turb'Flow* and a finite differences approach, whereas the Navier-Stokes equations are discretised using finite-volumes.

4.1.1 Metrics calculation

The gradient computation programming depends on the mesh chosen in a general case, due to the fact that the mesh size intervene in the general formulation. To generalise the programming, a change of coordinates is realised at each point, in order to transform a given mesh into a Cartesian mesh at each point. This section details the metrics construction realised in *Turb'Flow*, on which the gradients computation relies.

The change of coordinates is made between the original mesh positions $\underline{x}$ and their associated Cartesian mesh positions $\underline{\xi}$. For a considered node in the original mesh and its associated node in the Cartesian mesh the indexes are noted with the capital letters I, J, and K, as presented in figure 4.1.

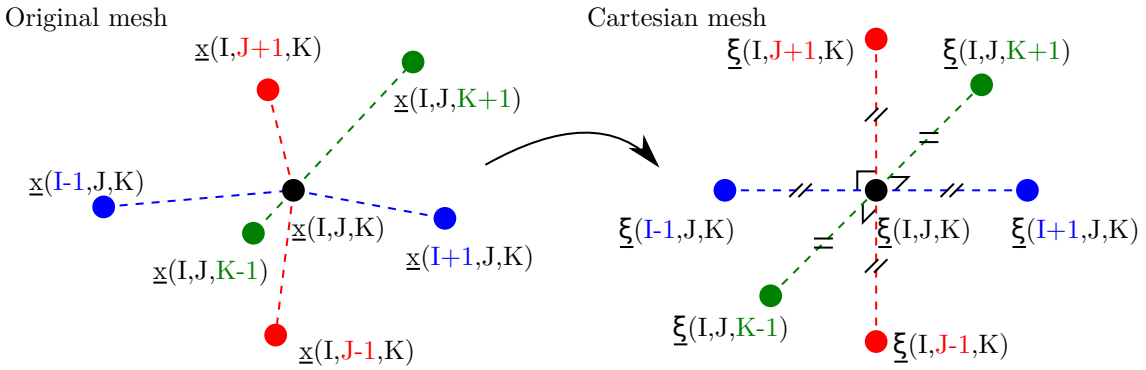

Figure 4.1: Mesh transformation from original to Cartesian.

The contravariant basis $(\underline{\varsigma}, \underline{\eta}, \underline{\gamma})$, is defined as:

$$\underline{\varsigma} = \left(\frac{\partial \xi_1}{\partial x_1}, \frac{\partial \xi_1}{\partial x_2}, \frac{\partial \xi_1}{\partial x_3} \right) \tag{4.1}$$

$$\underline{\eta} = \left(\frac{\partial \xi_2}{\partial x_1}, \frac{\partial \xi_2}{\partial x_2}, \frac{\partial \xi_2}{\partial x_3} \right) \tag{4.2}$$

$$\underline{\gamma} = \left(\frac{\partial \xi_3}{\partial x_1}, \frac{\partial \xi_3}{\partial x_2}, \frac{\partial \xi_3}{\partial x_3} \right) \tag{4.3}$$

The contravariant basis has the particularity that $\underline{\varsigma}$ is normal to a constant I surface locally, $\underline{\eta}$ is normal to a constant J surface locally and $\underline{\gamma}$ is normal to a constant K surface locally (Fig. 4.2).

For a given quantity at a given point $\varphi = \varphi[I, J, K]$, the partial derivative with respect to a direction is given by:

$$\forall i \in [\![1 \ ; \ 3]\!], \ \frac{\partial \varphi}{\partial x_i} = \varsigma_i \frac{\partial \varphi}{\partial \xi_1} + \eta_i \frac{\partial \varphi}{\partial \xi_2} + \gamma_i \frac{\partial \varphi}{\partial \xi_3} \tag{4.4}$$

where the derivatives of the quantity φ with respect to the Cartesian mesh coordinates can be computed using a finite difference scheme. Such a formulation relies on the computation of the contravariant basis.

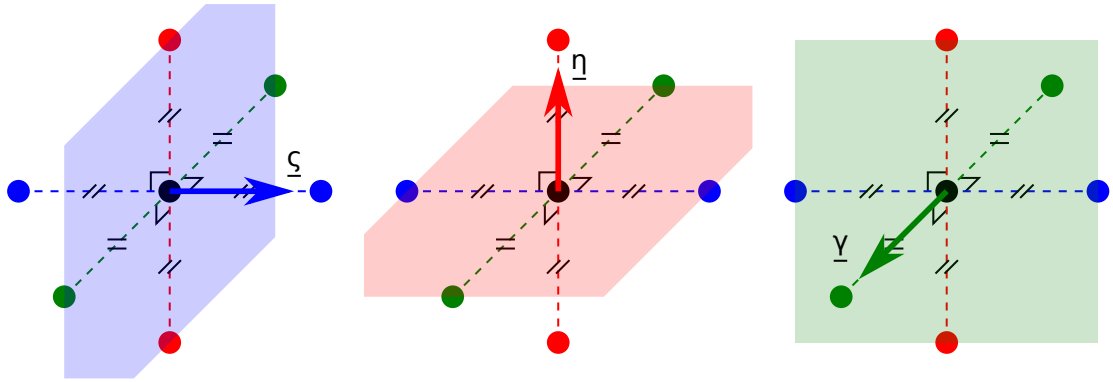

Figure 4.2: Contravariant basis.

Usual formulation

Usually, the computation begins with the computation of the covariant basis. The Jacobian is deduced from the covariant basis, and then the contravariant basis is obtained as a cross product of the covariant basis multiplied by the inverse of the square root of the Jacobian R_J, as presented in Merle and Robinet (2009) for a two dimensional formulation or Aubert (1993) (appendix D) for a three dimensional formulation.

The contravariant basis and the square root of the Jacobian are used in *Turb'Flow* chiefly to calculate the oriented surfaces of the discretisation cell in the finite volume method:

$$\underline{n}_I dS = R_J \underline{\xi} \tag{4.5}$$
$$\underline{n}_J dS = R_J \underline{\eta} \tag{4.6}$$
$$\underline{n}_K dS = R_J \underline{\gamma} \tag{4.7}$$

For this calculation, the usual formulation presents the inconvenient of not being conservative if the meshes are too distorted. An example of very distorted mesh is given in figure 4.3. The solution adopted is to calculate the square root of the Jacobian directly as the volume of the integration cell V centred on the considered node, and the contravariant basis using the normals of the surfaces.

Implemented formulation

In order to build the integration cell, 27 phantom points are constructed around each node. For a considered node at indices (I, J, K), the phantom points are constructed as barycentres of the surrounding nodes. The generic formula to obtain a given point coordinates is:

$\forall (\Delta I, \Delta J, \Delta K) \in \{-1, 0, 1\}^3,\ \forall i \in [\![\ 1\ ;\ 3\ ]\!]$,

$$\begin{aligned} x_i^{(\Delta I, \Delta J, \Delta K)}[I, J, K] = \frac{1}{8}\Big(& x_i[I, J, K] + x_i[I + \Delta I, J, K] + x_i[I, J + \Delta J, K] \\ & + x_i[I + \Delta I, J + \Delta J, K] + x_i[I, J, K + \Delta K] + x_i[I + \Delta I, J, K + \Delta K] \\ & + x_i[I, J + \Delta J, K + \Delta K] + x_i[I + \Delta I, J + \Delta J, K + \Delta K]\Big) \end{aligned} \tag{4.8}$$

with $\underline{x}^{(\Delta I,\Delta J,\Delta K)}$ the phantom points coordinates. A two dimensional slice of a discretisation cell, representing the points for $\Delta K = 0$, is presented in figure 4.4.

The integration cell is cut into eight hexahedral sub-volumes, as presented in figure 4.5a. For a given sub-volume, with the notation given in figure 4.5b, the volume V_{hex} is computed using the triple product of the diagonals:

$$V_{hex} = \frac{1}{16}\Big(\underline{AH} : (\underline{BG} \wedge \underline{DE}) + \underline{BG} : (\underline{DE} \wedge \underline{CF}) + \underline{DE} : (\underline{CF} \wedge \underline{AH}) + \underline{CF} : (\underline{AH} \wedge \underline{BG})\Big) \quad (4.9)$$

with : the scalar product operator and $\wedge$ the cross product operator. The total volume V is computed as the sum of the eight sub-volumes:

$$V = \sum_{\substack{\text{hexahedral} \\ \text{sub-volumes}}} V_{hex} \quad (4.10)$$

The contravariant basis is then built by summing the oriented surface vectors of the four small surfaces generated by the phantom points when one of the superscript index is equal to zero. For each element of surface, the oriented surface vector is computed as the cross-product of the diagonals of these small surfaces. For instance, the participation of the constant I surface $(ACGE)$ presented in figure 4.5b is equal to $-\underline{AG} \wedge \underline{EC}$. It can be expressed, in terms of coordinates, as $-(\underline{x}^{(0,1,1)} - \underline{x}^{(0,0,0)}) \wedge (\underline{x}^{(0,0,1)} - \underline{x}^{(0,1,0)})$. The formulation when all the elementary surfaces are taken into account is:

$$\begin{pmatrix} \varsigma_1 \\ \eta_1 \\ \gamma_1 \end{pmatrix} = \frac{1}{V} \sum_{\substack{j\in\{-1,1\} \\ k\in\{-1,1\}}} j \times k \times \left(\underline{x}^{(0,j,k)} - \underline{x}^{(0,0,0)}\right) \wedge \left(\underline{x}^{(0,0,k)} - \underline{x}^{(0,j,0)}\right) \quad (4.11)$$

$$\begin{pmatrix} \varsigma_2 \\ \eta_2 \\ \gamma_2 \end{pmatrix} = \frac{1}{V} \sum_{\substack{i\in\{-1,1\} \\ k\in\{-1,1\}}} i \times k \times \left(\underline{x}^{(i,0,k)} - \underline{x}^{(0,0,0)}\right) \wedge \left(\underline{x}^{(i,0,0)} - \underline{x}^{(0,0,k)}\right) \quad (4.12)$$

$$\begin{pmatrix} \varsigma_3 \\ \eta_3 \\ \gamma_3 \end{pmatrix} = \frac{1}{V} \sum_{\substack{i\in\{-1,1\} \\ j\in\{-1,1\}}} i \times j \times \left(\underline{x}^{(i,j,0)} - \underline{x}^{(0,0,0)}\right) \wedge \left(\underline{x}^{(0,j,0)} - \underline{x}^{(i,0,0)}\right) \quad (4.13)$$

The same metrics construction is made at each interface between the integration cells too, in order to have coherent oriented surfaces for two adjacent integration cells. The finite volume method is guaranteed conservative by this construction. The gradient computation for the TKE budget relies on the metrics presented, centred on the nodes, in order to stay coherent with the metrics used by the solver to solve the Navier-Stokes equations.

4.1.2 Finite differences formulation

The derivatives of the quantity φ with respect to the ξ_i, $i \in [\![1 ; 3]\!]$, introduced in equation (4.4), are computed using a second order centred finite difference scheme.

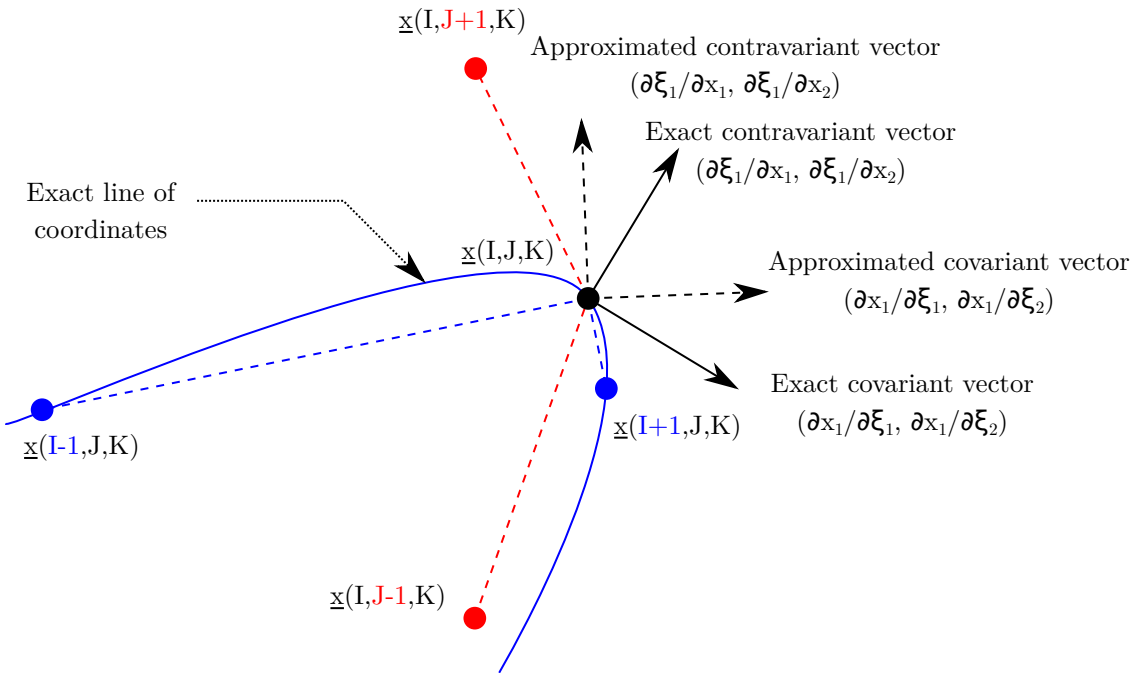

Figure 4.3: Strongly distorted mesh. Only the participation of the blue line covariant vector

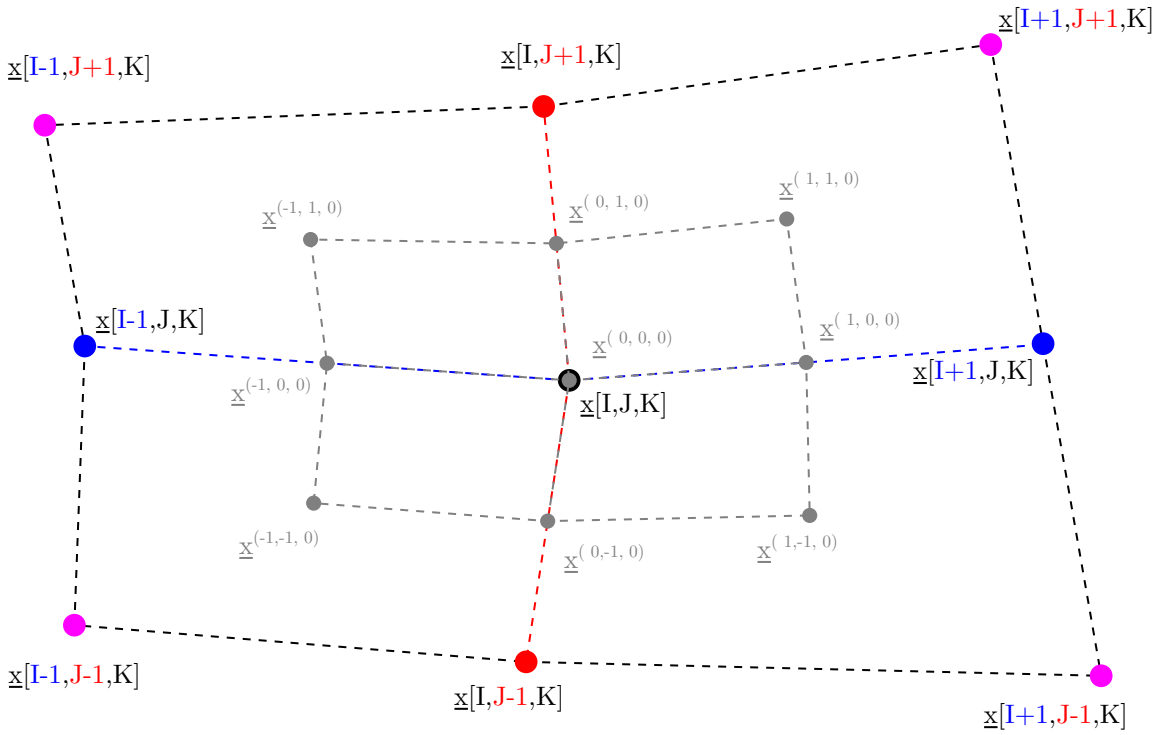

Figure 4.4: 2D slice of a 3D integration cell. The generalisation from 2D to 3D is done by constructing the same points as for the 2D cell, but at $\Delta K \pm 1$ too, the 2D cell presenting the points at $\Delta K = 0$.

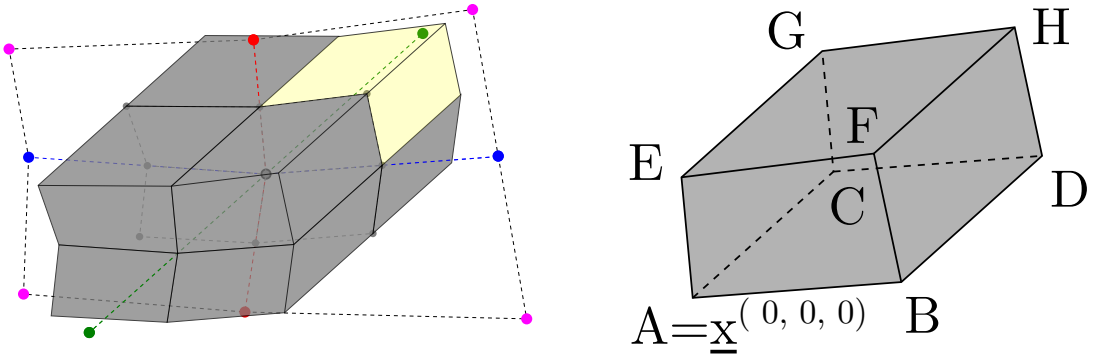

(a) Hexahedral sub-volumes of an integration cell (b) Hexahedral sub-volume details

Figure 4.5: Hexahedral sub-volumes of an integration cell. The sub-volume in pale yellow in (a) is reproduced in (b)

The formulation with this set of coordinates depends only, at a given set of indices I, J, K, on the surrounding points:

$$\frac{\partial \varphi}{\partial \xi_1} = \frac{1}{2}\left(\varphi[I+1,J,K] - \varphi[I-1,J,K]\right) \tag{4.14}$$

$$\frac{\partial \varphi}{\partial \xi_2} = \frac{1}{2}\left(\varphi[I,J+1,K] - \varphi[I,J-1,K]\right) \tag{4.15}$$

$$\frac{\partial \varphi}{\partial \xi_3} = \frac{1}{2}\left(\varphi[I,J,K+1] - \varphi[I,J,K-1]\right) \tag{4.16}$$

For the points inside the calculation domain, the computation is straightforward. For the points at the border of the calculation domain, the computation relies on the supplementary planes, as presented by Smati (1997).

4.2 Statistics extraction

4.2.1 Averaged values calculation

The ensemble average is practically computed as a time average, on the fly. For a given value φ at a given time t (noted $\varphi(t)$), the average is computed as:

$$\langle\varphi\rangle(t) = \frac{1}{t - t_{\text{start}}}\left(\sum_{T=t_{start}+\Delta t(t_{start})}^{t} \varphi(T)\Delta t(T)\right) \tag{4.17}$$

with t_{start} the time at which the time average begins and Δt the time step that separates a given instant from the precedent.

The gradients of the averaged values are computed at the end of the averaging and yield the averaged gradients.

Practically, a field variable is declared for each value to average, and a scalar variable is declared for the averaging time. The fields and averaging time are initialised to zero, and then at each time step the value φ times the time-step Δt is accumulated in the corresponding field. The time step is added to the averaging time. The division by the total averaging time is done at the last iteration.

4.2.2 Fluctuating values calculation

The Reynolds stress budget relies on second order and third order correlations. These correlations are reconstructed *via* the average quantities. For instance, for ρ the density and three given quantities φ_1, φ_2 and φ_3, a first order correlation $\langle\overline{\varphi_1}\varphi_2''\rangle$ is computed as:

$$\langle\overline{\varphi_1}\varphi_2''\rangle = \langle\overline{\varphi_1}\widetilde{\varphi_2}\rangle - \langle\overline{\varphi_2}\rangle\,[\widetilde{\varphi_2}] \tag{4.18}$$

The second order correlation $\langle\overline{\rho}\varphi_1''\varphi_2''\rangle$ is reconstructed as:

$$\langle\overline{\rho}\varphi_1''\varphi_2''\rangle = \langle\overline{\rho}\widetilde{\varphi_1}\widetilde{\varphi_2}\rangle - \langle\overline{\rho}\rangle\,[\widetilde{\varphi_1}]\,[\widetilde{\varphi_2}] \tag{4.19}$$

and the third order correlation $\langle\overline{\rho}\varphi_1''\varphi_2''\varphi_3''\rangle$ is reconstructed as:

$$\begin{aligned}\langle\overline{\rho}\varphi_1''\varphi_2''\varphi_3''\rangle = \langle\overline{\rho}\widetilde{\varphi_1}\widetilde{\varphi_2}\widetilde{\varphi_3}\rangle - \langle\overline{\rho}\rangle\,[\widetilde{\varphi_1}\widetilde{\varphi_2}]\,[\widetilde{\varphi_3}] - \langle\overline{\rho}\rangle\,[\widetilde{\varphi_1}\widetilde{\varphi_3}]\,[\widetilde{\varphi_2}] - \langle\overline{\rho}\rangle\,[\widetilde{\varphi_2}\widetilde{\varphi_3}]\,[\widetilde{\varphi_1}]\\ + 2.0\,\langle\overline{\rho}\rangle\,[\widetilde{\varphi_1}]\,[\widetilde{\varphi_2}]\,[\widetilde{\varphi_3}]\end{aligned} \tag{4.20}$$

4.2.3 Computational cost

This approach needs an important amount of RAM to store the 138 fields necessary. A list of the fields extracted to reconstruct the Reynolds stress budget is given in appendix A. This approach does not require the storage of the intermediate unsteady flow fields. The storage cost is then drastically reduced, and becomes independent of the number of samples needed. In addition, the computation cost increase of the simulation due to the accumulation of values is not too expensive. The cost increase is around 5% for the cases investigated in the present work.

4.3 Validation on a flat-plate boundary-layer

The implementation is validated on a flat-plate boundary layer simulation, against DNS results from Jiménez et al. (2010). The test-case has already been extensively studied during the author's master thesis (Monier, 2014).

4.3.1 Simulation protocol

The flow characteristics, mesh characteristics and numerical characteristics are chosen as similar as possible to the characteristics used for the corner separation case and the tip-leakage case, presented in chapter 6.

Flow characteristics

The turbulent flat-plate boundary-layer is described with large-eddy simulation. The boundary-layer is described up to $\mathrm{Re}_x = 1.3\times10^6$, with a virtual roughness element to trip transition at $\mathrm{Re}_x = 3.0\times10^5$. The details of the trip implementation are presented in Boudet et al. (2015b). The position of the trip is represented in figure 4.6 by a cone.

Because the solver uses a compressible formulation, the Mach number is chosen small enough to limit compressible effects but high enough to improve convergence speed, *i.e.* $M = 0.2$, which gives $u_e = 70\mathrm{m.s}^{-1}$, where u_e is the free stream

velocity. The air density is $\rho_e = 1.117\text{kg.m}^{-3}$ and the dynamic viscosity is $\mu = 1.81 \times 10^{-5}\text{kg.m}^{-1}\text{.s}^{-1}$.

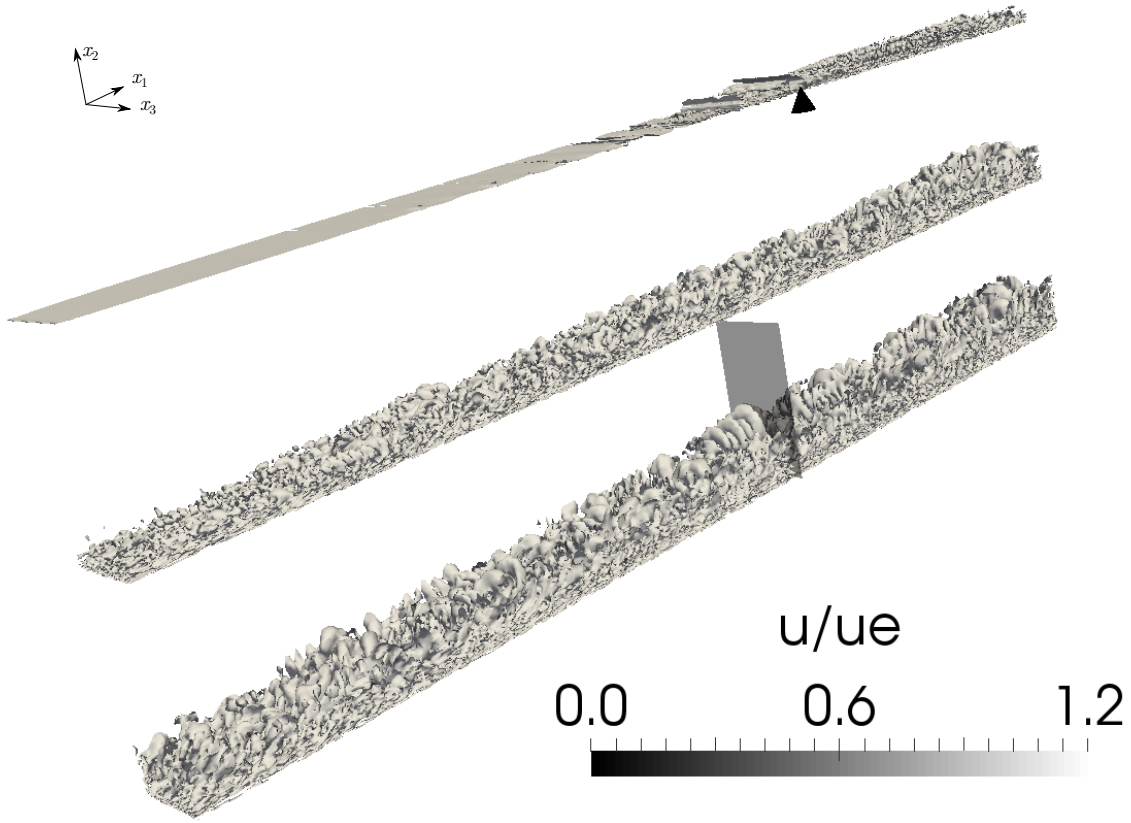

Figure 4.6: Flat-plate boundary layer representation with instantaneous iso-surface of Q-criterion, coloured by normalised streamwise velocity. For visualisation, the total length is cut into three pieces, which are piled from top to bottom. A cone marks the trip abscissa, and the grey plane the extraction abscissa for the TKE budget.

Dimensions of the computational domain

In order to get $\text{Re}_x \simeq 1.3 \cdot 10^6$ at the outlet, the length of the computational domain in the stream-wise direction is $L_{x_1} = 0.3\text{m}$. To take correctly into account the boundary-layer at the outlet, the computational domain height is set to twice the estimated boundary-layer thickness, thus $L_{x_2} = 0.0117\text{m}$. Concerning the span-wise direction, the width chosen corresponds to the estimated boundary-layer thickness at the outlet, $L_{x_3} = 0.00586\text{m}$.

Mesh

Mesh is uniform in the stream-wise and span-wise directions. In the wall-normal direction, the point distribution follows a geometrical law with an expansion coefficient of 1.10. In terms of cell sizes at the wall, in wall units: $\Delta x_1^+ \leqslant 60$, $\Delta x_2^+ \leqslant 2$ and $\Delta x_3^+ \leqslant 30$. This refinement level is classical in wall resolved LES. The wall unit is defined, for a given value φ, as:

$$\varphi^+ = \frac{u_\tau \rho \varphi}{\mu} \tag{4.21}$$

with ρ the density, μ the dynamic viscosity, and u_τ the friction velocity:

$$u_\tau = \sqrt{\frac{\tau_w}{\rho}};\ \tau_w = \left\| \left(\underline{\underline{\tau}} \cdot \underline{n} - \left(\underline{n} : \underline{\underline{\tau}} \cdot \underline{n} \right) \underline{n} \right) \right\| \tag{4.22}$$

with τ_w the wall shear-stress, $\underline{\underline{\tau}}$ the viscous stress and $\underline{n}$ the wall normal. The *a posteriori* check of the cell sizes at the wall, given in figure 4.7, shows that the conditions are verified with even $\Delta x_2^+ < 1$. Thus, the computational domain is made of $1035 \times 60 \times 44 = 2\,732\,400$ points, and divided into 47 sub-domains ($23 \times 60 \times 44$ points) in the stream-wise direction for parallelisation. A representation of the first sub-domain is given in figure 4.8.

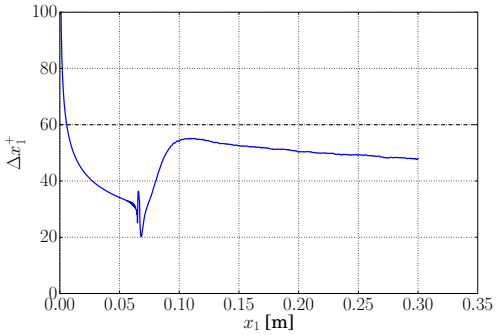

(a) Δx_1^+

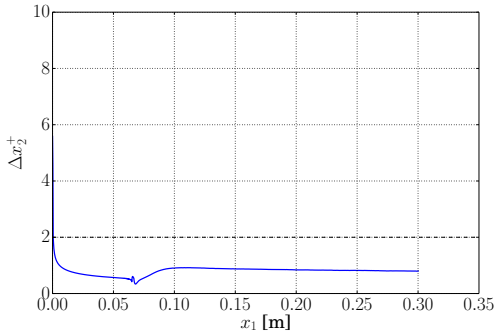

(b) Δx_2^+

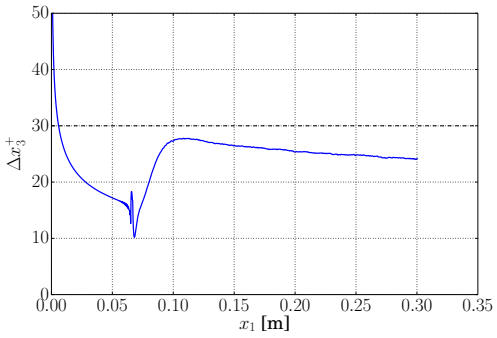

(c) Δx_3^+

Figure 4.7: Cell sizes at the wall in wall units. The conditions for wall-resolved LES are verified.

Boundary conditions

At the inlet boundary condition, velocity and density are set. The outlet boundary condition and upper boundary condition are set to a mixed pressure outlet condition, which mixes atmospheric static pressure prescription ($p = 101\,340$Pa) and a non-reflection condition. It allows pressure waves to exit the computational domain. The wall boundary condition is set to non-slip adiabatic. The lateral boundary conditions are set to periodic.

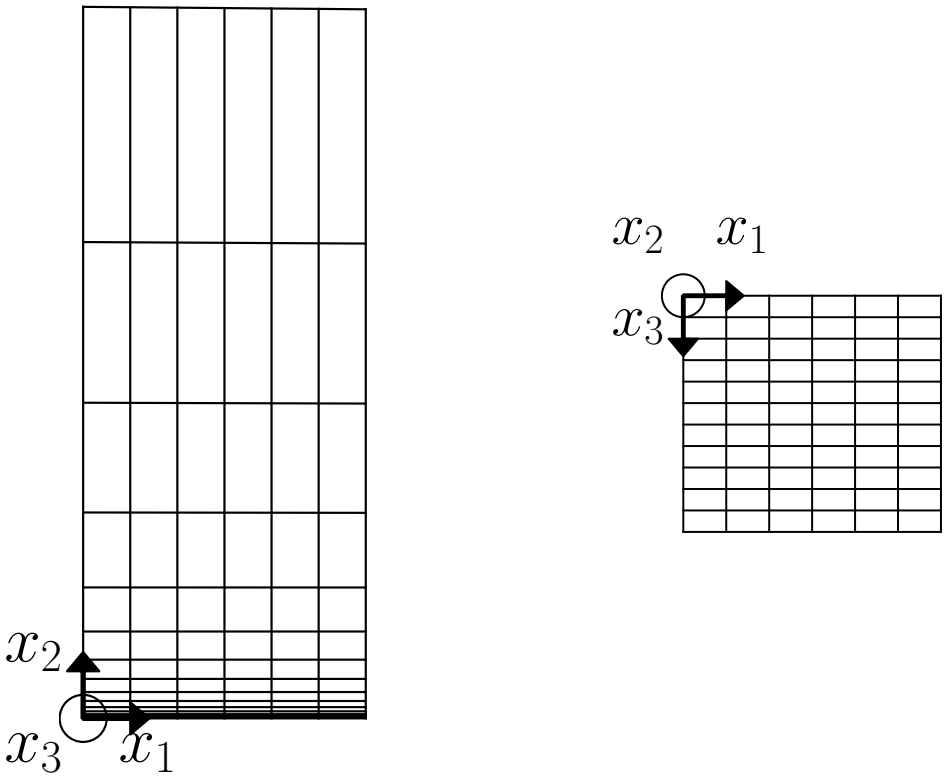

(a) $x_3 = 0$ plane (b) $x_2 = 0$ plane

Figure 4.8: Flat-plate boundary layer test-case mesh. Due to the length of the flat-plate compared to its height, only the first sub-domain is represented. Every fourth line is plotted in each direction.

Numerical schemes

The spatial scheme for the inviscid fluxes is a 4-point Jameson centred scheme, with a fourth-order artificial viscosity (coefficient: 0.002, see (Boudet et al., 2015b) for its definition). A 2-point centred scheme is used for the viscous fluxes. The temporal scheme is a three-step Runge-Kutta scheme, with a global constant time step of 10^{-8}s, which corresponds to a CFL of 0.95 (based on the inflow velocity plus the speed of sound and the minimal grid size).

SGS model

The computations are carried out with the SISM SGS model from Lévêque et al. (2007), presented in chapter 2, section 2.3.2. The exponential average used to extract the mean flow for the SISM (Cahuzac et al., 2010) is calibrated with a frequency of $13,340$Hz. This choice is based on the ratio between a characteristic velocity (the stream-wise friction velocity at the transition point) and a characteristic length (the boundary-layer displacement thickness at the transition point).

4.3.2 Flow analysis

Boundary-layer thicknesses

The boundary-layer thicknesses are used to assess the correct development of the boundary-layer along the plate, including the correct turbulent transition. The 99% thickness δ, the displacement thickness δ_1, the momentum thickness δ_2 and the shape factor H_{12} are defined as:

$\forall (x_1, x_2, x_3) \in [0, L_{x_1}] \times [0, L_{x_2}] \times [0, L_{x_3}]$,

$$u_1(x_1, \delta(x_1), x_3) = 0.99 u_e \tag{4.23}$$

$$\delta_1(x_1) = \int_0^{\delta(x_1)} 1 - \frac{u_1(x_1, x_2, x_3)}{u_e} dx_2 \tag{4.24}$$

$$\delta_2(x_1) = \int_0^{\delta(x_1)} \frac{u_1(x_1, x_2, x_3)}{u_e} \left(1 - \frac{u_1(x_1, x_2, x_3)}{u_e}\right) dx_2 \tag{4.25}$$

$$H_{12}(x_1) = \frac{\delta_1(x_1)}{\delta_2(x_1)} \tag{4.26}$$

The boundary-layer thicknesses are presented in figure 4.9, against Schlichting and Gersten (2000) law for δ and Michel laws (Cousteix, 1989) for δ_1 and δ_2.

The simulation begins spatially with a laminar boundary layer and becomes turbulent after the trip. The boundary-layer thickness δ is a bit underestimated compared with the experiment. The difference tends to increase along the flat-plate. On the other hand, the displacement thickness δ_1 and the momentum thickness δ_2 are correctly estimated. A very good agreement is observed with the analytical and experimental results, in laminar and turbulent regimes respectively. The shape factor H_{12} shows the transition is rapid and terminated before $x_1 = 0.15$m.

Profile analysis

An extraction is realised at a constant x_1 position with $\mathrm{Re}_{\delta_2} = 1968$ and compared with DNS results from Jiménez et al. (2010). In term of coordinates, the profile and TKE budget are extracted at $x_1 = 0.26$m.

The fluctuating velocities, defined as:

$$\forall i \in [\![1 \ ; \ 3]\!], \ u_i'' = \sqrt{-\frac{\tau_{tii}}{\langle \rho \rangle}} = \sqrt{[u_i''^2]} \text{ and } u_i''^+ = \frac{u_i''}{u_\tau} \tag{4.27}$$

are given, in wall units, in figure 4.10.

The stream-wise fluctuating velocity is presented in figure 4.10a. Both DNS and LES results present a peak at $x_2^+ \approx 1.5 \times 10^1$, and then an inflexion at $x_2^+ \approx 2 \times 10^2$. The LES estimation is good, compared with the DNS results, in the viscous sub-layer ($x_2^+ < 10^1$) and in the outer layer ($x_2^+ > 2 \times 10^2$). However, in the buffer layer and log-law region ($10^1 < x_2^+ < 2 \times 10^2$), the LES overestimates the fluctuating velocity by around 10%. For the cross-stream fluctuating velocity, presented in figure 4.10b, a peak is visible at ($x_2^+ \approx 2 \times 10^2$). The LES underestimates the cross-stream fluctuating velocity in the viscous sub-layer and buffer-layer ($x_2^+ < 8 \times 10^1$) and slightly overestimates it in the log-law region ($8 \times 10^1 < x_2^+ < 2 \times 10^2$). In the outer layer

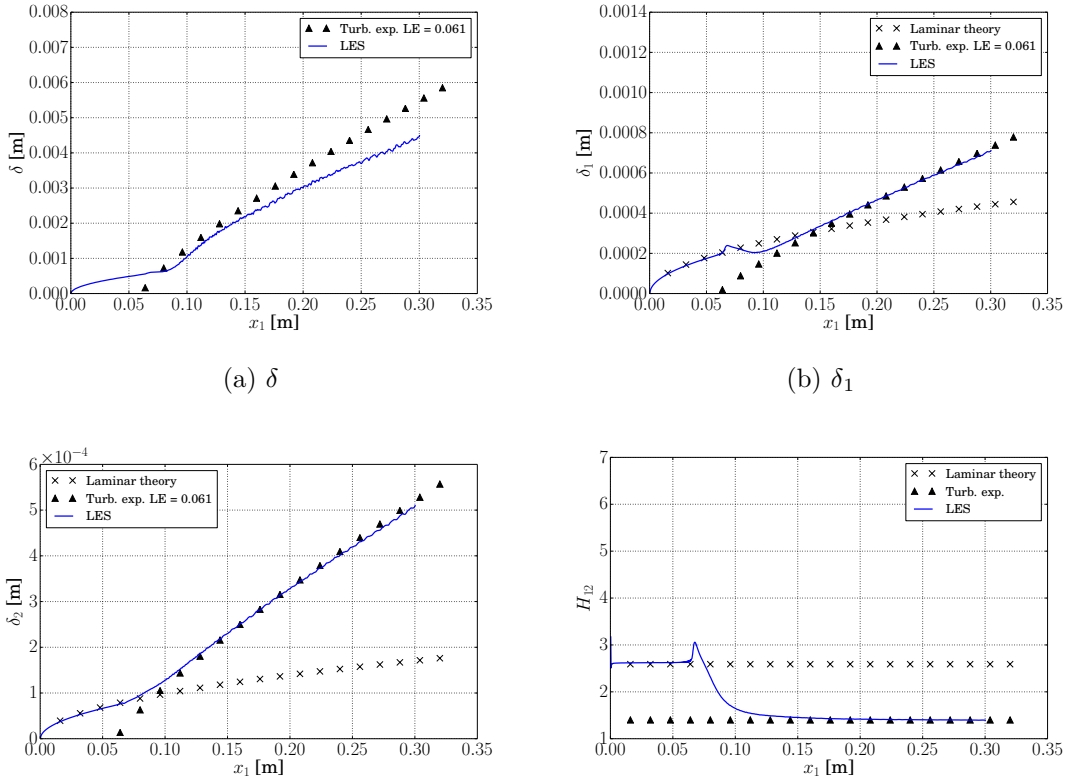

(a) δ (b) δ_1

(c) δ_2 (d) H_{12}

Figure 4.9: Boundary layer thicknesses for the flat-plate test case. The LES results are compared with Blasius laminar solution and experimental turbulent results from Schlichting and Gersten (2000) for δ and Michel (Cousteix, 1989) for δ_1 and δ_2.

($x_2^+ > 2 \times 10^2$), the DNS and LES results match. The span-wise fluctuating velocity, presented in figure 4.10c, shows a typical bell curve. LES yields a vary good prediction, according to DNS, in all the parts of the boundary-layer.

4.3.3 Validation of the TKE budget extraction

The turbulent kinetic energy budget is extracted at the same position as the fluctuating velocities, *i.e.* at a constant x_1 position with $\mathrm{Re}_{\delta_2} = 1968$. The sampling period is $10^{-2}\mu$s (= LES time step), and a total time of 12.0ms is used for the complete statistics computation. Some of the TKE budget terms, presented in equation (2.36), are grouped for the presentation. The advection and production are kept alone. The viscous and SGS dissipations are summed into a dissipation term. The viscous diffusion and SGS diffusion are summed into a viscous diffusion term. The remaining terms are summed into a single term, representing the pressure dilatation and turbulent diffusion. The numerical residual is computed in order to gauge the validity of the budget reconstruction. The budget terms are normalised by $(\rho_e^2 u_e^2)/\mu$.

Statistical convergence check

The budget relies on statictics, so the statistical convergence, *i.e.* the constance of the terms when new samples are added, is checked. In order to do so, the budget evolution

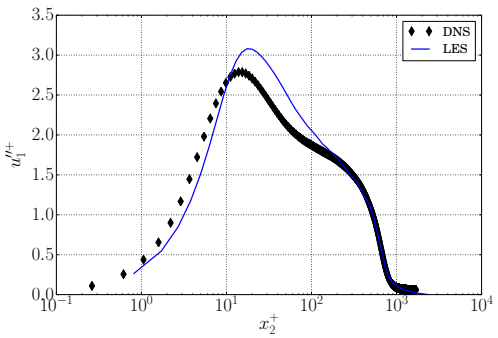

(a) $u_1''^+$

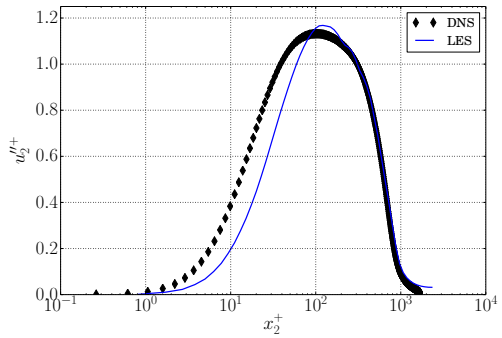

(b) $u_2''^+$

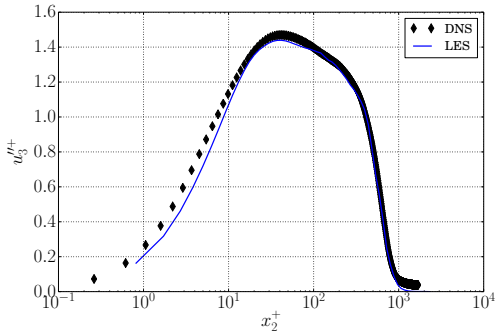

(c) $u_3''^+$

Figure 4.10: Flat-plate boundary layer fluctuating velocities, normalised by u_τ.

is analysed against the sample time used for its calculation. For a given sample time, a term is represented by the integral of its absolute value over the height, and divided by the production term computed with the maximal sample time. The convergence is considered reached when the integrals remain constant when the sample time is increased.

The results are presented in figure 4.11. All terms are stationary, which indicates the statistical convergence is correct. However, a non null numerical residual is present. This term is also stationary, inferring that the numerical residual is not due to a statistical convergence default.

Comparison with DNS

The comparison is realised with the budget computed over the entire sample time, against DNS results from Jiménez et al. (2010). A budget from a two-dimensional RANS test-case using Wilcox $k-\omega$ turbulence model, extracted at the same position, is also presented for comparison. For the RANS simulations with a k equation, it shows the ability of the model to describe correctly the fine physics of turbulence. The RANS set-up is not presented here, but can be found in Monier (2014), under the appellation RA_WStd.

The results are presented in figure 4.12. Figure 4.12a shows that the LES is able to describe the TKE budget compared with the DNS. The production and transport terms of the LES are very close to the DNS and the difference on the dissipation term remains

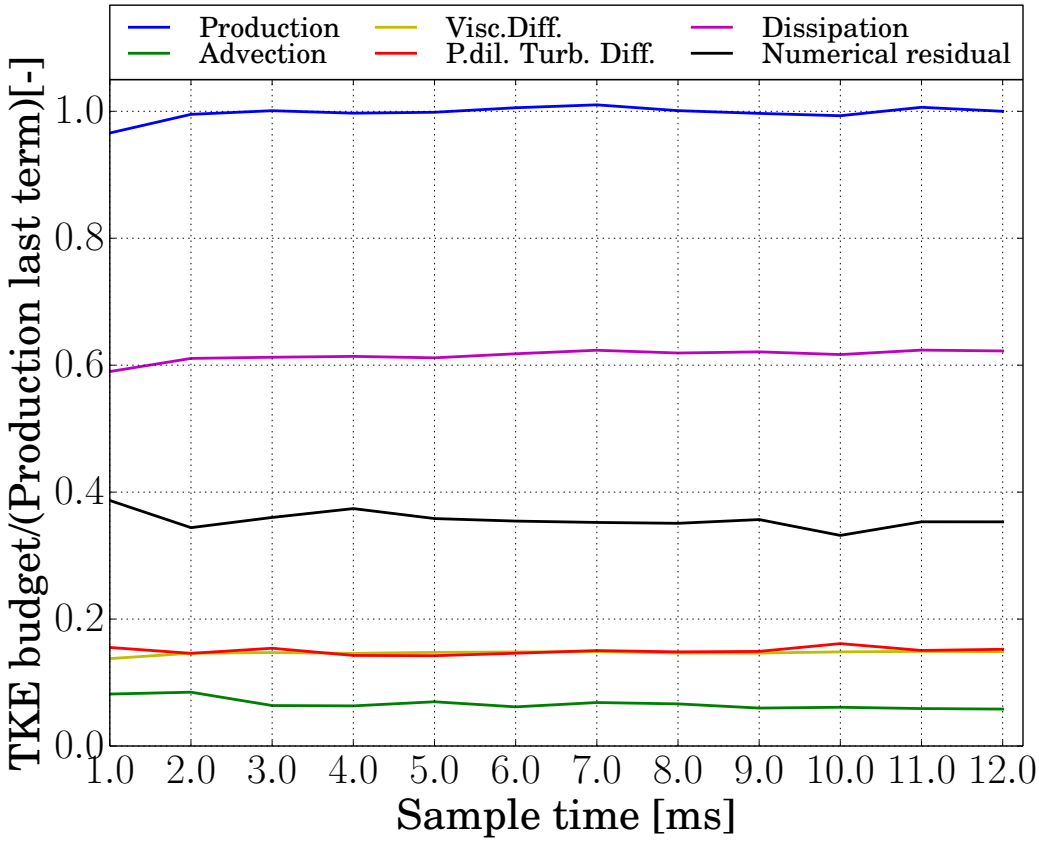

Figure 4.11: TKE budget terms against sample time. The terms are divided by the production term computed with the maximal sample time.

moderate. The viscous diffusion term is a little over estimated, whereas the pressure dilatation and turbulent diffusion term is slightly underestimated. The numerical residual is negative, thus acting as a numerical dissipation. The numerical dissipation is maximal at $x_2^+ \approx 10$, but remains smaller than the other terms. The RANS results show significant differences compared with the LES and DNS. In figure 4.12b, the production term is well represented, but the dissipation differs significantly from the DNS. The production and the dissipation are superimposed (in absolute value) in the buffer layer. The dissipation at the wall is also very weak, which is non physical. Concerning the viscous diffusion and the pressure dilatation and turbulent diffusion terms, they are underestimated. The residual remains very small since the equation on k is directly solved.

In order to summarise the physical meaning of the terms, the advection term, the viscous diffusion term and the pressure dilatation and turbulent diffusion term are grouped into a single transport term. The results are presented in figure 4.13. As already stated, the numerical residual of the LES budget presents a dissipative behaviour. In order to gauge the global dissipative effect on the budget, the sum of the dissipation term and the numerical residual term is also plotted in figure 4.13. For the LES, presented in figure 4.13a, the transport term presents a very good agreement with the DNS, better than the two terms taken separately. It means that the transport of the turbulent kinetic energy is globally correctly represented. When the dissipation and the numerical dissipation are summed, the resulting term is very close to the DNS dissipation term. The numerical residual represents various numerical effects, that are

not taken into account by the viscous and SGS dissipation. Among these effects, we can cite the effects of the numerical schemes, the effects of the mesh, or the effect of the computational methods (finite differences) used to compute the TKE budget for instance. It is a non exhaustive list. Finally, the LES yields an excellent result close to the wall ($x_2^+ \leqslant 3$), where the three physical terms are very similar to the DNS. For the RANS case, presented in figure 4.13b, the transport term has the correct topology but is greatly underestimated. This is a known issue of RANS with two equation models, mentionned by Wilcox (2006): production and dissipation are superimposed, with only a small amount of transport.

Another test was realised in order to gauge the implementation of the extraction method. The stream-wise direction, for which the terms of the budget are dominant, is borne by x_1 in the test-case. A permutation of the coordinate system has been operated, in order to have the stream-wise direction borne by x_2, and then x_3. The results obtained were exactly similar for each direction, the stream-wise, cross-stream, and span-wise, no matter by which coordinate it was represented. This lead to the conclusion that the implementation is correct, and that the budget extraction is robust to the choice of a coordinate system.

Although the LES results present more numerical dissipation than the DNS, the prediction of the different terms is considered correct enough to be exploited for a physical analysis. This behaviour is common for LES TKE budget extraction. A similar phenomenon, with a similar amount of numerical dissipation can be found on the work of Schiavo et al. (2017). The extraction of the turbulent kinetic energy budget is considered validated against the DNS simulation.

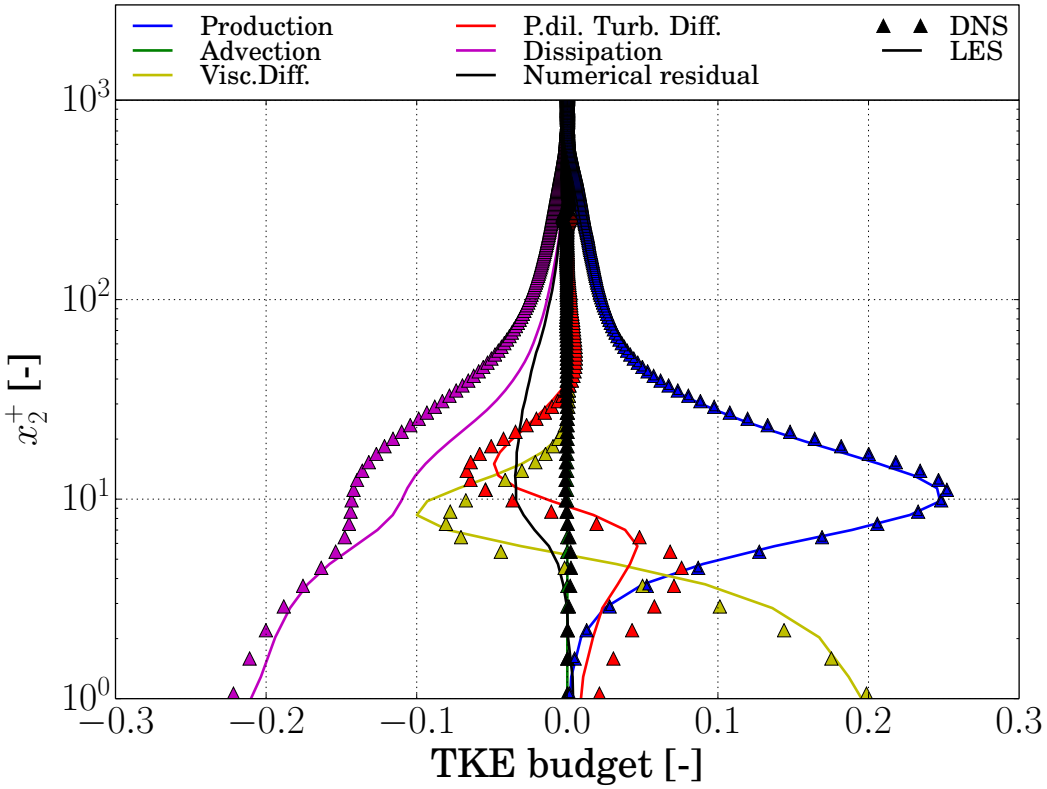

(a) LES

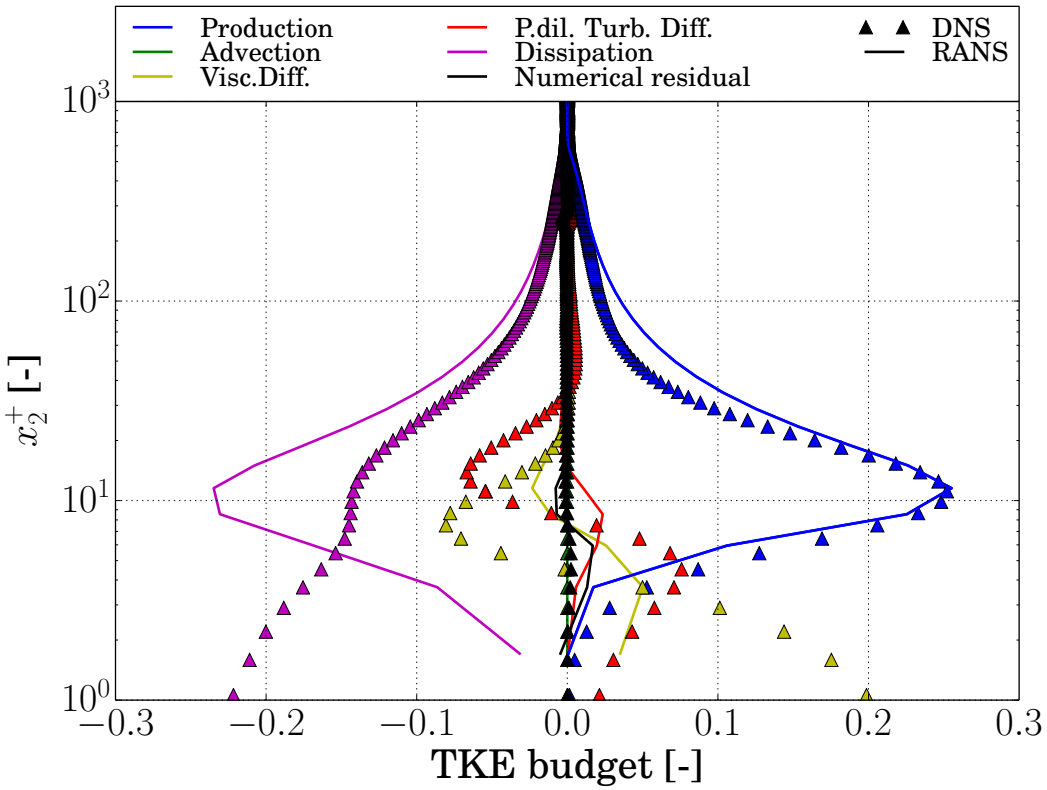

(b) RANS

Figure 4.12: Turbulent kinetic energy budget in a flat-plate boundary layer, extracted at $\mathrm{Re}_{\delta_2} = 1968$.

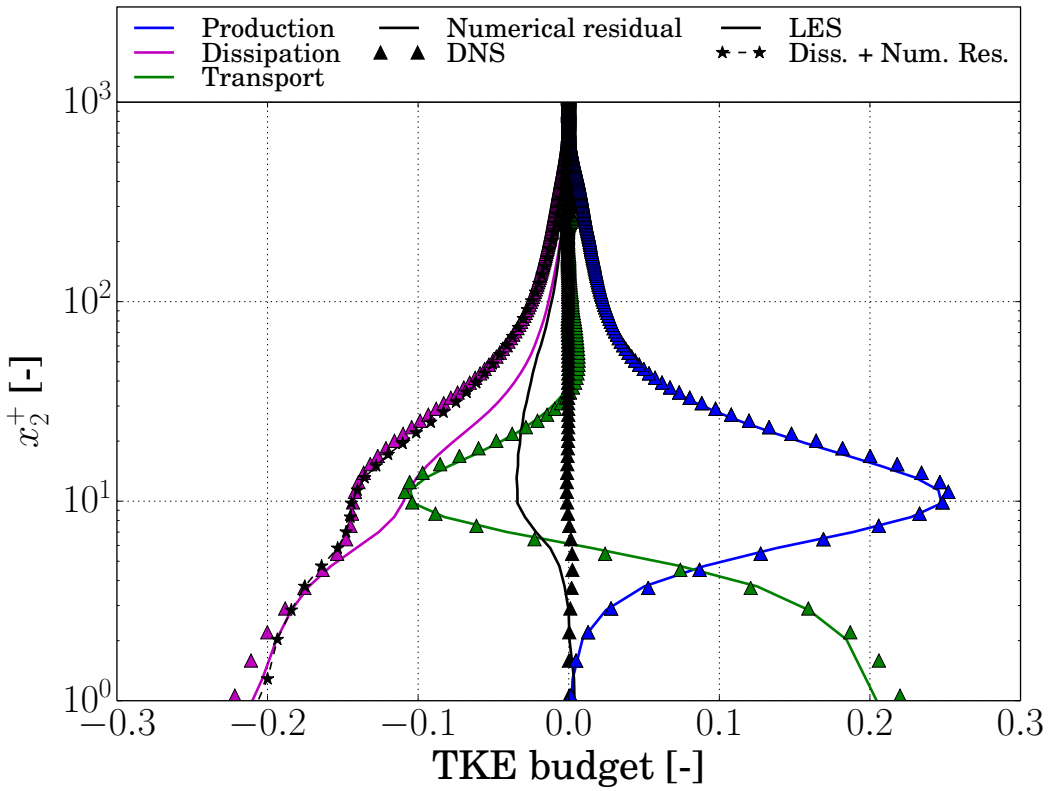

(a) LES

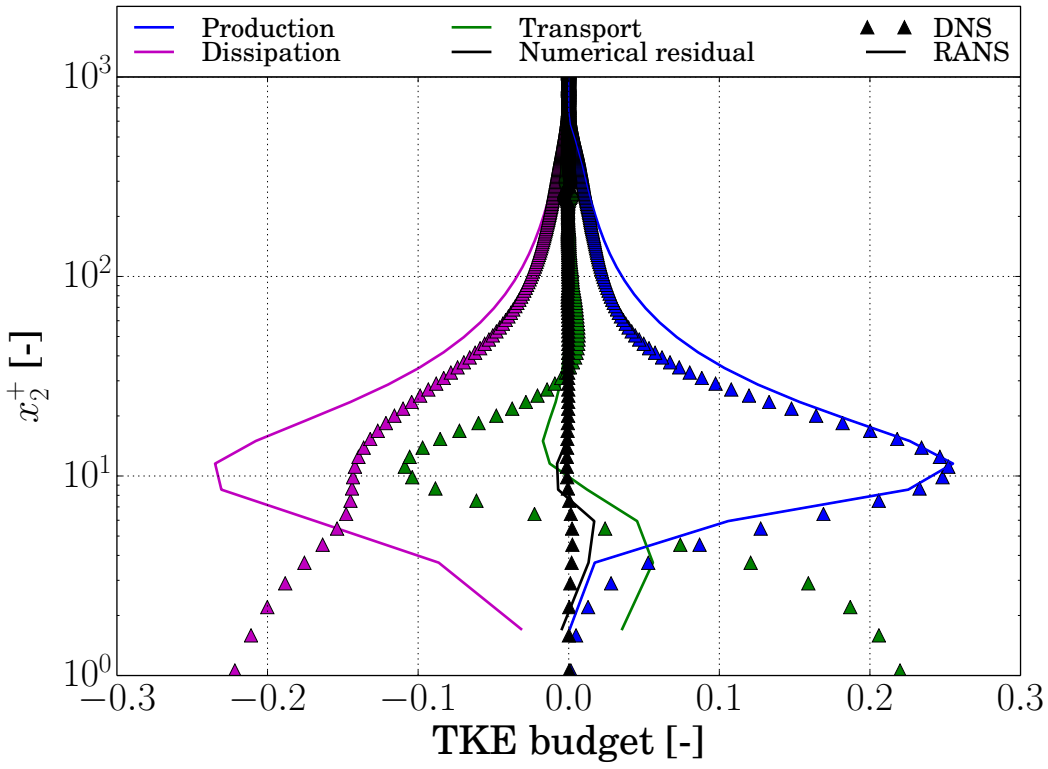

(b) RANS

Figure 4.13: Turbulent kinetic energy budget in a flat-plate boundary layer, extracted at $\mathrm{Re}_{\delta_2} = 1968$. The advection term, the viscous diffusion term and the pressure dilatation and turbulent diffusion term are grouped into a single transport term.

Chapter 5

Proposed hybrid RANS-LES formulation

Sections

All the hybrid methods presented in chapter 3 have advantages and limitations. The method presented here has its own. This approach is inspired by both the ZLES (Boudet et al., 2016a), and Tucker's model (Tucker et al., 2012a). The main goal is to create an hybrid model that allows the use of any desired RANS model relying on a turbulent viscosity and any desired SGS model relying on a sub-grid scale viscosity, but without the user-defined zone set-up present in the ZLES. If the hybridisation is kept on the turbulent/SGS viscosity, the criterion for transition shall be based on d^+, the nearest wall distance in wall units, which is found to be more physical for turbulence modelling than a criterion on the dimensional wall-distance.

5.1 Formulation

The following formulation has been retained:

$$\mu_{hyb} = \left(1 - f_{hyb}(d^+)\right) \mu_t + f_{hyb}(d^+)\mu_{SGS} \tag{5.1}$$

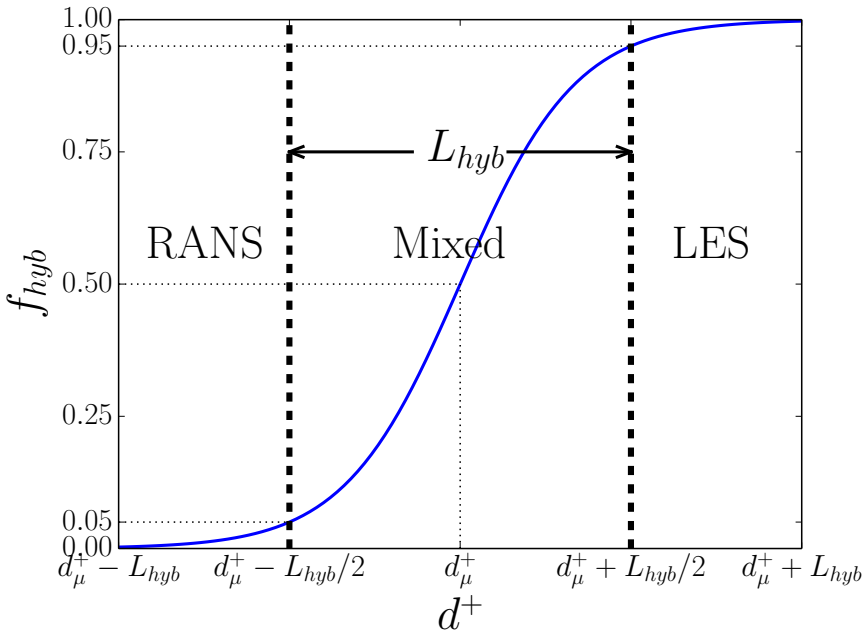

Figure 5.1: Proposed hybridisation function.

with μ_{hyb} the hybrid eddy-viscosity, μ_t the RANS eddy-viscosity and μ_{SGS} the sub-grid scale eddy-viscosity.

The hybridisation function is defined as follows:

$$f_{hyb}\left(d^+\right) = \frac{1}{2}\left[1 + \tanh\left(f_\mu(L_{hyb}) \times (d^+ - d^+_\mu)\right)\right] \tag{5.2}$$

$$f_\mu(L_{hyb}) = \frac{2\ \mathrm{artanh}\,(0.9)}{L_{hyb}} \tag{5.3}$$

with d^+_μ the wall distance in wall-units at the center of the RANS-LES hybridisation area, and L_{hyb} the width of the hybridisation area at $\pm 5\%$.

The hybridisation function presented in Eq. (5.2) is an hyperbolic tangent[1]. It presents two major advantages. First, it is indefinitely differentiable $\mathbb{C}^\infty(\mathbb{R})$, and secondly, it is a simple function. The smoothness of the transition ensured by such a function is a great advantage (Fig. 5.1).

The values of d^+_μ ans L_{hyb} can be tuned by the user. For instance $d^+_\mu \approx 20$ and $L_{hyb} \approx 10$ allow a transition between RANS and LES in the buffer layer.

5.2 d^+ calculation

Such a formulation presents an evident difficulty, the computation of d^+. Three possibilities are presented. They are classified from the easiest to implement and less costly, to the hardest to implement and most costly, as presented in Fig. 5.2.

[1]The notation tanh and artanh are preferred to tanh and $\tanh^{-1}$ for the hyperbolic tangent and the inverse hyperbolic tangent to respect the ISO 80000-2:2009(E) standard.

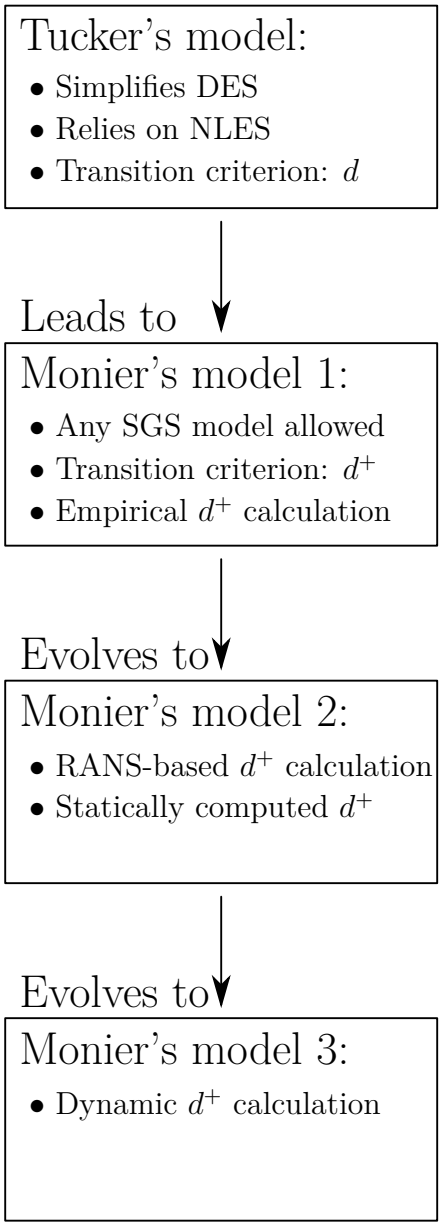

Figure 5.2: Classification of the proposed hybrid models with respect to Tucker's model (Tucker et al., 2012a).

5.2.1 Model 1: Empirical d^+ calculation

The first method consists in realising only one calculation of d^+, at the beginning. The friction velocity used for the computation is derived from a flat-plate correlation. Michel's empirical relation (Cousteix, 1989) is used as follows:

$$C_f = \frac{\tau_w}{0.5\rho_e u_e^2} = 0.0368 \mathrm{Re}_{x_1}^{-1/6} \Rightarrow u_\tau = \sqrt{0.0184} u_e \mathrm{Re}_{x_1}^{-1/12} \tag{5.4}$$

with C_f the friction coefficient, τ_w the wall shear stress, $u_\tau = \sqrt{\tau_w/\rho_e}$ the friction velocity (defined in equation (4.22)) and $\mathrm{Re}_{x_1} = \rho_e u_e x_1/\mu$ the Reynolds number based on the free-stream velocity u_e, the free-stream density ρ_e and the stream-wise position x_1. This correlation is in very good agreement with the experimental data in the range $\mathrm{Re}_{x_1} \in [10^5,\ 10^8]$, adapted for turbomachinery flows.

Then, d^+ is directly obtained:

$$d^+ = \frac{u_\tau \rho_e d}{\mu} = \frac{\sqrt{0.0184} u_e \mathrm{Re}_{x_1}^{-1/12} \rho_e d}{\mu} \tag{5.5}$$

The friction velocity u_τ evolves slowly with the evolution of x_1, which can justify the use of a constant user-defined Re_{x_1}. Moreover, u_τ tends to decrease in separations, which is not captured by the correlation. So the transition between RANS and LES predicted from the correlation should be closer to the wall than necessary, which is not a problematic behaviour.

Only this first approach is tested in the present thesis.

5.2.2 Model 2: RANS-based d^+ calculation

The idea is to evaluate d^+ from a preliminary RANS simulation, typically used to initialise the hybrid simulation. In that case, d^+ is still computed only once at the beginning:

$$d^+ = \frac{\rho_e d u_\tau}{\mu} = \frac{\rho_e d}{\mu} \sqrt{\frac{\tau_w}{\rho_e}} \tag{5.6}$$

5.2.3 Model 3: Dynamic d^+ calculation

The last improvement is to compute dynamically the d^+ field, using again Eq. (5.6). This method is more complex to implement and would increase the computational cost. A smoothing strategy should be implemented to estimate τ_w. Moreover, at each time step, all the points in all the domains should communicate with the wall points in order to obtain the information on the friction velocity.

5.3 Limitations

Some limitations remain with this model. The attention to the mesh is a little bit less important than for DES. However, the transition between RANS and LES is a burning issue. The user has to define the width of the transition zone and the position of its center. The LES area have to be close enough to the walls, in order to capture a lot of physics on the turbulent boundary layer, but far enough not to impact too much the computational cost.

5.4 Implementation strategy

The RANS-LES hybridisation relies on the similarity of the LES equations (2.30) and the RANS equations (2.48). The flow equations (*i.e.* the mass conservation equation, the three momentum equations and the energy equation) and the equations of the chosen RANS turbulence model are solved everywhere. In the RANS region, $\mu_{hyb} \simeq \mu_t$, all the equations are used and they correspond to the RANS formulation. In the LES region, $\mu_{hyb} \simeq \mu_{SGS}$, the RANS turbulence model equations are solved but not used and the flow equations correspond to the LES formulation.

When it is part of a RANS model, the k equation is solved everywhere. For this reason, the turbulent kinetic energy appears in the equations (e.g. ideal gas law) even in the LES regions. The working hypothesis is that k rapidly becomes small in LES areas, so its effects are negligible. This approximation is kept in order to simplify the implementation of the present hybrid strategy.

5.5 Validation on a bi-periodical channel flow

The implementation is validated on a bi-periodical channel flow test-case at $\mathrm{Re}_\tau = 395$ ($\mathrm{Re}_\tau = \rho_e u_\tau \delta_{1/2}/\mu$, with ρ_e the reference density, u_τ the friction velocity defined in equation (4.22), $\delta_{1/2}$ the channel half-width and μ the dynamic viscosity), against DNS results from Moser et al. (1999).

5.5.1 Simulation protocol

The simulation protocol is presented in this section. The flow characteristics, mesh characteristics and numerical characteristics are chosen similar to the *Turb'Flow* test-case set-up by Boudet et al. (2007) and used by Cahuzac (2012) for a zonal LES formulation validation.

Flow characteristics

The canal half-height is $\delta_{1/2} = 0.01\mathrm{m}$. The objective is to reach a Reynolds number $\mathrm{Re}_\tau = 395$. The density is equal to $\rho_e = 1.214\mathrm{kg.m}^{-3}$ and the viscosity is equal to $\mu = 1.81 \times 10^{-5}\mathrm{kg.m}^{-1}.\mathrm{s}^{-1}$, yielding a target friction velocity $u_\tau = 0.59\mathrm{m.s}^{-1}$. The Mach number in the center of the channel is $M = 0.2$ in order to limit compressible effects but improve convergence speed. The flow is initialised with a laminar Poiseuille parabolic profile in the stream-wise direction, perturbed with a white noise whose amplitude is 2% of the local velocity. For the RANS and hybrid simulations, k is also initialised with local velocity fluctuations of 2%. A representation of the Q criterion (defined as the second invariant of the velocity gradient tensor (Holmén, 2012)), for $Q = 10^6$, coloured by the instantaneous flow velocity magnitude in wall units ($\|\underline{u}^+\| = \|\underline{u}\|/u_\tau$, with $u_\tau = 0.59$), is given in figure 5.3.

Dimensions of the computational domain

The geometry of the channel is the same as in Moser et al. (1999). The origin is set at the center of the channel. Two walls are placed at $x_2 = \pm\delta_{1/2}$ in the cross-stream direction. The inflow and outflow faces are placed at $x_1 = \pm\pi\delta_{1/2}$, and the lateral faces are placed at $x_3 = \pm\pi\delta_{1/2}/2$.

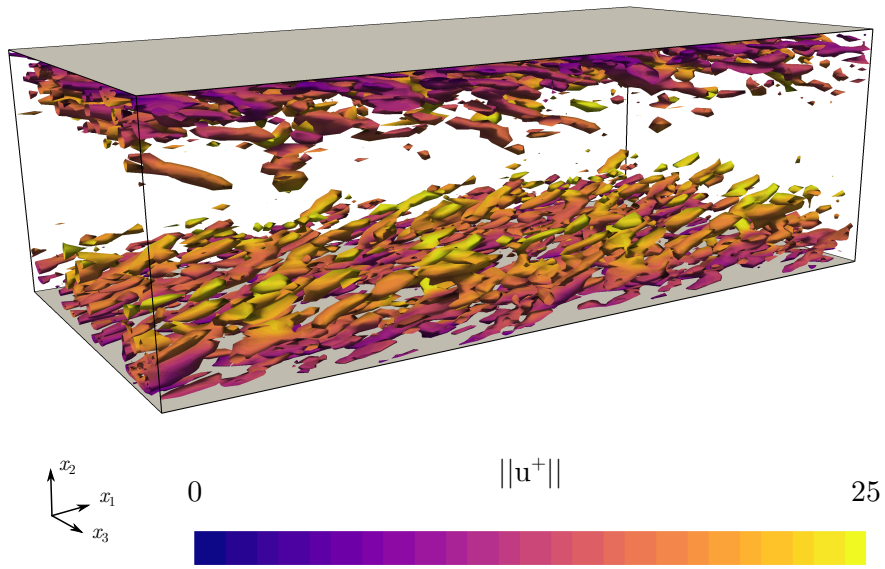

Figure 5.3: Q criterion 10^6, coloured by the instantaneous flow velocity magnitude in wall units, for the pure LES simulation.

Mesh

The mesh is refined in order to allow a wall resolved large-eddy simulation. The stream-wise and span-wise grid steps are taken constant, with $\Delta x_1^+ = 52$ and $\Delta x_3^+ = 31$ in wall units. The cross-stream grid step is set equal to $\Delta x_2^+ = 0.5$ at the wall and to $\Delta x_2^+ = 24$ in the center of the channel, and follows a hyperbolic tangent law in between. The computational domain is made of $49 \times 89 \times 41 = 178\,801$ points, divided into 8 domains ($25 \times 45 \times 21$ points) for parallel computing. A representation of the mesh is given in figure 5.4. The same mesh is used for the LES, RANS and hybrid RANS-LES simulations.

Boundary conditions

The boundary conditions of the faces in the stream-wise direction are set to periodic. The boundary conditions of the lateral faces are set to periodic. The top and bottom walls are set as no-slip adiabatic. In order to maintain the flow, a source term is added at each point in order to compensate the friction dissipation. The source term added is equal to $\rho u_\tau^2/\delta_{1/2}$ in the x_1-momentum equation, and $\rho u_1 u_\tau^2/\delta_{1/2}$ in the total energy equation.

Numerical schemes

For the LES and hybrid simulations, the spatial scheme for the inviscid fluxes is a 4-point Jameson centred scheme without artificial viscosity. A 2-point centred scheme is used for the viscous fluxes. The temporal scheme is a five-step Runge-Kutta scheme, with a global constant time step of 5.0×10^{-7}s.

For the RANS simulations, the spatial scheme for the inviscid fluxes is a 2-point Jameson centred scheme with a fourth-order artificial viscosity (coefficient: 0.02, see Boudet et al. (2015b) for its definition). A two-point centred scheme is used for the

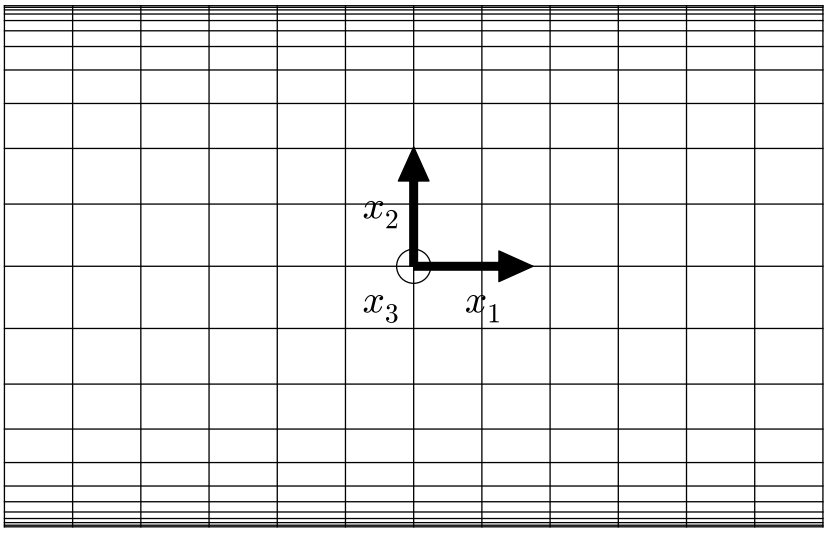

(a) $x_3 = -\pi\delta_{1/2}/2$ plane

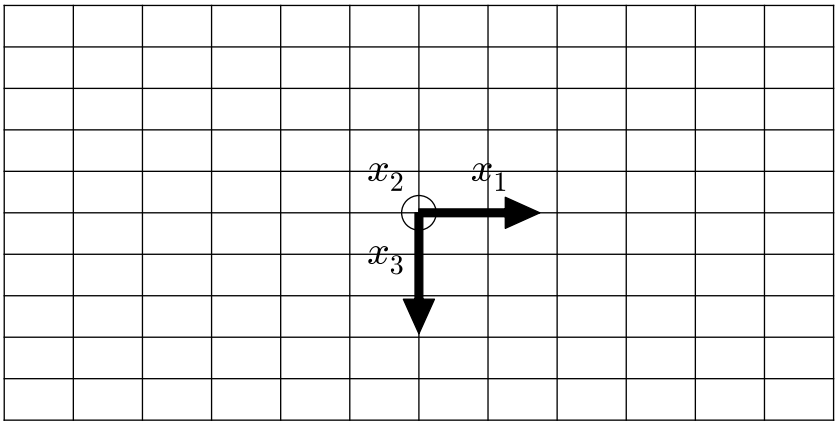

(b) $x_2 = -\delta_{1/2}$ plane

Figure 5.4: Bi-periodical channel test-case mesh. Every fourth line is plotted in each direction.

viscous fluxes. The temporal scheme is a five-step Runge-Kutta scheme, with a local variable time step corresponding to a CFL number of 0.7 (based on the velocity plus the speed of sound and the local grid size).

Turbulence/SGS models

The LES and the LES regions of the hybrid simulations rely on the SISM SGS model from Lévêque et al. (2007), presented in chapter 2, section 2.3.2. The characteristic frequency of the exponential average is set to 59.0Hz. This choice is based on the ratio between the target friction velocity u_τ and the canal half-height $\delta_{1/2}$.

The RANS simulation and the RANS regions of the hybrid simulations rely on the original Wilcox $k-\omega$ model (Wilcox, 1988), presented in chapter 2, section 2.4.3. Both use the Boussinesq constitutive relation.

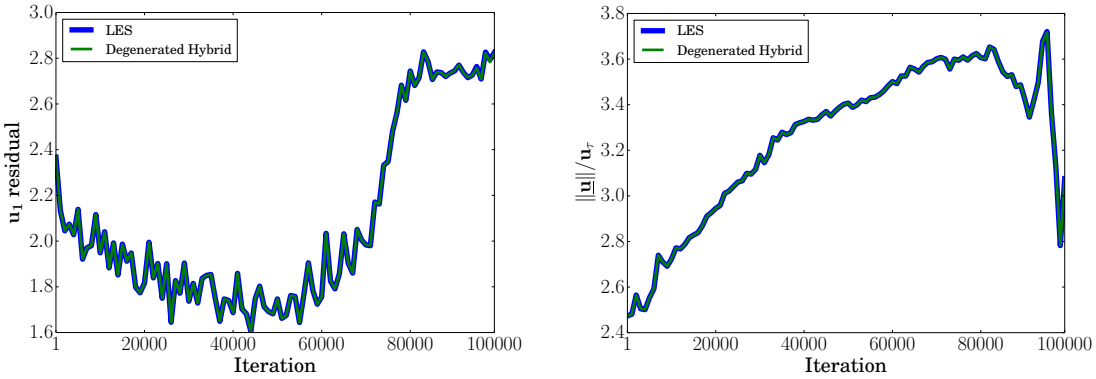

(a) Residual (b) Velocity magnitude

Figure 5.5: Hybrid simulation degenerated into a LES. (a): comparison of the residual on u_1, (b): comparison of the instantaneous velocity magnitude at $d^+ = 25$ from the bottom wall.

5.5.2 Degenerated hybrid model validation

First, a non regression test is realised. Degenerated versions of the model are tested, which means that d_μ^+ is set to $\pm\infty$. In the case $d_\mu^+ = -\infty$, $\mu_{hyb} = \mu_{SGS}$ in the entire domain and the simulation should be a pure LES simulation. In the case $d_\mu^+ = +\infty$, $\mu_{hyb} = \mu_t$ in the entire domain and the simulation should be a pure RANS simulation.

In both cases, the simulation is compared to a real pure LES (resp. pure RANS) simulation using numerical criteria, in order to validate the implementation in *Turb'Flow*. In order to see if the two approaches are numerically equivalent, the residuals on u_1 are compared between the degenerated hybrid simulation on the first 100 000 iterations and the pure LES (resp. RANS) simulation. Moreover, a numerical probe is placed at $d^+ = 25$ from the bottom wall, in order to obtain the instantaneous velocities. The instantaneous velocity magnitudes at $d^+ = 25$ are compared over the first 100 000 iterations too.

Hybrid simulation degenerated into a LES

The first case tested is a degeneration of the hybrid modelling into a LES. In that case, $d_\mu^+ = -1 \times 10^{30}$ and $L_{hyb} = 1.0$.

The comparison with the pure LES simulation is presented in figure 5.5. The blue curves representing the LES results and the green curves representing the hybrid simulation (degenerated into a LES) are superimposed at each point, over the entire sample. This indicates that the two approaches are numerically equivalent, the LES region of the hybrid simulation behaves as a pure LES if d^+ is big enough compared with d_μ^+.

Hybrid simulation degenerated into a RANS simulation

The second case tested is a degeneration into a RANS simulation. In that case, $d_\mu^+ = 1 \times 10^{30}$ and $L_{hyb} = 1.0$.

The comparison with the pure RANS simulation is presented in figure 5.6. First, a comparison with the curves in figure 5.5 shows that the residual and the instantaneous velocity magnitude evolve differently during these first 100 000 iterations for the

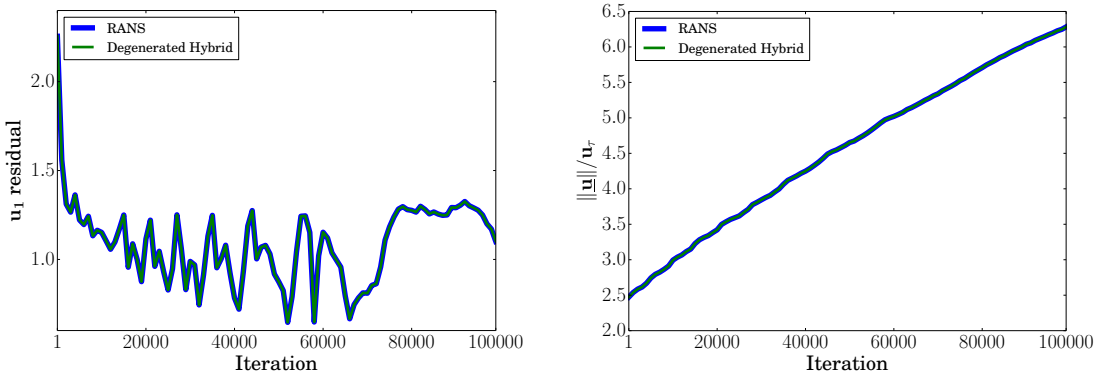

(a) Residual (b) Velocity magnitude

Figure 5.6: Hybrid simulation degenerated into a RANS simulation. (a): comparison of the residual on u_1, (b): comparison of the instantaneous velocity magnitude at $d^+ = 25$ from the bottom wall.

LES and the RANS simulation. This ensures that the superimposition of the curves is not due to some persistent behaviour of the code at the beginning. Two superimposed curves, in this case, represent actually two numerically identical simulations. In Fig. 5.6, the blue curves representing the RANS results and the green curves representing the hybrid simulation (degenerated into a RANS simulation) are superimposed at each point, over the entire sample for this test too. This indicates that the two approaches are equivalent, the RANS region of the hybrid simulation behaves as a pure RANS if d^+ is small enough compared with d^+_μ.

5.5.3 Hybrid model validation

An hybrid simulation is realised and compared with a full LES and a full RANS simulation. The mean and fluctuating velocities are compared. A spatial autocorrelation is also calculated to compare the LES and the LES region of the hybrid simulation.

Hybrid simulation characteristics

The hybrid simulation uses a target wall distance for RANS-LES transition $d^+_\mu = 50$ (in wall units) and a RANS-LES transition width $L_{hyb} = 10.0$. A visualisation of the different regions is given in figure 5.7. The a posteriori evaluation of the wall distance for RANS-LES transition, computed with the actual friction velocity instead of Michel's empirical correlation, gives a transition for an actual $d^+_\mu = 27$, with an actual RANS-LES transition width $L_{hyb} = 6.0$.

Convergence analysis

A numerical probe is placed in the first domain, in order to assess the numerical convergence of the computation for the pure LES and the hybrid simulation. The three components of velocity are presented every 1000 iterations, as a function of the number of iterations, in figure 5.8. The simulations are considered numerically converged after 300 000 iterations.

The statistics are computed from iteration 300 000 to iteration 500 000, with a sampling every 1000 iterations. The directions of homogeneity and the symmetry

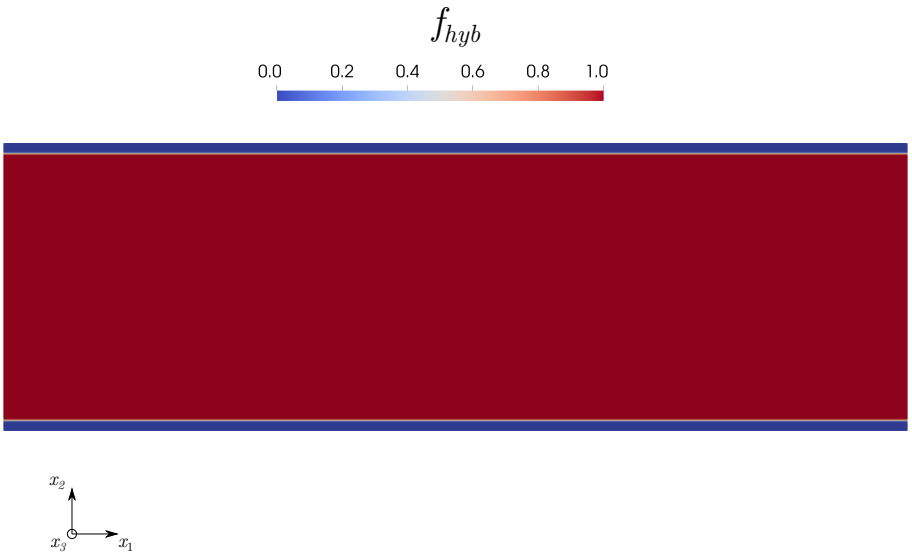

Figure 5.7: Hybridisation function for the bi-periodical channel on a $x_3 = 0$ plane. The red region is the LES region while the blue area is the RANS region.

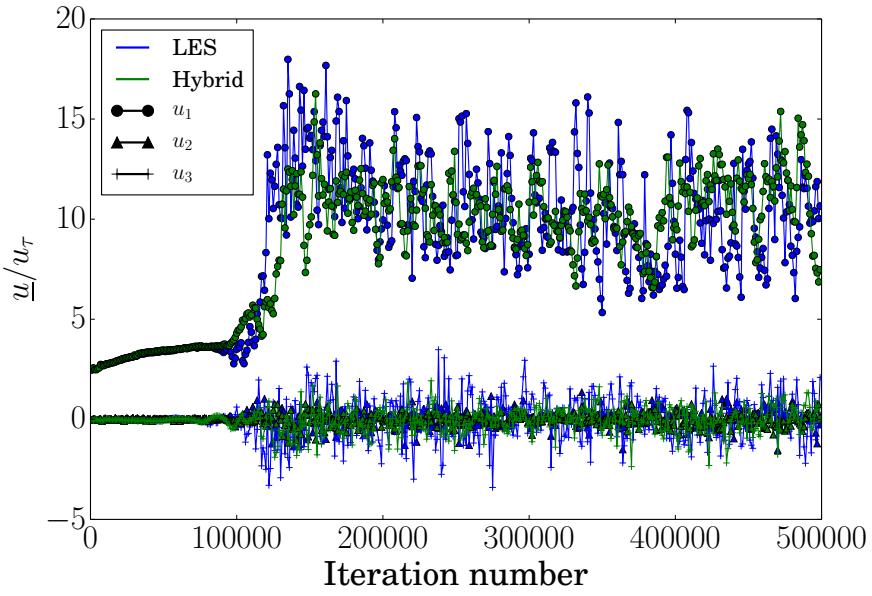

Figure 5.8: Instantaneous velocity components at $x_2^+ = 25$ from the bottom wall, normalised by $u_\tau = 0.59$.

along the cross-stream direction are used in order to increase the number of samples, yielding a total of $200 \times 48 \times 40 \times 2 = 768\,000$ samples.

Mean velocities

The mean velocities are computed, for LES, as the sum of the samples divided by the number of samples:

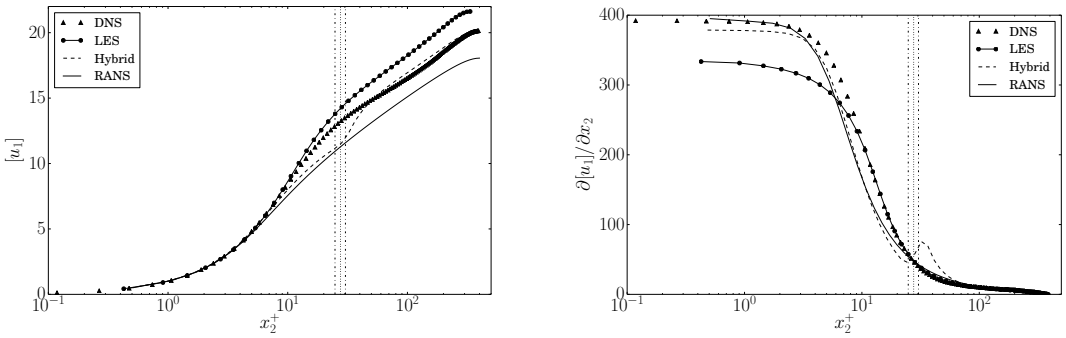

(a) Mean velocity

(b) Mean velocity derivative

Figure 5.9: Mean velocity and derivative along the cross-stream direction in the bi-periodical channel. The velocity is normalised by the actual u_τ of the calculation and the derivative is normalised by $u_\tau/\delta_{1/2}$. The three vertical lines represent from left to right respectively $f_{hyb} = 0.05$, $f_{hyb} = 0.50$, and $f_{hyb} = 0.95$.

$$\forall i \in [\![\ 1\ ;\ 3\ ]\!],\ [u_i] = \frac{1}{N_{\text{samples}}} \sum_{l=1}^{N_{\text{samples}}} u_{i,l} \tag{5.7}$$

with N_{samples} the number of samples and $u_{i,l}$ the l^{th} sample of the i^{th} component of velocity. For RANS, the mean values of the velocities are directly known. The mean stream-wise velocity profiles, and their derivatives in the cross-stream direction, are presented against DNS results in figure 5.9.

Concerning the mean stream-wise velocity profiles, presented in sub-figure 5.9a, all the approaches are similar in the viscous sub-layer, *i.e.* for $x_2^+ \leqslant 8$. A divergence appears in the buffer sub-layer, for $x_2^+ > 10$. Then, the LES over-predicts the velocity and the RANS simulation under-predicts the velocity. The hybrid simulation under-predicts the velocity in the buffer sub-layer region, and shows a velocity deficit in the hybridisation region, enclosed by the vertical bars. Where the hybrid simulation follows a LES formulation, for $x_2^+ > 30$, the velocity profile is correctly estimated compared with DNS. The hybrid formulation may present a more dissipative behaviour than the pure LES, which could explain why the over-prediction of the velocity profile is reduced, yielding a better agreement with DNS.

Concerning the derivatives, presented in sub-figure 5.9b, the different approaches behave differently. All the simulations present curves of the same shape, comparable with the DNS. Both the RANS and hybrid simulations succeed in predicting correctly the levels at low x_2^+, while the LES under-predicts significantly the levels. The RANS and hybrid simulations then slightly under-predict the derivative for $x_2^+ > 3$, while the LES shows a good agreement with the DNS for $x_2^+ > 10$. Around the hybridisation region, the hybrid results yield a bump that is absent from the DNS. The maximum of the bump is located outside the hybridisation area, in the LES region ($x_2^+ > 30$), and have a width of $x_2^+ \simeq 40$. Its amplitude remains small.

The hybrid formulation gives correct results compared with DNS, with only a local increase of the velocity gradient in the direct vicinity of the hybridisation region.

Fluctuating velocities

The fluctuating velocities can be computed in two different ways. For the LES, the main part of the fluctuating velocities energy is directly simulated. In order to extract the information from the instantaneous velocity fields, the results undergo a two pass treatment. First, the mean velocities are extracted, as previously mentioned in eq. (5.7). Then, for each sample, the instantaneous fluctuating velocity is obtained as the difference between the instantaneous value and the mean value:

$$\forall i \in [\![1 ; 3]\!],\ \forall l \in [\![1 ; N_{\text{samples}}]\!],\ u''_{i,l} = u_{i,l} - [u_{i,l}] \tag{5.8}$$

with the same notations as for equation (5.7).

The averaging of the products of fluctuating velocities is obtained as the sum of these values over every sample, divided by the number of samples:

$$\forall (i,j) \in [\![1 ; 3]\!]^2,\ \left[u''_i u''_j\right] = \frac{1}{N_{\text{samples}}} \sum_{l=1}^{N_{\text{samples}}} u''_{i,l} u''_{j,l} \tag{5.9}$$

For the RANS approach, the Reynolds stresses are obtained using the Boussinesq constitutive relation, presented in equation (2.49), with the hybrid viscosity $(1 - f_{hyb}(d^+))\mu_t$ instead of μ_t for the hybrid simulation. The fluctuating velocity products are then calculated at any grid point as:

$$\forall (i,j) \in [\![1 ; 3]\!]^2,\ \left[u''_i u''_j\right] = -\frac{\tau^*_{tij}}{\langle\rho\rangle} \tag{5.10}$$

with τ^*_t the Reynolds stress tensor calculated with the Boussinesq constitutive relation and $\overline{\overline{\langle\rho\rangle}}$ the averaged density.

The fluctuating velocity products along the cross-stream direction are presented in figure 5.10. Due to the symmetry of the flow, the only relevant velocity products are those composed of the diagonal terms of the Reynolds stress tensor $[u''_1 u''_1]$, $[u''_2 u''_2]$, $[u''_3 u''_3]$ and the one composed of the first extra diagonal term of the Reynolds stress tensor $[u''_1 u''_2]$. In each sub-figure, for the hybrid results, both the fluctuating velocity products computed with the LES approach and the ones computed with the RANS approach are given. The LES approach is supposed to give a null value in the RANS area, due to the subtraction in equation (5.8). The RANS approach gives 0 by construction in the LES area. The two estimates are also summed and presented under the name hybrid value. Three vertical bars delimit the hybridisation region. The RANS region for the hybrid simulation is always the closest to the wall (smallest x_2^+), while the LES region is always the furthest from the wall (largest x_2^+).

The stream-wise fluctuating velocity products are presented in sub-figure 5.10a. The LES represents accurately the topology of the fluctuating velocity product, compared with the DNS, but overestimates moderately its intensity. On the opposite, the RANS simulation presents a maximum further from the wall and underestimates the fluctuating velocity product intensity. In the RANS region of the hybrid simulation, the fluctuating velocity product computed with the RANS approach follows the pure RANS results. However, the fluctuating velocity product computed with the LES approach is not small, but presents a plateau at half the maximal value computed with pure LES. This suggests that the flow field presents resolved scales of turbulence that penetrate the RANS region. This may be due to the strong refinement used for

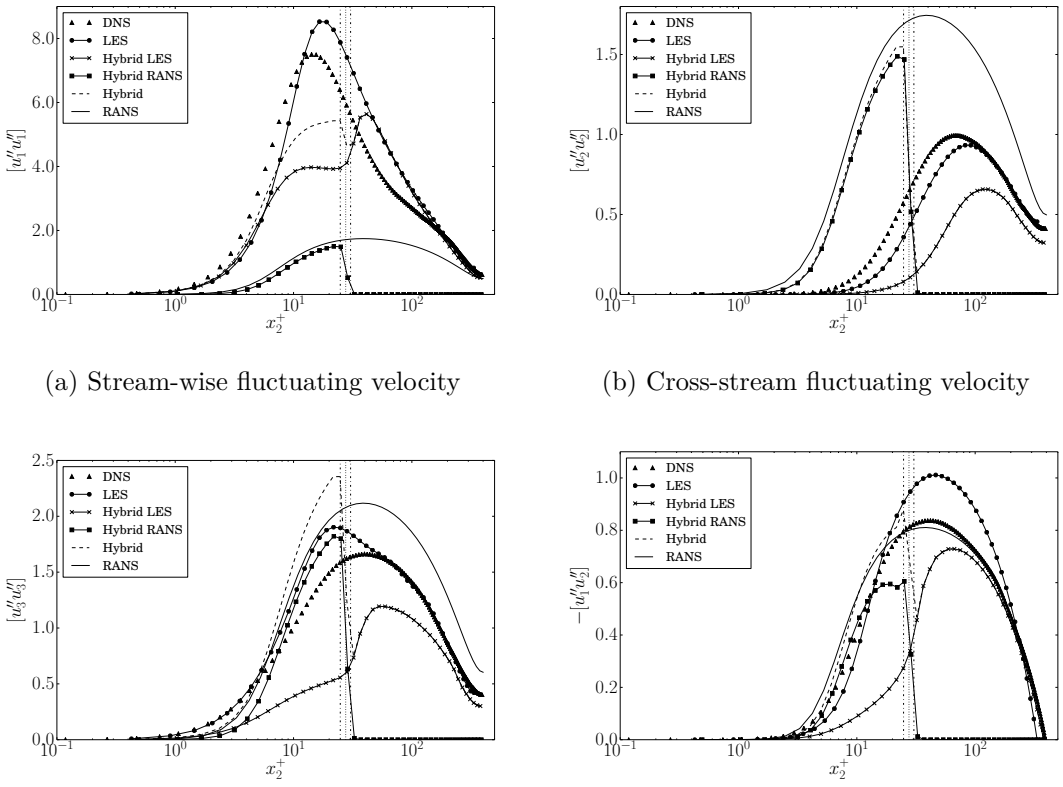

(a) Stream-wise fluctuating velocity

(b) Cross-stream fluctuating velocity

(c) Span-wise fluctuating velocity

(d) Extra-diagonal fluctuating velocity

Figure 5.10: Fluctuating velocity products along the cross-stream direction in the bi-periodical channel. The fluctuating velocity products are normalised by the actual u_τ^2. The three vertical lines represent from left to right respectively $f_{hyb} = 0.05$, $f_{hyb} = 0.50$, and $f_{hyb} = 0.95$.

the computation close to the walls. In the LES region of the hybrid simulation, the fluctuating velocity product computed with the LES approach follows the pure LES results. The sum of the two estimates of the hybrid approach gives a fluctuating velocity product that presents roughly the correct topology, with a dent in the hybridisation region, but an incorrect intensity. The fluctuating velocity product is underestimated by about 30%.

The cross-stream fluctuating velocity products are presented in sub-figure 5.10b. The pure LES is still accurate in term of topology compared with the DNS, but slightly underestimates its intensity. The maximum is located further from the wall than for the stream-wise fluctuating velocity product. On the opposite, the pure RANS simulation presents a maximum too close to the wall, compared with the DNS, and overestimates strongly this fluctuating velocity product intensity. In the RANS region of the hybrid simulation, the fluctuating velocity product computed with the RANS approach follows the fluctuating velocity product for the pure RANS simulation, with a slight reduction of its intensity. The fluctuating velocity product computed with the LES approach is small in this region. In the LES region of the hybrid simulation, the fluctuating velocity product computed with the LES approach has the correct topology, but presents a smaller intensity than for the pure LES. The sum of the two estimates of the hybrid approach gives a fluctuating velocity product that evolves

strongly between the RANS region and the LES region.

The span-wise fluctuating velocity products are presented in sub-figure 5.10c. In this case, the pure LES presents a peak located closer to the wall than for the DNS, and overestimates its intensity. The pure RANS simulation is correct in term of topology, but shows an overestimation of around 30% of the intensity at the maximum. In the RANS region of the hybrid simulation, the fluctuating velocity product calculated with the RANS approach presents the same topology as the one calculated in the pure RANS simulation. The intensity is again overestimated. The fluctuating velocity product calculated with the LES approach is small, but not negligible. As for the stream-wise fluctuating velocity product, the flow field presents resolved scales of turbulence that penetrate the RANS region. In the LES region, the fluctuating velocity product computed with the LES approach has the correct topology, but its intensity is underestimated, compared with the pure LES and the DNS. As for the cross-stream fluctuating velocity product, the sum of the two estimates of the hybrid approach gives a fluctuating velocity product that evolves strongly between the RANS region and the LES region.

The extra-diagonal fluctuating velocity products are presented in figure 5.10d. Both the pure LES and the pure RANS simulation give the correct topology compared with the DNS. In the viscous and buffer sub-layers, the RANS simulation slightly overestimates the intensity. The LES overestimate is larger and located in the log region. As previously, in the RANS region of the hybrid simulation, the fluctuating velocity product calculated with the RANS approach follows the trend of the pure RANS simulation. The fluctuating velocity product calculated with the LES approach is smaller than the one calculated with the RANS approach, but not negligible. In the LES region, the fluctuating velocity product computed with the LES approach has the correct topology, but its intensity is underestimated, compared with the pure LES and with the DNS. As for the previous results, the sum of the two estimates of the hybrid approach gives a fluctuating velocity product that evolves strongly between the RANS region and the LES region.

The fluctuating velocity products present discrepancies between the RANS region and the LES region of the hybrid simulation. However, a rather smooth evolution is obtained for the dominant component, in the stream-wise direction. Moreover, in the LES region, the topology of the fluctuating velocity products is correct, even though the intensity is always underestimated compared to pure LES.

Spatial autocorrelation

The spatial autocorrelation of the fluctuating velocity $\underline{u}''$ is defined, for a given spatial step in the stream-wise direction Δx_1 or in the span-wise direction Δx_3, as:

$\forall i \in [\![1 \ ; \ 3]\!]$,

$$R_{ii}\left(\Delta x_1\right) = \int_{x_{3,min}}^{x_{3,max}} \sum_{\substack{x_{2,ref} \in \\ \{x_{2,ref}^{lw}, x_{2,ref}^{up}\}}} \int_{x_{1,min}}^{x_{1,max}} u_i''\left(x_1 + \Delta x_1, x_{2,ref}, x_3\right) \times u_i''\left(x_1, x_{2,ref}, x_3\right) \mathrm{d}x_1 \mathrm{d}x_3 \quad (5.11)$$

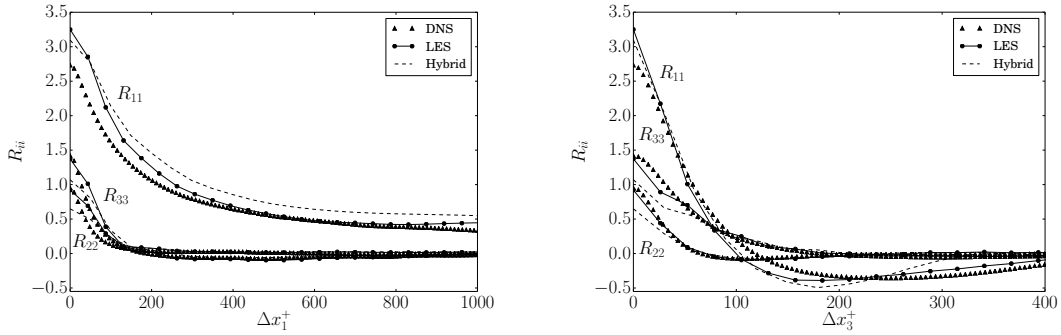

(a) Along the stream-wise direction

(b) Along the span-wise direction

Figure 5.11: Velocity autocorrelations along the stream-wise and span-wise directions in the bi-periodical channel. The correlations are computed at $x_2^+ = 100$, and normalised by the actual u_τ^2.

$$R_{ii}\left(\Delta x_3\right) = \int_{x_{3,min}}^{x_{3,max}} \sum_{\substack{x_{2,ref} \in \\ \{x_{2,ref}^{lw}, x_{2,ref}^{up}\}}} \int_{x_{1,min}}^{x_{1,max}} u_i''\left(x_1, x_{2,ref}, x_3 + \Delta x_3\right) \times u_i''\left(x_1, x_{2,ref}, x_3\right) \mathrm{d}x_1 \mathrm{d}x_3 \quad (5.12)$$

with $x_{3,min} = -\pi\delta_{1/2}/2$, $x_{3,max} = \pi\delta_{1/2}/2$, $x_{1,min} = -\pi\delta_{1/2}$, $x_{1,max} = \pi\delta_{1/2}$, and $x_{2,ref}^{lw}$ (resp. $x_{2,ref}^{up}$) chosen to yield $x_{2,ref}^{lw\,+} = 100$ (resp. $x_{2,ref}^{up\,+} = 100$) from the lower (resp. upper) wall. The fluctuating velocity is computed as the instantaneous velocity minus the mean velocity, as presented in equation (5.8). The choice of $x_2^+ = 100$ ensures that the autocorrelation is calculated in the LES region of the hybrid simulation, and can be compared with the pure LES and DNS.

The spatial autocorrelations of the fluctuating velocity components, along the stream-wise direction and the span-wise direction, are presented in figure 5.11.

The spatial autocorrelations along the stream-wise direction are presented in figure 5.11a. The DNS shows that R_{11} presents a maximum at $\Delta x_1^+ = 0$ and rapidly decreases for $0 \leqslant \Delta x_1^+ \leqslant 300$. R_{22} and R_{33} present a similar intensity, about half that of R_{11}, and decrease over $0 \leqslant x_2^+ \leqslant 100$. The spatial autocorrelations along the span-wise direction are presented in figure 5.11b. The same trend as in the stream-wise direction can be observed in the DNS, with a maximum for $\Delta x_3^+ = 0$ and a rapid decrease. R_{11} is still around twice bigger than R_{22} and R_{33}, and R_{33} is slightly bigger than R_{22}.

The autocorrelation gives an insight on the size and relative intensity of the turbulent eddies. The eddies are stronger and larger in the stream-wise direction, and of similar size and intensity in the other directions. For the three fluctuating components in both correlation directions, the autocorrelation gives similar results for the LES and the hybrid simulation. The size and intensity of the turbulent eddies are correctly represented by both the LES and the hybrid simulation, compared with DNS.

The mean velocity and autocorrelations show that the hybrid approach developed

in the present thesis is quite able to represent the physics of the flow. Discrepancies remain in the computation of the fluctuating velocities. This is mainly due to the fact that the hybridisation occurs on these quantities, so they suffer the approximations inherently present in the model. Given the presented results, the hybrid approach is considered validated, and will be used on the corner separation case (*c.f.* chapter 10).

Chapter 6

Simulation protocols

Sections

The present work relies on the study of two academic flows, representative of turbomachinery phenomena. First, a corner separation case in a linear cascade at low Mach number is considered. Then, a tip-clearance flow of a single blade in the potential core of a jet is considered. Both flows are studied using LES and RANS simulations. The corner separation case will also be investigated using the hybrid approach developed in chapter 5. The simulation protocols are presented in the present chapter.

6.1 Corner separation simulation protocols

The corner separation test-case represents a passage of the LMFA-NACA65 linear compressor cascade. Two experimental campaigns were lead on this test-case, with the work of Ma (2012) (see also Ma et al. (2011, 2013)) and later the work of Zambonini et al. (2017) (see also Zambonini and Ottavy (2015); Zambonini (2016)).

The corner separation case presented here has been numerically studied by Gao (2014) (see also Gao et al. (2015a,b, 2017)). The LES simulation was realised during Gao's PhD thesis, and is used as a reference database for this work. The RANS simulations and the hybrid simulation presented in this work have been performed by the author.

6.1.1 Flow characteristics

The free-stream velocity is set to the same value as for the experiment, *i.e.* $u_e = 40\text{m.s}^{-1}$. It yields a Mach number $M \approx 0.1$, and the flow can be considered as incompressible. The reference density is set to $\rho = 1.177\text{kg.m}^{-3}$, and the dynamic viscosity is set to $\mu = 1.81 \times 10^{-5}\text{kg.m}^{-1}\text{s}^{-1}$, for a chord based Reynolds number $\text{Re}_c = 3.82 \times 10^5$. All the simulations are realised with an incidence angle of 4°. The flow characteristics are summarised in table 6.1.

Name	Symbol	Value
Free-stream velocity	u_e	40m.s^{-1}
Mach number	M	0.1
Density	ρ	1.177kg.m^{-3}
Dynamic viscosity	μ	$1.81 \times 10^{-5}\text{kg.m}^{-1}\text{s}^{-1}$
Chord based Reynolds number	Re_c	3.82×10^5

Table 6.1: Summary of the corner separation test-case flow characteristics.

6.1.2 Geometry and dimensions of the computational domain

The experimental linear compressor cascade is composed of 13 identical NACA 65-009 blades, whose camber angle has been modified. The original geometry and the modifications can be found in the theses of Ma (2012) and Gao (2014). The blades have a chord length $c = 150\text{mm}$, a stagger angle $\gamma = 42.7°$, a pitch length $s = 134.0\text{mm}$ and a span length $h = 370.0\text{mm}$. The passage is simulated up to one chord length upstream of the blade leading edge and one chord length downstream of the blade trailing edge. In order to restrain the computational cost of Gao's LES, only half the channel span was simulated ($h/2 = 185.0\text{mm}$). The same half channel is simulated in RANS, in order to have comparable cases. More information concerning the geometry of the linear compressor cascade can be found in Zambonini et al. (2017) and in Gao (2014). The dimensional characteristics are summarised in table 6.2.

6.1.3 Mesh

Two different meshes are considered in this work, a wall-resolved LES mesh and a mesh for wall-resolved RANS simulations. The RANS mesh is also used for the hybrid simulation.

Name	Symbol	Value
Chord length	c	150mm
Stagger angle	γ	42.7°
Pitch length	s	134.0mm
Span length	h	370.0mm
Simulated span length	$h/2$	185.0mm

Table 6.2: Summary of the corner separation test-case dimensions.

The LES mesh of half the blade passage is built as a HOH blade-to-blade mesh reproduced 481 times along the span-wise direction. A representation of the HOH mesh (truncated upstream and downstream) of this blade-to-blade plane is given in figure 6.1. The refinement is chosen to yield *a priori* $\Delta x_1^+ \approx 60$ for the smallest cell length in the stream-wise direction, $\Delta x_2^+ \approx 1$ for the smallest cell length in the wall-normal direction at the blade (resp. $\Delta x_3^+ \approx 1$ at the end-wall) and $\Delta x_3^+ \approx 30$ for the smallest cell length in the transverse direction at the blade (resp. $\Delta x_2^+ \approx 30$ at the end-wall). *A posteriori*, the simulation yields $\Delta x_2^+ \leqslant 2$ at the blade (resp. $\Delta x_3^+ \leqslant 2$ at the end-wall), which is a correct refinement for wall-resolved LES. The *a posteriori* check of the wall cell sizes can be found in Gao (2014). The tripping bands used to force the laminar/turbulent transition in the experiment are represented in the LES by the removal of some grid points at the same locations. The total number of points is about 200×10^6 points, split into 642 blocks for parallel computing.

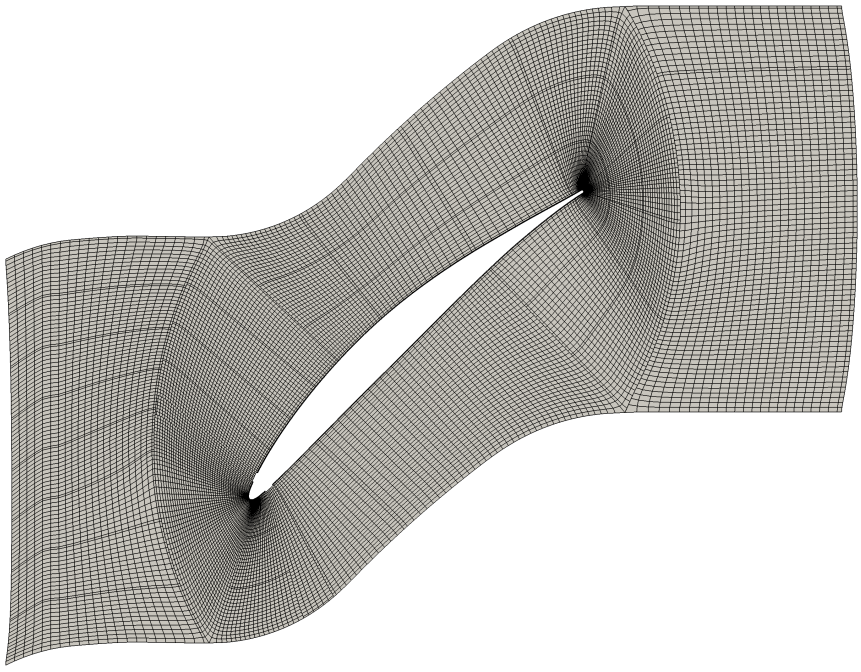

Figure 6.1: LES mesh for the corner separation case. Every fourth point in every direction is plotted.

The RANS and hybrid mesh of half the blade passage is built in the same way as the LES mesh. A HOH mesh in the blade-to-blade plane is reproduced 77 times along the span-wise direction. The refinement is chosen to yield *a priori* $\Delta x_2^+ \leqslant 2$, which is verified *a posteriori* in Gao (2014). For the RANS simulations, as soon as

the turbulence model is activated, the flow is considered turbulent. The addition of tripping bands is not necessary. The total number of points is about 2.8×10^6, split into 48 blocks for parallel computing.

The mesh characteristics are summarised in table 6.3.

Simulation	Tripping bands	Δx_1^+	Δx_2^+	Δx_3^+	Number of points ($\times 10^6$)
LES	Yes	$\leqslant 60$	$\leqslant 2$	$\leqslant 30$	280
RANS/Hybrid	No	$[-]$	$\leqslant 2$	$[-]$	2.8

Table 6.3: Summary of the corner separation mesh characteristics.

6.1.4 Boundary conditions

Generating a turbulent inflow for LES is a burning issue. In order to provide a physically-sound turbulent boundary layer to the LES, a flat-plate boundary layer simulation using three-dimensional, wall resolved LES is realised in parallel with the passage simulation. The instantaneous density and velocity are extracted on a plane from the flat-plate boundary-layer simulation at the location where the time-averaged displacement thickness equals the experimental one at the inlet of the blade passage. The flat-plate simulation has a limited cross-stream extension ($\sim \delta$) which is repeated periodically to feed the blade passage inlet. In the free-stream region, due to the weak intensity of the turbulence, the quantities are averaged in space and injected in the inlet plane of the blade passage. This ensures consistent inflow conditions between the LES and the experiment. A representation of the inflow generation is given in figure 6.2. The flat-plate domain is 2.54m long, its width is $\sim \delta$ and its height is $\sim 2\delta$ (δ estimated at the blade passage inlet). The refinement is similar to the refinement of the flat-plate test-case in chapter 4. The total number of points in the flat-plate domain is around 100×10^6. Unlike for the flat-plate boundary-layer used in chapter 4, the transition is triggered by a tripping band represented by a step in the grid. The band is located at $\mathrm{Re}_x = 1.3 \times 10^6$, and measures 4.8×10^{-3}m long by 6.73×10^{-4}m thick, and modelled by removing cells from the smooth mesh.

For the inflow of the RANS and hybrid simulations, a two dimensional steady RANS, flat-plate boundary-layer simulation is carried out. As for the LES, a profile is extracted at the location where the displacement thickness matches the experimental one. The density, the three components of the velocity, and the two turbulent variables are injected as inlet profile.

The pitch-wise boundary condition is set to periodic for all the simulations. As already mentioned, only half of the experimental channel height (or blade span) is simulated. The boundary condition at mid-span is set as symmetric, for all the simulations. All the walls, *i.e.* the end-wall and the blade surface, are set as non-slip adiabatic.

For the LES, hybrid and RANS simulations, the outlet boundary condition is set to a partially non reflective pressure condition. In LES, a special attention has to be paid to the correct evacuation of the numerical acoustic waves at the outlet. In order to damp the unwanted numerical reflections, the mesh is stretched in the stream-wise direction and an explicit filter (Bogey and Bailly, 2002) is implemented in the last 20

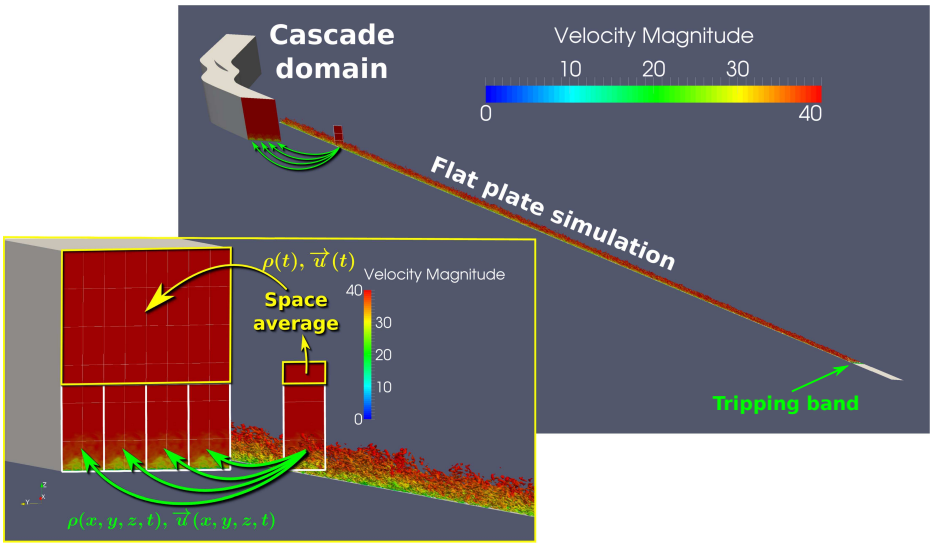

Figure 6.2: Corner separation inflow configuration (Gao, 2014).

grid planes (whose normals are in the stream-wise direction). The formulation of the filter is:

$$\forall I \in [\![\ I_{\text{begin}}\ ;\ I_{\text{end}}\ ]\!],\ \eta_{flt}[I] = \frac{I - I_{\text{begin}} + 1}{I_{\text{end}} - I_{\text{begin}} + 1} \tag{6.1}$$

$$\sigma_{flt}\left(\eta_{flt}[I]\right) = \alpha_{flt} \times \eta_{flt}[I]^{\beta_{flt}} \tag{6.2}$$

with I the index in the stream-wise direction, I_{begin} the index in the stream-wise direction of the first plane where the filter is implemented, I_{end} the index of the last plane, and $\alpha_{flt} \in [0,\ 0.45]$, $\beta_{flt} \in [1,\ 2]$ constants of the filter. The constants have been set to $\alpha_{flt} = 0.05$ and $\beta_{flt} = 2.0$. A filtered quantity φ is given by:

$$\varphi[I,J,K] = \varphi[I,J,K] - \sigma_{flt}\left(\eta_{flt}[I]\right)\Big(\varphi[I,J,K] - \Big(\varphi[I-1,J,K] + \varphi[I+1,J,K] + \varphi[I,J-1,K] + \varphi[I,J+1,K] + \varphi[I,J,K-1] + \varphi[I,J,K+1]\Big)/6\Big) \tag{6.3}$$

The filter is also used near the blade leading and trailing edges over five grid points in the whole span, in order to smooth the oscillations present close to stagnation points.

The boundary condition characteristics are summarised in table 6.4.

Simulation	Inlet	Lateral	Mid-span	Walls	Outlet
LES	Turbulent inflow from 3D boundary-layer	Periodic	Symmetric	Non-slip adiabatic	Semi-reflective pressure condition + filter
RANS & hybrid	Turbulent profile from 2D boundary-layer	Periodic	Symmetric	Non-slip adiabatic	Semi-reflective pressure condition

Table 6.4: Summary of the corner separation boundary-condition characteristics.

6.1.5 Numerical schemes

For all the simulations, the spatial scheme used for the inviscid fluxes is a four-point centred scheme discretisation from Jameson et al. (1981), with a fourth-order artificial viscosity (coefficient: 0.002 for the LES, 0.02 for the RANS and hybrid simulations, see Boudet et al. (2015b) for its definition). The spatial scheme for the viscous fluxes is a two-point centred scheme.

For the LES and the hybrid simulation, the temporal scheme is a three-step Runge-Kutta scheme with a constant time step of 2.5×10^{-8}s, yielding a Courant-Friedrichs-Lewy (CFL) number of 0.95 based on the minimum grid size 1.0×10^{-5}m, the reference velocity 40m.s^{-1} and the speed of sound 340m.s^{-1}. For the RANS simulations, the temporal scheme is a five-step Runge-Kutta scheme with a local variable time step, based on a local CFL number of 0.7 (based on the local grid size, the local velocity and the local speed of sound).

A summary of the numerical schemes used is given in table 6.5.

Simulation	Spatial scheme	Artificial viscosity coefficient	Temporal scheme	CFL number
LES	Jameson 4-points	0.002	3-step Runge-Kutta	0.95
RANS	Jameson 4-points	0.02	5-step Runge-Kutta	0.70
Hybrid	Jameson 4-points	0.02	3-step Runge-Kutta	0.95

Table 6.5: Summary of the corner separation numerical schemes.

6.1.6 Turbulence/SGS models

The large-eddy simulation of the corner separation case is carried out with the SISM SGS model from Lévêque et al. (2007), presented in chapter 2, section 2.3.2. The characteristic frequency of the exponential average used in the model is calculated using the free-stream velocity u_e and the chord length c, as $2u_e/c = 533$Hz.

For the RANS simulations, the three turbulence models presented in chapter 2, section 2.4.3 are used. These turbulence models are the original Wilcox $k-\omega$ turbulence model, the quadratic Wilcox $k-\omega$ turbulence model, and the modified Wilcox $k-\omega$ turbulence model.

For the hybrid simulation, the SGS turbulence in the LES region is modelled using the SISM, with the same characteristic frequency of 533Hz as for the pure LES simulation, and the turbulence in the RANS region is modelled using the original Wilcox $k-\omega$ model. The hybrid model 1 is used, with $d_\mu^+ = 50$ and $L_{hyb} = 10$ (*cf* equation (5.2) for their definition). A summary of the turbulence models used is given in table 6.6.

6.1.7 Statistics

For LES, that is naturally unsteady, the transient regime at the beginning of the computation corresponds to the phase of numerical convergence. The statistics have to be computed on a numerically converged case to be physically relevant. The LES has been carried over ten through-flow periods (defined as the ratio between the chord length c and the free-stream velocity u_e), corresponding to the evacuation of the transient

Simulation name	Simulation type	SGS model	Turbulence model
LES	LES	SISM	[–]
RANS_BSQ	RANS	[–]	Original wilcox $k-\omega$
RANS_QCR	RANS	[–]	Quadratic wilcox $k-\omega$
RANS_BUA	RANS	[–]	Modified wilcox $k-\omega$
HYBR	Hybrid	SISM	Original wilcox $k-\omega$

Table 6.6: Summary of the corner separation turbulence models.

regime, plus about ten more through-flow periods. The statistics have been computed over these last ten periods (40.25ms), with a sample every 50μs (every 2000 iterations), for a total number of 805 samples.

For the RANS simulations, the mean values of the conservatives variables and the turbulent kinetic energy budget are directly known after the numerical convergence, which is determined by the vanishing residuals (the residuals have to be stable in time and reduced for about three order of magnitude compared with the beginning of the computation).

For the hybrid simulation, the same approach as for the LES is necessary. The statistics have to be computed on a numerically converged case to be physically relevant. The hybrid simulation has been carried over about ten through-flow periods, corresponding to the evacuation of the transient regime, plus ten more through-flow periods. The statistics have been computed over these last ten periods (40.0ms), with a sample every 2.5μs (every 100 iterations).

6.1.8 Summary of the cases

In total, one large-eddy simulation, three RANS simulations and an hybrid RANS-LES simulation are analysed. The LES had been realised by Gao, and has been extensively studied (Gao, 2014; Gao et al., 2015a,b, 2017). It is compared to the three RANS simulations, carried out by the author. The hybrid simulation, using the model developed in chapter 5, was also carried out by the author.

6.2 Tip-leakage simulation protocols

The tip-leakage analysis relies on several numerical simulations that reproduce an academic experimental configuration of an isolated NACA5510 blade placed in the potential core of a jet. The simplicity of this configuration allowed a detailed experimental characterisation with advanced measurement techniques. Two experimental campaigns were lead on the configuration. The first campaign results are presented in Jacob et al. (2010). The analyses on the second experimental campaign can be found in Jacob et al. (2016a,b).

A numerical campaign, simultaneous with the second experimental campaign, has been carried out on the same configuration using zonal large-eddy simulation (ZLES). The ZLES was realised by Caro. The zonal model used is presented in section 3.6. The validation against experimental results and an analysis of the ZLES results can be found in Boudet et al. (2016a,b). The ZLES is used as a reference database in the

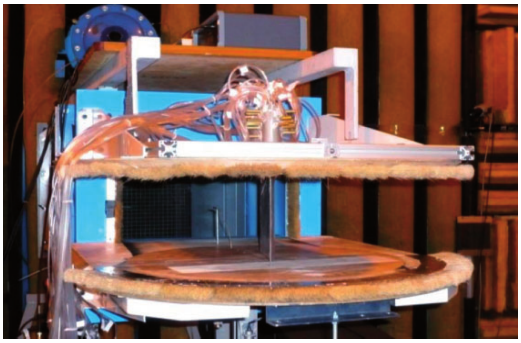

(a) Experimental setup (Jacob et al., 2016a)

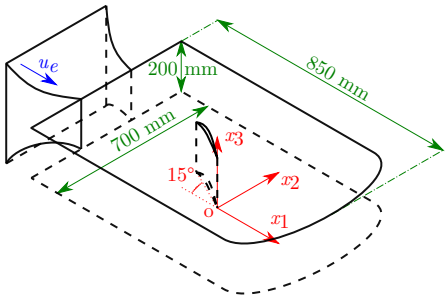

(b) Sketch

Figure 6.3: Geometry of the tip-leakage case. (a): Experimental installation from Jacob et al. (2016a), (b): Sketch of the geometry.

present work. Three RANS simulations, performed by the author, were realised and are compared with the reference ZLES.

6.2.1 Geometry and flow characteristics

The studied blade is a NACA5510 airfoil, whose chord length equals 0.2m, span length equals 0.19m, thickness equals 0.02m, and camber equals 5%. The airfoil is attached to an end-plate at the top and set above an end-plate at the bottom. The set-up presents a tip-clearance at the bottom with a $h = 0.01$m clearance height. A sketch of the configuration is presented in figure 6.3. The tip-clearance height is large ($h/c = 0.05$), compared to what is usually used in industrial compressors. In the original experiment, this choice was lead by acoustic considerations. The gap is large in order to increase the tip-clearance noise with respect to the trailing edge noise. Although the present study does not consider the acoustics, this tip-clearance height has been kept in order to be comparable with the available experimental and ZLES results.

The jet velocity is set to the same value as the experimental one, *i.e.* $u_e = 70\text{m.s}^{-1}$. It yields a Mach number $M \approx 0.2$. The flow can be considered as incompressible. The reference density is set to $\rho = 1.200\text{kg.m}^{-3}$ and the dynamic viscosity is set to $\mu = 1.81 \times 10^{-5}\text{kg.m}^{-1}\text{s}^{-1}$, yielding a chord based Reynolds number $\text{Re}_c = 9.3 \times 10^5$. All the simulations are realised for an angle of attack of 15°.

The dimensions and flow characteristics are summarised in table 6.7.

6.2.2 Computational domains

Two computational domains are considered in this work. For the ZLES, the domain extends over $29c$ axially, $37c$ laterally and $1c$ span-wise. In order to reduce the computational cost, only the region around the tip-clearance is simulated using pure LES, as presented in figure 6.4. The inlet flow, generated by a LES flat-plate boundary layer, is located half a chord length upstream of the blade leading edge. The outer regions

Name	Symbol	Value
Chord length	c	0.2m
Blade Span length	$[-]$	0.19m
Blade thickness	$[-]$	0.02m
Blade camber	$[-]$	5%
Clearance height	h	0.01m
Clearance height to chord ratio	h/c	0.05
Free-stream velocity	u_e	70m.s^{-1}
Mach number	M	0.2
Density	ρ	1.200kg.m^{-3}
Dynamic viscosity	μ	$1.81 \times 10^{-5}\text{kg.m}^{-1}\text{.s}^{-1}$
Chord based Reynolds number	Re_c	9.3×10^5

Table 6.7: Summary of the tip-leakage flow characteristics.

are simulated with RANS, as presented on figure 6.5. More information can be found in Boudet et al. (2016a,b).

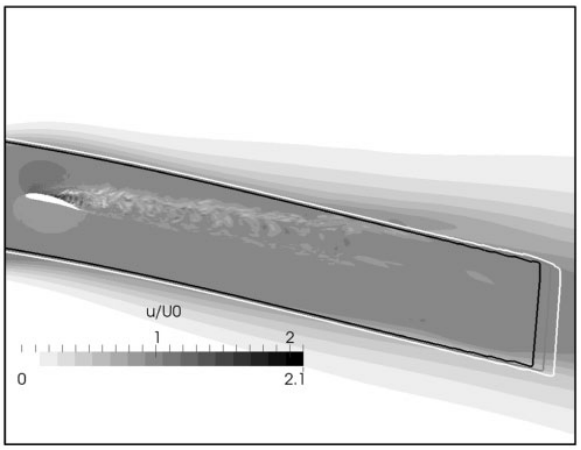

Figure 6.4: Zonal decomposition around the airfoil tip region from Boudet et al. (2016a). The black, grey and white lines correspond respectively to $\beta = 0.1$, $\beta = 0.5$, and $\beta = 0.9$ with the notations of eq. (3.39) in section 3.6.

For the RANS simulations, the computational domain extends over $12.3c$ axially, $20c$ laterally and $1c$ span-wise.

The dimensions of the computational domains are summarised in table 6.8.

6.2.3 Mesh

Two different meshes are used in this work, corresponding to the two different simulation domains. The ZLES mesh is built as an HOH mesh around the blade, with a fine resolution in the tip-clearance (62 points through the clearance). In the LES region, the refinement is chosen to yield $\Delta x_1^+ \leqslant 80$, $\Delta x_2^+ \leqslant 1.5$, and $\Delta x_3^+ \leqslant 30$, which is a correct refinement for wall-resolved LES. The grid is made up with 150×10^6 points, split into 524 domains for parallel computing. A global view of the mesh and a close-up view around the tip-clearance leading edge are given in figure 6.6. A special attention was paid to the LES and inlet regions, and to the jet flow. The outer RANS

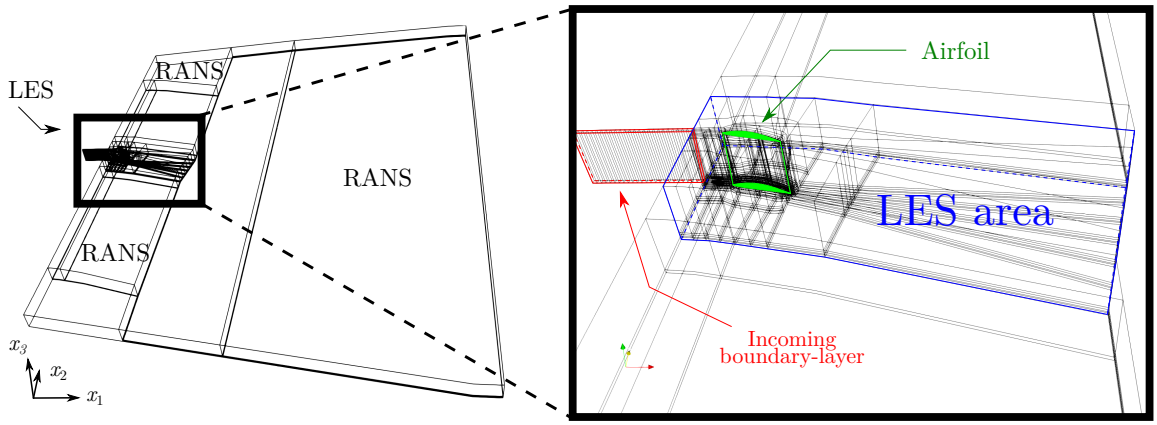

Figure 6.5: ZLES calculation domains of the tip-leakage case. Left: view of the full calculation domain. Right: zoom on the LES region.

Simulation	Axial extent	Lateral extent	Span-wise extent
ZLES	$29c$	$37c$	$1c$
RANS	$12.3c$	$20c$	$1c$

Table 6.8: Dimensions of the tip-leakage computational domains.

regions are much coarser. The close-up view in the tip-clearance shows that a special attention was paid to the junction between the tip-clearance and the end-wall around.

The RANS mesh used has been designed by Li (2016). The RANS mesh is built in the same manner as the LES region of the ZLES, but coarser. A fine resolution in the tip-clearance is kept, with 69 points span-wise. The boundary-layers are well resolved, with $\Delta x_2^+ \leqslant 1.5$. The grid is made up with 5.4×10^6 points, split into 62 domains for parallel computing.

The mesh characteristics are summarised in table 6.9.

Simulation	Δx_1^+	Δx_2^+	Δx_3^+	Number of points ($\times 10^6$)
ZLES	$\leqslant 80$	$\leqslant 1.5$	$\leqslant 30$	150
RANS	[–]	$\leqslant 1.5$	[–]	5.4

Table 6.9: Summary of the characteristics of the tip-leakage grids.

6.2.4 Boundary conditions

As for the corner separation case, the inlet conditions are a burning issue. The region of interest being a full LES, the inlet condition must present the correct turbulent behaviour compared to the experiment. In the present case, a special attention is paid to have a similar boundary-layer displacement thickness between the outlet of the experimental jet and the inlet of the ZLES. The generation is realised with a flat-plate boundary-layer simulation placed upstream of the profile, as presented in figure 6.5. The turbulence of the boundary-layer is triggered by a source term as for the flat-plate boundary-layer case presented in chapter 4 (see Boudet et al. (2015b) for more details). The width of the boundary layer domain is $\sim \delta$ (δ measured at the inlet of the ZLES).

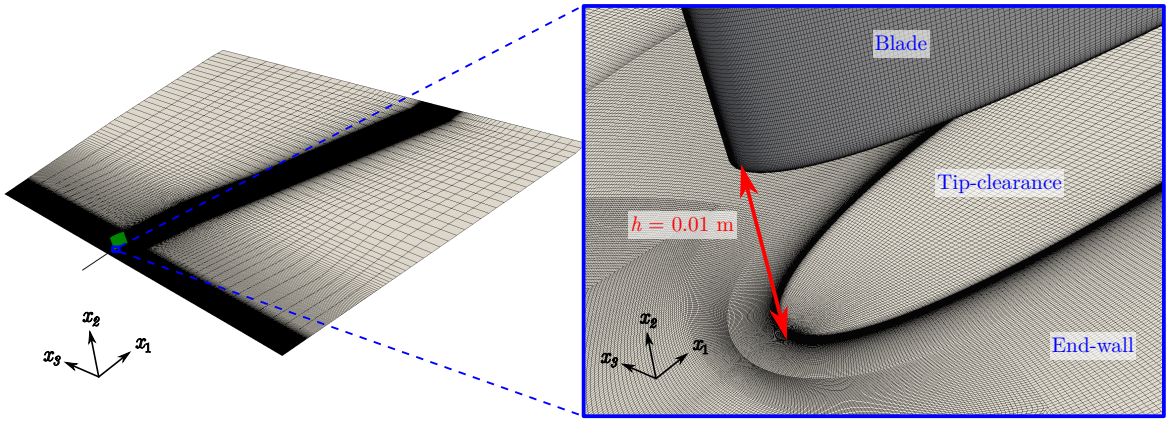

Figure 6.6: Mesh of the tip-leakage case configuration, for the ZLES simulation. Left: the entire mesh, at the end-wall. In green, the profile. Right: a close-up view around the tip-clearance at the leading edge.

It is repeated periodically (4 times) to feed the LES region around the tip-clearance. For the RANS simulation, a mean profile with the correct turbulent characteristics is imposed.

For all the simulations, the walls are set as non-slip adiabatic. The top and bottom boundaries are walls, respectively the top-wall, where the blade is attached, and the end-wall, where the tip-clearance is located. The other boundaries, *i.e.* the lateral and outlet boundaries, are set to a partially non-reflective pressure condition. The boundary condition characteristics are summarised in table 6.10.

Simulation	Inlet	Lateral	Walls	Outlet
ZLES	Turbulent inflow from 3D boundary-layer	Semi-reflective pressure condition	Non-slip adiabatic	Semi-reflective pressure condition
RANS	Mean turbulent profile	Semi-reflective pressure condition	Non-slip adiabatic	Semi-reflective pressure condition

Table 6.10: Summary of the tip-leakage boundary condition characteristics.

6.2.5 Numerical schemes

For all the simulations, the spatial scheme used for the inviscid fluxes is a four-point centred scheme from Jameson et al. (1981). The ZLES uses a fourth-order artificial viscosity (coefficient: $\leqslant 0.003$ for the LES region, increased up to 0.03 in the outer RANS regions, see Boudet et al. (2015b) for its definition) and the RANS simulations use a second-order artificial viscosity (coefficient: 0.02). The spatial scheme for the viscous fluxes is a two-point centred scheme.

For the ZLES, the temporal scheme is a three-step Runge-Kutta scheme with a constant time step of 1.6×10^{-8}s ($5.6 \times 10^{-6} c.u_e^{-1}$), yielding a CFL of 0.90 (based on the inlet velocity plus the speed of sound and the minimal grid size). For the RANS simulations, the temporal scheme is a three-step Runge-Kutta scheme with a local variable time step, based on a local CFL number of 0.6 (based on the local grid size, the local velocity and the local speed of sound).

A summary of the numerical schemes used is given in table 6.11.

Simulation	Spatial scheme	Artificial viscosity	Temporal scheme	CFL number
ZLES	Jameson 4-points	0.002 (4^{th} order)	3-step Runge-Kutta	0.90
RANS	Jameson 4-points	0.020 (2^{nd} order)	3-step Runge-Kutta	0.60

Table 6.11: Summary of the tip-leakage numerical schemes.

6.2.6 Turbulence/SGS models

The zonal large-eddy simulation of the tip-leakage is carried out with the SISM SGS model from Lévêque et al. (2007) (presented in chapter 2 section 2.3.2) in the LES region, and the original Wilcox $k-\omega$ turbulence model in the outer RANS regions. The characteristic frequency of the exponential average of the SISM is calculated as $1.8u_e/c = 630$Hz, using the free-stream velocity u_e and the chord length c.

For the RANS simulations, the three turbulence models presented in chapter 2, section 2.4.3, are used. These turbulence models are the original Wilcox $k-\omega$ turbulence model, the quadratic Wilcox $k-\omega$ turbulence model, and the modified Wilcox $k-\omega$ turbulence model.

A summary of the turbulence models used is given in table 6.12.

6.2.7 Statistics

For the ZLES, the region of interest is simulated with pure LES. The computation was initiated with a converged RANS simulation, in order to reduce the numerical convergence phase. The statistics have to be computed after numerical convergence for relevance. The LES has been carried over six through-flow periods (defined as the ratio between the chord length c and the free-stream velocity u_e), corresponding to the evacuation of the transient regime, plus ten more through-flow periods. The statistics have been computed over these last ten periods (28.57ms), with a sample every 48μs (every 3000 iterations), for a total number of 595 samples.

For the RANS simulations, the mean values of the conservatives variables and the turbulent kinetic energy budget are directly known after the numerical convergence, which is determined by the vanishing residuals (the residuals have to be stable in time and reduced for about three order of magnitude compared with the beginning of the computation).

Simulation name	Simulation type	SGS model	Turbulence model
ZLES	LES/RANS	SISM	Original wilcox $k-\omega$
RANS_BSQ	RANS	[−]	Original wilcox $k-\omega$
RANS_QCR	RANS	[−]	Quadratic wilcox $k-\omega$
RANS_BUA	RANS	[−]	Modified wilcox $k-\omega$

Table 6.12: Summary of the tip-leakage turbulence models.

6.2.8 Summary of the cases

In total, one zonal large-eddy simulation and three RANS simulations are analysed. The ZLES has been realised by Caro, and has been extensively studied (Boudet et al., 2016a,b). It is compared to the three RANS simulations, carried out by the author, using the three turbulence models presented in chapter 2, section 2.4.3.

Part III

Results

Chapter 7

Corner separation mean flow analysis

Sections

As presented in chapter 1, the corner separation is a three dimensional, highly vortical flow. For these reasons, the usual turbulence models, often calibrated on more academic, less complex flows, have difficulties to predict accurately the physical phenomena of this flow. The present analysis aims at investigating some turbulence modelling strategies for the RANS simulations of a corner separation flow, using LES as a reference.

First, some results on the mean values, such as the pressure coefficient around the blade or the total pressure losses, are presented to gauge the overall quality of the simulation. Then, the Reynolds stresses, which are the quantities that directly impact the momentum and energy equations (see equations (2.48b) and (2.48c)), are analysed on various extraction planes.

7.1 Pressure coefficient and total pressure losses

7.1.1 Mean flow visualisation

The corner separation occurs at the junction of the blade suction side and the end-wall, in the aft part of the blade. This separation is promoted by the interaction between

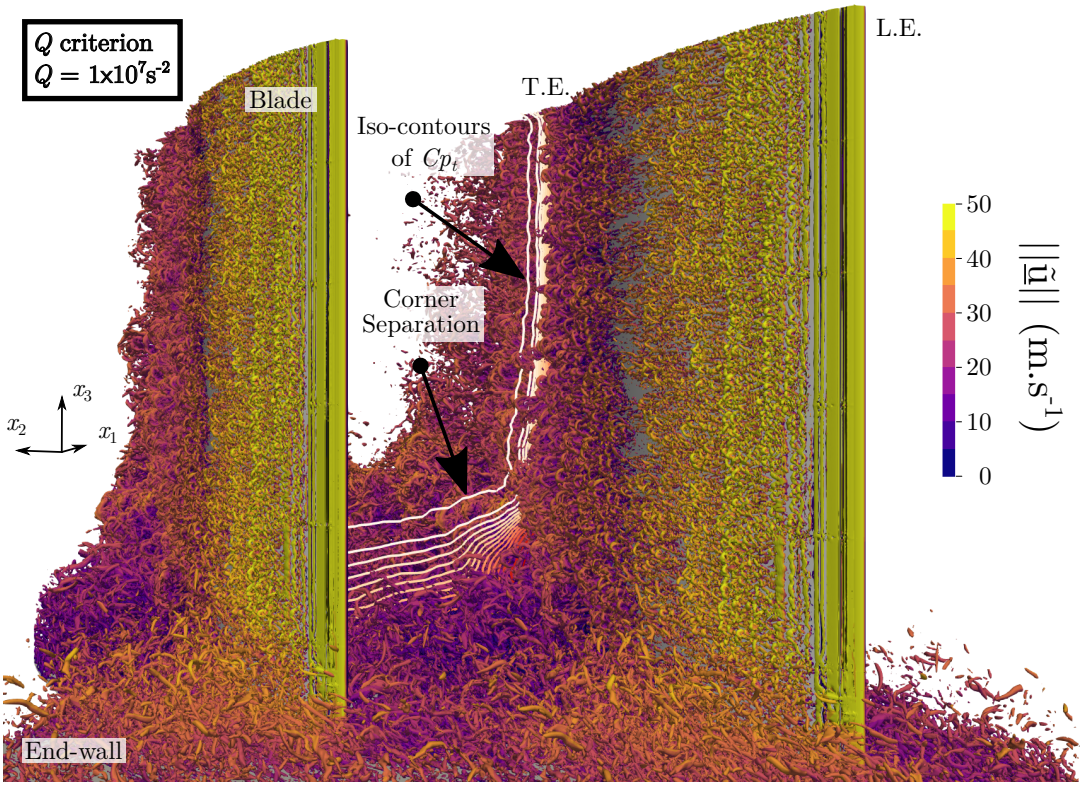

(a) Q criterion of the instantaneous LES flow

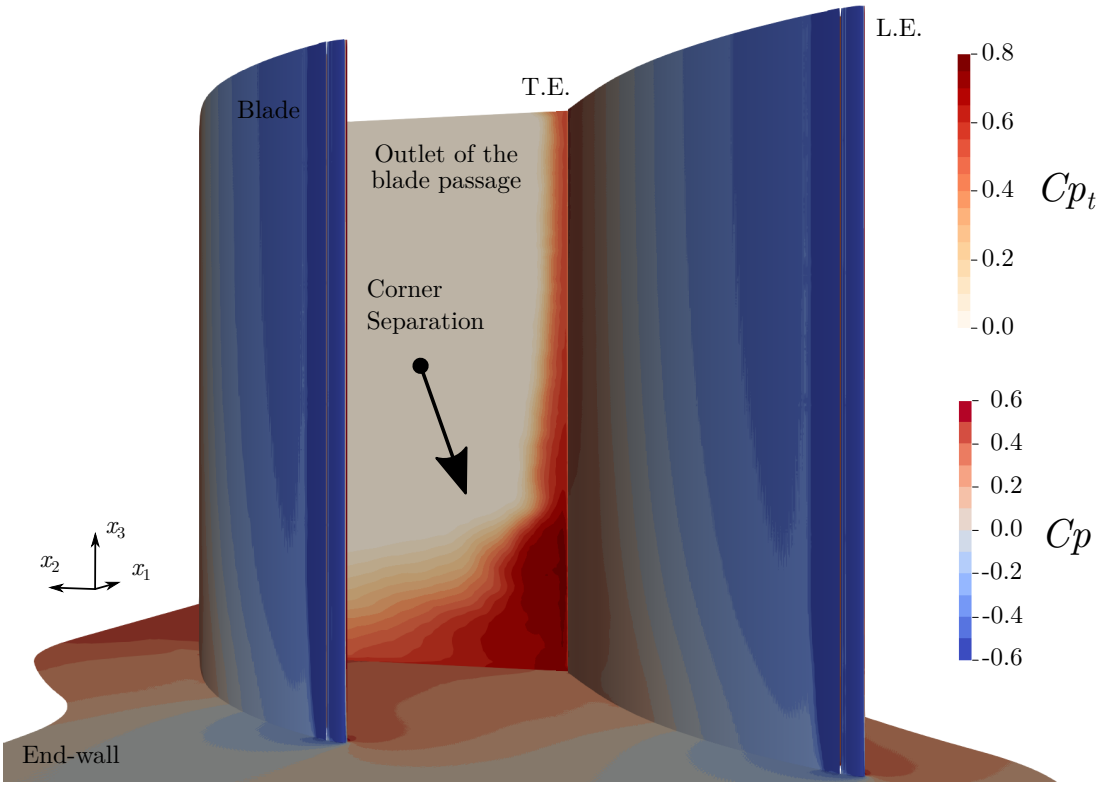

(b) Mean pressure coefficient and mean total pressure coefficient

Figure 7.1: Visualisation of the LES flow field in the corner separation case. (a): instantaneous Q criterion for a constant $Q = 1 \times 10^7 \mathrm{s}^{-2}$. (b): Mean pressure coefficient on the blade and at the end-wall, and mean total pressure coefficient at the outlet of the blade passage. The same scale and colourmap are used for Cp_t in both figures.

the blade boundary-layer and the end-wall boundary-layer. This highly vortical phenomenon can be visualised using the Q criterion, defined as the second invariant of the velocity gradient tensor (Holmén, 2012):

$$Q = \frac{1}{2}\left(\left\|\widetilde{\underline{\underline{\Omega}}}\right\|^2 - \left\|\widetilde{\underline{\underline{S}}}\right\|^2\right) \tag{7.1}$$

with $\widetilde{\underline{\underline{S}}}$ the strain rate tensor defined in equation (2.6), and $\widetilde{\underline{\underline{\Omega}}}$ the vorticity tensor defined as follows:

$$\forall (i,j) \in [\![\ 1\ ;\ 3\ ]\!]^2,\ \widetilde{\Omega}_{ij} = \frac{\partial \widetilde{u}_i}{\partial x_j} - \frac{\partial \widetilde{u}_j}{\partial x_i} \tag{7.2}$$

The criterion is represented for $Q = 1 \times 10^7 \mathrm{s}^{-2}$ in figure 7.1a for an instantaneous snapshot of the flow. The losses are also represented using the mean total pressure loss coefficient, defined as:

$$Cp_t = \frac{p_{te} - p_t}{p_{te} - p_e} \tag{7.3}$$

with p_{te} the inflow total pressure, p_t the local total pressure and p_e the inflow static pressure. The Q criterion compares the magnitude of rotation and strain. A positive Q means that rotation exceeds strain. The value of the criterion is related to the size of the structures. A small value shows large structures, while a large value shows small structures. The criterion shows that the flow is turbulent in the end-wall boundary-layer and on the blade, as expected. The structures are more dense in the area of the corner separation. The maximum of losses, represented by the maximum of the total pressure loss coefficient, is located inside the corner separation.

In figure 7.1b, the mean pressure coefficient is represented at the end-wall and on the blade, along with the mean total pressure loss coefficient at the outlet of the blade passage. The mean pressure coefficient is defined as:

$$Cp = \frac{p - p_e}{\frac{1}{2}\rho u_e^2} \tag{7.4}$$

with p the local static pressure.

In order to gauge the quality of the simulations, the mean pressure coefficient and the mean total pressure coefficient calculated using LES and RANS are compared with the coefficients from the experiment of Zambonini et al. (2017). The pressure coefficient is extracted around the blade at six span-wise positions, and the total pressure loss coefficient is extracted on three planes downstream of the blade passage outlet. The extraction locations are presented in figure 7.2.

7.1.2 Pressure coefficient around the blade

The pressure coefficient $-Cp$ is presented in figure 7.3. The black lines represent the LES, the blue lines represent the RANS simulation with the original Wilcox model, the green lines represent the RANS simulation with the quadratic Wilcox model, and the red lines represent the RANS simulation with the modified Wilcox model. Oscillations are present close to the leading edge in the LES simulation due to the implementation of the tripping bands. The upper branch of the curves represent the suction side, while the lower branch represent the pressure side.

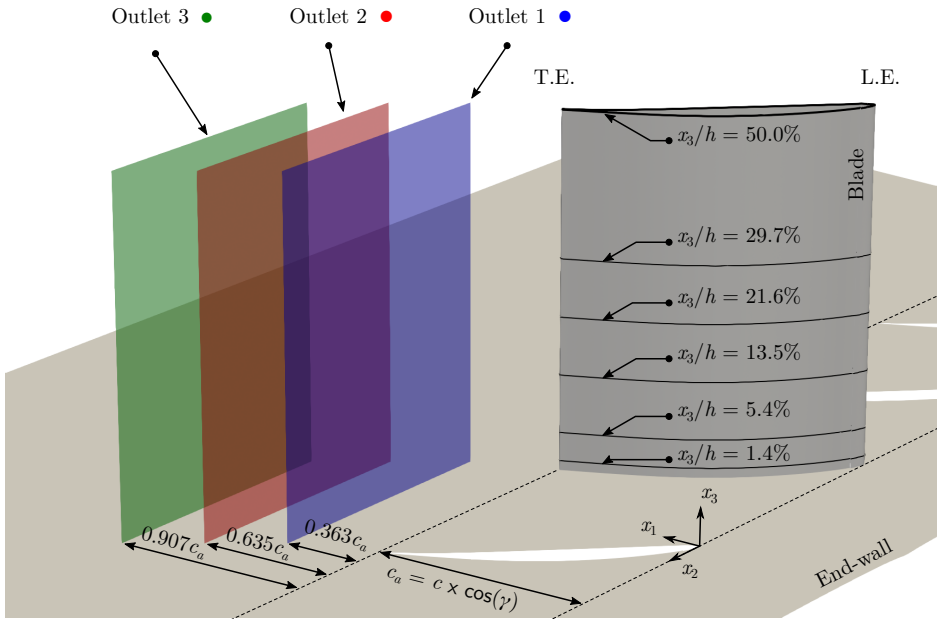

Figure 7.2: Extraction locations for Cp and Cp_t for comparison with the experimental results of Zambonini et al. (2017). The pressure coefficient is extracted on the blade surface at different span-wise positions, and the total pressure coefficient is exctracted on the outlet planes 1 to 3.

At mid span (Fig. 7.3a) and at 30% of span (Fig. 7.3b), all the simulations are consistent. In these areas, the flow is attached to the blade. At 21.6% of the span length (Fig. 7.3c) a difference can be observed between the LES and the RANS_BUA simulation on one side, and the RANS_BSQ and RANS_QCR simulations on the other side. The RANS_BSQ and RANS_QCR simulations present a flattening of the pressure distribution on the suction side for $x_1/c_a \geqslant 0.75$, indicating a thickening of the boundary-layer. This behaviour is even more marked closer to the end-wall, where the corner separation develops (Fig. 7.3d, 7.3d and 7.3d). At these positions, the RANS_BUA becomes less consistent with the LES than before, but stays closer to it than the two other RANS simulations. For all the RANS simulations, the region of quasi-constant Cp (marking the corner separation) is clearly over-estimated. The modification of the Wilcox model has a visible impact, but not sufficient to stick to the LES results when confronted to the corner separation. However, the results are slightly better than with the original Wilcox model or with the quadratic Wilcox model. The impact of the QCR is limited, the RANS_QCR simulation results being almost superimposed with the RANS_BSQ simulation results.

A sudden and important static pressure drop is visible at the trailing edge. This is a known feature of steady simulations, that Denton (2010) explains by the difficulty to capture the separation at the trailing edge. A refined mesh on that case would worsen the prediction, by retarding even more the separation. He suggests to use a coarse mesh with a cusp at the trailing edge in steady calculations to avoid this drop of pressure.

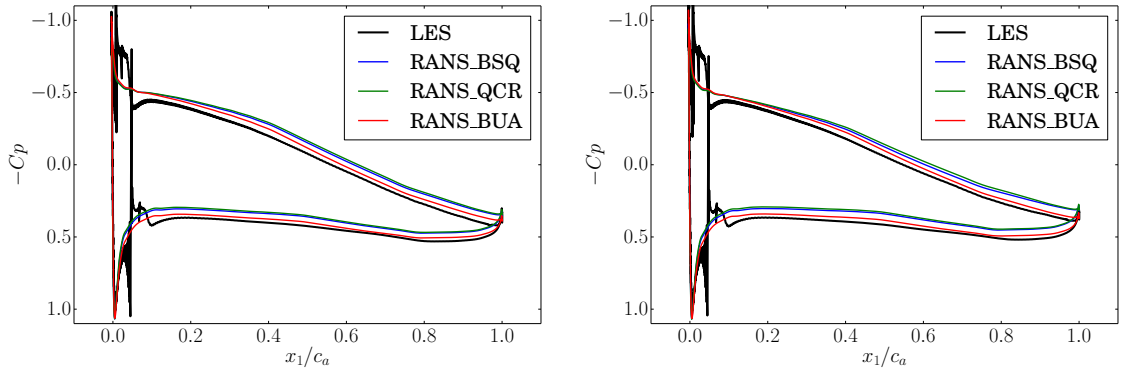

(a) $x_3/h = 50.0\%$

(b) $x_3/h = 29.7\%$

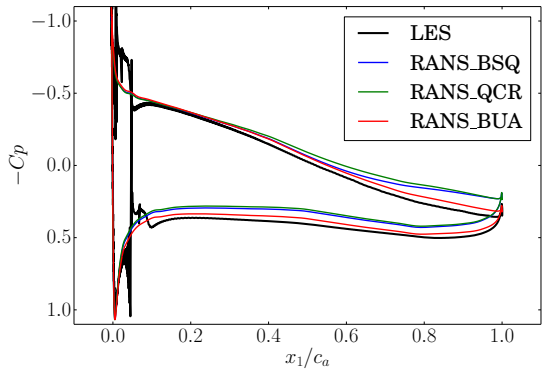

(c) $x_3/h = 21.6\%$

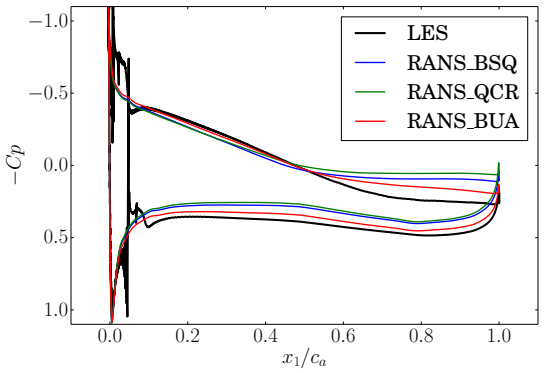

(d) $x_3/h = 13.5\%$

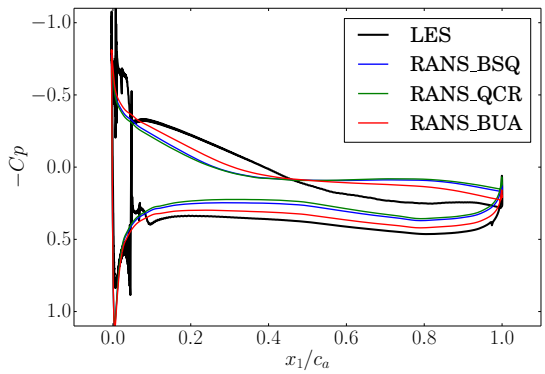

(e) $x_3/h = 5.4\%$

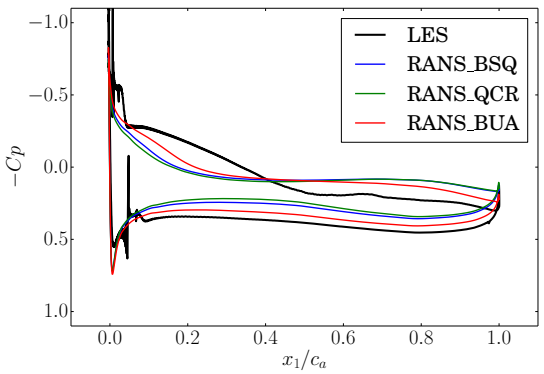

(f) $x_3/h = 1.4\%$

Figure 7.3: Mean static pressure coefficient around the blade at various span-wise positions.

7.1.3 Total pressure coefficient on outlet planes

The total pressure loss coefficients on outlet plane 1 are given in figure 7.4. Experimental pressure losses (Fig. 7.4a) and LES pressure losses (Fig. 7.4b) are very similar. A particular attention was paid to the consistency of the experimental and numerical inlet values (such as boundary layer thickness). The pressure losses results legitimate the usage of LES as a reference. The RANS simulations over-predict the losses in each

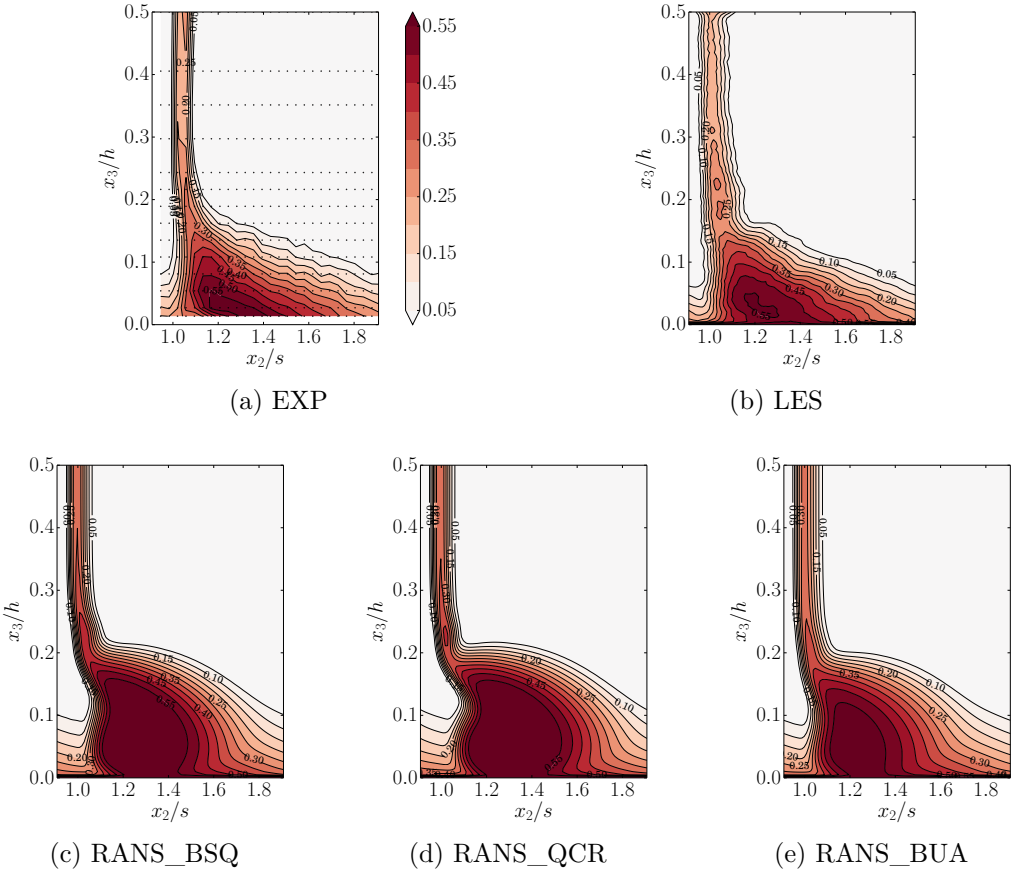

(a) EXP (b) LES

(c) RANS_BSQ (d) RANS_QCR (e) RANS_BUA

Figure 7.4: Mean total pressure loss coefficient on outlet plane 1.

case. The use of a non-linear constitutive relation (QCR) yields almost no effect on the results (Fig. 7.4d) compared to the original Wilcox model (Fig. 7.4c). The use of the modified Wilcox model has a beneficial impact on the intensity of the losses (Fig. 7.4e) compared to the original Wilcox model, but not on the topology or the size of the loss region. The corner separation remains too curvy and too large spatially compared with the experimental or LES results.

The results on the outlet plane 2 (Fig. 7.5) follow the same trends as those on the outlet plane 1. The experiment (Fig. 7.5a) and the LES (Fig. 7.5b) are slightly less alike, but remains very similar. The RANS simulations keep over-predicting the loss intensities (Fig. 7.5c, 7.5d and 7.5e). They also over-predict the size of the region of losses, which is a consequence of the over-prediction of the corner separation size.

The results on the outlet plane 3 follow the same trends as upstream. The shape of the corner separation wake is again triangular for the experiment (Fig. 7.6a) and the LES (Fig. 7.6b), but it is notably twisted in the RANS simulations (Fig. 7.6c, Fig. 7.6d, Fig. 7.6e). This may be due to the more intense separation, and the induced effect on its wake. In term of levels, the RANS with the modified Wilcox model is more comparable to the LES than the two other RANS simulations, as for the planes upstream.

The RANS simulations fail to represent accurately the physics at stakes. The most heavily modelled part in a RANS simulation is the turbulence, and more precisely its effect on the mean flow, with the modelling of the Reynolds stresses. In order to

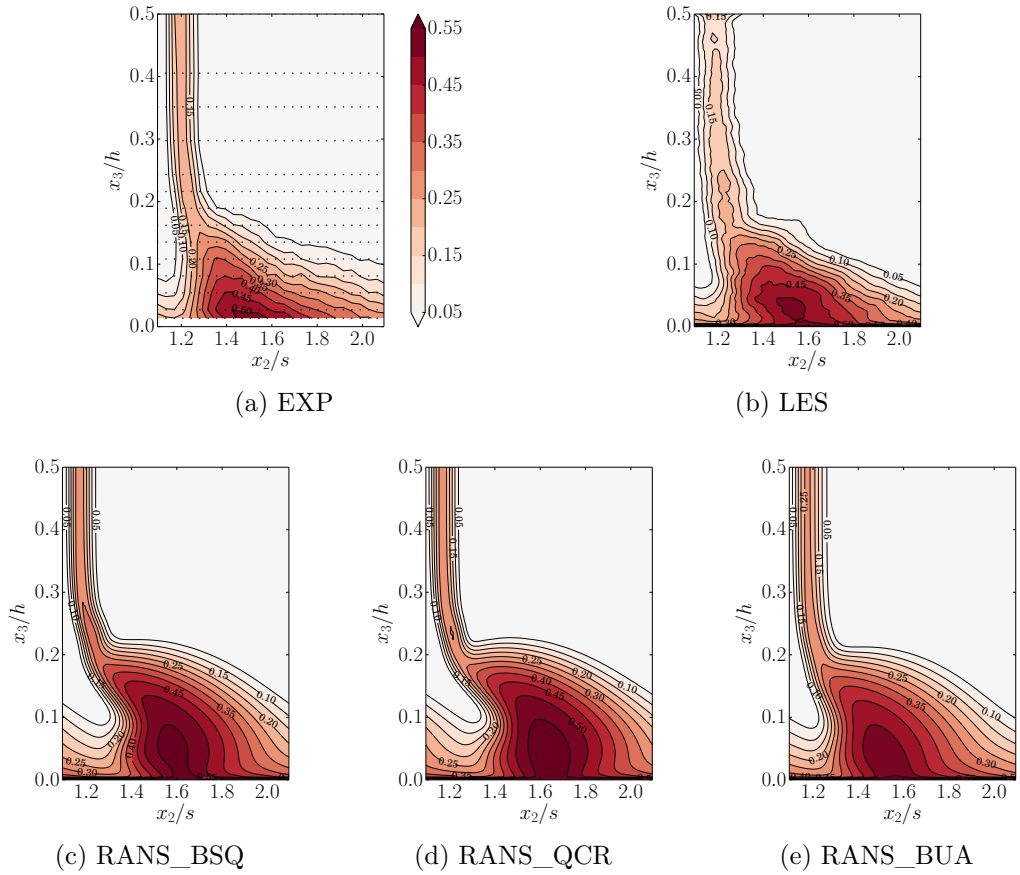

(a) EXP (b) LES

(c) RANS_BSQ (d) RANS_QCR (e) RANS_BUA

Figure 7.5: Mean total pressure loss coefficient on outlet plane 2.

evaluate the validity of such a modelling, the Reynolds stresses computed with the RANS simulations are extracted on various planes and compared with the LES results on the same planes in the following section. Such results are not available from the experiment, but the quality of the LES flow prediction has been demonstrated above.

7.2 Reynolds stress analysis

7.2.1 Extraction planes

The levels and topology of the Reynolds stresses are investigated on 6 different planes, presented in figure 7.7. The first plane is located close to the passage inlet, and normal to the blade, in a region upstream of the corner separation emergence. The point at the junction of the blade and the end-wall is at $x_1/c_a = 0.064$, with $c_a = c \times \cos(\gamma \times \pi/180)$. This plane is referenced as the inlet plane. The second plane is placed through the passage, at x_3 equals two percent of the blade span length. It is referred to as the passage plane. The four last planes are all located at constant x_1, and cover the pitch length s and half the span height. The outlet 0 plane is placed right at the outlet of the passage, and the outlet 1, 2 and 3 planes are placed respectively $0.363c_a$, $0.635c_a$, and $0.907c_a$ downstream. These three last planes are the ones on which the total pressure loss coefficient have been extracted and presented.

Only three planes are presented in the following sections: the inlet plane, the

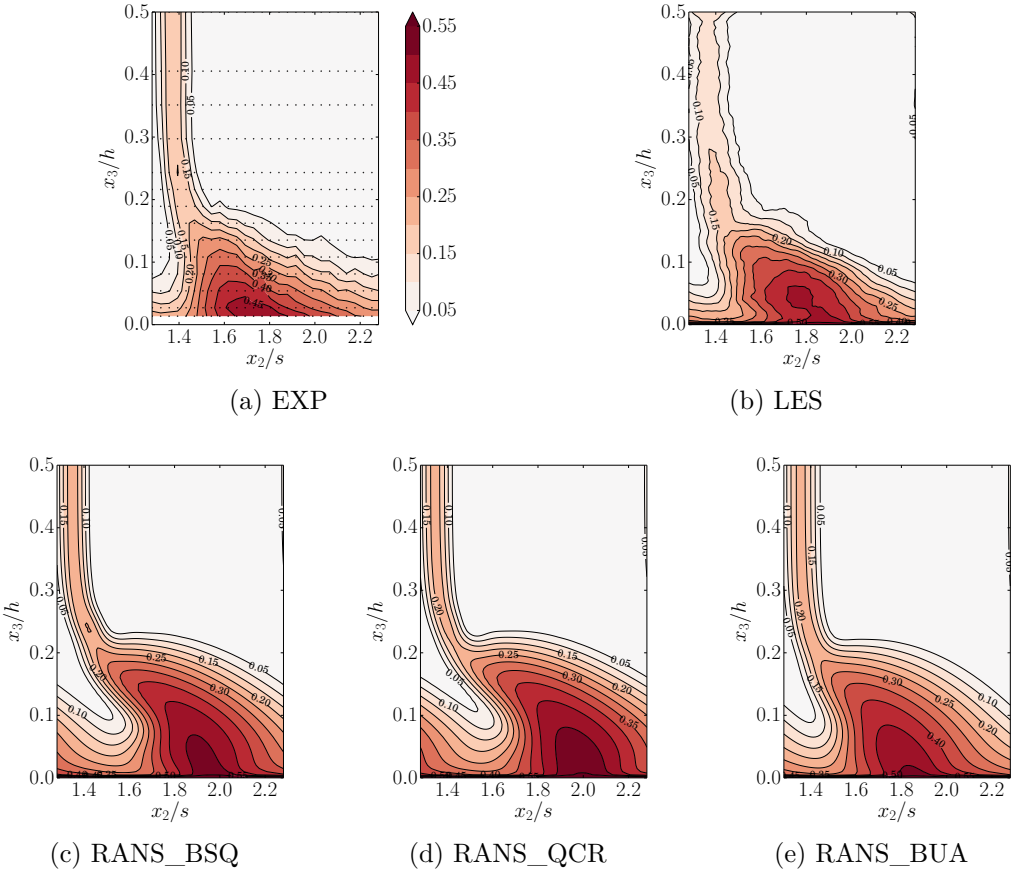

(a) EXP (b) LES

(c) RANS_BSQ (d) RANS_QCR (e) RANS_BUA

Figure 7.6: Mean total pressure loss coefficient on outlet plane 3.

passage plane, and the outlet 1 plane. The three other outlet planes present the same physical behaviour as on the outlet 1 plane. Nevertheless, the results are available in appendix C.

7.2.2 On the inlet plane

Normal stresses

The normal stresses at the inlet are given in figures 7.8, 7.9 and 7.10. Two distinct regions can be seen on each LES figure (Fig. 7.8a, 7.9a and 7.10a). First, very close to the blade ($d/s \approx 0$, with d the distance to the wall), where the normal stresses are important, is the blade boundary layer. Secondly, represented by the horizontal stratification of the Reynolds stresses, is the end-wall boundary layer. This boundary-layer is thicker than the blade one. A bubble of high intensity of the Reynolds stresses can be found close to the corner, around $d/s = 0.025$ and $x_3/h = 0.005$.

In the three figures, the RANS with the original Wilcox model mis-predicts the extent and intensity of the normal Reynolds stresses in the area of the blade boundary-layer. For τ_{t11} (Fig. 7.8b), the area is thicker and less intense than in LES, while for τ_{t22} (Fig. 7.9b) the area of high intensity is detached from the blade. For τ_{t33} (Fig. 7.10b), the intense region in the corner is wider than in LES. The QCR corrects the size of the area for τ_{t11} (Fig. 7.8b) but not the intensity. It corrects both the size and the intensity for τ_{t22} (Fig. 7.9b), but the area is still detached from the blade. Its action

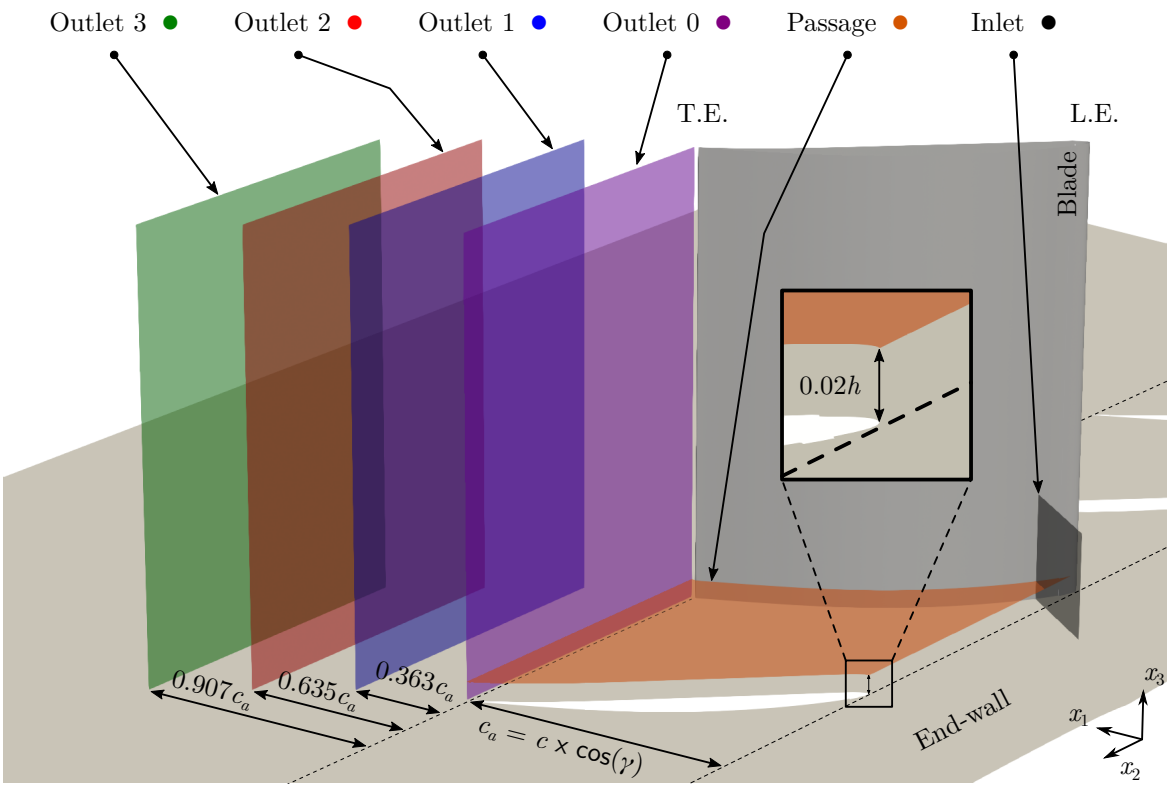

Figure 7.7: Extraction locations for the Reynolds stresses and the TKE budget.

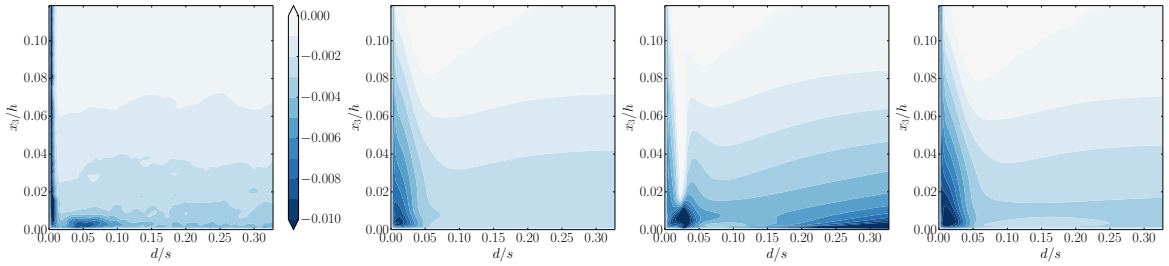

(a) LES (b) RANS_BSQ (c) RANS_QCR (d) RANS_BUA

Figure 7.8: τ_{t11} on the inlet plane, normalised by ρu_e^2.

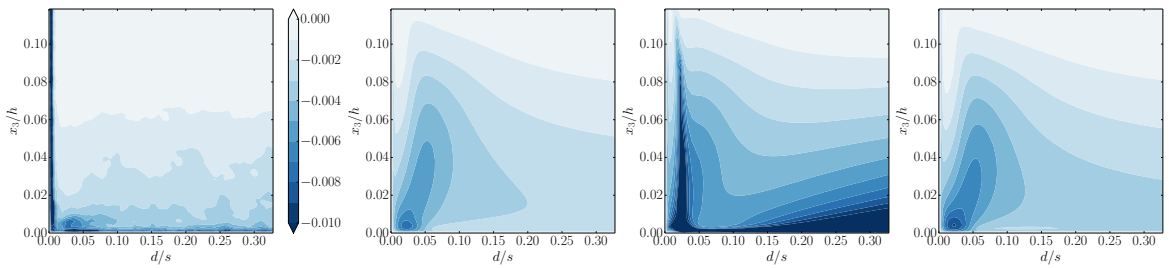

(a) LES (b) RANS_BSQ (c) RANS_QCR (d) RANS_BUA

Figure 7.9: τ_{t22} on the inlet plane, normalised by ρu_e^2.

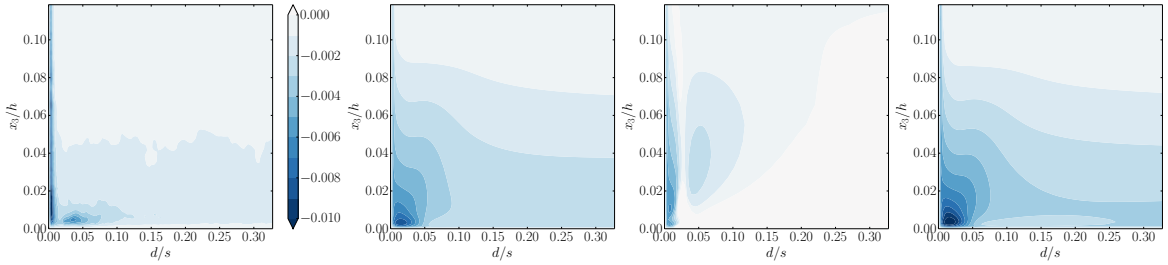

(a) LES (b) RANS_BSQ (c) RANS_QCR (d) RANS_BUA

Figure 7.10: τ_{t33} on the inlet plane, normalised by ρu_e^2.

on τ_{t33} (Fig. 7.10b) is negligible concerning the area in the blade boundary layer, but the corner region is reduced. The modified Wilcox model shows results similar to the original Wilcox model. For the three normal Reynolds stresses (Figs. 7.8d, 7.9d and 7.10d), the topology is the same. The stresses are slightly more intense than with the original Wilcox model, and closer to the LES intensities.

RANS with the original Wilcox model is quite correct with the τ_{t11} representation in the end-wall boundary layer, missing only a few layers close to end-wall, but shows an area highly twisted for τ_{t22} and thicker and more intense for τ_{t33}. The QCR corrects the number of layers and the intensity for τ_{t11}, but increase too much the intensity of τ_{t22} and decreases too much the intensity of τ_{t33} in the end-wall boundary layer compared to the LES. The modified Wilcox model shows again results similar to the original Wilcox model.

Concerning the bubble of stresses in the corner, the three RANS simulations predict its existence. The quadratic Wilcox model gives results more comparable to the LES concerning the position, the size of the area and the intensity than the original Wilcox model or the modified Wilcox model, which appear to overestimate this region.

Shear stresses

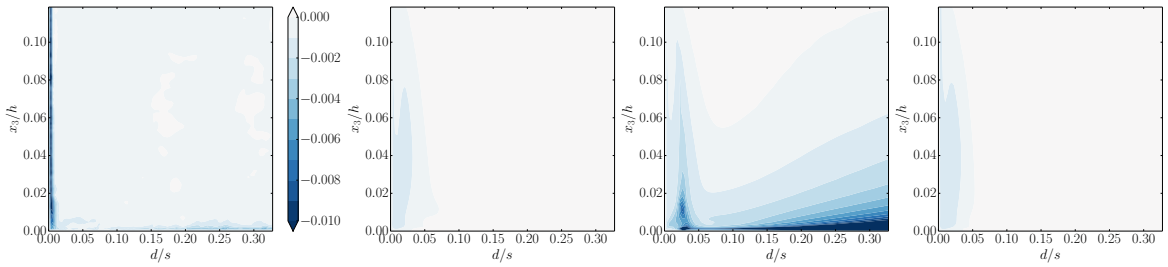

(a) LES (b) RANS_BSQ (c) RANS_QCR (d) RANS_BUA

Figure 7.11: τ_{t12} on the inlet plane, normalised by ρu_e^2.

The shear stresses at the inlet are given in figures 7.11, 7.12 and 7.13. The different areas visible in the LES results (Fig. 7.11a, 7.12a and 7.13a) are the same as those previously described for the normal stresses.

The RANS with the original, the quadratic and the modified Wilcox models all mis-predict the extent and the intensity of the shear Reynolds stresses in the area of the blade boundary layer. For the three shear stresses (Fig. 7.11b, 7.12b and 7.13b),

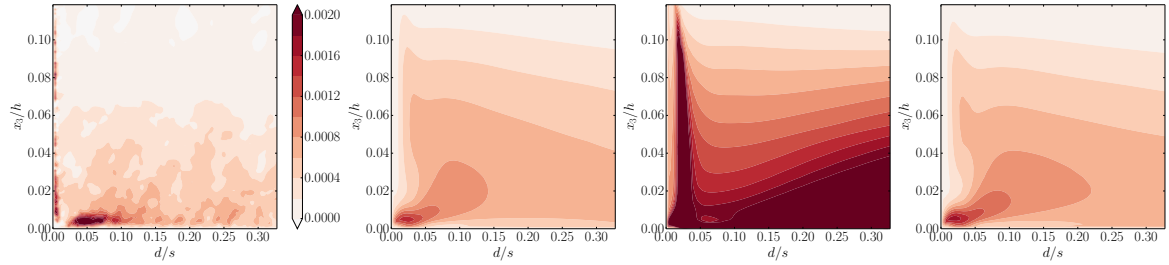

(a) LES (b) RANS_BSQ (c) RANS_QCR (d) RANS_BUA

Figure 7.12: τ_{t13} on the inlet plane, normalised by ρu_e^2.

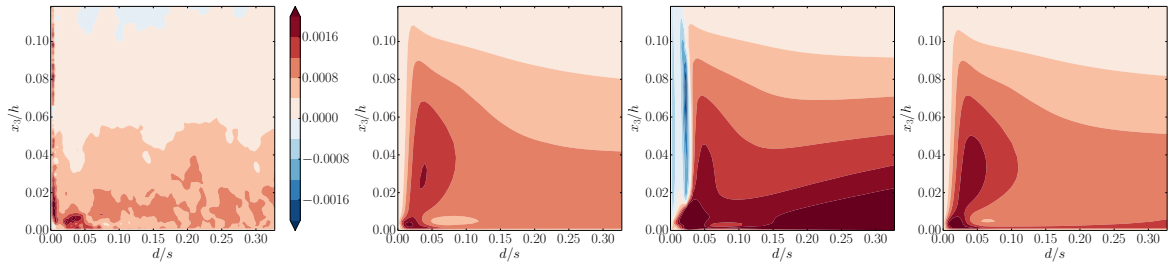

(a) LES (b) RANS_BSQ (c) RANS_QCR (d) RANS_BUA

Figure 7.13: τ_{t23} on the inlet plane, normalised by ρu_e^2.

the RANS with the original Wilcox model under-predicts the intensity. This may be due to the weak anisotropy in the Boussinesq constitutive relation. The similarity of the results with the modified Wilcox model, that relies on the same constitutive relation, confirms this idea. On the opposite, the RANS with the quadratic Wilcox model over-predicts the size of the area and the intensity of τ_{t13} (Fig. 7.12c). This is certainly due to the increased anisotropy of the QCR, but with a too important intensity. It yields less important modifications on the two other stresses (Fig. 7.11c and 7.13c). Finally, a remarkable feature is observed for the three RANS models on τ_{t13} and τ_{t23}: the region of high intensity is detached from the wall. This is a well known drawback of RANS models around the leading edge of airfoils.

The intensity of the stresses in the area of the end-wall boundary layer is correctly represented by the two RANS with the Boussinesq constitutive relation, but over-predicted by the RANS with the QCR for each stress.

Concerning the bubble of Reynolds stresses in the corner, the three RANS simulations predict its existence. However, it is correctly represented only by the RANS with the original and modified Wilcox models, that rely on the Boussinesq constitutive relation, and over-predicted by the RANS with the quadratic Wilcox model, that relies on the QCR, compared to LES. This is opposite to the observations on the normal stresses.

7.2.3 On the passage plane

Normal stresses

The normal Reynolds stresses on the passage plane are given in figures 7.14, 7.15 and 7.16. On the LES results (Fig. 7.14a, 7.15a and 7.16a), three areas are visible. First,

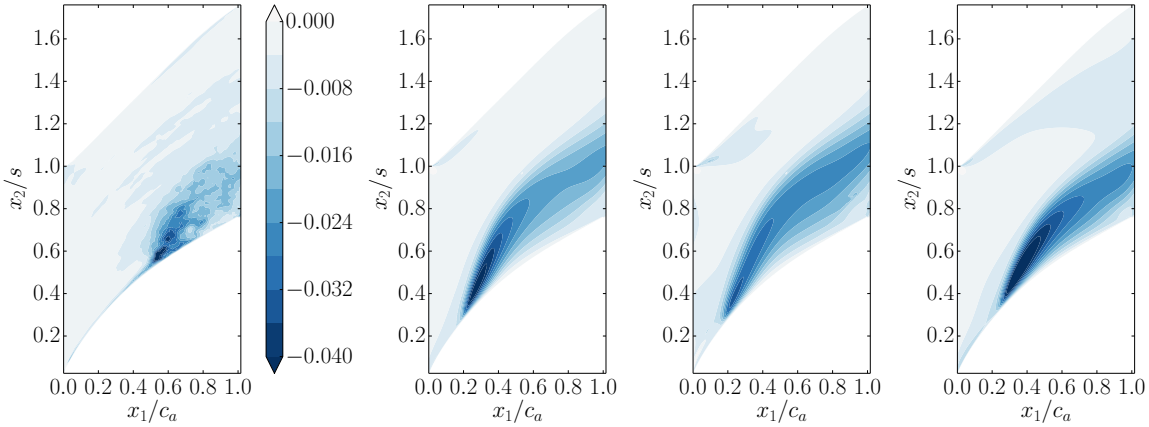

(a) LES (b) RANS_BSQ (c) RANS_QCR (d) RANS_BUA

Figure 7.14: τ_{t11} on the passage plane, normalised by ρu_e^2.

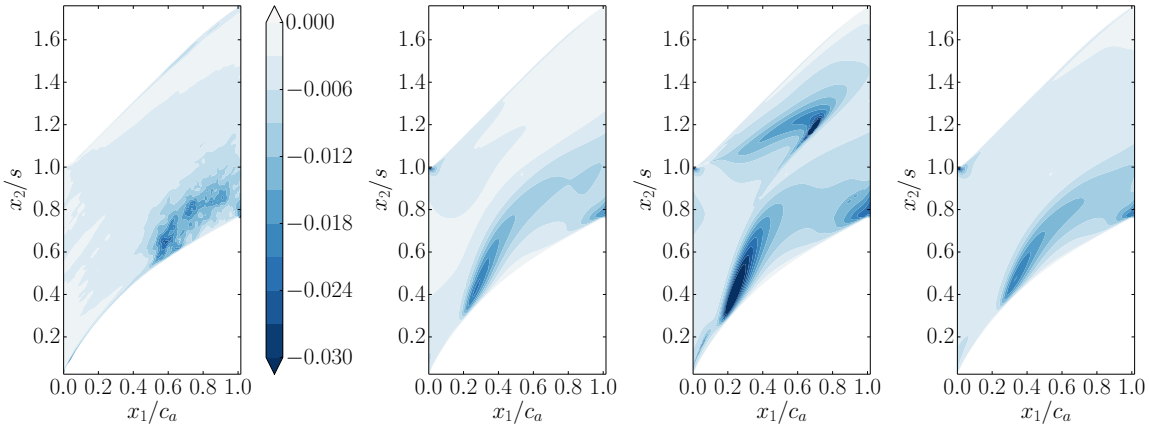

(a) LES (b) RANS_BSQ (c) RANS_QCR (d) RANS_BUA

Figure 7.15: τ_{t22} on the passage plane, normalised by ρu_e^2.

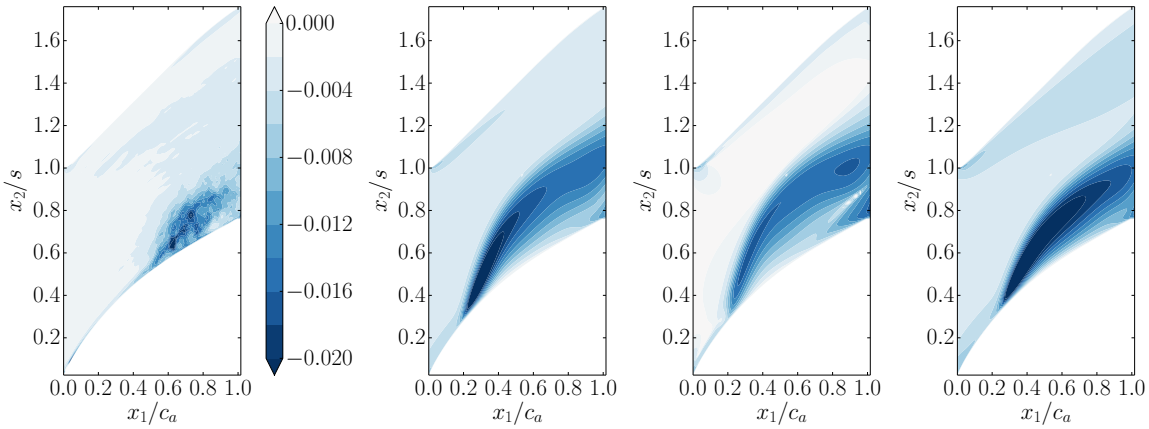

(a) LES (b) RANS_BSQ (c) RANS_QCR (d) RANS_BUA

Figure 7.16: τ_{t33} on the passage plane, normalised by ρu_e^2.

the area of the boundary-layer development on the suction side, for $x_1/c_a \leqslant 0.4$ and $x_2/s \leqslant 0.4$, where the stresses are important only close to the wall. Then, the area of the corner separation, for $x_1/c_a \in [0.4, 1.0]$ and $x_2/s \in [0.4, 0.8]$, characterized by the high intensity of the normal Reynolds stresses. Last, the area close to the pressure side wall, for $x_2/s \in [0.8, 1.6]$, where the normal Reynolds stresses are weak.

The RANS with the original Wilcox model (Fig. 7.14b, 7.15b and 7.16b), the RANS with the quadratic Wilcox model (Fig. 7.14c, 7.15c and 7.16c), and the RANS with the modified Wilcox model (Fig. 7.14d, 7.15d and 7.16d) over-predict the extent of the Reynolds stresses in the area of the suction side boundary layer development. They all anticipate the separation point, putting it closer to the leading edge, around $x_1/c_a \approx 0.2$ and $x_2/s \approx 0.3$. The RANS with the modified Wilcox model shows a separation point slightly downstream (around $x_1/c_a \approx 0.25$ and $x_2/s \approx 0.35$) compared with the two other RANS, but the difference is not significant enough to yield results comparable with LES ($x_1/c_a \approx 0.5$ and $x_2/s \approx 0.5$).

The intensity of τ_{t11} and τ_{t33} in the corner separation is over-predicted by the two RANS with the Boussinesq constitutive relation and correctly predicted by the QCR. τ_{t22} intensity in the corner separation is correctly predicted by the two RANS with the Boussinesq constitutive relation but the QCR correction over-predicts it.

Close to the pressure side wall, the three RANS simulations represent correctly the normal stresses, except for the important over-prediction of τ_{t22} by the RANS with the quadratic Wilcox model (Fig. 7.15c, for $x_1/c_a = 0.7$ and $x_2/s = 1.1$).

Shear stresses

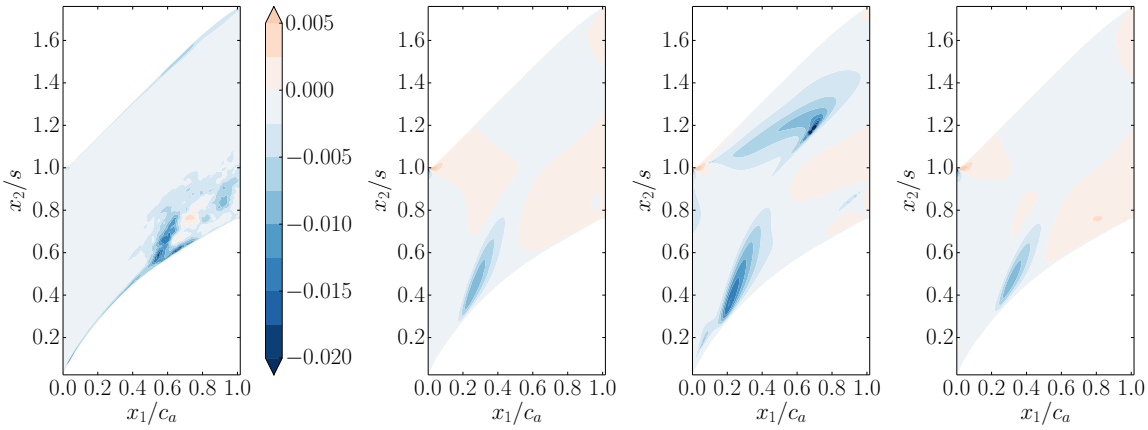

(a) LES (b) RANS_BSQ (c) RANS_QCR (d) RANS_BUA

Figure 7.17: τ_{t12} on the passage plane, normalised by ρu_e^2.

The shear Reynolds stresses on the passage plane are given in figures 7.17, 7.18 and 7.19. The different areas visible in the LES results (Fig. 7.17a, 7.18a and 7.19a) are the same as those previously identified for the normal Reynolds stresses.

Due to the misplacement of the separation point in the RANS simulations (original Wilcox: fig. 7.17b, 7.18b and 7.19b, quadratic wilcox: fig. 7.17c, 7.18c and 7.19c, modified Wilcox: fig. 7.17d, 7.18d and 7.19d), the area of maximal stresses in the corner separation is closer to the leading edge, compared with the LES. The topology of this area is different from the one obtained with LES. The area is more elongated

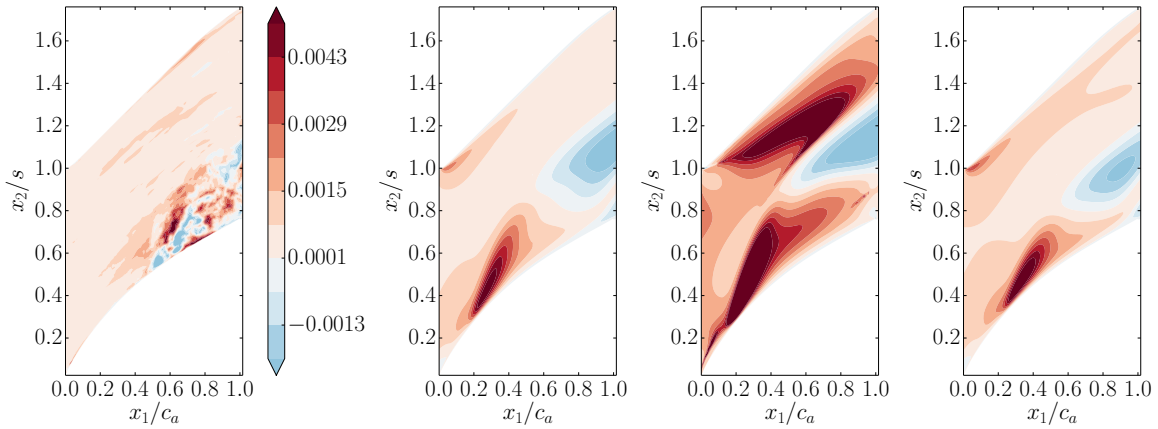

(a) LES (b) RANS_BSQ (c) RANS_QCR (d) RANS_BUA

Figure 7.18: τ_{t13} on the passage plane, normalised by ρu_e^2.

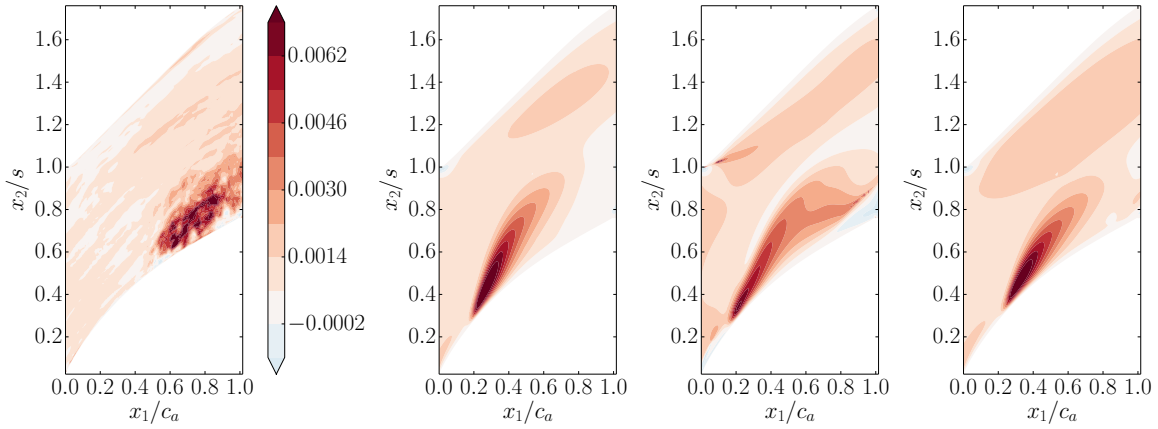

(a) LES (b) RANS_BSQ (c) RANS_QCR (d) RANS_BUA

Figure 7.19: τ_{t23} on the passage plane, normalised by ρu_e^2.

and develops away from the wall. The intensity of the stresses in the corner separation is correctly represented by the two RANS with the Boussinesq constitutive relation. τ_{t23} is under-predicted while τ_{t13} is over-predicted by the RANS with QCR.

Close to the pressure side wall, the RANS with QCR creates an area of high intensity, non-existent in the two other RANS simulations and in the LES. This area is particularly intense for τ_{t23}.

7.2.4 On outlet 1

Normal stresses

The normal Reynolds stresses at the outlet section 1 are given in figures 7.20, 7.21 and 7.22. Two zones are visible on the LES results (Fig. 7.20a, 7.21a and 7.22a), the wake of the blade boundary-layer ($x_2/s \in [1.0, 1.1]$, $x_3/h \in [0.2, 0.5]$) and the wake of the corner separation ($x_2/s \in [0.9, 1.5]$, $x_3/h \in [0.0, 0.2]$).

For the three components, the intensity in the wake of the blade is under-predicted by RANS when $x_3/h \geqslant 0.3$, compared to the LES.

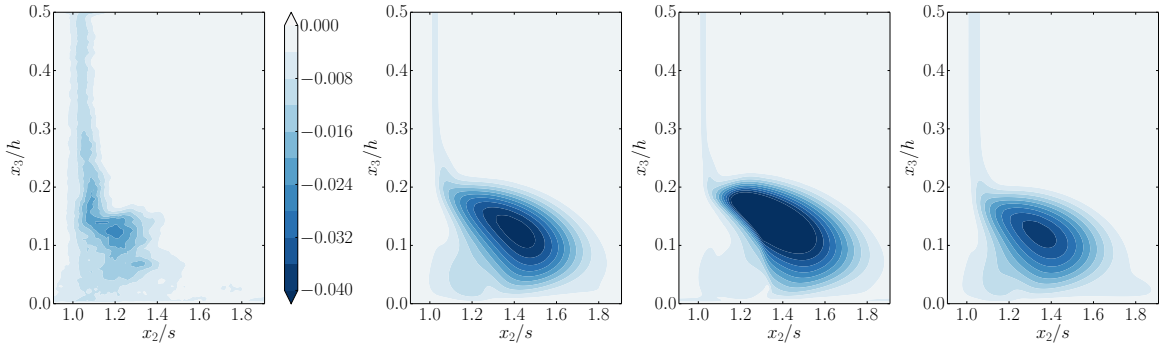

(a) LES (b) RANS_BSQ (c) RANS_QCR (d) RANS_BUA

Figure 7.20: τ_{t11} on the plane outlet 1, normalised by ρu_e^2.

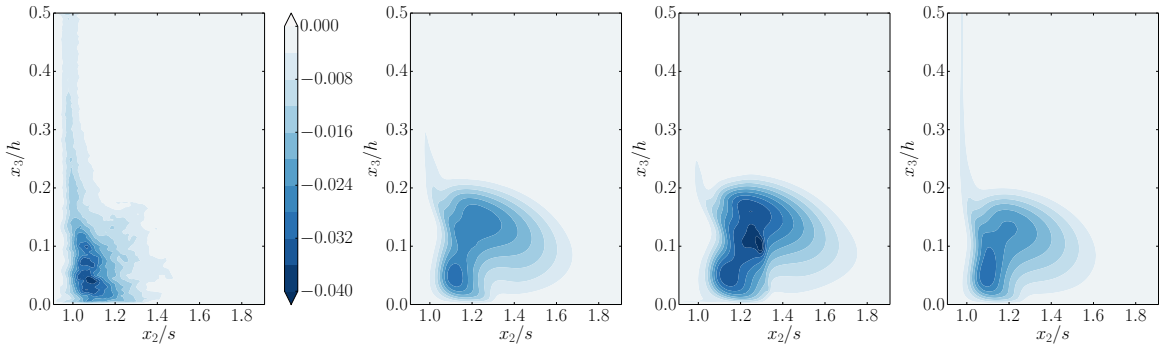

(a) LES (b) RANS_BSQ (c) RANS_QCR (d) RANS_BUA

Figure 7.21: τ_{t22} on the plane outlet 1, normalised by ρu_e^2.

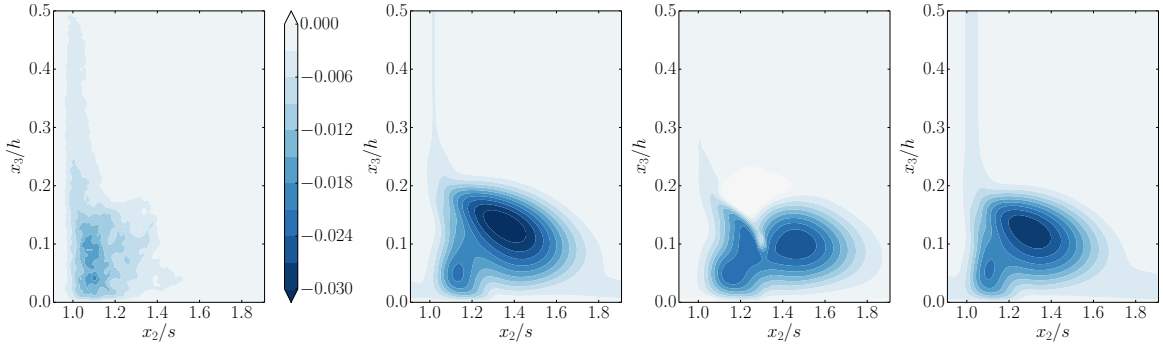

(a) LES (b) RANS_BSQ (c) RANS_QCR (d) RANS_BUA

Figure 7.22: τ_{t33} on the plane outlet 1, normalised by ρu_e^2.

In the wake of the corner separation, the RANS simulations mis-predict the intensity of the normal Reynolds stresses compared to LES, by over-predicting τ_{t11} and τ_{t33}, and under-predicting τ_{t22}. For each component, the RANS wake areas are also wider and further from the wake of the blade than for the LES. The QCR increases the intensity of the first and second normal Reynolds stress (τ_{t11} and τ_{t22}) but decreases it for the third one (τ_{t33}). For the first two components, the effect of the QCR is small. For τ_{t33} (Fig. 7.22), the minimum of the stress calculated with the QCR is more

comparable to the LES than the minimum calculated with the other RANS simulations. The modified Wilcox model (Fig. 7.20d, 7.21d and 7.22d) yields results that are similar to the original Wilcox model for each normal Reynolds stress, with a small modification that each time goes in the right direction. However, the modification is never sufficient to get close to the LES results.

Shear stresses

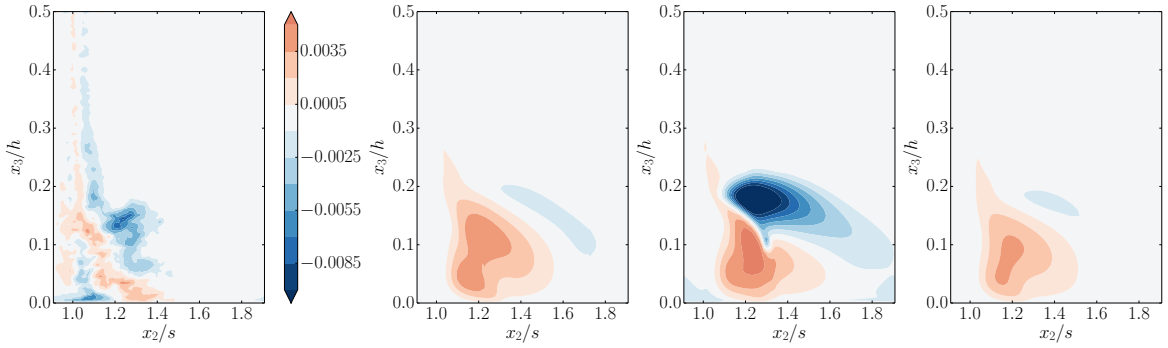

(a) LES (b) RANS_BSQ (c) RANS_QCR (d) RANS_BUA

Figure 7.23: τ_{t12} on the plane outlet 1, normalised by ρu_e^2.

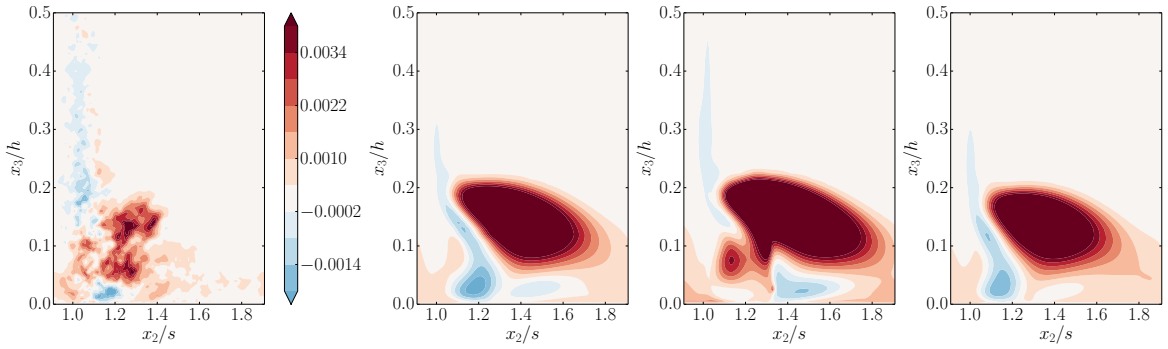

(a) LES (b) RANS_BSQ (c) RANS_QCR (d) RANS_BUA

Figure 7.24: τ_{t13} on the plane outlet 1, normalised by ρu_e^2.

The shear Reynolds stresses on the outlet 1 plane are given in figures 7.23, 7.24 and 7.25. The different areas visible in the LES results (Fig. 7.23a, 7.24a and 7.25a) are the same as those previously identified for the normal Reynolds stresses.

For the three components, the intensity in the wake of the blade is again under-predicted by RANS when $x_3/h \geqslant 0.3$, compared to the LES.

The RANS simulations mis-predict again the size and the intensity of the Reynolds stresses compared to LES. For τ_{t12}, contrary to the tendency for the normal stresses, the RANS simulations with the original Wilcox model (Fig. 7.23b) and the modified Wilcox model (Fig. 7.23d) under-predict the intensity of the stress compared to the LES (Fig. 7.23a). The quadratic Wilcox model corrects this behaviour by increasing the intensity of the stress (Fig. 7.23d) beyond the LES value. For τ_{t13} and τ_{t23} (Fig. 7.24 and 7.25), the two RANS with the Boussinesq constitutive relation over-predict the

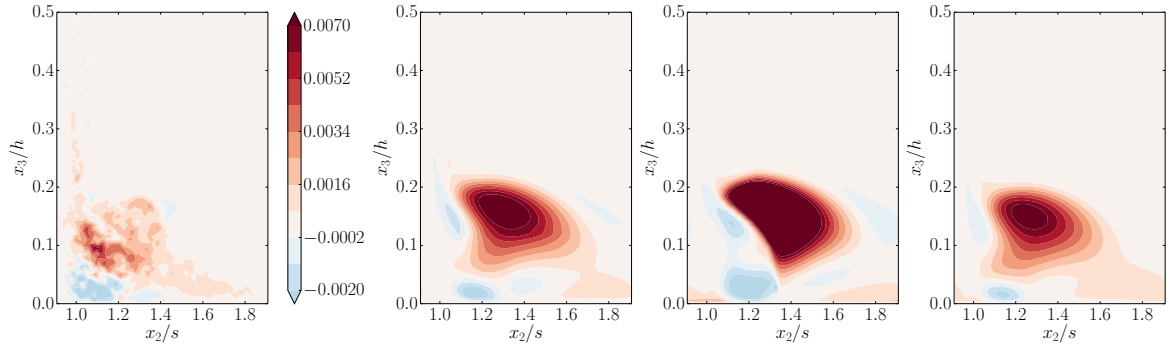

(a) LES (b) RANS_BSQ (c) RANS_QCR (d) RANS_BUA

Figure 7.25: τ_{t23} on the plane outlet 1, normalised by ρu_e^2.

stresses compared to the LES. The over-prediction is slightly less important with the modified Wilcox model. The quadratic Wilcox model further increases the intensity of the stresses, but yields almost no effect on the position of their maximum.

7.3 Partial conclusion

The LES demonstrates its capacity to be used as reference when compared with experimental results.

For the mean flow values, such as the wall static pressure coefficient or the total pressure loss coefficient, none of the RANS simulations were able to yield results comparable with the experiment or the LES. The modified Wilcox model tends to improve slightly the estimations.

The study of the Reynolds stresses shows that each stress is mis-predicted (either over-predicted or under-predicted) by the RANS simulations, compared with LES. The original and modified Wilcox models, that rely on the Boussinesq constitutive relation, yield comparable results, with slightly better ones for the modified Wilcox model. The quadratic Wilcox model, that uses the QCR, yields results quite different from the two other RANS simulations. However, if the correction goes in the right direction in the major part of the cases, the correction is too intense, mostly on the shear stresses. Moreover, an artificial area of intense shear stresses is generated by the QCR in the passage, between the corner separation and the adjacent blade pressure side. This seems to indicate that in highly vortical areas with moderate Reynolds stresses, the QCR term depending on the normalised rotation tensor is dominant and much more important than the Reynolds stress tensor from the Boussinesq constitutive relation. The impact of the vorticity is too important on the correction.

The modelling of the Reynolds stresses bears the joint effect of the constitutive relation used and the eddy-viscosity modelling, with the use of equations on k and ω. The following chapters aim at inspecting the validity of the constitutive relation and the validity of the k equation.

Chapter 8

Corner separation constitutive relation analysis

Sections

The comparison between the LES Reynolds stresses and the RANS Reynolds stresses in the previous chapter lead to the conclusion that the turbulence modellings on which the RANS simulations rely do not accurately predict the physics. The present chapter tackles the analysis of turbulence modelling, through one of its two main components, the constitutive relation. LES is used as reference to test the validity of the two hypotheses of the constitutive relations studied (Boussinesq constitutive relation and QCR): the tensor alignment hypothesis and the turbulent viscosity estimate (proportionality coefficient).

8.1 Evaluation methods

8.1.1 Constitutive relation alignment

Boussinesq constitutive relation

The Boussinesq constitutive relation, presented in equation (2.49), relies on the hypothesis of alignment of two tensors. This hypothesis can be written, in its tensorial form, as:

$$\underline{\underline{\tau}}_t^* + \frac{2}{3}\langle\rho\rangle[k]\,\underline{\underline{I_3}} = \mu_t\left[\underline{\underline{\sigma}}\right] \tag{8.1}$$

with $\underline{\underline{I_3}}$ the identity tensor and $\left[\underline{\underline{\sigma}}\right]$ the mean zero-trace strain rate tensor.

In LES, both the Reynolds stress tensor, noted $\underline{\underline{\tau_t}}$ and the mean zero-trace strain rate tensor, noted $[\underline{\underline{\widetilde{\sigma}}}]$ are known independently, so the alignment hypothesis can be tested. The alignment between the tensors is measured using an indicator similar to Schmitt's indicator (Schmitt, 2007), introduced in equation (2.50). The main disadvantage of Schmitt's indicator is its incapacity to discriminate between aligned and anti-aligned tensors. Two tensors are said anti-aligned if they are aligned with opposite directions. An example of anti-aligned vectors is given in figure 8.1. The following indicator, which corresponds to Schmitt's indicator without the absolute value, is preferred:

$$\Upsilon = \frac{\underline{\underline{\tau_t^{**}}} : \left[\underline{\underline{\widetilde{\sigma}}}\right]}{\left\|\underline{\underline{\tau_t^{**}}}\right\| \left\| \left[\underline{\underline{\widetilde{\sigma}}}\right] \right\|} \tag{8.2}$$

with $\underline{\underline{\tau_t^{**}}}$ the Reynolds stress tensor plus $2[\widetilde{k}]/3$ on the diagonal:

$$\underline{\underline{\tau}}_t^{**} = \underline{\underline{\tau}}_t + \frac{2}{3}\langle\overline{\rho}\rangle\left[\widetilde{k}\right] \tag{8.3}$$

with $[\widetilde{k}] = 1/2\tau_{tii}/ < \overline{\rho} >$. As for Schmitt's one, when this indicator is equal to 1, the tensors are aligned, *ergo* proportional, and the Boussinesq hypothesis is valid. When this indicator is equal to 0, the tensors are orthogonal, and the Boussinesq hypothesis is invalid. Contrary to Schmitt's one, this indicator can be negative. In this case, the tensors are anti-aligned, which means that using the Boussinesq constitutive relation would yield non-physical results. The same threshold of 0.86 is kept. If the indicator is greater than 0.86, the alignment hypothesis is considered valid. An illustration is given in figure 8.1, for vectors in place of tensors.

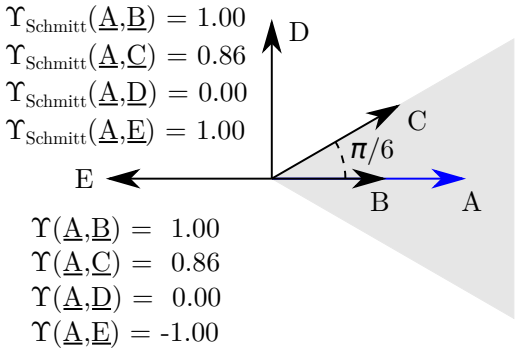

Figure 8.1: Illustration of the tensor alignment criterion. The grey cone represents the area where the Boussinesq constitutive relation is considered valid.

Quadratic constitutive relation

The quadratic constitutive relation (QCR), presented in equation (2.54), relies also on the hypothesis of alignment of two tensors. The Reynolds stress tensor computed

with Boussinesq constitutive relation, present in the second member of the equation, can be developed to yield the following tensorial formulation of the QCR:

$$\underline{\underline{\tau}}_t^{QCR} - \frac{2}{3}\langle\rho\rangle[k]\,\underline{\underline{I_3}} = \mu_t\left(\left[\underline{\underline{\sigma}}\right] + c_{QCR}(\left[\underline{\underline{\sigma}}\right]\underline{\underline{O}} - \underline{\underline{O}}\left[\underline{\underline{\sigma}}\right])\right) \tag{8.4}$$

with $\underline{\underline{O}}$ the normalised rotation tensor introduced in equation (2.55).

The indicator previously introduced is adapted to the QCR as follows:

$$\Upsilon^{QCR} = \frac{\underline{\underline{\tau_t^{**}}} : \left[\underline{\underline{\sigma^{QCR*}}}\right]}{\left\|\underline{\underline{\tau_t^{**}}}\right\| \left\|\left[\underline{\underline{\sigma^{QCR*}}}\right]\right\|} \tag{8.5}$$

with:

$$\left[\underline{\underline{\sigma^{QCR*}}}\right] = \left[\underline{\underline{\widetilde{\sigma}}}\right] + c_{QCR}(\left[\underline{\underline{\widetilde{\sigma}}}\right]\underline{\underline{\widetilde{O}}} - \underline{\underline{\widetilde{O}}}\left[\underline{\underline{\widetilde{\sigma}}}\right]) \tag{8.6}$$

8.1.2 Turbulent viscosities

The turbulent viscosity represents the proportionality coefficient between the Reynolds stress tensor and the constitutive relation tensor (*i.e.* $\left[\underline{\underline{\widetilde{\sigma}}}\right]$ for the Boussinesq constitutive relation and $\left[\underline{\underline{\sigma^{QCR*}}}\right]$ for the QCR). Given the LES data available, a first approach is to reconstruct an turbulent viscosity as the ratio of the tensor norms:

$$\mu_t^{(0)} = \frac{\left\|\underline{\underline{\tau_t^{**}}}\right\|}{\left\|\left[\underline{\underline{\widetilde{\sigma}}}\right]\right\|} \;;\; \mu_t^{(0)QCR} = \frac{\left\|\underline{\underline{\tau_t^{**}}}\right\|}{\left\|\left[\underline{\underline{\sigma^{QCR*}}}\right]\right\|} \tag{8.7}$$

If the tensors are aligned, *i.e.* $\Upsilon = 1.0$ (resp. $\Upsilon^{QCR} = 1.0$), this value is the turbulent viscosity that verifies the Boussinesq constitutive relation (resp. QCR).

This proportionality coefficient is homogeneous, for the considered RANS k–ω models to:

$$\mu_t^{(1)} = \langle\overline{\rho}\rangle\,\frac{\left[\widetilde{k}\right]}{\left[\widetilde{\omega}\right]} \tag{8.8}$$

This second estimate of μ_t can also be computed from the LES results with $[\widetilde{\omega}] = [\widetilde{\varepsilon}]([\widetilde{k}]C_\mu)^{-1}$, $C_\mu = 0.09$ a constant, and $[\widetilde{\varepsilon}]$ derived from the turbulent kinetic energy budget equation (2.36) as:

$$\langle\overline{\rho}\rangle\,[\widetilde{\varepsilon}] = \underbrace{\left\langle\overline{\tau_{ik}}\frac{\partial u_i''}{\partial x_k}\right\rangle}_{\text{Viscous dissipation}} + \underbrace{\left\langle\overline{\Pi_{ik}}\frac{\partial u_i''}{\partial x_k}\right\rangle}_{\text{SGS dissipation}} \tag{8.9}$$

8.2 Alignment analysis

The alignment is gauged with the Υ indicator (resp. Υ^{QCR} indicator) presented in equation (8.2) (resp. (8.5)), plotted as probability density functions (PDF) and cumulative distribution functions (CDF) of the indicator value. Concerning the PDF (for instance, in Fig. 8.3a), there are two sets of bars, a left black bar with a right green bar for each value. A couple of bars occupies a range of 0.05. The black one (resp.

green one) represents the mass weighted percentage of points with Υ (resp. Υ^{QCR}) in the given 0.05 range. Concerning the CDF (for instance in Fig. 8.3b), the integration of the PDF is made from -1 upward, so practically, the ordinate corresponding to the abscissa $\Upsilon = 0.86$ (resp. $\Upsilon^{QCR} = 0.86$) represents the mass weighted percentage of points for which the Boussinesq constitutive relation (resp. QCR) is not valid.

The analysis is focused on the regions where turbulence is significant. Only the points where the turbulence rate (defined as $(2/3[\widetilde{k}]/([\widetilde{u_i}][\widetilde{u_i}]))^{1/2}$) is superior to 5% participate to the PDF and CDF. This value is chosen so that the corner separation wake and the blade wake are included in the analysis. In order to be grid independent, each point considered is weighted by its mass, calculated as the square root of the Jacobian at that point (homogeneous to a volume) times the density. The analysis focuses first on the entire domain, which includes the inlet domain, passage domain and outlet domain, as presented in figure 8.2. Then, each individual domain is analysed separately.

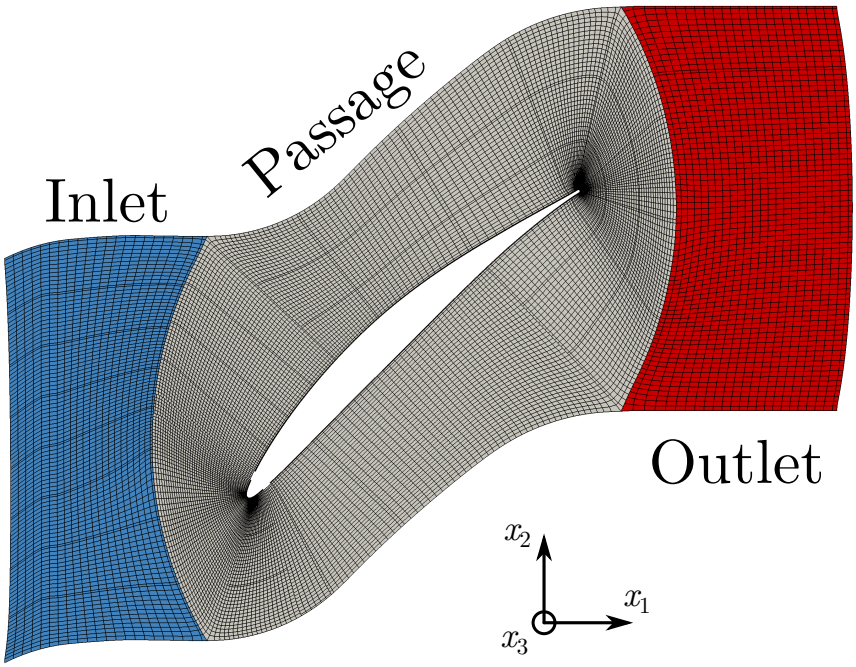

Figure 8.2: Domains used for the alignment criterion analysis. Blue: inlet, grey: passage, red: outlet

8.2.1 Entire domain

The probability density function (PDF) and cumulative distribution function (CDF) of the alignment criterion for the entire domain are plotted in figure 8.3. Both the Boussinesq constitutive relation and the QCR present points with a negative criterion, meaning a negative alignment between the Reynolds stress tensor and the constitutive relation tensor. For both constitutive relations, the quantity of anti-aligned points remains small, with less than 4% of the points concerned. The PDF of Υ (Boussinesq) increases evenly from 0 to 0.75 and then decreases abruptly, showing that the vast majority of the points tested does not present a correct alignment between the tensors. The peak of the distribution is in the interval $[0.7,\ 0.75]$. In comparison, Υ^{QCR} presents lower densities under 0.75 and more points in the upper values, with its peak in the

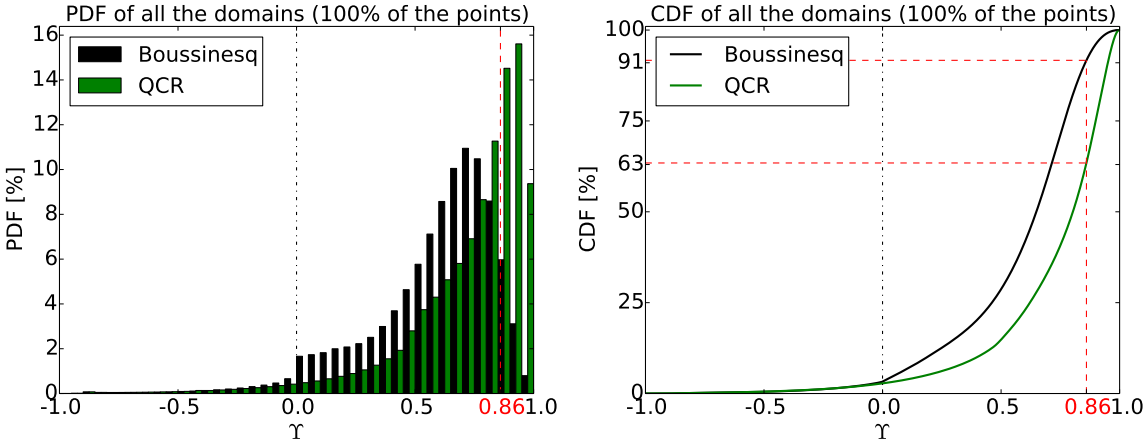

(a) PDF (b) CDF

Figure 8.3: PDF (a) and CDF (b) of the Υ and Υ^{QCR} criteria on the entire domain.

interval [0.9, 0.95]. The CDF shows the Boussinesq constitutive relation is not valid for 91% of the points, whereas for the QCR only 63% of the points are not valid. The QCR, though far from perfect, has a significant beneficial impact on the alignment of the tensors.

The analysis will now focus specifically on the inlet domain, the passage domain and the outlet domain in order to see if the constitutive relations present different behaviours for different parts of the flow.

8.2.2 Inlet domain

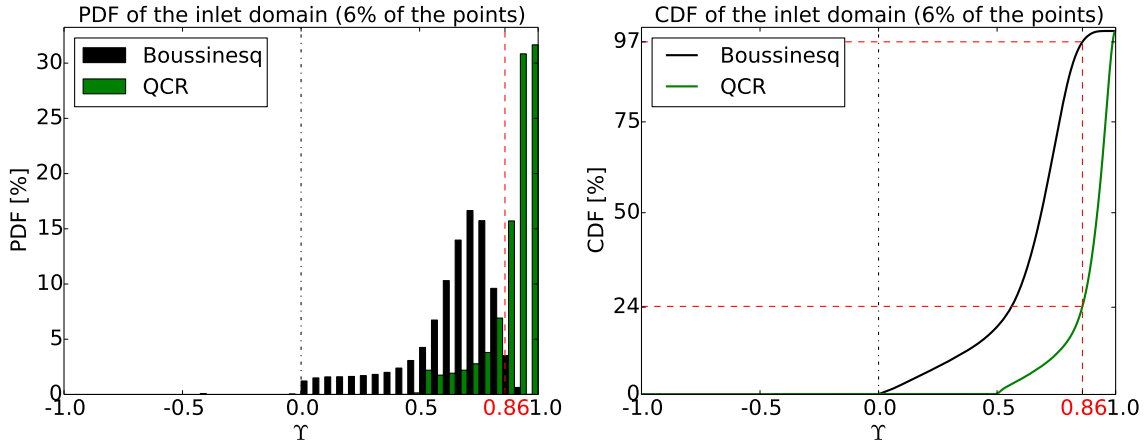

(a) PDF (b) CDF

Figure 8.4: PDF (a) and CDF (b) of the Υ and Υ^{QCR} criteria on the inlet domain.

The inlet domain, located upstream the blades and the corner separation, presents the characteristics of a fully turbulent boundary layer. The Boussinesq constitutive relation is expected to present better results on this canonical case. The number of points from this domain, weighted by the mass, represents 6% of the total mass-weighted number of points. The PDF and CDF of the inlet domain are given in

figure 8.4. Contrary to the expectations, the Boussinesq constitutive relation yields bad results on this inlet domain. The distribution is similar to the one of the entire domain, with a peak in the interval [0.7, 0.75], except there are no negative alignments. The CDF shows that the overall alignment is worse, with 97% of the points for which the Boussinesq constitutive relation is not valid. In comparison, the QCR presents quite an improvement in this area. The peak of the PDF is in the interval [0.95, 1.0], and the CDF shows that the constitutive relation is valid, in term of alignment, for 76% of the points. The QCR have an important effect on this canonical flow. This may be partly explained by the fact that the calibration of the constant c_{QCR} has been done originally in the outer region of a simple boundary layer (Spalart, 2000).

8.2.3 Passage domain

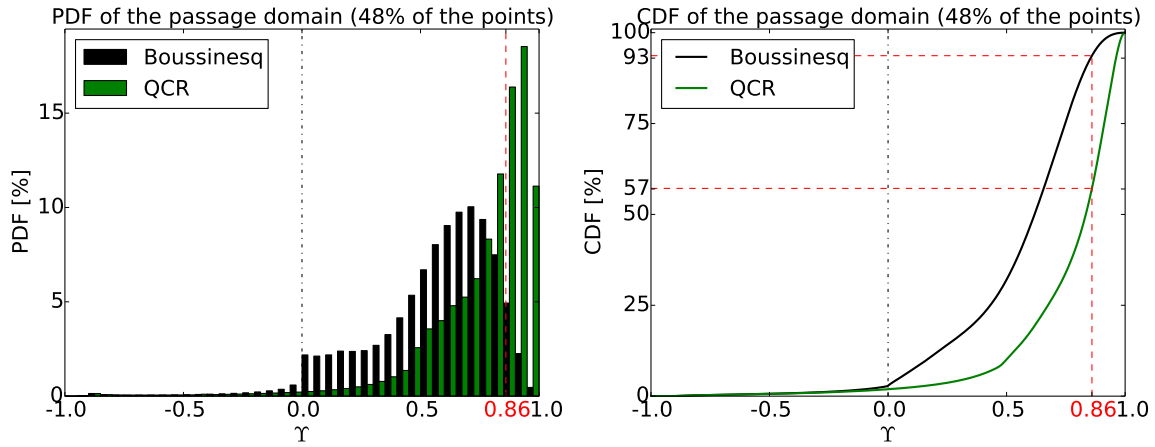

(a) PDF (b) CDF

Figure 8.5: PDF (a) and CDF (b) of the Υ and Υ^{QCR} criteria on the passage domain.

The passage domain, located in between the blades, presents three boundary layers: at the end-wall and on both sides of the blades. The interaction of the end-wall and suction-side boundary layers forms the corner separation. The phenomenon is three dimensional and vortical, and more complex than the inlet domain boundary layer. The number of points from this domain, weighted by the mass, represents 48% of the total mass-weighted number of points. The PDF and CDF of the passage domain are given in figure 8.5. Around 2% of the points are anti-aligned, for both the Boussinesq and quadratic constitutive relations. The Boussinesq constitutive relation yields similar results to the inlet domain. The peak of the PDF is still located in the interval [0.7, 0.75]. Looking at the CDF, the Boussinesq hypothesis is not verified for 93% of the points. The QCR still yields better results in term of tensor alignment, but the improvement is not as important as for the inlet domain. The peak of the PDF is still inside the area where the alignment hypothesis is verified, but the CDF indicates 57% of the points are not valid.

8.2.4 Outlet domain

The last domain is located at the outlet. In this domain, the wake of the corner separation develops downstream. The flow is again three-dimensional and vortical.

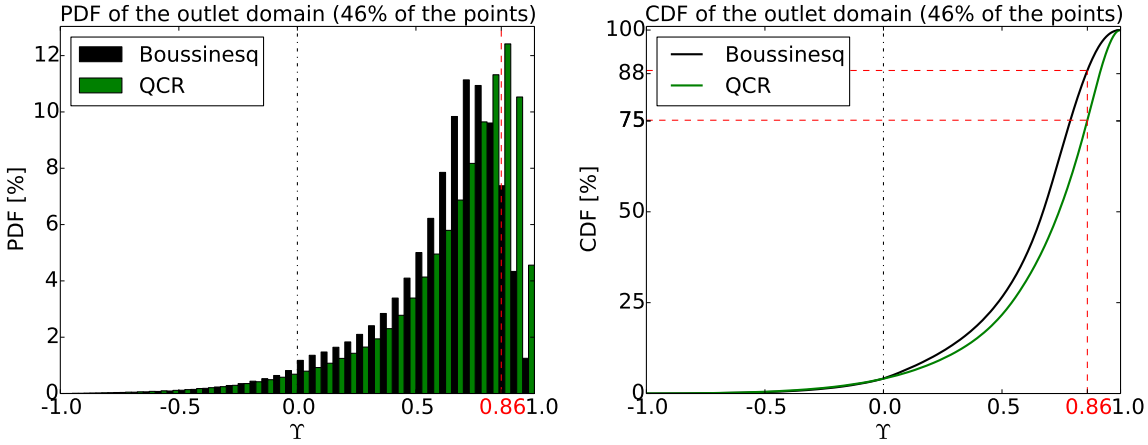

(a) PDF (b) CDF

Figure 8.6: PDF (a) and CDF (b) of the Υ and Υ^{QCR} criteria on the outlet domain.

The number of points from this domain, weighted by the mass, represents 46% of the total mass-weighted number of points. The PDF and CDF of the outlet domain are given in figure 8.6. The Boussinesq constitutive relation yields again similar results, with a little improvement, but not enough to consider that it behaves well. Almost all the anti-aligned points of the entire domain are located in the outlet part, in the corner separation wake. Concerning the QCR, an improvement is still visible compared to the Boussinesq constitutive relation, but the improvement is less significant than for the upstream domains. In this complex wake region, the QCR behaviour, in term of tensor alignment, is much closer to the Boussinesq constitutive relation than in the boundary layer at the inlet. The CDF shows that the quantity of misaligned points is comparable to the Boussinesq results: 75% of misaligned points for Υ^{QCR}, closer to the value of 88% for Υ. This result is counter-intuitive. Given that the formulation of the QCR explicitly contains a normalised rotation tensor, it was expected to be more effective in highly vortical areas.

8.3 Turbulent viscosity comparisons

The turbulent viscosities, defined in equations (8.7−8.8), are plotted in figure 8.7. They are compared to the turbulent viscosities extracted from the three RANS simulations studied. The turbulent viscosities are plotted on the outlet 1 plane, presented in figure 7.7, and normalised by the dynamic viscosity $\mu = 1.81 \times 10^{-5}\text{kg.m}^{-1}\text{.s}^{-1}$.

It is first remarkable that the LES turbulent viscosity computed as $\mu_t^{(1)} =< \overline{\rho} > [\widetilde{k}]/[\widetilde{\omega}]$ is of a comparable order of magnitude as the RANS turbulent viscosities computed as $\mu_t =< \rho > [k]/[\omega]$, where $[k]$ and $[\omega]$ are provided by the transport equations of the models. In term of topology, as already observed for this configuration with the Reynolds stresses in chapter 7 section 7.2.4, RANS simulations are unable to correctly predict the size of the corner separation, where the turbulent viscosity is maximal. Concerning the turbulent viscosities computed as the ratio of two tensor norms, $\mu_t^{(0)}$, they are also of the same order of magnitude as the turbulent viscosities computed as $< \rho > [k]/[\omega]$. $\mu_t^{(0)}$ and $\mu_t^{(0)QCR}$ are superior to $\mu_t^{(1)}$, but their maxima are similar to the maxima of the other turbulent viscosities. Given the similarity between the

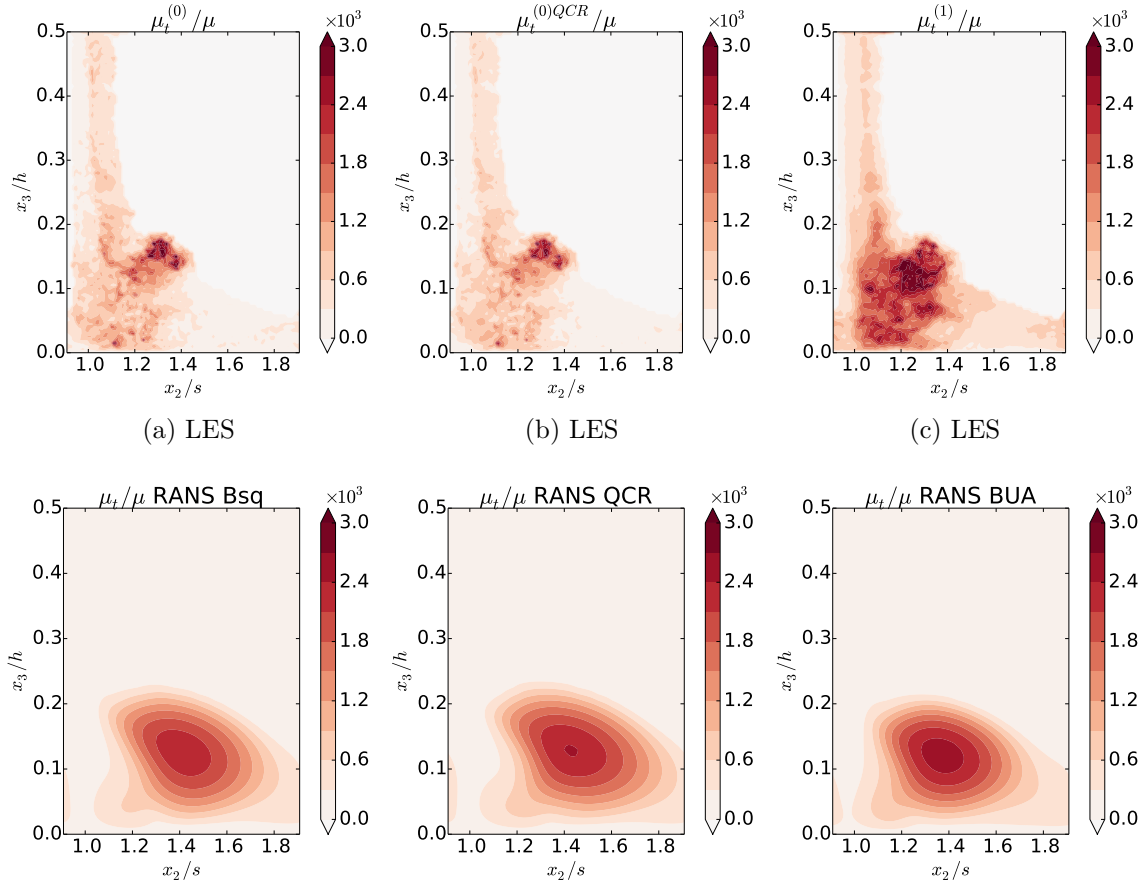

(a) LES (b) LES (c) LES

(d) RANS (e) RANS (f) RANS

Figure 8.7: Turbulent viscosities on the outlet 1 plane.

$\mu_t^{(0)}$ and $\mu_t^{(0)QCR}$ values, the QCR bears no significant modification on the norm of the constitutive relation tensor. Its influence is essentially a rotation of the tensor.

8.4 Partial conclusion

The two constitutive relations tested rely on a set of two hypotheses, an hypothesis of tensor alignment and an hypothesis on the manner to calculate the proportionality coefficient (turbulent viscosity). The first hypothesis has been tested with an alignment indicator, derived from the inner product of the two tensors. The hypothesis of alignment is rarely verified for the Boussinesq constitutive relation, with around 90% of the mass-weighted points where the misalignment is higher than an angle of $\pi/6$. The Boussinesq constitutive relation yields similar results in all the studied sub-domains. The QCR succeeds in realigning the constitutive relation tensor with the Reynolds stress tensor for around 30% of the mass-weighted points. The correction impacts strongly the inlet, where a flat-plate boundary layer develops, with flow characteristics close to the ones used for the QCR calibration. The impact of the QCR decreases in the passage and in the outlet region, where the wake of the corner-separation lies. In the outlet region, the QCR yields results closer to the Boussinesq constitutive relation.

The second hypothesis has been tested by measuring the ratios of the tensor norms, and by comparing them with the ratio $< \overline{\rho} > [\widetilde{k}]/[\widetilde{\omega}]$ extracted from LES, and with the

turbulent viscosities calculated with the three RANS simulations. All these estimates present similar amplitudes, so the choice of k and ω to compute the turbulent viscosity is legitimate, and the transport equations of the $k-\omega$ models provide meaningful values. Furthermore, the viscosities computed as the ratios of the norms of the tensors are very similar, indicating that the QCR rotates the constitutive relation tensor without dilating it.

Finally, the Boussinesq constitutive relation shows an important alignment default, but the calculation of the coefficient of proportionality from modelled statistics is legitimate. To correct the alignment, the path seems to add a rotation to the zero-trace mean strain-rate tensor in order to realign it with the Reynolds stress tensor. The QCR goes in that direction, but is not sufficient in the highly vortical part of the flow. The correction may be improved. A general solution, introduced by Pope (1975), would be to express the Reynolds stress tensor as a linear combination of no more than 10 tensors derived from the zero-trace mean strain-rate tensor and the mean vorticity tensor, yielding a general non-linear constitutive relation approach:

$$T_1 = \underline{\underline{\sigma}} \ (\approx \text{Boussinesq}) \qquad T_2 = \underline{\underline{\sigma\Omega}} - \underline{\underline{\Omega\sigma}} \ (\approx \text{QCR})$$

$$T_3 = \underline{\underline{\sigma}}^2 - \frac{1}{3}\left\|\underline{\underline{\sigma}}\right\|^2 \underline{\underline{I_3}} \qquad T_4 = \underline{\underline{\Omega}}^2 - \frac{1}{3}\left\|\underline{\underline{\Omega}}\right\|^2 \underline{\underline{I_3}}$$

$$T_5 = \underline{\underline{\Omega\sigma}}^2 - \underline{\underline{\sigma}}^2\underline{\underline{\Omega}} \qquad T_6 = \underline{\underline{\Omega}}^2\underline{\underline{\sigma}} - \underline{\underline{\sigma\Omega}}^2 - \frac{2}{3}\left\|\underline{\underline{\sigma\Omega}}^2\right\|^2 \underline{\underline{I_3}}$$

$$T_7 = \underline{\underline{\Omega\sigma\Omega}}^2 - \underline{\underline{\Omega}}^2\underline{\underline{\sigma\Omega}} \qquad T_8 = \underline{\underline{\sigma\Omega\sigma}}^2 - \underline{\underline{\sigma}}^2\underline{\underline{\Omega\sigma}}$$

$$T_9 = \underline{\underline{\Omega}}^2\underline{\underline{\sigma}}^2 - \underline{\underline{\sigma}}^2\underline{\underline{\Omega}}^2 - \frac{2}{3}\left\|\underline{\underline{\sigma}}^2\underline{\underline{\Omega}}^2\right\|^2 \underline{\underline{I_3}} \qquad T_{10} = \underline{\underline{\Omega\sigma}}^2\underline{\underline{\Omega}}^2 - \underline{\underline{\Omega}}^2\underline{\underline{\sigma}}^2\underline{\underline{\Omega}}$$

The first term of this formulation corresponds to the Boussinesq constitutive relation, while the addition of the first two terms gives a model close to the QCR. This method has been used and calibrated by Shih et al. (1996) for their turbulence model, but its complexity makes it not very popular in the turbomachinery community.

The main drawback of such a model is its complex calibration. As a perspective, a two step approach is proposed. First, high fidelity LES or DNS databases can be used to find the predominant terms in Pope expression, if they exist, using for instance a statistical approach. Then, the calibration of this reduced model can be done statistically with the same databases.

Chapter 9

Corner separation TKE budget analysis

Sections

THE turbulent kinetic energy (TKE) budget shows the physics of turbulence through the production, dissipation and transport. For the RANS simulations with a k equation, it shows the ability of the model to represent correctly the fine physics of turbulence. The TKE budget is extracted on the same plane as the Reynolds stresses presented in chapter 7 (*c.f.* Fig. 7.7) and normalised by $(\rho^2 u_e^4)/\mu$. The results on the outlet 0, outlet 2 and outlet 3 planes are similar to the results on the outlet 1 plane. These results are not presented in the present chapter, but can be found in appendix D. In the LES figures, horizontal and vertical lines are visible. These lines are a consequence of the interpolation between different blocks for visualization.

9.1 On the inlet plane

This plane allows to analyse the interaction of the thick end-wall boundary-layer with the blade suction-side boundary-layer.

9.1.1 Numerical residual

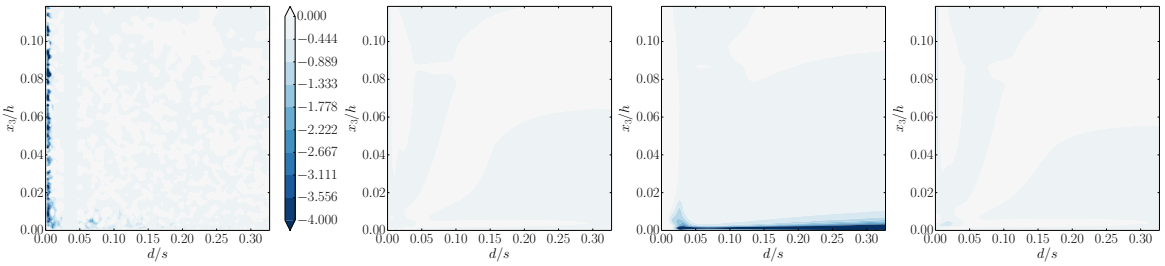

(a) LES (b) RANS_BSQ (c) RANS_QCR (d) RANS_BUA

Figure 9.1: Numerical residual on the inlet plane, normalised by $(\rho^2 u_e^4)/\mu$.

The numerical residual term is added to close the physical budget presented in equations (2.36) and (2.69). The term is calculated as minus the sum of all the other terms. The numerical residual term on the inlet plane is represented in the figure 9.1. For all the simulations, the numerical residual is negative, thus corresponding to a dissipative effect. For the LES simulation, in figure 9.1a, the numerical residual is located only in the blade boundary-layer area ($d/s \simeq 0$), with non negligible levels. Its maximal intensity is of similar level as the maximal production and transport intensities. Consequently, any physical interpretation in this area must be considered with caution. The main reason of such an important numerical residual term is supposed to be the numerical error, influenced by the mesh distribution. The blade boundary-layer area is the location where the numerical effects are the strongest compared to the rest of the flow, and the hardest to control.

For the RANS simulations, two different behaviours can be observed. The RANS simulations with the original Wilcox model and the modified Wilcox model scarcely show any numerical residual (Figs. 9.1b and 9.1d). On the contrary, the RANS simulation with the quadratic Wilcox model (Fig. 9.1c) shows an important numerical residual in the end-wall boundary-layer area ($x_3/h \approx 0$), superimposed where an important production intensity is seen in figure 9.2c. For RANS simulations, since the k equation is directly solved, the numerical residual indicates that the k production limitation is activated. This k production limitation is normally active in highly anisotropic areas. RANS with the quadratic Wilcox model tends to over-predict the value of production compared to LES in the end-wall boundary-layer (Fig. 9.2a), and it is clipped by an important k production limitation.

9.1.2 Production

The production term on the inlet plane is represented in figure 9.2. The two main areas where the production term is important on the LES results, in figure 9.2a, are the blade boundary-layer ($d/s \simeq 0$) and the end-wall boundary-layer ($x_3/h \approx 0$). While a bubble of Reynolds stresses is present in the corner, no bubble of production

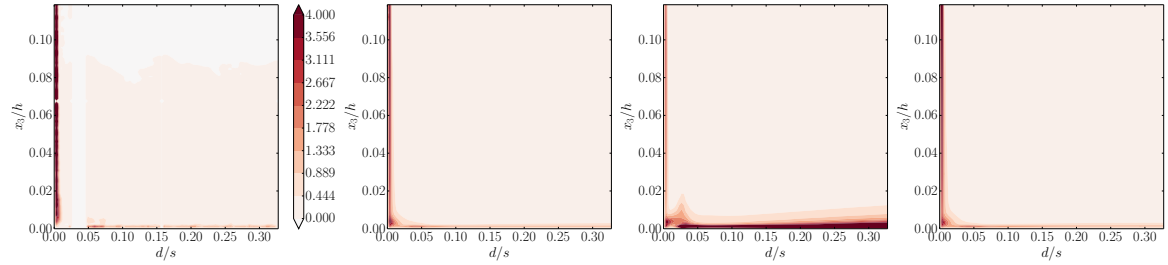

(a) LES (b) RANS_BSQ (c) RANS_QCR (d) RANS_BUA

Figure 9.2: Production on the inlet plane, normalised by $(\rho^2 u_e^4)/\mu$.

can be seen there on the figure. This may be due to a lack of resolution in this area, directly located on a block intersection, where the budget is not correctly computed.

The RANS simulations with the original and modified Wilcox models, in figures 9.2b and 9.2d, show a correct representation of the production term in the boundary-layers, compared to the LES, and no production bubble in the corner. The RANS simulation with the quadratic Wilcox model, in figure 9.2c, decreases the production term intensity in the blade boundary-layer and increases the intensity in the end-wall boundary-layer, beyond the LES values in both cases, and shows a bubble of production in the corner.

9.1.3 Dissipation

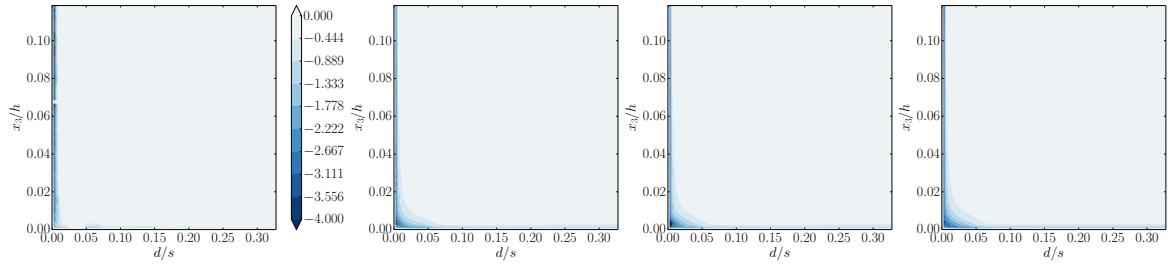

(a) LES (b) RANS_BSQ (c) RANS_QCR (d) RANS_BUA

Figure 9.3: Dissipation on the inlet plane, normalised by $(\rho^2 u_e^4)/\mu$.

The dissipation term at the inlet is represented in figure 9.3. The areas where the dissipation is important for the LES results, in figure 9.3a, are the same areas as for the production term, i.e. in the boundary-layers. The intensity of dissipation is the highest close to the suction side of the blade, but still smaller than the intensity of production at the same location. Not all the turbulent kinetic energy produced is dissipated on the same place.

In all the RANS cases (Figs. 9.3b, 9.3c and 9.3d), the dissipation term is superimposed with the production term in the blade boundary-layer, with almost the same intensity (opposite). In the end-wall boundary-layer, the RANS simulations with the original and modified Wilcox models show a dissipation at equilibrium with production, while for the RANS simulation with the quadratic Wilcox model, the dissipation is weak compared to the intense production. No bubble of dissipation can be seen in

the corner, as counterpart of the bubble of production for RANS with the quadratic model.

9.1.4 Transport

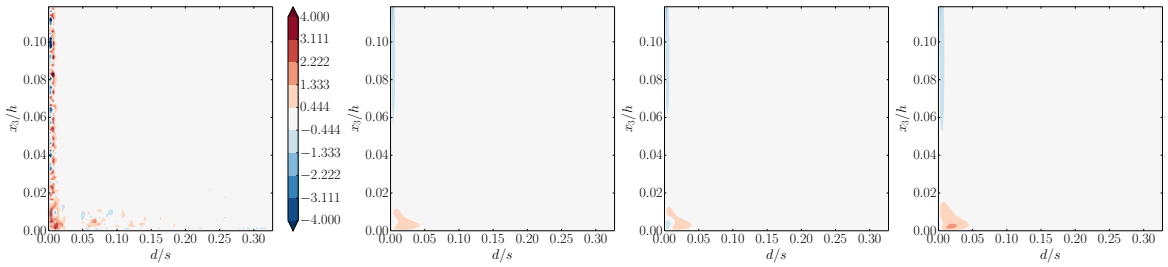

(a) LES (b) RANS_BSQ (c) RANS_QCR (d) RANS_BUA

Figure 9.4: Transport on the inlet plane, normalised by $(\rho^2 u_e^4)/\mu$.

The transport term at the inlet is represented in figure 9.4. The LES simulation shows an important transport in the blade boundary-layer, in figure 9.4a, and a weak transport in the end-wall boundary-layer.

The RANS simulations (Figs. 9.4b, 9.4c and 9.4d) present a very weak transport term, with a maximum ten times smaller than for the production or dissipation terms. This is a known default of RANS modelling, and the quadratic constitutive relation has no influence on it.

9.2 On the passage plane

9.2.1 Numerical residual

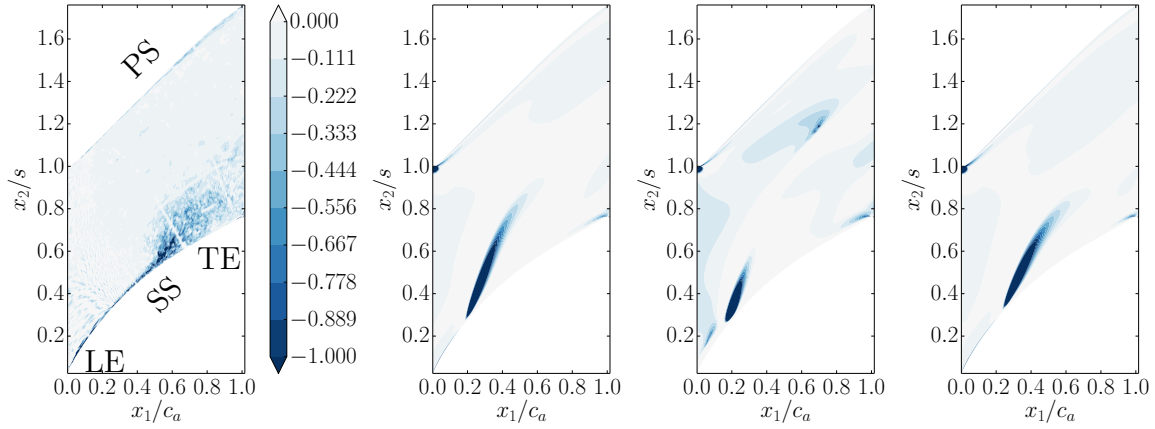

(a) LES (b) RANS_BSQ (c) RANS_QCR (d) RANS_BUA

Figure 9.5: Numerical residual on the passage plane, normalised by $(\rho^2 u_e^4)/\mu$.

The numerical residual term on the passage plane is represented in figure 9.5. This term is maximal, for the LES results (Fig. 9.5a), very locally at the beginning of the corner separation ($x_1/c_a \approx 0.5$), and small enough elsewhere compared to the

production term or the transport term. This result allows the physical analysis of the budget from the LES.

For the three RANS results (Fig. 9.5b, 9.5c and 9.5d), the numerical dissipation, representing the k production limitation, is present in highly anisotropic areas where the two-equation RANS modelling over-produces turbulent kinetic energy. For the RANS simulation with the quadratic Wilcox model, a bubble of high numerical dissipation is present at $x_1/c_a = 0.7$ and $x_2/s = 1.1$, superimposed with the peak of production (Fig. 9.6c), and cancelling completely its effect.

9.2.2 Production

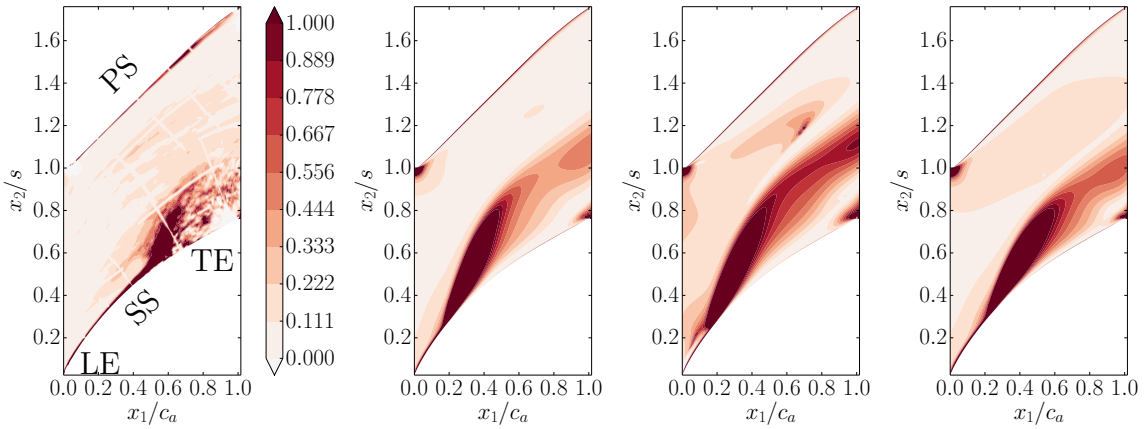

(a) LES (b) RANS_BSQ (c) RANS_QCR (d) RANS_BUA

Figure 9.6: Production on the passage plane, normalised by $(\rho^2 u_e^4)/\mu$.

The production term on the passage plane is represented in figure 9.6. The production term is important, for the LES (Fig. 9.6a) and the RANS simulations (Fig. 9.6b, 9.6c and 9.6d), on the blade suction side close to the leading edge, at the beginning of the corner separation, and on the blade pressure side close to the trailing edge. The maximum of production is each time superimposed with the maximum of τ_{t11} , shown in figure 7.14.

The two RANS simulations with the Boussinesq constitutive relation (Fig. 9.6b and 9.6d) over-estimate the production intensity in the corner separation, at the leading edge on the pressure side and at the trailing edge on the suction side. This is a known behaviour of two-equation models to over predict production at stagnation points and in highly anisotropic areas. The RANS simulation with the QCR (Fig. 9.6c) presents the same behaviour as the other RANS simulations, with the addition of a bubble of production at $x_1/c_a = 0.7$ and $x_2/s = 1.1$, where a maximum of τ_{t22} is present (Fig. 7.15c).

9.2.3 Dissipation

The dissipation term on the passage plane is represented in figure 9.7. The dissipation is important, for the LES (Fig. 9.7a), in the suction side boundary-layer upstream the corner separation. It is also significant at the beginning of the corner separation itself, but its intensity is weaker than the production intensity.

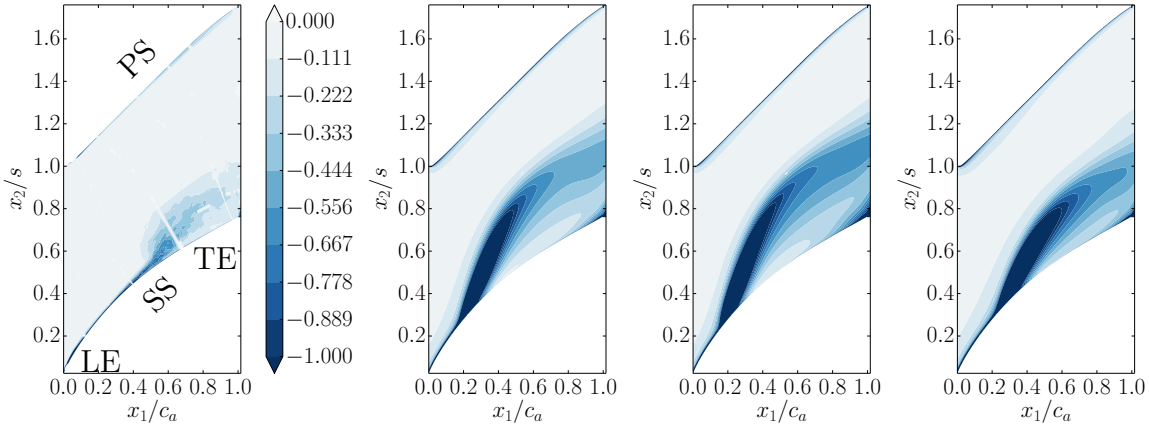

(a) LES (b) RANS_BSQ (c) RANS_QCR (d) RANS_BUA

Figure 9.7: Dissipation on the passage plane, normalised by $(\rho^2 u_e^4)/\mu$.

For the RANS simulations (Fig. 9.7b, 9.7c and 9.7d), the dissipation is mainly superimposed with the production in the boundary-layers and at the beginning of the corner separation. There is no over estimation of dissipation at the leading edge or in the middle of the passage at $x_1/c_a = 0.7$ and $x_2/s = 1.1$, where a peak of production is visible for the RANS simulation with the quadratic Wilcox model.

9.2.4 Transport

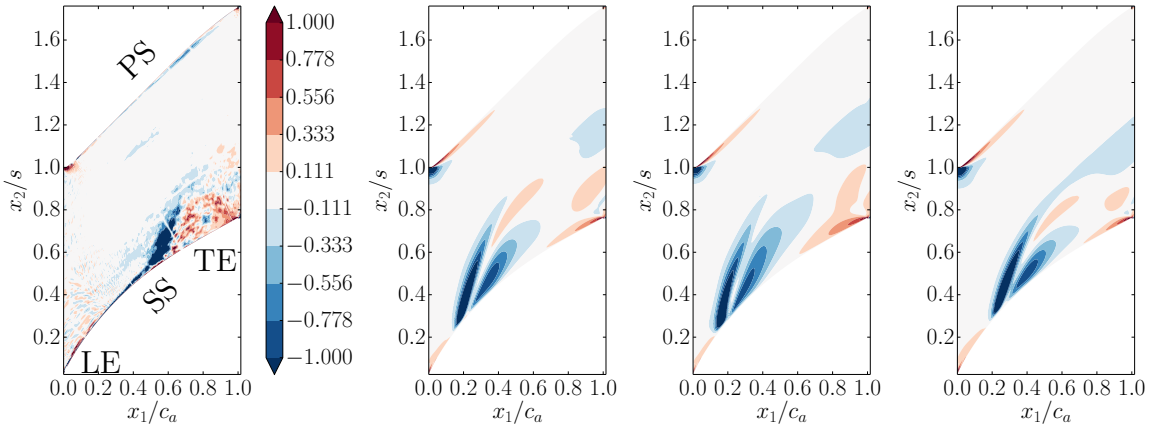

(a) LES (b) RANS_BSQ (c) RANS_QCR (d) RANS_BUA

Figure 9.8: Transport on the passage plane, normalised by $(\rho^2 u_e^4)/\mu$.

The transport term on the passage plane is represented in figure 9.8. The transport term for the LES (Fig. 9.8a) is the most intense in the corner separation, where the turbulent and rotational effects are the most important. This, and the topology of the transport term, suggest that the turbulent transport is mainly due to convective effects in the separation.

For the RANS simulations (Fig. 9.8b, 9.8c and 9.8d), the transport topology is correctly represented in the corner separation, but with weaker intensities and a larger extent than for the LES. The transport at the leading edge on the pressure side has

opposite signs for LES and RANS, showing a complete mis-prediction of the turbulent physics at this stagnation point.

9.3 On outlet 1

9.3.1 Numerical residual

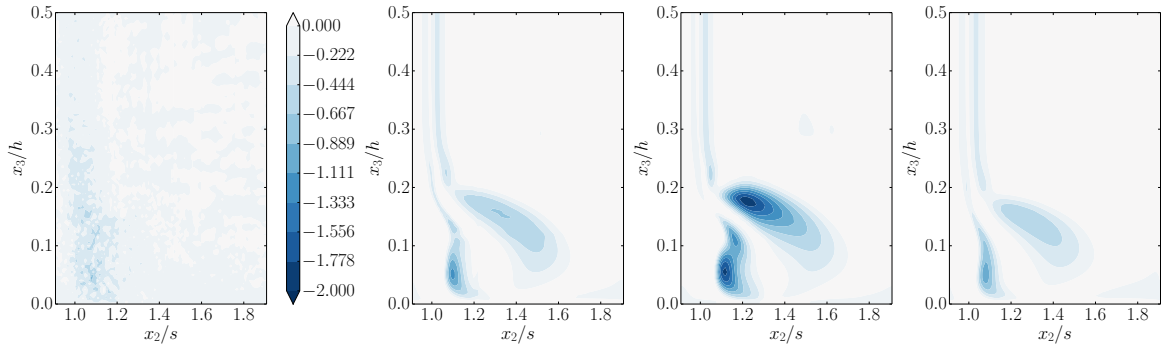

(a) LES (b) RANS_BSQ (c) RANS_QCR (d) RANS_BUA

Figure 9.9: Numerical residual on the plane outlet 1, normalised by $(\rho^2 u_e^4)/\mu$.

The numerical dissipation term at the outlet section 1 is represented in figure 9.9. The numerical residual term for the LES (Fig. 9.9a) is not negligible compared to the other terms but remains again moderate. Its extremum is almost four times smaller than the extrema of production and dissipation, thus its impact on the budget does not modify the physical analysis.

The three RANS simulations show a non-negligible numerical dissipation (Figs. 9.9b, 9.9c and 9.9d), corresponding to the activation of the k production limiter. This behaviour is coherent with what was expected, given that the limitation is to occur in areas of high anisotropy. Because the QCR was designed to improve modelling in highly vortical areas, it was expected to reduce the use of the k-production limiter. However, the exact opposite occurs. For the RANS simulation with the quadratic Wilcox model, the k production limitation is even more important than for the two RANS simulations relying on the Boussinesq constitutive relation, given that the production intensity is increased (Fig. 9.10c) and the dissipation intensity decreased (Fig. 9.11c).

9.3.2 Production

The production term at outlet section 1 is represented in figure 9.10. The production term for the LES (Fig. 9.10a) shows two clearly visible lobes of maximal intensity. The first lobe, centred around $x_2/s = 1.1$ and $x_3/h = 0.05$, is the main area of production. A second lobe of lower intensity is found around $x_2/s = 1.3$ and $x_3/h = 0.1$. These two areas are inside the area of maximal Reynolds stresses and maximal losses, as shown in figures 7.4 and 7.20-7.25.

The RANS results (Fig. 9.10b, 9.10c and 9.10d) present a similar topology to LES, *i.e.* two lobes well delimited. However, all the RANS simulations over-predict the size of the lobes and the intensity of the term. The over-prediction is remarkable for the second lobe (at $x_2/s \simeq 1.3$ and $x_3/h \simeq 0.15$), where the levels are very different

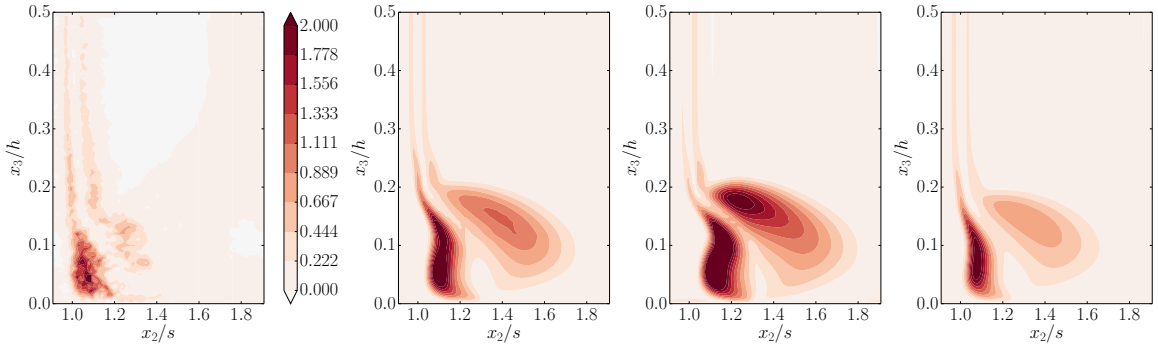

(a) LES (b) RANS_BSQ (c) RANS_QCR (d) RANS_BUA

Figure 9.10: Production on the plane outlet 1, normalised by $(\rho^2 u_e^4)/\mu$.

from the LES. The quadratic Wilcox model tends to further increase the intensity of the production term and the area of maximal intensity, while the modified Wilcox model tends to reduce a little the intensity of the production and the area of maximal intensity. This latter model yields the best comparison to LES.

9.3.3 Dissipation

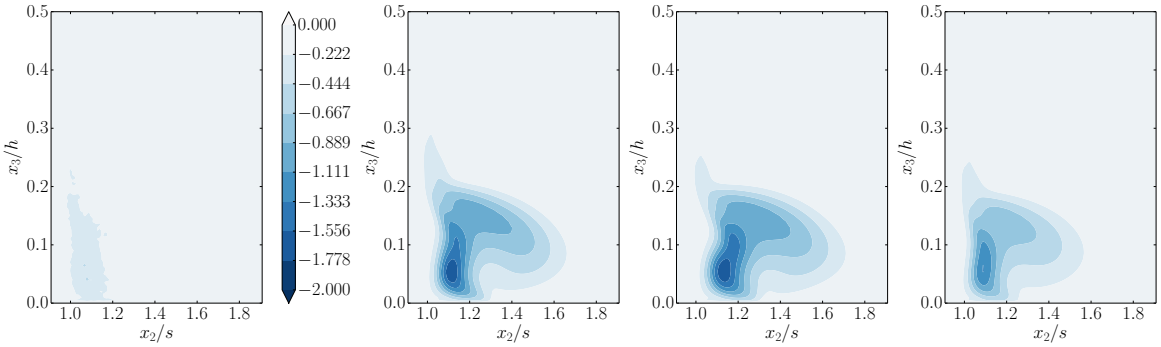

(a) LES (b) RANS_BSQ (c) RANS_QCR (d) RANS_BUA

Figure 9.11: Dissipation on the plane outlet 1, normalised by $(\rho^2 u_e^4)/\mu$.

The dissipation term at outlet section 1 is represented in figure 9.11. In the LES, the dissipation is very weak, as seen in figure 9.11a.

The behaviour of RANS is quite different. For the three simulations (Figs. 9.11b, 9.11c and 9.11d), the area of dissipation is again superimposed with the area of production.

The original and quadratic Wilcox models yield very similar results, with a notable overestimation of the dissipation. The intensity is reduced in the modified Wilcox model, but not sufficiently in comparison to LES.

9.3.4 Transport

The transport term at outlet section 1 is represented in figure 9.12. In the LES, the transport develops in the same region as the production, as seen in figure 9.12a. The

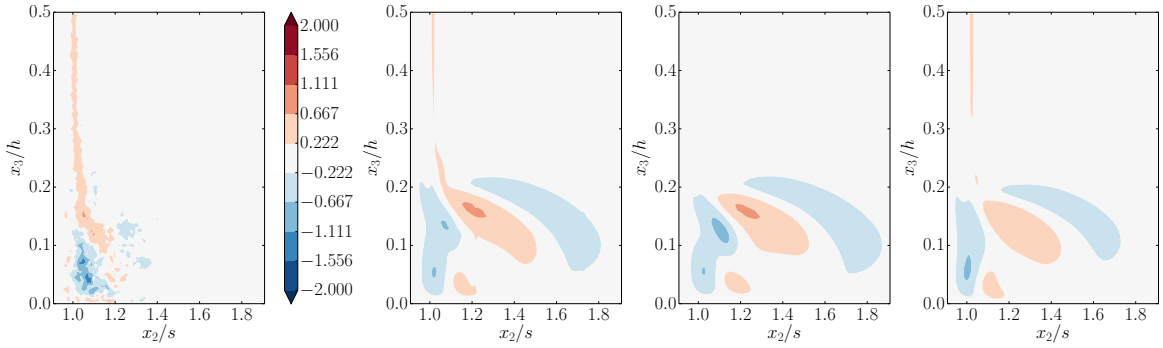

(a) LES (b) RANS_BSQ (c) RANS_QCR (d) RANS_BUA

Figure 9.12: Transport on the plane outlet 1, normalised by $(\rho^2 u_e^4)/\mu$.

TKE is taken from the area of production to be transported to a dissipative place, close to the blade wall and downstream. In the separation, the transport of turbulent kinetic energy can be associated with the convection due to the rotation of the fluid, which explains the sign change at $x_2/s \simeq 1.1$ and $x_3/h \simeq 0.1$.

The amplitude of the transport term for the RANS simulations is moderate (Figs. 9.12b, 9.12c and 9.12d) compared with the production or dissipation terms. This is again the counterpoint of the non-physical behaviour of the RANS models. Turbulent kinetic energy is dissipated where it is produced, and not transported. However, given the overestimation of production and dissipation, transport reaches intensities comparable with LES. Neither the quadratic model nor the modified model modify strongly the size of the area of maximal transport or its intensity

9.4 Partial conclusion

The TKE budget extraction methodology used on this configuration allows a fine understanding of the turbulence physics in the corner separation. The LES TKE budget presents an important production inside the wake of the corner separation, superimposed with transport. The dissipation inside the wake of the corner separation is very weak, except within a thin layer near the end-wall. The LES is used as a reference to evaluate the RANS turbulence models.

The RANS simulations reproduce reasonably the topologies of the TKE budget terms. However, the levels are not correctly estimated. The production is slightly overestimated inside the corner separation and the corner separation wake, while the dissipation is excessive and the transport underestimated. This is a typical behaviour of RANS to consider the turbulence at equilibrium, *i.e.* with production and dissipation superimposed and little transport (Wilcox, 2006). Concerning the differences between the RANS models, the TKE budget analysis shows that for the four terms, the original and modified Wilcox models are similar. The modification of the ω production term improves slightly the results, but the differences with LES remain important. The modification of the constitutive relation in the quadratic Wilcox model produces stronger variations compared to the original Wilcox model and tends to degrade further the results.

Chapter 10

Corner separation hybrid simulation

Sections

In the previous chapters, the turbulence modelling of three RANS approaches has been investigated in the corner separation case, using LES as reference. The conclusion is that the RANS simulations fail to represent accurately the turbulent physics of the corner separation. The LES is much more accurate, but at a prohibitive computational cost for an everyday design application. The approach tested here is a compromise between the precision of a LES and the moderate computational cost of a RANS simulation. RANS is used close to the wall, where the need for a refined mesh in LES is the most demanding.

The quality of the present approach is gauged with mean values of the flow, such as the pressure coefficient around the blade at various heights and the total pressure losses. These are values of interest for industrials.

A reference simulation is run, with the default parameters of the hybrid method. The results are presented in sections 10.1 to 10.5. Then, in section 10.6, a second hybrid RANS-LES simulation, with an increased RANS-LES transition distance, is presented. This simulation aims at assessing the sensitivity of the flow solution to this parameter.

10.1 Computational cost

The simulation was performed with *Turb'Flow*, an in-house solver. The simulation ran on 42 Haswell cores with a 2.60GHz frequency, during two full months ($\sim$ 45 000 CPU hours), for a total physical time of 20 through-flow periods. This is a longer computation time than a RANS simulation, but a much less important one than a LES.

10.2 RANS-LES transition location

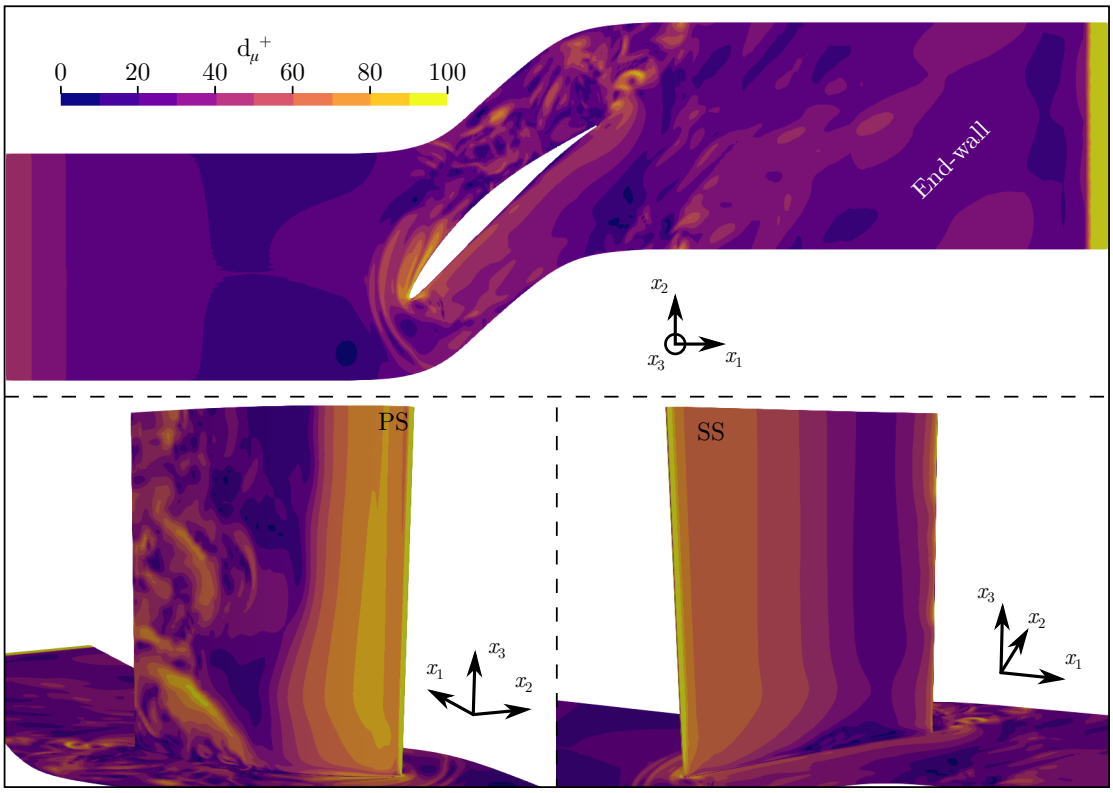

Figure 10.1: Visualisation of the instantaneous RANS-LES transition location in the corner separation case, determined *a posteriori*.

As presented in chapter 5, the RANS-LES transition location occurs at a given distance from the wall, in wall units. The normalisation of the wall-distance requires a friction velocity, which is obtained at the beginning of the computation using Michel's empirical relation (Cousteix, 1989), presented in equation (5.4). Consequently, the transition function value is fixed for each grid point from the beginning of the computation. This estimated friction velocity is generally different from the actual friction velocity of the computation, and this will have an influence on the final transition location. Indeed, if the actual friction velocity is smaller than the one estimated from Michel's relation, the grid points where the transition function equals 0.5 will correspond to a smaller d^+, so the transition will occur deeper in the boundary-layer.

The *a posteriori* transition location is presented in figure 10.1. The transition should occur at $d^+ = 50$. However, the actual transition is located between $d^+ = 30$ and $d^+ = 50$. The over-estimation of the friction velocity by Michel's empirical

relation leads to a RANS-LES transition deeper in the boundary-layer than expected. This behaviour has to be taken into account for future simulations in order to choose transition parameters d_μ^+ and L_{hyb} that yield the desired transition location.

10.3 Flow visualisation

The corner separation, occurring at the junction of the blade suction side and the end-wall, in the aft part of the blade, is visualised using the Q criterion defined in equation (7.1). The $Q = 5 \times 10^5 \mathrm{s}^{-2}$ surface is presented in figure 10.2a, for an instantaneous snapshot of the flow. The losses are also represented using the mean total pressure loss coefficient, defined in equation (7.3).

On the first hand, the corner separation presents a size and intensity of losses comparable with the LES case, presented in figure 7.1a. The vortical structures are bigger, but this is due to the coarser mesh used for the hybrid simulation.

On the other hand, vortical structures are present on the suction side of the blade. These structures, absent from the LES case, are caused by a separation occurring at around one third of the chord, on the blade suction side. The separation is thought to be a consequence of the hybrid RANS-LES transition location. This is a classical behaviour present in the DES family models, known as grid-induced separation (Menter et al., 2003; Spalart et al., 2006), when the RANS to LES transition is too close to the walls.

In figure 10.2b, the mean pressure coefficient is represented at the end-wall and on the blade, along with the mean total pressure loss coefficient at the outlet of the blade passage. On both the blade and the outlet of the passage, the effects of the separation are clearly visible.

10.4 Pressure coefficient around the blade

The pressure coefficient $-Cp$ is extracted at various span heights (indicated in figure 7.2) and presented in figure 10.3. The black lines represent the LES, the blue lines represent the RANS simulation with the original Wilcox model, and the green lines represent the hybrid simulation. Oscillations are present close to the leading edge in the LES simulation due to the implementation of the tripping bands. The upper branch of the curves represents the suction side, while the lower branch represents the pressure side.

For the LES and RANS simulations, at mid span (Fig. 10.3a) and at 30% of span (Fig. 10.3b), the results are consistent. In these areas, the flow is expected to be attached to the blade. However, in the hybrid simulation, the separation on the suction side, seen in figure 10.2, creates a plateau of Cp. The separation is located at $x_1/c_a \geqslant 0.3$, from mid span down to 13.5% of span (Fig. 10.3d). At 5.4% of span and 1.4% of span, a small reminiscence of the suction-side separation is still visible in the hybrid simulation, between $x_1/c_a \approx 0.4$ and $x_1/c_a \approx 0.6$. Then, the simulation presents a flattening of the pressure distribution on the suction side, for $x_1/c_a \geqslant 0.6$, characteristic of the corner separation. The sudden and important static pressure drop is visible at the trailing edge.

The suction-side separation perturbs the flow, and does not really permit a comparison with the RANS simulation or the LES. The overall quality of the flow prediction is

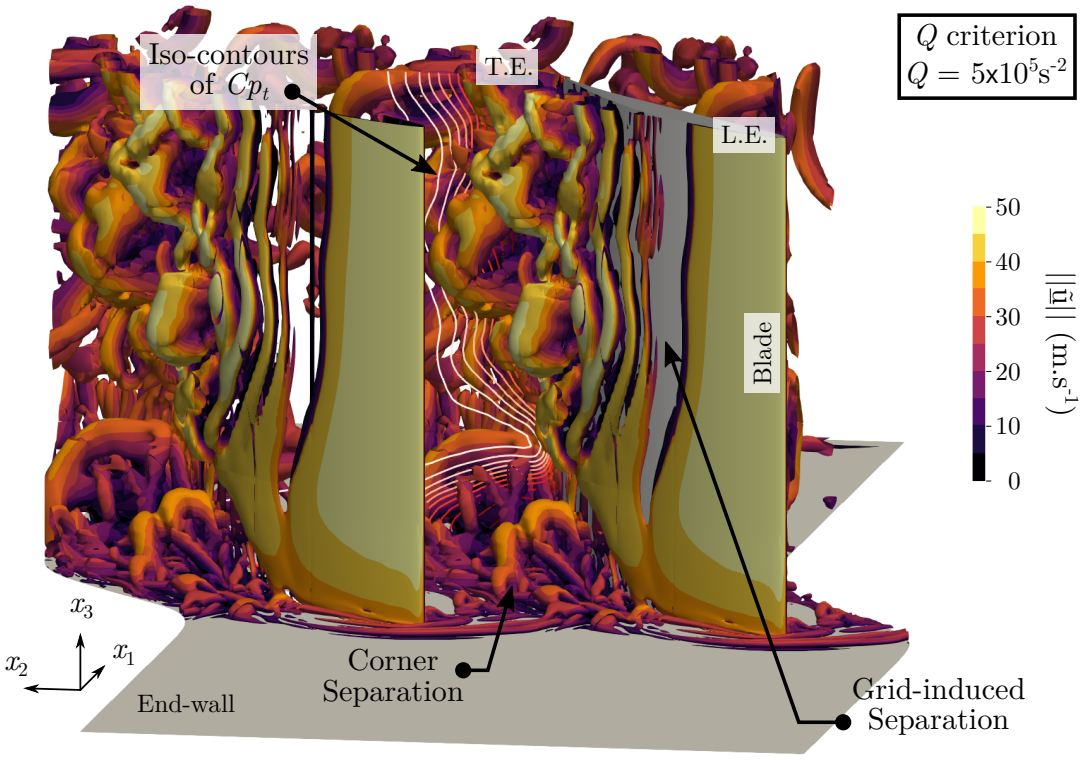

(a) Q criterion of the instantaneous hybrid flow

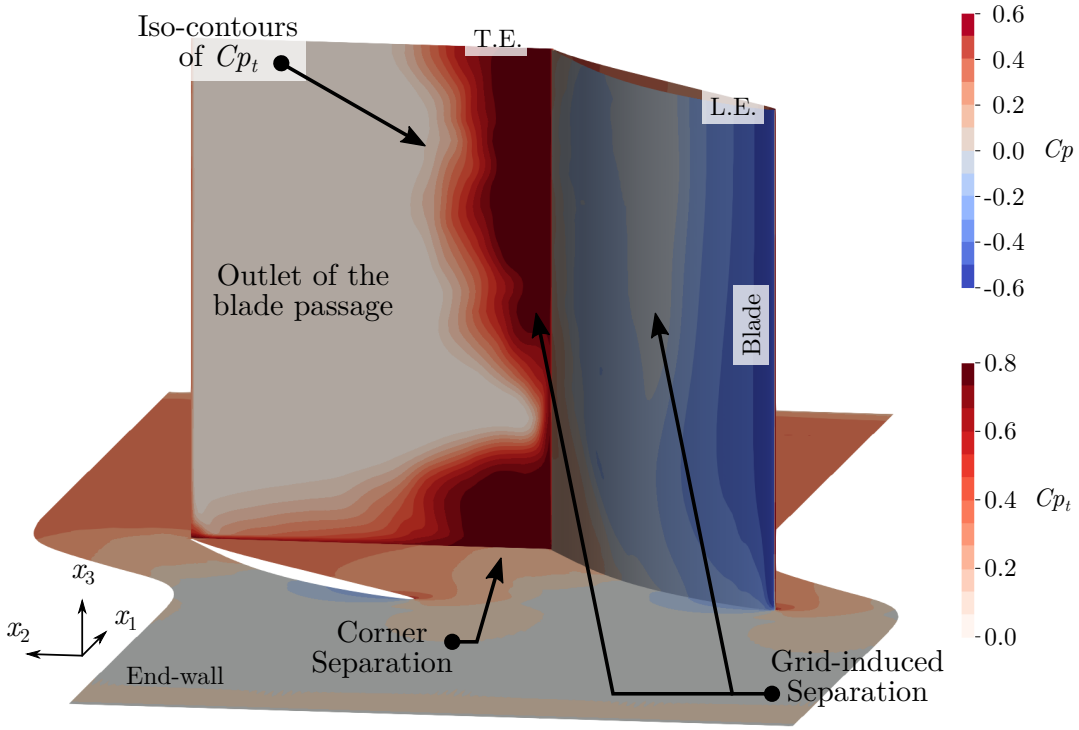

(b) Mean pressure coefficient and mean total pressure coefficient

Figure 10.2: Visualisation of the hybrid flow field in the corner separation case. (a): instantaneous Q criterion for $Q = 5 \times 10^5 \text{s}^{-2}$. (b): Mean pressure coefficient on the blade and at the end-wall, and mean total pressure coefficient at the outlet of the blade passage. The same scale and colourmap are used for Cp_t in both figures.

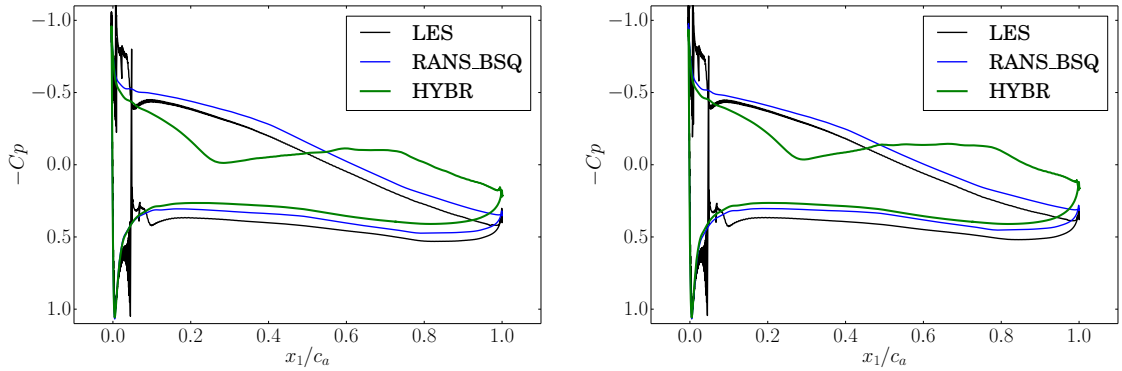

(a) $x_3/h = 50.0\%$

(b) $x_3/h = 29.7\%$

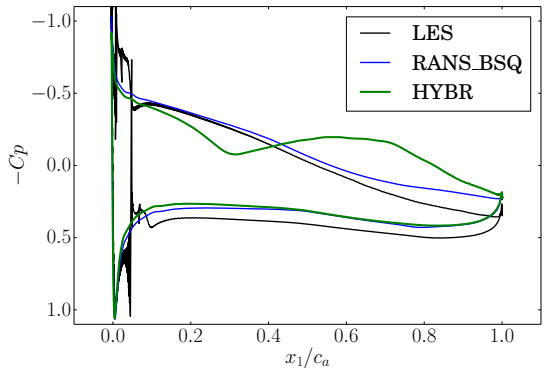

(c) $x_3/h = 21.6\%$

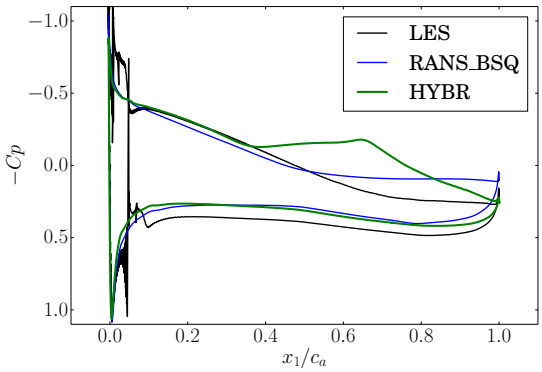

(d) $x_3/h = 13.5\%$

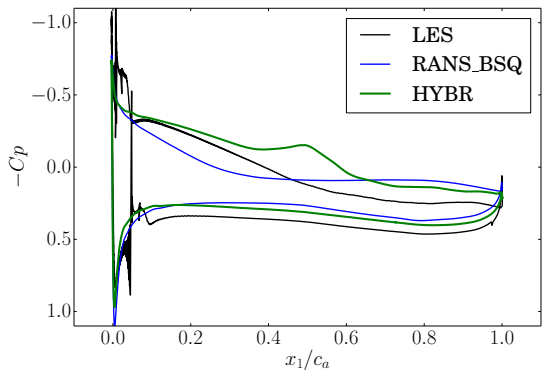

(e) $x_3/h = 5.4\%$

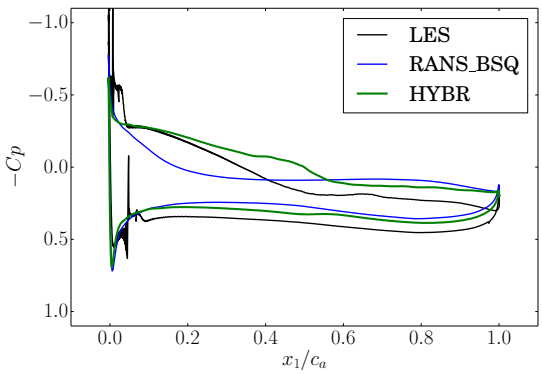

(f) $x_3/h = 1.4\%$

Figure 10.3: Mean static pressure coefficient around the blade, at various span-wise positions.

bad, but the reason for this failure, a grid-induced separation or the inherent capacity of the hybrid approach, is not determined.

10.5 Total pressure coefficient on the outlet planes

The total pressure coefficient Cp_t is extracted on the three outlet planes, presented in figure 7.2. On each plane, it is compared with the experiment, the LES and the RANS simulation with the original Wilcox model.

10.5.1 On outlet 1

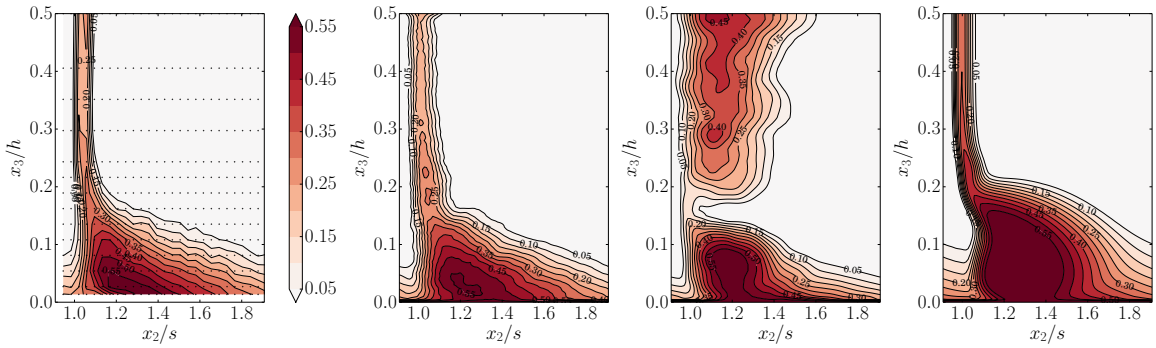

(a) EXP (b) LES (c) HYBR (d) RANS_BSQ

Figure 10.4: Mean total pressure loss coefficient on outlet plane 1.

The results on the outlet plane 1 are presented in figure 10.4. Two different areas are visible. The area of losses for $x_2/s \in [1.0,\ 1.4]$ and $x_3/h \geqslant 0.2$ corresponds to the wake of the blade. It is particularly thick for the hybrid simulation, because of the suction-side separation. The triangular area of losses at the bottom of each figure is due to the corner separation wake.

The area of the wake of the suction-side separation can not be analysed. As a numerical artefact, it should not be present in the simulation, so it is not physically relevant. But the corner separation wake area presents an interesting behaviour. In term of intensity, this area of losses in the hybrid simulation is more comparable to the experimental results or the LES results, though still a bit higher, than to the RANS results. In term of topology, the size of the area is similar to the experimental one or the LES one, and smaller than the RANS one. This may indicate a capacity of the hybrid approach to simulate more accurately this flow than a RANS approach. However, due to the suction-side separation, a blockage is induced in the passage. The reduction of the corner separation could also be a mere consequence of this blockage. It is not yet possible to arbitrate on this point.

10.5.2 On outlet 2

The results on the outlet plane 2 are presented in figure 10.5. They follow the same trends as those on the outlet plane 1. The prediction of the size and intensity of the corner separation wake by the hybrid simulation is still closer to the experimental and LES results than to the RANS results.

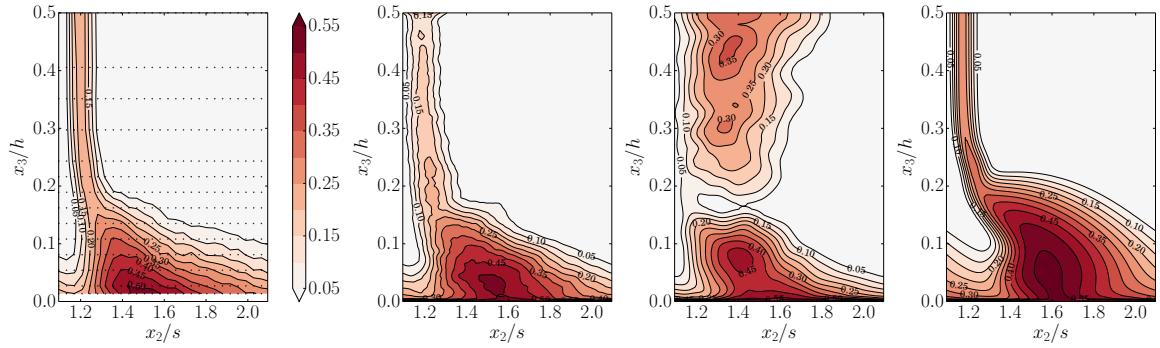

(a) EXP (b) LES (c) HYBR (d) RANS_BSQ

Figure 10.5: Mean total pressure loss coefficient on outlet plane 2.

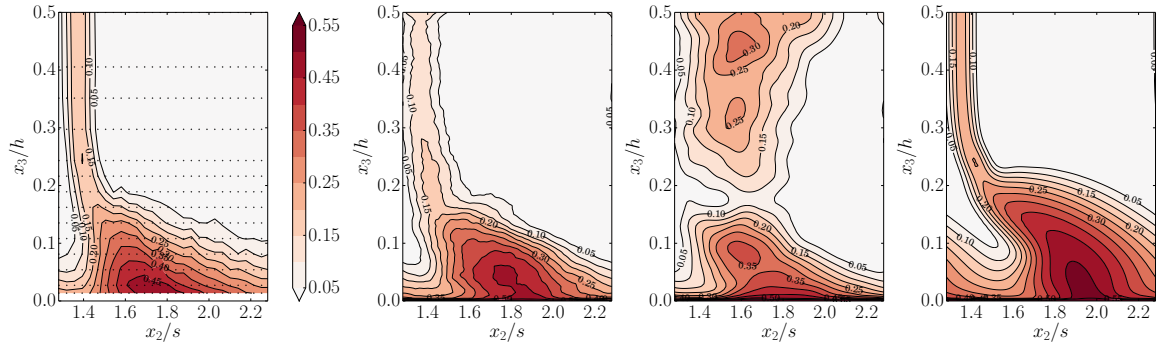

(a) EXP (b) LES (c) HYBR (d) RANS_BSQ

Figure 10.6: Mean total pressure loss coefficient on outlet plane 3.

10.5.3 On outlet 3

The results on the outlet plane 3 are presented in figure 10.6, and follow the same trends as upstream. The shape of the corner separation wake is again triangular for the experiment, the LES, and the hybrid simulation. As already noted in chapter 7, it is twisted for the RANS simulation. The hybrid simulation provides a good description of the corner-separation wake evolution downstream of the blade passage.

10.6 Increased RANS-LES transition distance

In order to try to get rid of the suction-side separation, a second hybrid simulation is run with a different target wall distance d_μ^+ and hybrid length L_{hyb}. The target wall distance and hybrid length need to be increased, in order to capture more of the boundary-layer with the RANS approach, so the chosen values are $d_\mu^+ = 200$ and $L_{hyb} = 50$. All the other simulation parameters remain unmodified.

10.6.1 Flow visualisation

The corner separation, occurring at the junction of the blade suction side and the end-wall, in the aft part of the blade, is visualised using the Q criterion defined in equation (7.1). The $Q = 5 \times 10^5 \mathrm{s}^{-2}$ surface is presented in figure 10.7a, for an instan-

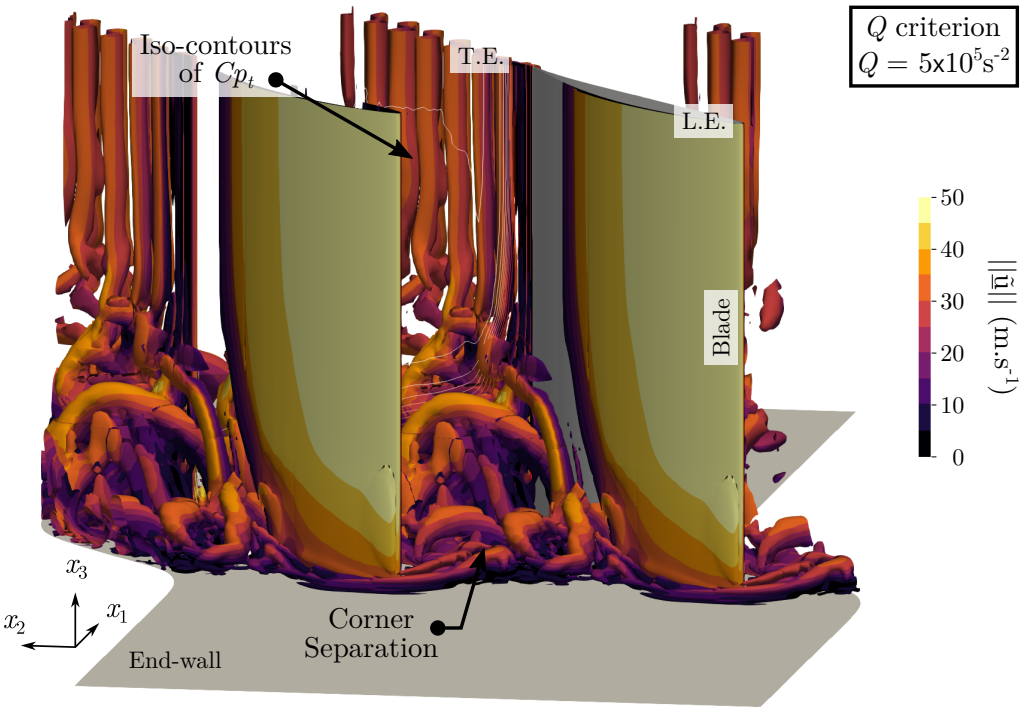

(a) Q criterion of the instantaneous hybrid flow

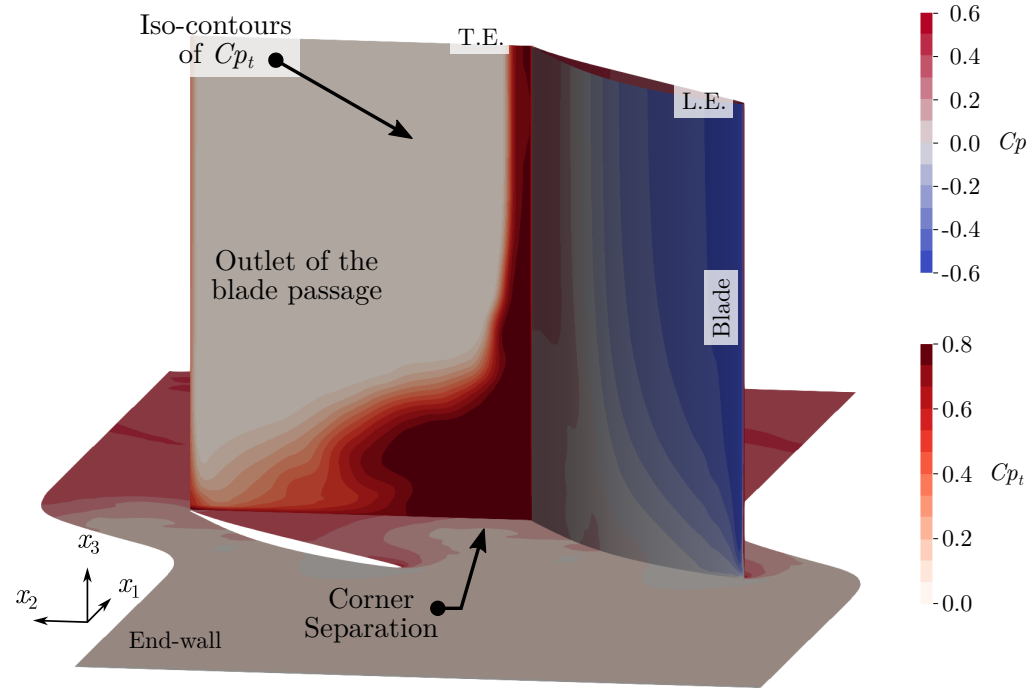

(b) Mean pressure coefficient and mean total pressure coefficient

Figure 10.7: Visualisation of the hybrid flow field in the corner separation case for a target RANS-LES transition distance $d_\mu^+ = 200$. (a): instantaneous Q criterion iso-surface for $Q = 5 \times 10^5 \mathrm{s}^{-2}$, and contours of Cp_t at the outlet of the blade passage. (b): Mean pressure coefficient on the blade and at the end-wall, and mean total pressure coefficient at the outlet of the blade passage. The same scale and colourmap are used for Cp_t in both sub-figures.

taneous snapshot of the flow. The losses are also represented using the mean total pressure loss coefficient, defined in equation (7.3). In figure 10.7b, the mean pressure coefficient is represented on the blade and at the end-wall, along with the mean total pressure loss coefficient at the outlet of the blade passage.

Compared to the case with a target wall distance for transition $d_\mu^+ = 50$, presented in figure 10.2, the separation on the suction side away from the end-wall has disappeared. This confirms that this separation was a consequence of a transition occurring too close to the walls, for the present mesh density.

Concerning the description of the corner separation, the size is more comparable to what is found in pure RANS simulations than in pure LES simulations, but with a less rounded topology.

10.6.2 Total pressure loss coefficient on outlet 1

The total pressure coefficient Cp_t is extracted on the outlet 1 plane, presented in figure 7.2. It is compared with the experiment, the LES, the hybrid RANS-LES simulation with a target wall distance for transition $d_\mu^+ = 50$ and the RANS simulation with the original Wilcox model. The results are presented in figure 10.8.

The results are similar to what has already been seen. The suction-side separation, whose effect is visible on the wake of the blade in figure 10.8d, is not anymore present, as visible in figure 10.8e. The counterpart of this disappearance is that the corner separation is no longer constrained. Its size is more comparable to what was obtained with pure RANS, in figure 10.8c, than with pure LES in figure 10.8b. The topology however is not exactly the same as in pure RANS simulation. It is more irregular.

Even though this result is not satisfactory, it is still an improvement compared with the simulation with $d_\mu^+ = 50$. An important point remaining to test is the influence of the mesh density. The mesh used for the hybrid simulations was designed for RANS simulations, thus not necessarily adapted for hybrid simulations. For example, for a ZDES hybrid approach, the typical mesh requirements are $\Delta x^+ \leqslant 200$, $\Delta y^+ \simeq 1$ and $\Delta z^+ \leqslant 100$, with a small expansion ratio (Riera, 2014). In the present case, the mesh is coarser but close enough to the requirements ($\Delta x^+ \leqslant 400$, $\Delta y^+ \simeq 1$ and $\Delta z^+ \leqslant 200$), but the expansion ratio may be too important. This could explain the weak improvement obtained with the hybrid simulation, when there is no separation on the suction side of the blade.

10.7 Partial conclusion

An hybrid simulation has been carried-out on the corner separation case with the default hybrid parameters, and compared against experimental, LES and RANS results. The comparisons have been made on an instantaneous snapshot of the flow, the pressure coefficient at various span-heights and the total pressure loss coefficient on three planes downstream of the blade, where the analysis has already been realised for the LES and RANS results.

The instantaneous view of the flow and the pressure coefficients show a separation on the suction side of the blade, that covers almost the whole span. Such separations occur with hybrid turbulence models from the DES family, when the RANS-LES transition is too close to the wall for a given mesh density. They are called grid-induced separations.

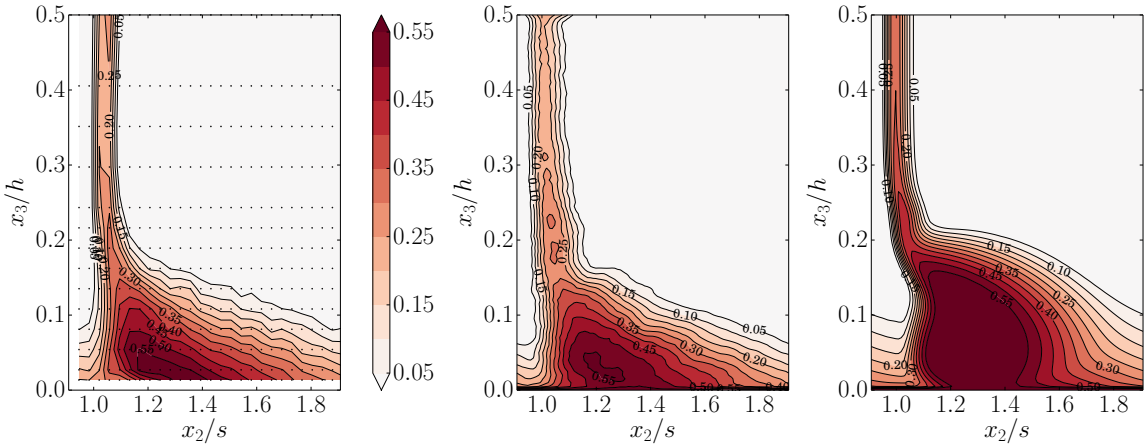

(a) EXP (b) LES (c) RANS_BSQ

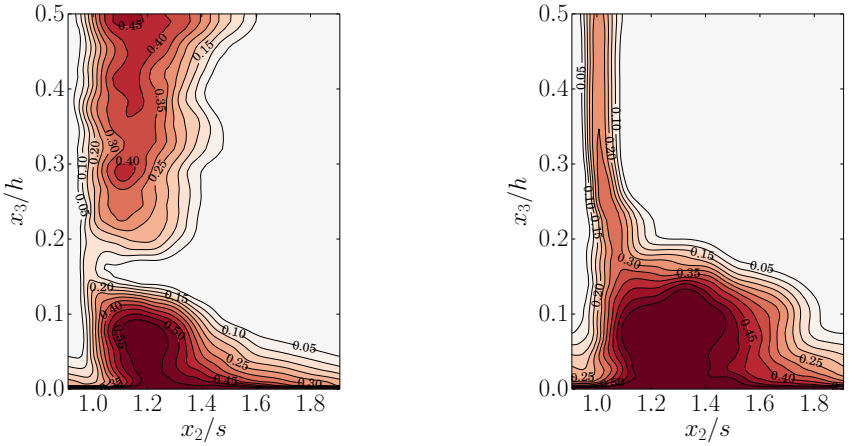

(d) HYBR (e) HYBR_200

Figure 10.8: Mean total pressure loss coefficient on outlet plane 1. The simulation labelled HYBR_200 (e) corresponds to the hybrid RANS-LES simulation with a target RANS-LES transition distance $d_\mu^+ = 200$.

The total pressure loss coefficient show that the losses due to the corner separation are closer, in terms of topology and intensity, to the experiment and the LES than to the RANS. It may be a consequence of the hybrid approach ability to predict more accurately this corner separation flow, but it could be also a side effect of the artificial suction side separation.

In order to test the influence of the RANS-LES transition location on the suction-side separation, a second simulation has been carried out with a larger target wall distance $d_\mu^+ = 200$. This modification successfully suppresses the suction-side separation, which tends to confirm this was a grid-induced separation. However the corner separation is bigger, with a size and intensity closer to what is found in pure RANS.

In order to conclude on this hybrid method, further studies are necessary, and principally a study on the mesh requirements. As a first attempt, the same mesh as for the pure RANS simulations has been used. This mesh is fine enough for the pure RANS approach, but may be too coarse for an hybrid RANS-LES approach. A mesh sensitivity analysis has not been possible in the allotted time of this work.

Chapter 11

Tip-leakage mean flow analysis

Sections

As presented in chapter 1, the tip-leakage flow is a three dimensional, vortical flow. For these reasons, the usual turbulence models, often calibrated on more academic, less complex flows, have difficulties to predict accurately this flow physics. The present analysis aims at investigating in details the capacities of RANS turbulence modelling in a tip-leakage flow.

First, some results on the mean values, such as the pressure coefficient at various span locations or mean velocities, are presented to gauge the overall quality of the simulation. Then, the Reynolds stresses, which are the turbulent quantities that directly impact the momentum and energy equations (see equations (2.48b) and (2.48c)), are analysed on two extraction planes, one through the tip-clearance and one that cuts the tip-leakage vortex.

11.1 Mean flow analysis

11.1.1 Flow topology

The tip-leakage flow is caused by the presence of a gap between the tip of a blade and a wall. The pressure difference between the pressure side and the suction side of the blade creates a flow that evolves rapidly into a vortex. The Q criterion, defined by equation (7.1), allows a visualisation of the end-wall turbulent boundary layer and

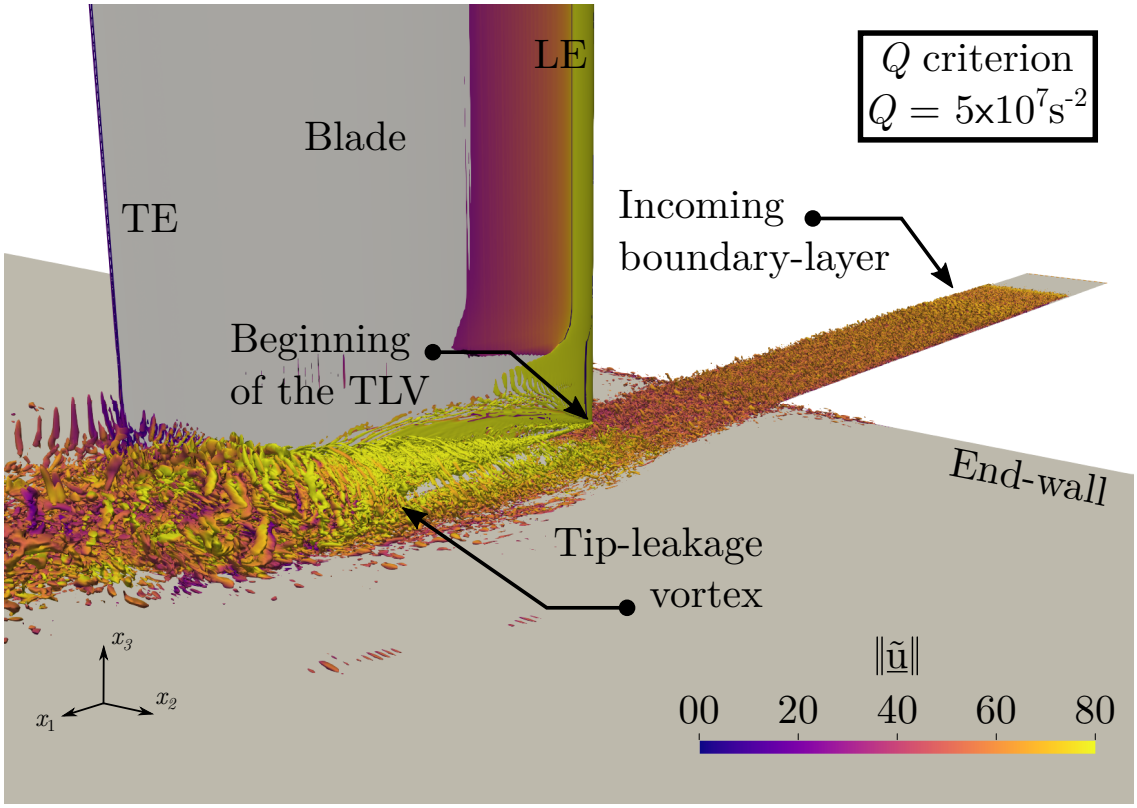

Figure 11.1: Visualisation of an instantaneous flow field in the tip-leakage case. Iso-surface $Q = 5 \times 10^7 \mathrm{s}^{-2}$.

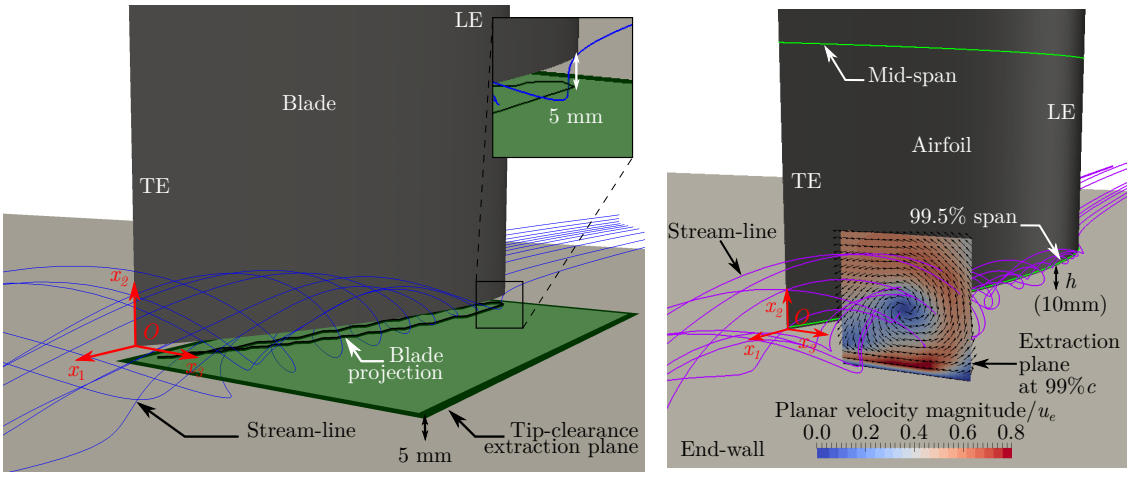

(a) (b)

Figure 11.2: Tip-leakage flow extraction planes. (a) extraction plane through the tip-clearance, (b) extraction plane through the tip-leakage vortex.

the tip-leakage vortex, from an instantaneous flow field. It is presented, for $Q = 5 \times 10^7 \mathrm{s}^{-2}$, in figure 11.1.

A special attention is paid to the LES description of the turbulent incoming boundary-layer, with a thickness consistent with the experiment of Jacob et al. (2016a,b). The tip-leakage vortex initiates at the leading-edge of the blade, and then grows downstream. This gain in energy and size is due to the leakage through the tip-clearance,

from pressure side to suction side. This phenomenon is known as jet-leakage flow.

11.1.2 Extraction locations

The pressure coefficient and the mean quantities extraction locations are presented in figure 11.2. The pressure coefficient is extracted at mid-span and at 99.5% of the span-length, close to the tip-gap (Fig. 11.2b), where Boudet et al. (2016a) validated the ZLES results with experimental results. The mean velocities, mean turbulent kinetic energy and Reynolds stresses are extracted on two different planes, one through the tip-clearance (Fig. 11.2a) and one through the tip-leakage vortex (Fig. 11.2b).

11.1.3 Pressure coefficient

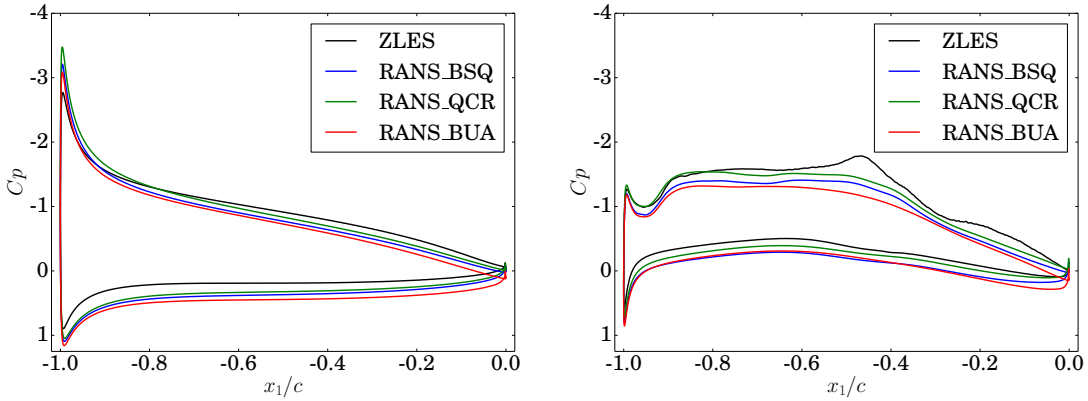

(a) Cp at 50% span ($x_3 = 95$mm) (b) Cp at 99.5% span ($x_3 = 1.0$mm)

Figure 11.3: Mean static pressure coefficient around the blade. (a): midspan, (b): 99.5% of the span length.

The pressure coefficient is computed at 50% span length and 99.5% span length (*i.e.* at $0.1h = 1$mm from the blade tip), as presented in figure 11.2b. The ZLES and the three RANS simulations present a fairly good agreement on the pressure coefficient, for both the mid-span (Fig. 11.3a) and the tip extractions (Fig. 11.3b). At mid-span, the pressure coefficient distribution is comparable to a compressor blade distribution. The three RANS simulations overestimate the pressure coefficient at the leading edge stagnation point. The RANS simulation with the modified Wilcox model presents a slight deterioration of the pressure coefficient prediction at the trailing edge compared with the original model.

At 99.5% span, the pressure coefficient presents a different topology. The pressure difference between the pressure side and the suction side is globally less important, and instead of monotonously decreasing along the chord, an increase of pressure difference is visible at $x_1/c \approx -0.45$. This is due to a pressure decrease on the suction side, because of the jet leakage. The RANS simulations with the original or quadratic Wilcox models underestimate the pressure drop, while the RANS simulation with the modified Wilcox model misses it.

11.1.4 Mean velocities

The mean velocities are extracted on the planes presented in figure 11.2. They are normalised by the inflow velocity u_e. The directions x_1, x_2 and x_3 are normalised respectively by c_a, c_a and c, with c the chord length and c_a its projection on x_1.

Through the clearance

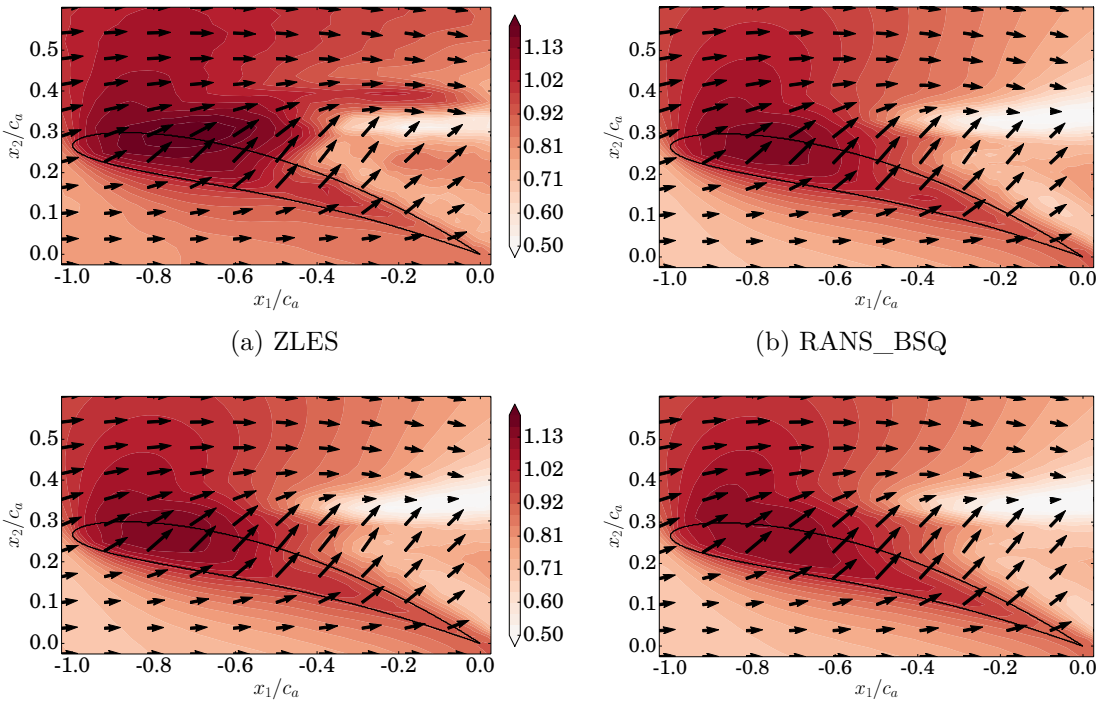

(a) ZLES (b) RANS_BSQ

(c) RANS_QCR (d) RANS_BUA

Figure 11.4: Mean axial velocity through the clearance. The velocity is normalised by u_e. The black arrows represent the planar velocity.

The axial velocity (resp. transverse and span-wise) through the tip-clearance is presented on figure 11.4 (resp. Fig 11.5 and 11.6). The projection of the blade on the plane is also shown (thin black line). The planar velocity direction and magnitude are presented with black arrows.

Concerning the direction of the flow, far from the blade, the flow is essentially axial. In the clearance, an important transverse component appears, with an acceleration from the pressure side to the suction side. This phenomenon is the tip-leakage jet. The ZLES shows an intense axial velocity, with a maximum at $x_1/c_a \approx -0.7$, on the suction side. An important area of lower velocity can be found inside the tip-leakage vortex, with a velocity twice as small as the reference velocity (Fig. 11.4a at $x_3/c_a \approx 0.33$). An important acceleration of the fluid is observed on the transverse component of the velocity in the clearance (Fig. 11.5a for $x_1/c_a \in [-0.7, -0.3]$ and $x_2/c_a \in [0.15, 0.30]$). This acceleration is maximum around 50% of the chord. Concerning the span-wise velocity, the ZLES shows a highly vortical flow. The fluid dive to the end-wall close to the pressure side (Fig. 11.6a), and is driven upward by the tip-leakage vortex on the suction side (Fig. 11.6a for $x_1/c_a \in [-0.5, -0.1]$ and $x_1/c_a \approx 0.3$).

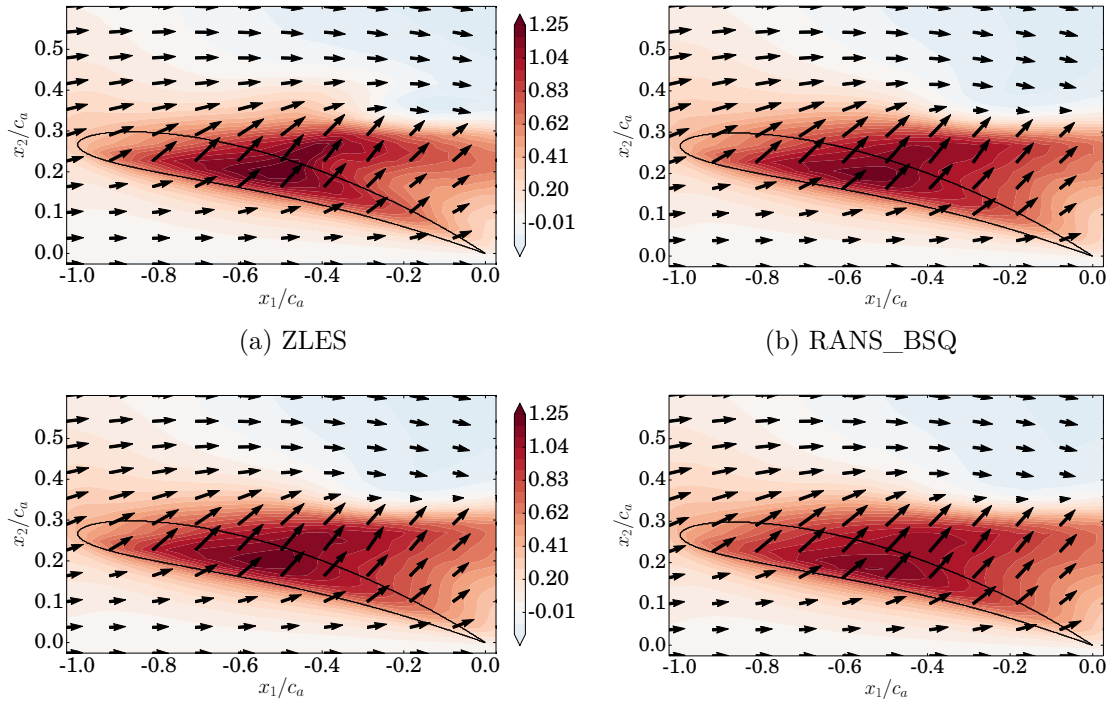

(a) ZLES (b) RANS_BSQ

(c) RANS_QCR (d) RANS_BUA

Figure 11.5: Mean transverse velocity through the clearance. The velocity is normalised by u_e. The black arrows represent the planar velocity.

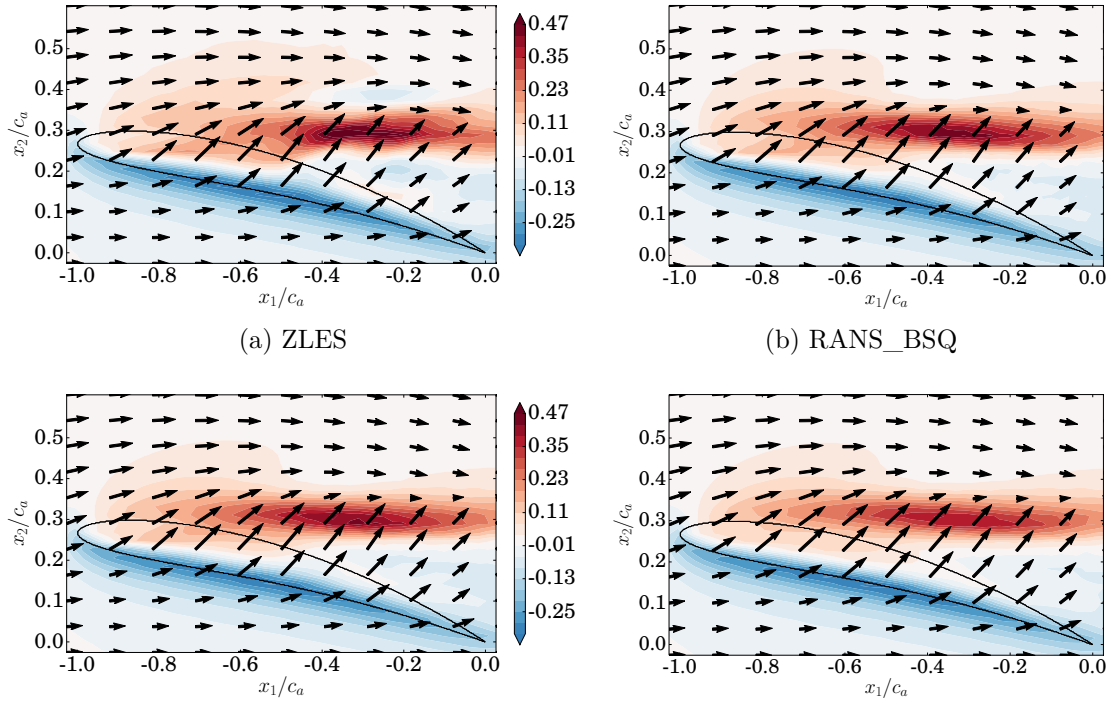

(a) ZLES (b) RANS_BSQ

(c) RANS_QCR (d) RANS_BUA

Figure 11.6: Mean span-wise velocity through the clearance. The velocity is normalised by u_e. The black arrows represent the planar velocity.

The three RANS simulations are able to represent correctly the axial, transverse and span-wise velocities, with comparable levels and topologies. The quadratic model yields little difference on the mean velocities, as does the modified model, compared with the original model. The small influence of the turbulence model on the mean values can be explained by the previous conclusions of Storer and Cumpsty (1991) that the tip-leakage flow is essentially pressure driven.

In the tip-leakage vortex

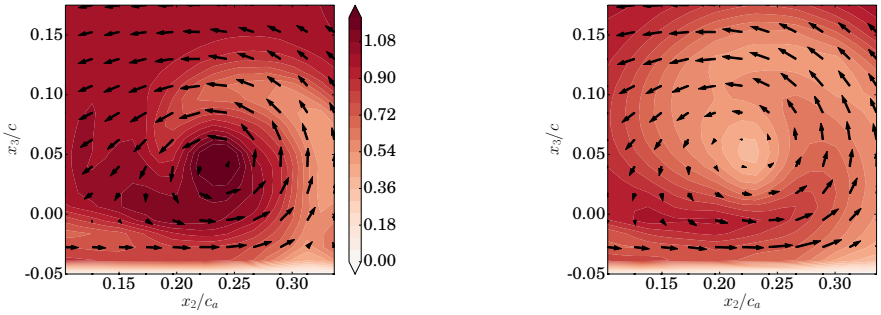

(a) ZLES

(b) RANS_BSQ

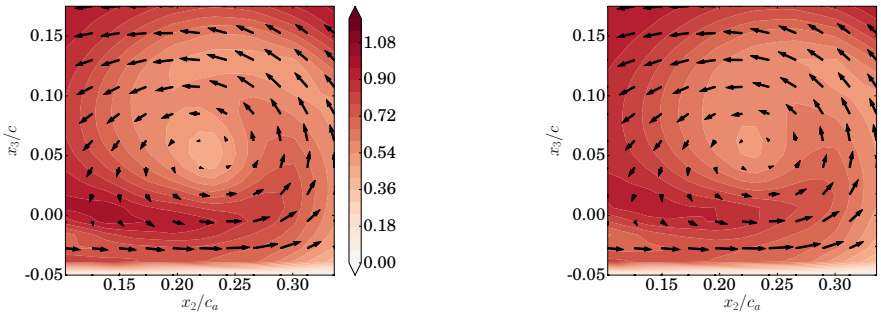

(c) RANS_QCR

(d) RANS_BUA

Figure 11.7: Mean axial velocity in the tip-leakage vortex. The velocity is normalised by u_e. The black arrows represent the planar velocity.

The axial velocity (resp. transverse and span-wise) in the tip-leakage vortex is presented on figure 11.7 (resp. Fig 11.8 and 11.9). The planar velocity direction and magnitude are presented with black arrows.

Concerning the direction of the flow, the vortical behaviour is clearly visible. With respect to the ZLES, the mean velocities calculated by the RANS simulations present a similar topology, but differ on the intensity. The most visible difference is for the axial velocity. The ZLES shows a maximum of axial velocity close to the centre of the vortex (Fig. 11.7a at $x_2/c_a \approx 0.24$ and $x_3/c \approx 0.04$), while for the three RANS simulations the center of the vortex corresponds to a minimum of axial velocity (for instance in figure 11.7b at $x_2/c_a \approx 0.23$ and $x_3/c \approx 0.05$). Moreover, while the ZLES simulation shows a highly vortical flow, the RANS simulations present a more diffused vortex. The RANS prediction of the vortex center is correct, even if it is located a little bit upper than in the ZLES ($x_3/c \approx 0.04$ for the ZLES and $x_3/c \approx 0.05$ for the RANS simulations). The effects of the QCR or the modified Wilcox model are weak compared with the original Wilcox model. Again, it strengthens the idea that the

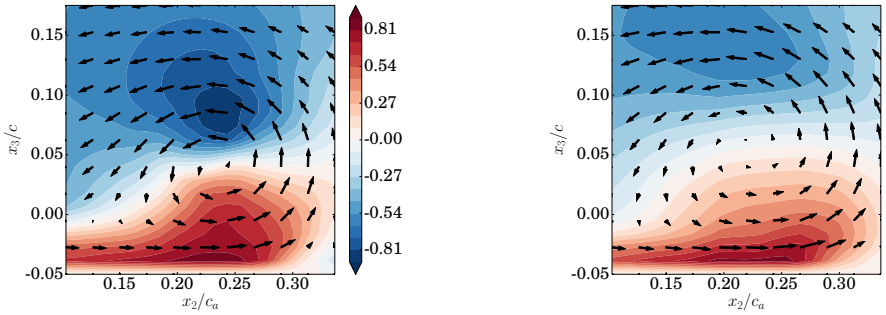

(a) ZLES (b) RANS_BSQ

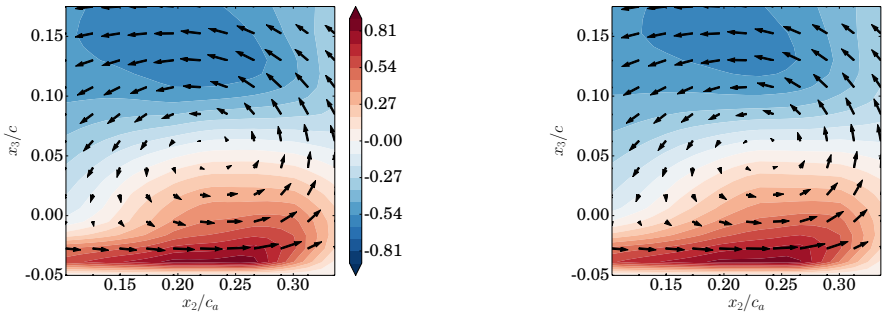

(c) RANS_QCR (d) RANS_BUA

Figure 11.8: Mean transverse velocity in the tip-leakage vortex. The velocity is normalised by u_e. The black arrows represent the planar velocity.

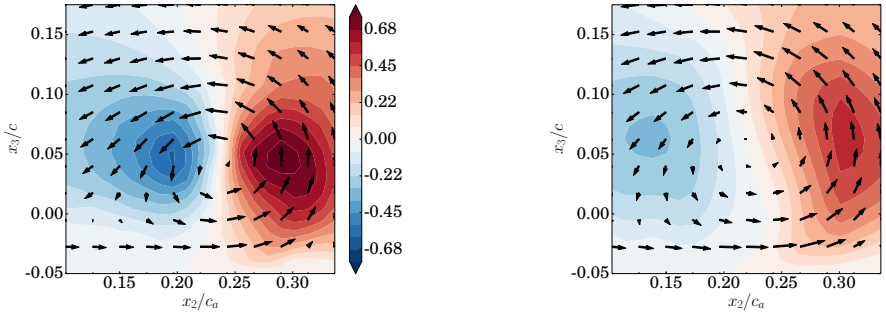

(a) ZLES (b) RANS_BSQ

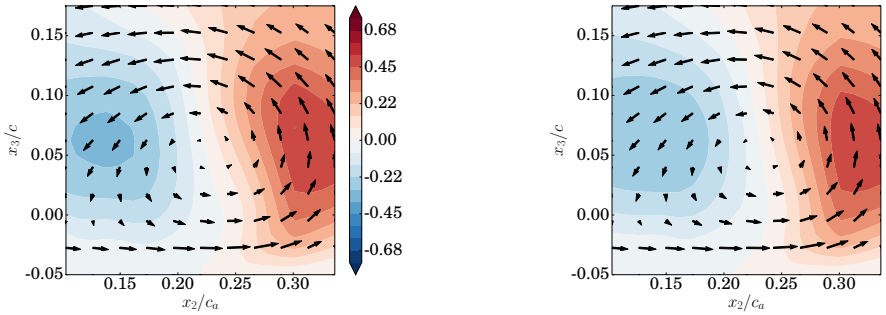

(c) RANS_QCR (d) RANS_BUA

Figure 11.9: Mean span-wise velocity in the tip-leakage vortex. The velocity is normalised by u_e. The black arrows represent the planar velocity.

tip-leakage flow is mainly an inviscid phenomenon.

11.1.5 Mean turbulent kinetic energy

Through the clearance

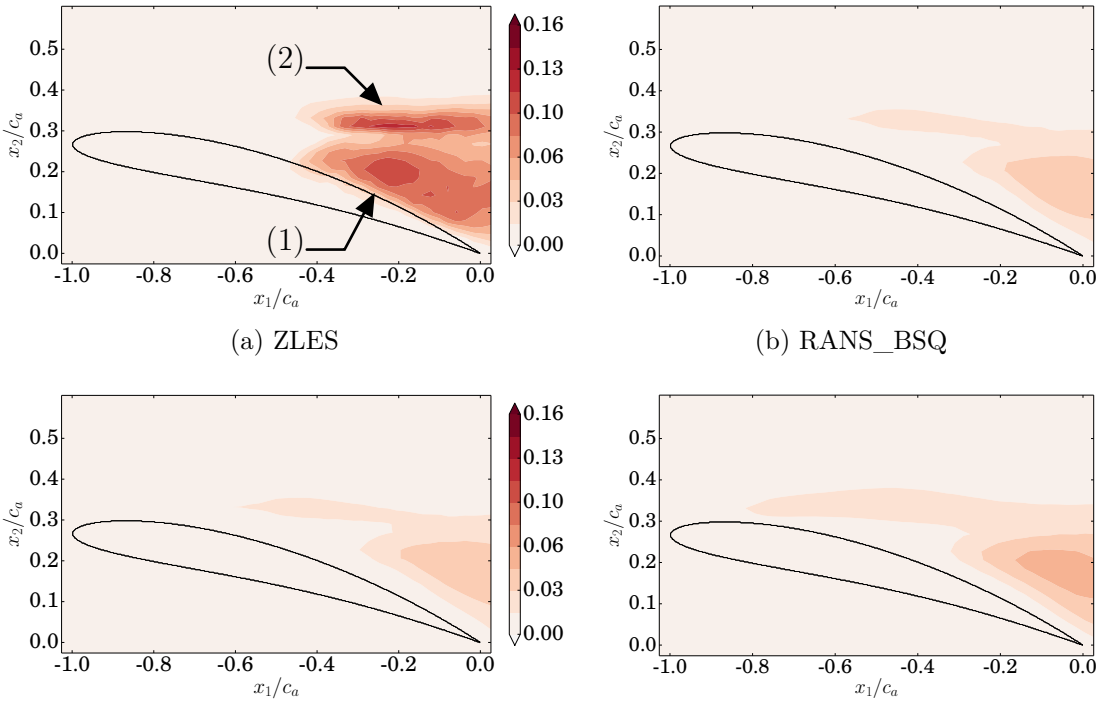

(a) ZLES (b) RANS_BSQ

(c) RANS_QCR (d) RANS_BUA

Figure 11.10: Mean turbulent kinetic energy through the clearance. The specific turbulent kinetic energy is normalised by u_e^2.

Two areas of high intensity can be seen for $[k]$ in the ZLES, one close to the trailing edge (Fig. 11.10a(1)) and the other further from the blade, in the area where the flow goes up through the measurement plane (Fig. 11.10a(2)). The turbulent kinetic energy develops from mid-chord, where the tip-leakage vortex cuts the extraction plane, even though the tip-leakage vortex begins upstream, close to the leading edge (Fig. 11.1). There is no significant turbulent kinetic energy inside the clearance, at mid-gap. This result is similar to what was already observed by Boudet et al. (2009).

The topology is quite well represented by the RANS simulations (Figs. 11.10b, 11.10c and 11.10d), but the intensities are too weak. As for the mean velocities, the modifications induced by the QCR or the modified Wilcox model are negligible. The results are similar to those obtained with the original Wilcox model.

In the tip-leakage vortex

Four areas of high intensity can be seen for $[k]$ in the ZLES: one in the leakage jet (Fig. 11.11a (1)), one in the right-hand side bottom corner of the plane (Fig. 11.11a (2)), one in the right-hand side top corner of the plane (Fig. 11.11a (3)), and one in the center of the tip-leakage vortex (Fig. 11.11a (4)). The leakage jet area and the right-

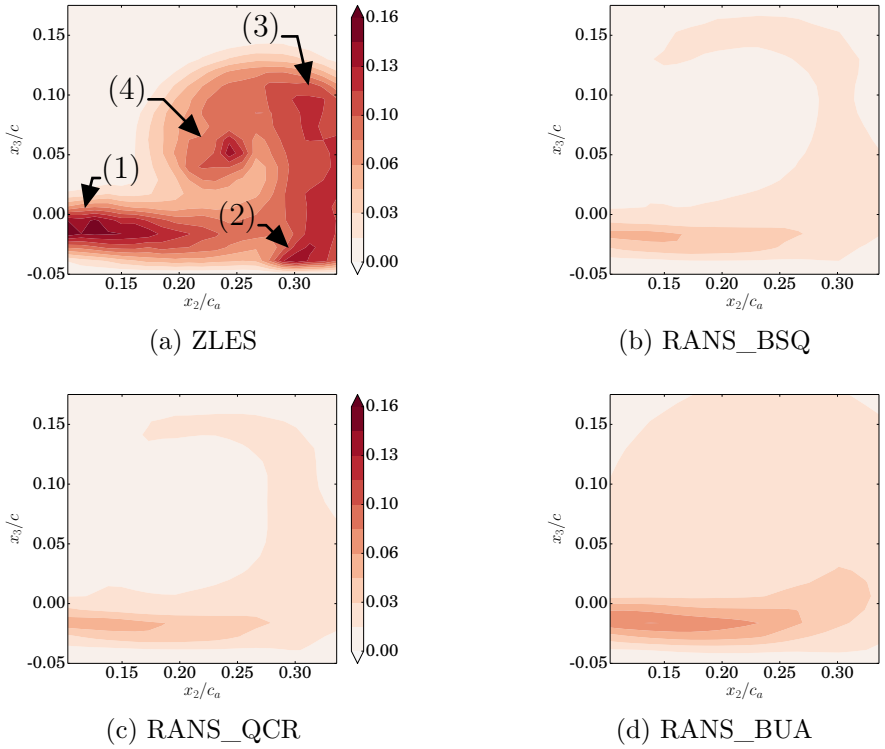

(a) ZLES

(b) RANS_BSQ

(c) RANS_QCR

(d) RANS_BUA

Figure 11.11: Mean turbulent kinetic energy in the tip-leakage vortex. The specific turbulent kinetic energy is normalised by u_e^2.

hand side bottom corner area are the same as on the plane through the clearance (Fig. 11.10a (1), (2)).

The topology is not well represented by the RANS simulations with the original and quadratic Wilcox models (Figs. 11.11b, and 11.11c). If the leakage jet area and the top corner area are present, although too weak, none of the two other areas is visible. There is no significant kinetic energy at the vortex center nor in the bottom corner, where the vortex interacts with the end-wall boundary layer. The three RANS simulations fail at describing these particular areas. The RANS simulation with the modified Wilcox model (Fig 11.11d) increases the levels, but not sufficiently, and does not capture the missing areas. Again, the modifications introduced by the QCR or the modified Wilcox model are weak with respect to the original Wilcox model.

11.2 Reynolds stress analysis

The Reynolds stresses are extracted on the same planes as the mean velocities, and normalised by ρu_e^2.

11.2.1 Through the tip-clearance

Normal stresses

The normal stresses are plotted in Figs. 11.12, 11.13 and 11.14. Two areas of high intensity can be seen in the ZLES. The first area of high intensity is present for all the normal stresses, close to the trailing edge, on the suction side (Figs. 11.12a, 11.13a and

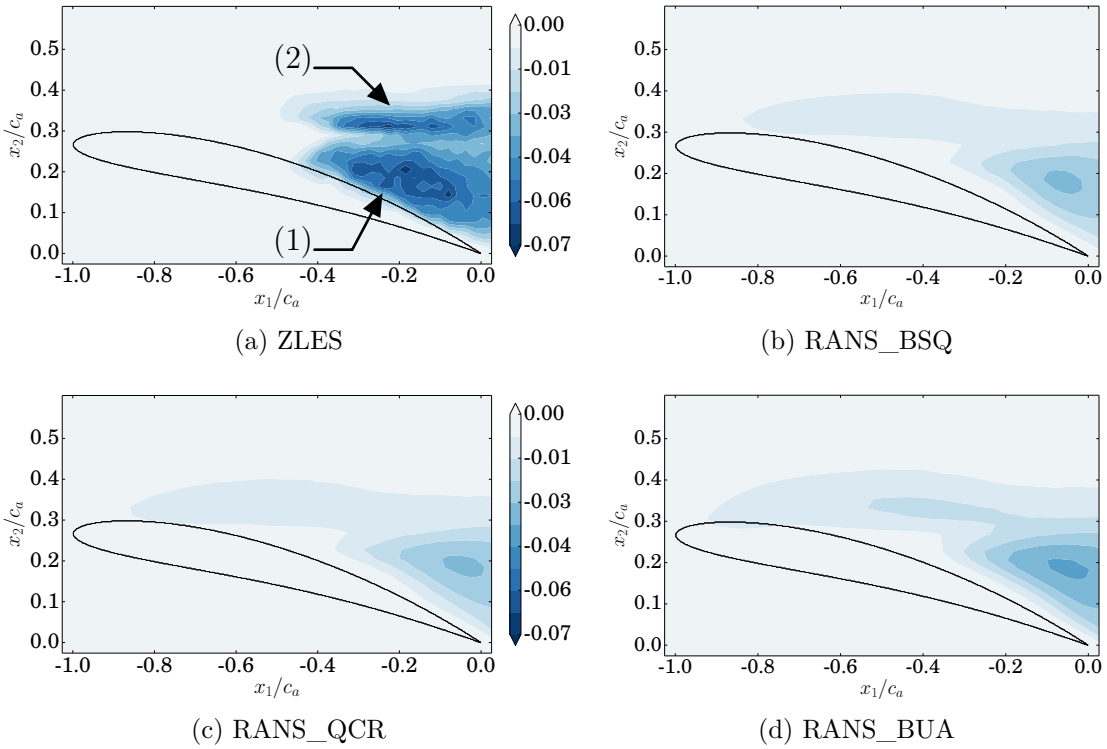

(a) ZLES (b) RANS_BSQ

(c) RANS_QCR (d) RANS_BUA

Figure 11.12: τ_{t11} through the clearance. The Reynolds stress is normalised by ρu_e^2.

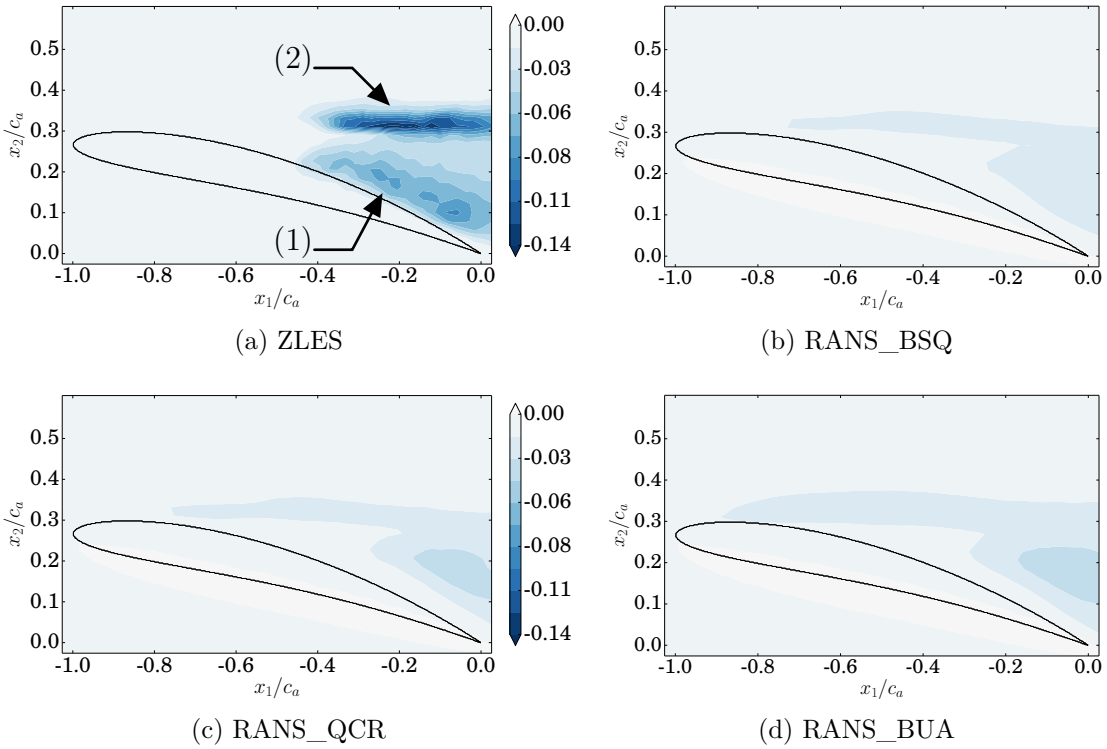

(a) ZLES (b) RANS_BSQ

(c) RANS_QCR (d) RANS_BUA

Figure 11.13: τ_{t22} through the clearance. The Reynolds stress is normalised by ρu_e^2.

11.14a, (1)). This part of the flow corresponds to the leakage jet. The second area of high intensity is further from the blade, where the flow goes up through the cutting

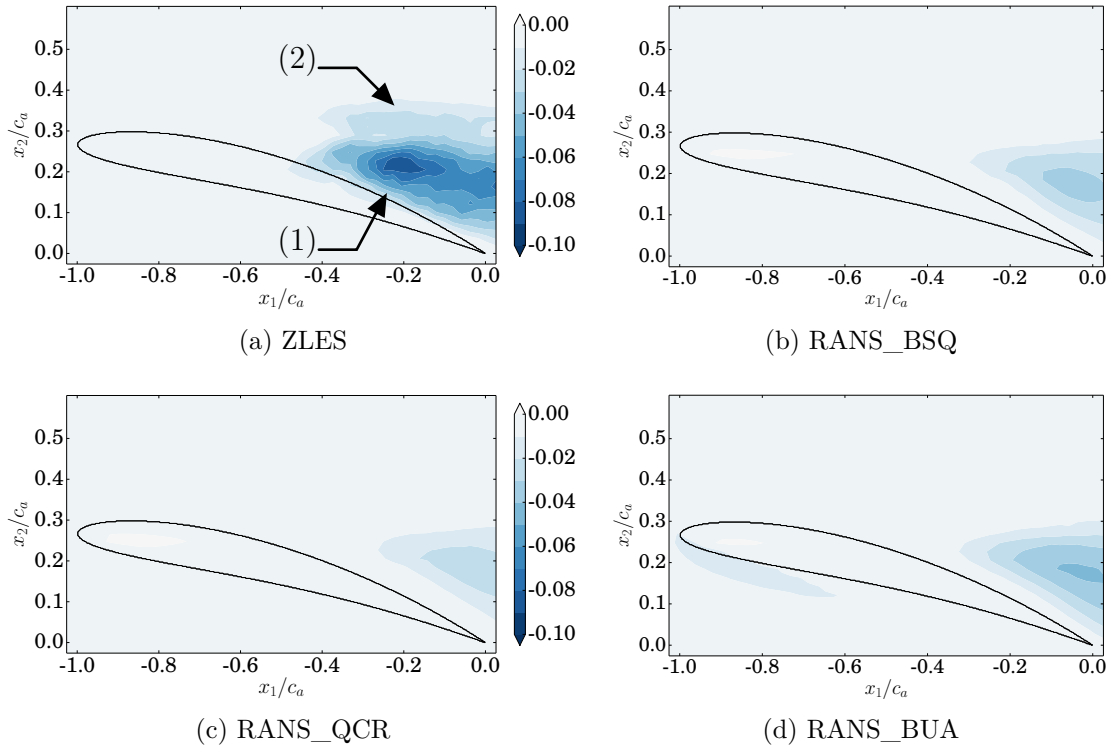

(a) ZLES (b) RANS_BSQ

(c) RANS_QCR (d) RANS_BUA

Figure 11.14: τ_{t33} through the clearance. The Reynolds stress is normalised by ρu_e^2.

plane. This region of high turbulence intensity is present for τ_{t11} and τ_{t22} (Figs. 11.12a and 11.13a, (2)), but is very weak for τ_{t33} (Fig. 11.14a). Both areas present similar intensities for τ_{t11}, while the leakage jet area is less intense than the second area for τ_{t22}. These areas correspond to the areas of high intensity of $[k]$, observed in Fig 11.10a (1) and (2). No area of high normal stress intensity can be found inside the clearance at mid-gap, despite the important acceleration of the transverse velocity. This must be due to the position of the plane inside the clearance, away from the walls.

The area of high intensity on the suction side in the ZLES is present for the three RANS simulations, for the three normal Reynolds stresses. However, this area presents normal Reynolds stresses much less intense than in the ZLES. The normal Reynolds stresses in the second area, further from the blade, are barely visible for both τ_{t11} and τ_{t22} in the RANS simulations. In this area, according to the ZLES, the stresses should be of similar intensity as in the jet area (Fig. 11.12a compared to Figs. 11.12b, 11.12c and 11.12d) or more intense than in the jet area (Fig. 11.13a compared to Figs. 11.13b, 11.13c and 11.13d). The quadratic model increases a little the stresses in the jet area for τ_{t11} and τ_{t22}, and so does the modified model. However, it is far from enough to have levels comparable to the ZLES Reynolds stresses. The quadratic model decreases a little the intensity of τ_{t33} in the jet area (Fig. 11.14c), which worsen the RANS prediction for this normal Reynolds stress, while the modified Wilcox model increases it a little, but still not enough to reach the ZLES levels. Neither the quadratic nor the modified model yield a significant effect on the normal Reynolds stresses in the second area, further from the blade.

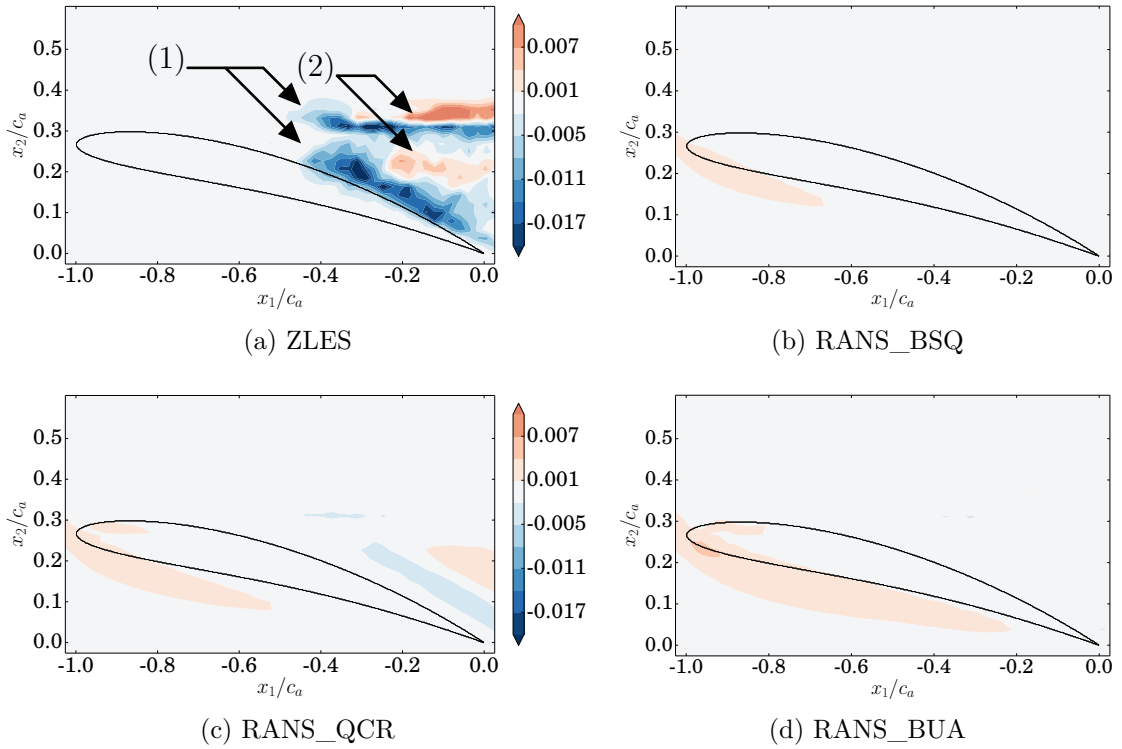

(a) ZLES (b) RANS_BSQ

(c) RANS_QCR (d) RANS_BUA

Figure 11.15: τ_{t12} through the clearance. The Reynolds stress is normalised by ρu_e^2.

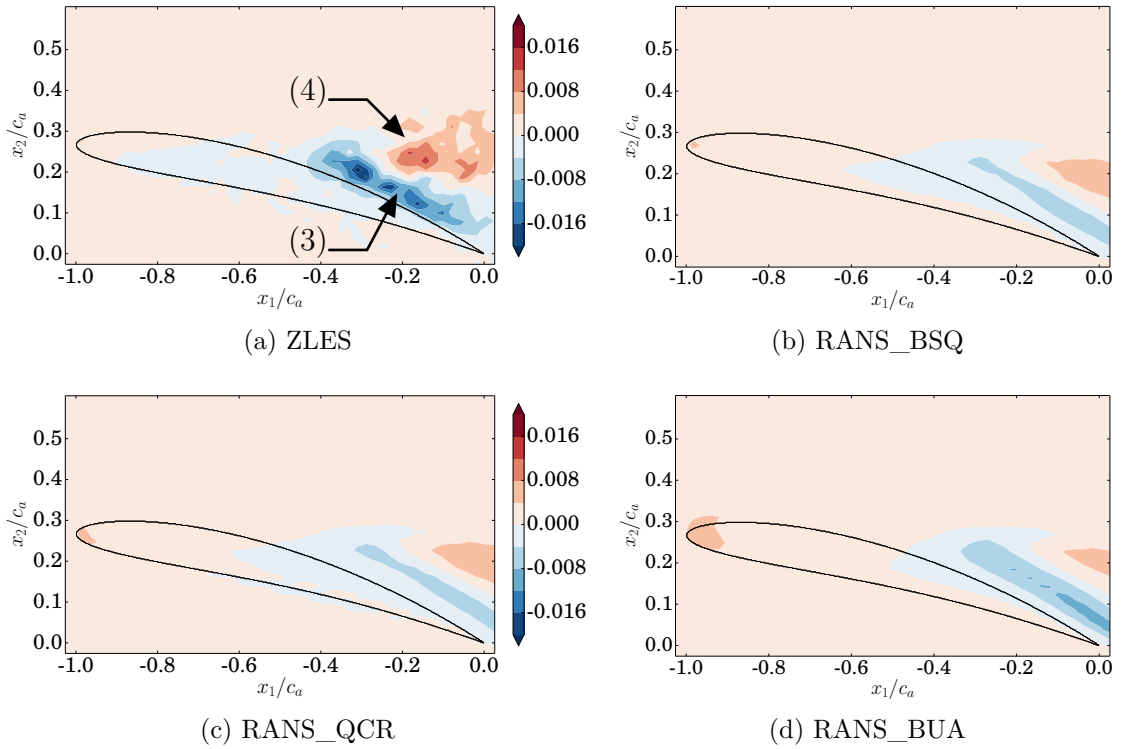

(a) ZLES (b) RANS_BSQ

(c) RANS_QCR (d) RANS_BUA

Figure 11.16: τ_{t13} through the clearance. The Reynolds stress is normalised by ρu_e^2.

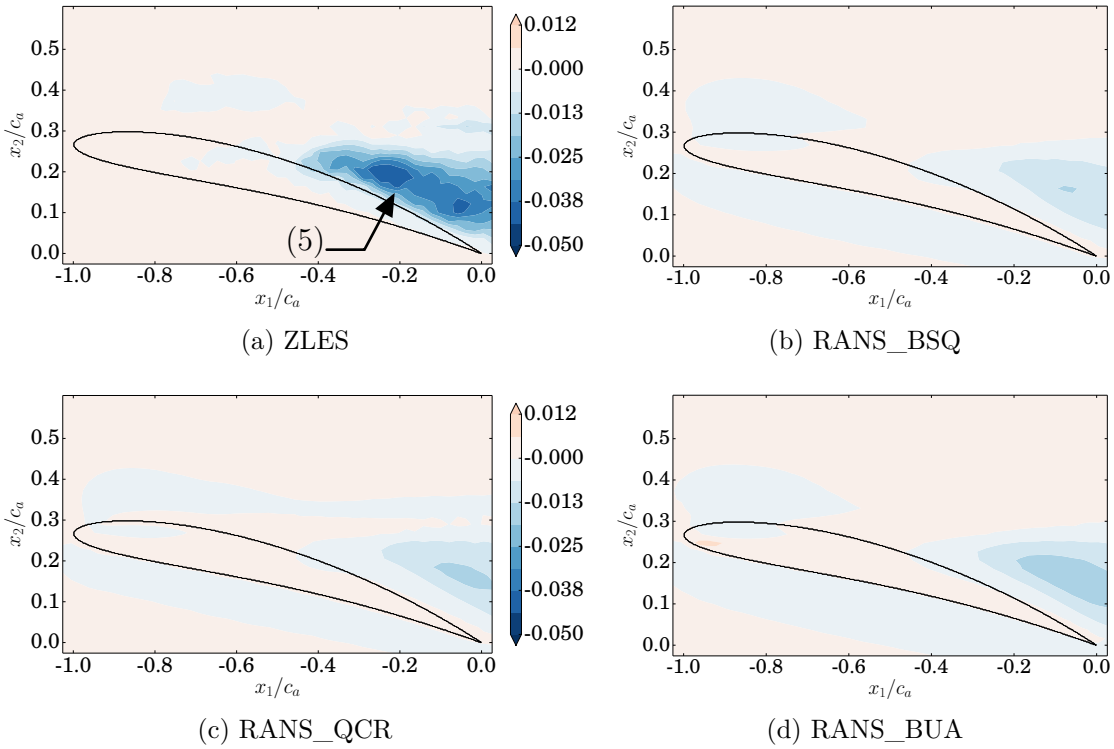

(a) ZLES (b) RANS_BSQ

(c) RANS_QCR (d) RANS_BUA

Figure 11.17: τ_{t23} through the clearance. The Reynolds stress is normalised by ρu_e^2.

Shear stresses

The shear stresses are plotted in Figs. 11.15, 11.16 and 11.17. The shear Reynolds stresses are null in the case of an isotropic flow. Therefore, the shear Reynolds stresses can be used as a measure of the anisotropy of the flow. Concerning the ZLES, the shear Reynolds stress τ_{t12} presents two areas of maximal negative intensity (Fig. 11.15a (1)), superimposed with the maxima of τ_{t11} (Fig. 11.12a), and interlaced with two areas of maximal positive intensity (Fig. 11.15a (2)). The shear Reynolds stress τ_{t13} presents one area of maximal negative intensity, in the leakage jet area close to the blade suction side (Fig. 11.16a (3)), and one area of maximal positive intensity further from the blade (Fig. 11.16a (4)). The last shear Reynolds stress τ_{t23} presents only one area of maximal negative intensity in the jet area (Fig. 11.17a (5)). Again, no area of high stress intensity can be found inside the clearance, at mid-gap.

The RANS shear Reynolds stresses follow the same trend as the normal stresses, *i.e.* an underestimation of the intensity of the stresses. In the case of τ_{t12}, the RANS simulations with the Boussinesq constitutive relation fail completely to represent the topology of the ZLES stress (Fig. 11.15b and 11.15d). The quadratic model yields a better result concerning the topology, with three lobes visible (Fig. 11.15c) out of four in the ZLES case. However, the shear Reynolds stress is still far from being as intense as in the ZLES case. Concerning the shear Reynolds stress τ_{t13}, the three RANS simulations manage to represent the correct topology with two lobes. The intensity is significant but still under-predicted. The quadratic model yields no visible effect on this stress, while the modified model increases the Reynolds stress intensity in the leakage jet. The last shear Reynolds stress is correctly represented in term of topology, for all the RANS simulations (Figs. 11.17b, 11.17c and 11.17d), but still not in term

of intensity. The QCR and the modified Wilcox model increase slightly the intensity of the stress, but it remains much smaller than in the ZLES.

11.2.2 In the tip-leakage vortex

Normal stresses

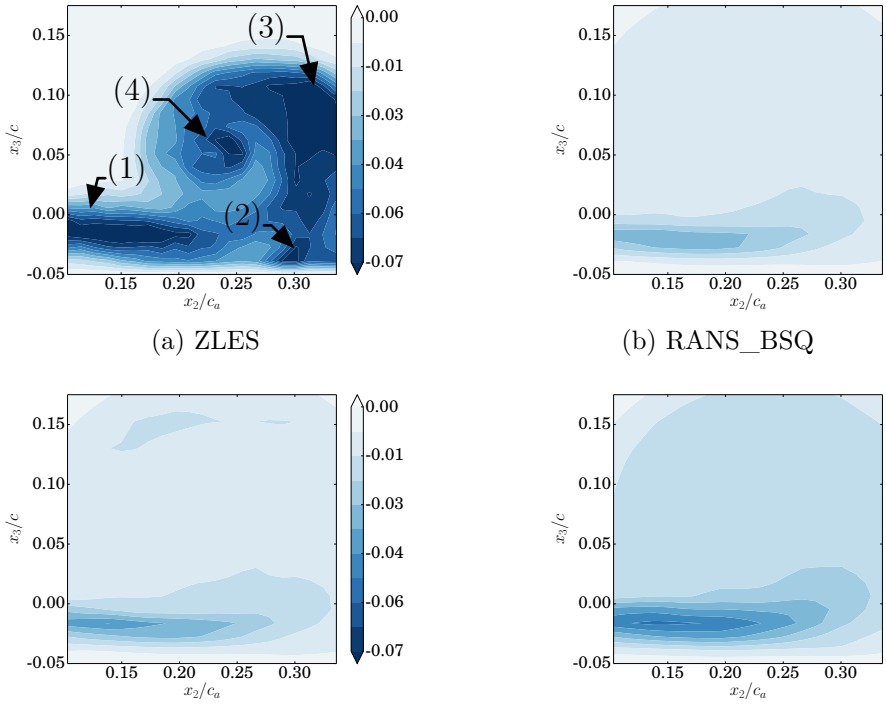

(a) ZLES (b) RANS_BSQ

(c) RANS_QCR (d) RANS_BUA

Figure 11.18: τ_{t11} in the tip-leakage vortex. The Reynolds stress is normalised by ρu_e^2.

The normal stresses are plotted in Figs. 11.18, 11.19 and 11.20. For τ_{t11}, four areas of high intensity can be seen in the ZLES simulation (Fig. 11.18a, (1) − (4)). These are the areas of high intensity of $[k]$, presented in figure 11.11a. For τ_{t22} and τ_{t33}, three out of the four areas are present each time in the ZLES simulation (Figs. 11.19a and 11.20a). The first area is at the bottom left of the figure ($x_3/c \approx -0.02$, Figs. 11.18a, 11.19a and 11.20a (1)), where the jet develops from the leakage through the tip-clearance. The second area is on the border of the vortex, where it interacts with the end-wall boundary-layer, and is particularly intense for τ_{t22} (Fig. 11.19a (2)). The third area is at the top right corner of the figure, on the outer part of the tip-leakage vortex. This area is intense for τ_{t11} and τ_{t33} (Fig. 11.18a, 11.20a (3)). The last area is close to the center of the vortex, for the three components (Fig. 11.18a, 11.19a and 11.20a, (4)).

For the RANS simulations, the normal Reynolds stresses are much less intense than in the ZLES. The most intense regions of the ZLES are partly described by RANS, with a lower intensity: the jet for the three components, the bottom right region for the second component and the top right region for the third component. These last two regions are barely visible in RANS. The quadratic model and the modified model increase a little the three stresses, but it is far from enough to have comparable levels

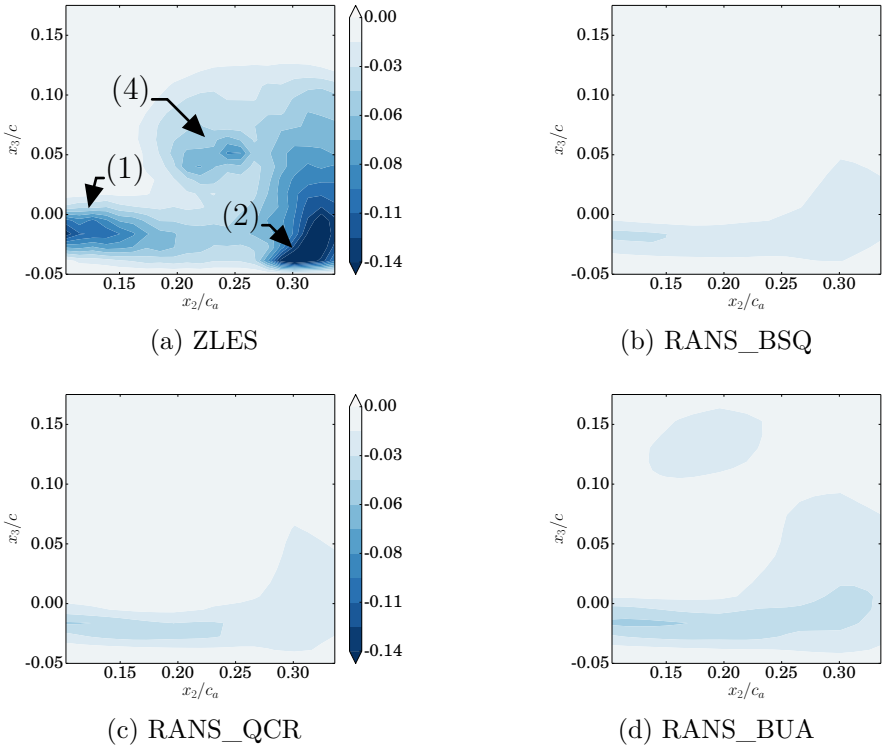

(a) ZLES (b) RANS_BSQ

(c) RANS_QCR (d) RANS_BUA

Figure 11.19: τ_{t22} in the tip-leakage vortex. The Reynolds stress is normalised by ρu_e^2.

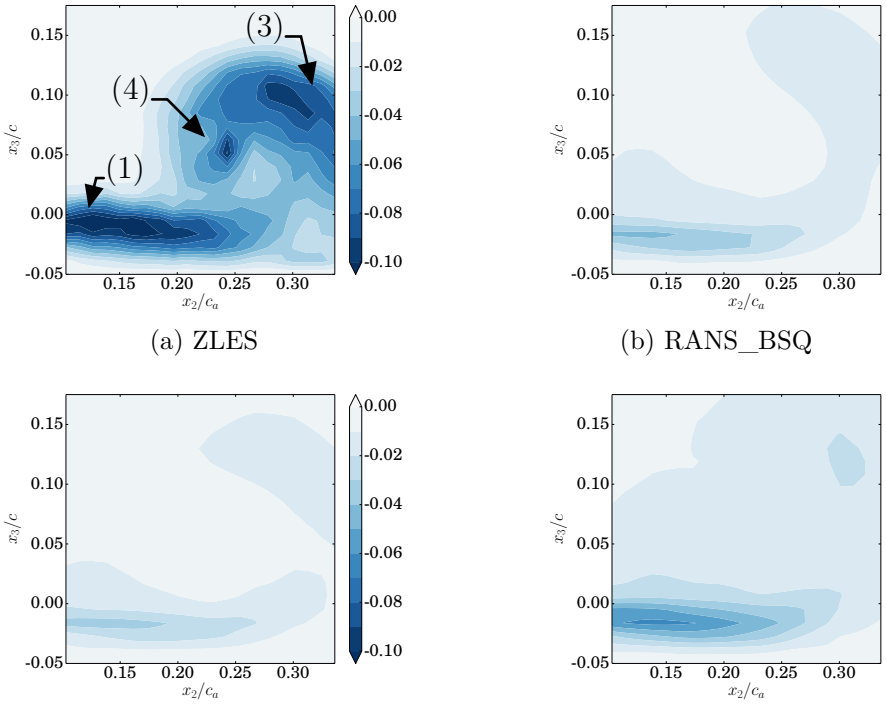

(a) ZLES (b) RANS_BSQ

(c) RANS_QCR (d) RANS_BUA

Figure 11.20: τ_{t33} in the tip-leakage vortex. The Reynolds stress is normalised by ρu_e^2.

with ZLES. The normal Reynolds stresses are clearly under-predicted by the RANS simulations, compared to the ZLES.

Shear stresses

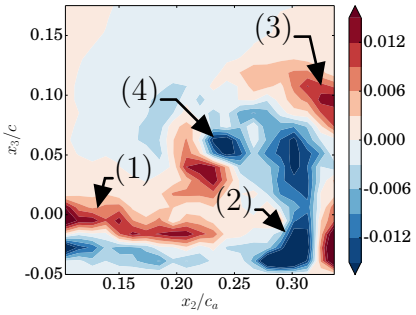

(a) ZLES

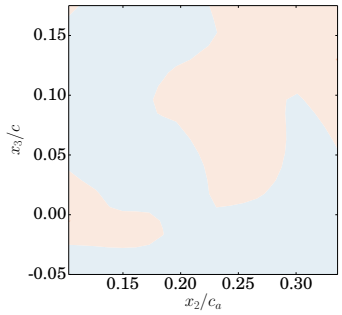

(b) RANS_BSQ

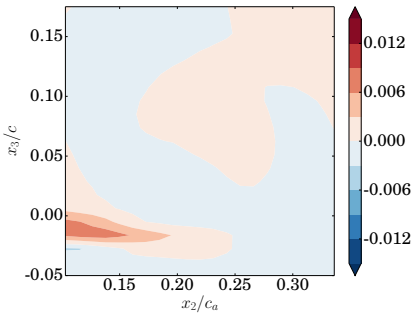

(c) RANS_QCR

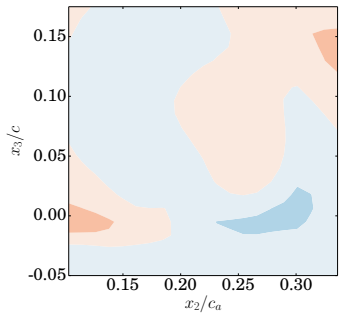

(d) RANS_BUA

Figure 11.21: τ_{t12} in the tip-leakage vortex. The Reynolds stress is normalised by ρu_e^2.

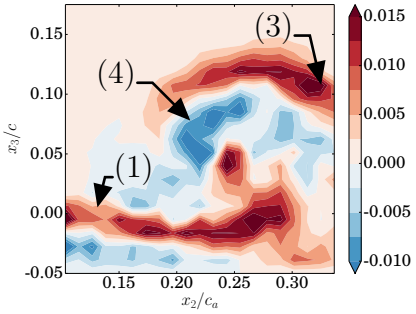

(a) ZLES

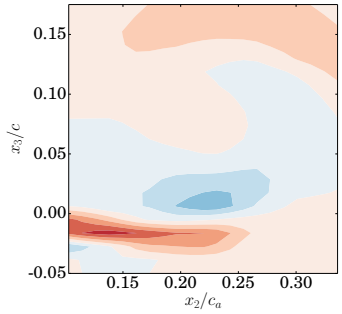

(b) RANS_BSQ

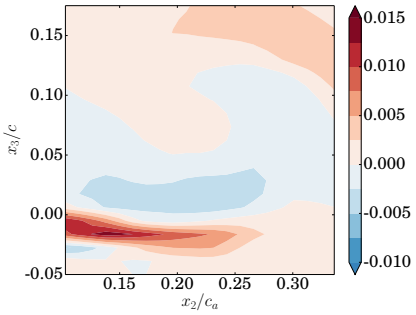

(c) RANS_QCR

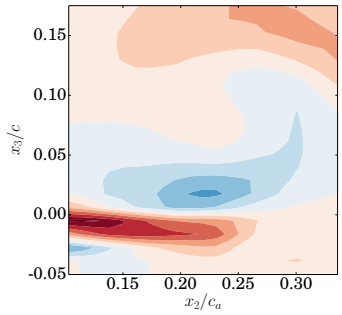

(d) RANS_BUA

Figure 11.22: τ_{t13} in the tip-leakage vortex. The Reynolds stress is normalised by ρu_e^2.

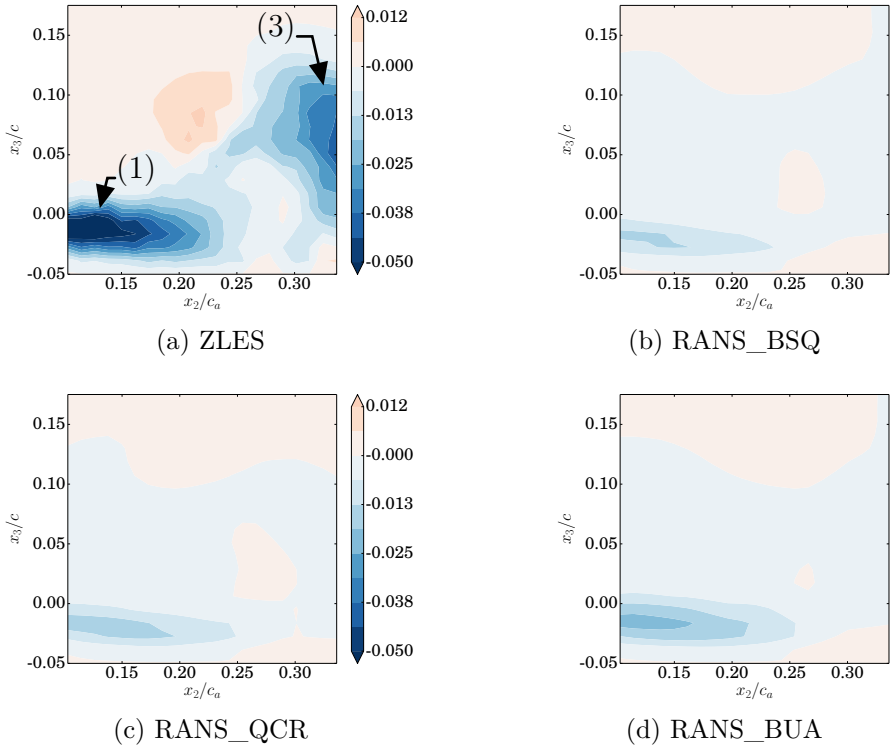

(a) ZLES (b) RANS_BSQ

(c) RANS_QCR (d) RANS_BUA

Figure 11.23: τ_{t23} in the tip-leakage vortex. The Reynolds stress is normalised by ρu_e^2.

The shear stresses are plotted in Figs. 11.21, 11.22 and 11.23. The shear Reynolds stresses follow similar trends as the normal Reynolds stresses, for the ZLES and the RANS simulations. The areas of higher intensity are placed for the ZLES in the jet, on the border of the vortex, and in its center. The values are not negligible, which demonstrates the high anisotropy of this flow. The four areas visible for τ_{t11} are also present for τ_{t12} (Fig. 11.21a, $(1) - (4)$). Each area is doubled into two adjacent areas where the stresses are opposed in sign. For τ_{t13}, three out of the four areas are visible, with again opposite sign lobes (Fig. 11.22a, (1), (3) and (4)). Finally, for τ_{t23}, only the jet area and the right-hand side top corner area are visible, and present only negative stresses, without lobe splitting (Fig. 11.23a, (1), (3)).

The RANS simulations show very weak shear Reynolds stresses. The main area of these stresses is in the jet, for the three simulations. Concerning the models, the main difference comes from the modified model for τ_{t13} in the jet region (Fig. 11.22d), where the intensity is quite comparable with the ZLES. It is not possible to conclude if the weakness of the shear stresses, compared to the ZLES, is due to the difficulties RANS two-equation models are known to have when the flow is anisotropic, or if it is due to the diffusion of the vortex, observed for instance in figure 11.7. The quadratic model, with the QCR, was expected to add anisotropy to the Reynolds stresses, but its effect appears not significant.

11.3 Partial conclusion

Once again, the LES demonstrates its capacity to be used for a fine physical analysis of complex phenomena, and as reference to analyse RANS simulations. For the mean flow values, such as the mean velocities, the RANS simulations present a good agreement

with the ZLES in this particular case, even though the RANS results are more diffused. This is mainly due to the pressure driven nature of the tip-leakage flow.

However, for the turbulent quantities, such as the mean turbulent kinetic energy or the Reynolds stresses, the RANS prediction is always incorrect. The topology of the Reynolds stresses is almost never accurately estimated. The jet leakage area is often present, but the other areas are not visible, due to the important underestimation of the stresses. The quadratic model and the modified model yields small improvements in term of levels, but not sufficient to have comparable results with the ZLES.

The RANS modelling of the Reynolds stresses depend on both the constitutive relation used and the eddy-viscosity modelling, with the use of equations on k and ω. The following chapters aim at inspecting the validity of the constitutive relation and the validity of the modelled k equation.

Chapter 12

Tip-leakage constitutive relation analysis

Sections

THE comparison between the LES Reynolds stresses and the RANS Reynolds stresses in the previous chapter lead to the conclusion that the turbulence modellings on which the RANS simulations rely do not accurately predict the physics. The present chapter analyses more precisely RANS turbulence modelling, through one of its two main components, the constitutive relation. LES is used as reference to test the validity of the two hypotheses of the constitutive relations studied, the Boussinesq constitutive relation and the QCR, which are the tensor alignment hypothesis and the hypothesis on the choice of the proportionality coefficient.

12.1 Evaluation methods

The evaluation methods have already been presented in details in chapter 8, section 8.1. The main aspects are merely recalled in the following sections.

12.1.1 Constitutive relation alignment

The constitutive relation alignment is tested using the two alignment indicators presented in equations (8.2) and (8.5). The first indicator concerns the alignment hypoth-

esis on which the Boussinesq constitutive relation relies, while the second indicator concerns the alignment hypothesis on which the QCR relies.

As for the Schmitt indicator, introduced in equation (2.50), when the alignment indicators are equal to 1, the tensors are aligned, *ergo* proportional, and the alignment hypothesis is, by definition, valid. When the alignment indicators are equal to 0, the tensors are orthogonal, and the alignment hypothesis is invalid. Contrary to the Schmitt one, the present alignment indicators can be negative. In this case, the tensors are anti-aligned, which means that the Boussinesq constitutive relation or the QCR yield non-physical results. The same threshold of 0.86 is kept. If the indicators are greater than 0.86, the alignment hypothesis is considered valid. An illustration has been given for vectors in figure 8.1 (chapter 8, section 8.1).

12.1.2 Eddy-viscosities

The eddy-viscosity represents the proportionality coefficient between the Reynolds stress tensor and the constitutive relation tensor. The same eddy-viscosity constructions as presented in equations (8.7) and (8.8) are investigated here.

12.2 Alignment analysis

The alignment is gauged with the Υ indicator (resp. Υ^{QCR} indicator) presented in equation (8.2) (resp. (8.5)), plotted as probability density functions (PDF) and cumulative distribution functions (CDF) of the indicator value. Concerning the PDF (for instance, in Fig. 12.2a), the bar goes by couple, a left black bar with a right green bar. A couple of bars occupies a range of 0.05. The black one (resp. green one) represents the mass weighted percentage of points with Υ (resp. Υ^{QCR}) in the given 0.05 range. Concerning the CDF (for instance in Fig. 12.2a), the integration of the PDF is made from -1 upward, so practically, the ordinate corresponding to the abscissa $\Upsilon = 0.86$ (resp. $\Upsilon^{QCR} = 0.86$) represents the mass weighted percentage of points for which the Boussinesq constitutive relation (resp. QCR) is not valid.

The analysis is focused on the regions where turbulence is sufficiently intense. Only the points where the turbulence rate (defined as $(2/3[\widetilde{k}]/([\widetilde{u_i}][\widetilde{u_i}]))^{1/2}$) is superior to 5% participate to the distribution. This threshold value is chosen so that the turbulent inlet boundary-layer and the tip-leakage vortex are included in the analysis. In order to be grid independent, each point considered is weighted by its mass, calculated as the square root of the Jacobian at that point (homogeneous to a volume) times the density. The analysis focuses first on the entire domain, which includes the inlet domain, the tip-clearance domain and the tip-leakage vortex domain, as presented in figure 12.1. Then, each individual domain is analysed separately. The inlet domain is the domain where the incoming boundary-layer develops, the clearance domain is the domain located in the tip-clearance, and the tip-leakage vortex domain is the volume on the suction side of the blade where the tip-leakage vortex develops downstream. All the domains are located inside the LES zone of the flow.

12.2.1 Entire domain

The probability density functions (PDF) and cumulative distribution functions (CDF) of the alignment criteria for the entire domain are plotted in figure 12.2. Both the

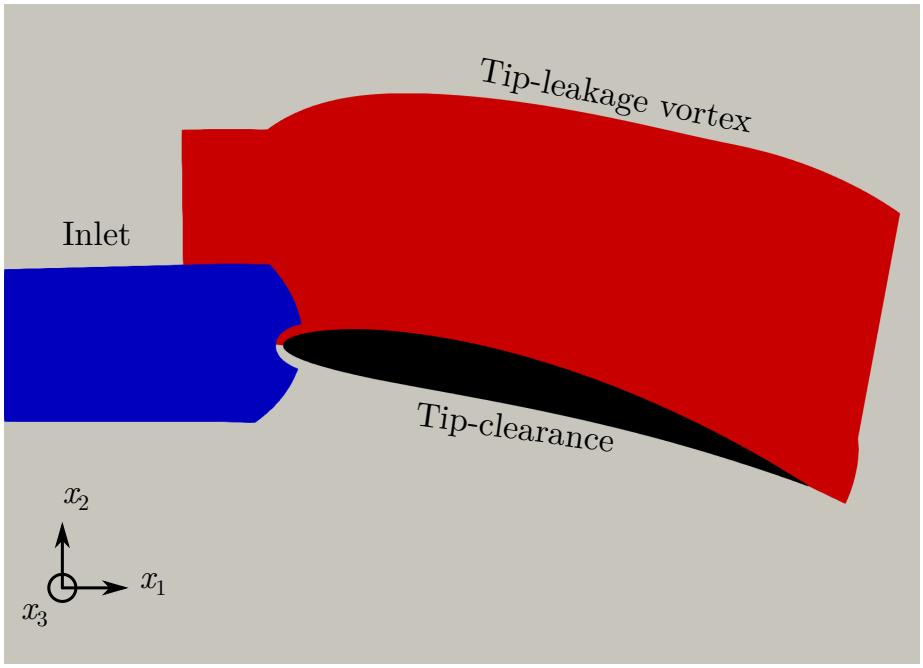

Figure 12.1: Domains used for the alignment criterion analysis. Blue: Inlet, black: tip-clearance, red: tip-leakage vortex, grey: unused

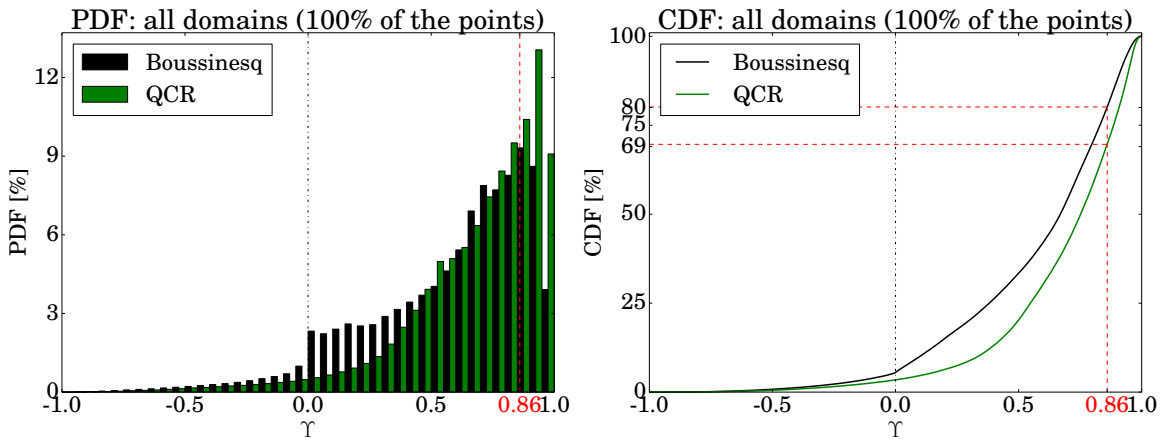

(a) PDF (b) CDF

Figure 12.2: PDF (a) and CDF (b) of the Υ and Υ^{QCR} criteria in the entire domain.

Boussinesq constitutive relation and the QCR present points with a negative criterion, meaning an opposite orientation between the Reynolds stress tensor and the constitutive relation tensor. For both constitutive relations, the quantity of anti-aligned points remains small, with less than 5% of the points concerned. The PDF of Υ increases from 0 to 0.75 and then decreases abruptly, showing that the vast majority of the points tested does not present a correct alignment between the tensors. The decreasing is more abrupt for the Boussinesq constitutive relation than for the QCR. The peak of the distribution is in the interval $[0.85,\ 0.90]$ for the Boussinesq constitutive relation. In comparison, Υ^{QCR} presents fewer points in each range between 0.0 and 0.5 and more points in the upper ranges, with its peak in the interval $[0.9,\ 0.95]$. The CDF shows the Boussinesq constitutive relation is not valid for 80% of the points, whereas

the QCR is not valid for 69% of the points. The QCR has a significant beneficial impact on the alignment of the tensors. However, this impact is less important than in the corner separation case (*c.f.* figure 8.3).

The analysis will now focus specifically on the inlet domain, the tip-clearance domain and the tip-leakage vortex domain in order to see if the constitutive relations present different behaviours when confronted to different flow types.

12.2.2 Inlet domain

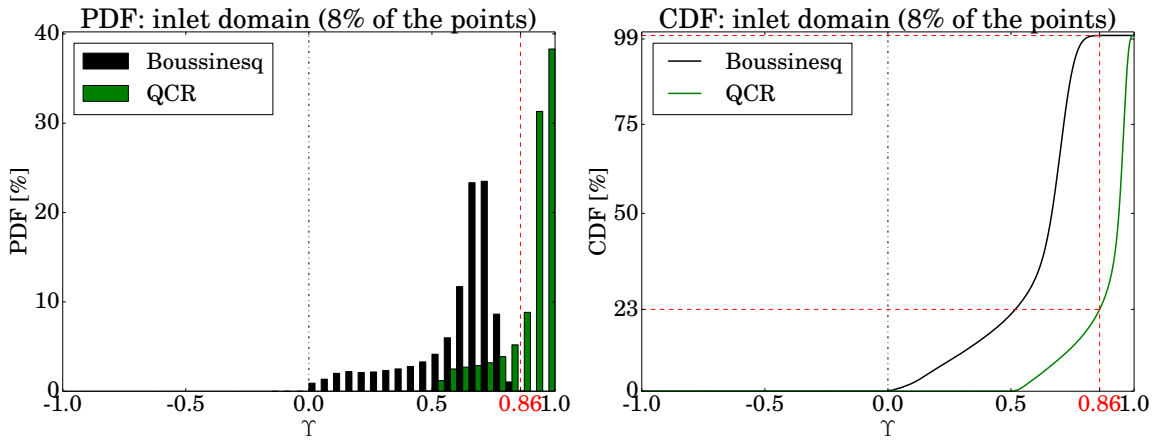

(a) PDF (b) CDF

Figure 12.3: PDF (a) and CDF (b) of the Υ and Υ^{QCR} criteria in the inlet domain.

The inlet domain, located upstream the blade, presents the characteristics of a fully turbulent boundary layer. The number of points from this domain, weighted by the mass, represents 8% of the total mass-weighted number of points. The PDF and CDF of the inlet domain are given in figure 12.3. Similarly to what was found for the corner separation case, the Boussinesq constitutive relation yields bad results on this canonical flow. The distribution is similar to the one of the entire domain, but the peak is in the interval $[0.7,\ 0.75]$, and there is no negative alignment. The CDF shows that the overall alignment is worse, with 99% of the points for which the Boussinesq constitutive relation is not valid. As in the corner separation inlet, the QCR presents quite an improvement in this area. The peak of the PDF is in the interval $[0.95,\ 1.0]$, and the CDF shows that the constitutive relation is valid, in term of alignment, for 77% of the points. This situation is very similar to what was found for the inlet of the corner separation, and confirms that the QCR have an important effect on this canonical flow. The explanation is the same as before: the calibration of the constant c_{QCR} has been done originally in the outer region of a simple boundary layer (Spalart, 2000).

12.2.3 Tip-clearance domain

The tip-clearance domain is located between the blade tip and the end-wall. The pressure difference between the pressure side and the suction side of the blade creates an important acceleration of the flow toward the suction side. The flow topology is more complex than the inlet domain boundary layer. The number of points from this

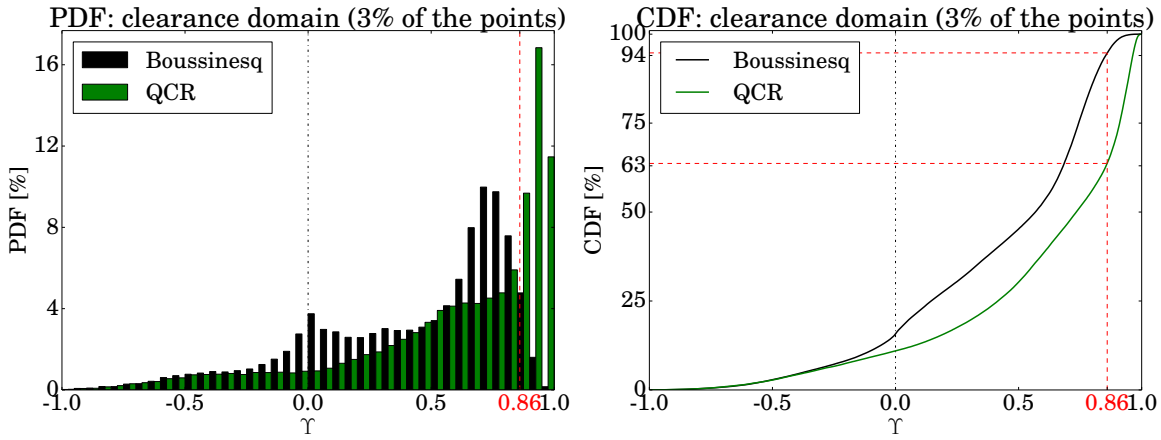

(a) PDF (b) CDF

Figure 12.4: PDF (a) and CDF (b) of the Υ and Υ^{QCR} criteria in the tip-clearance domain.

domain, weighted by the mass, represents only 3% of the total mass-weighted number of points. The PDF and CDF of the clearance domain are given in figure 12.4. The Boussinesq constitutive relation yields a distribution with two peaks: a small peak in the interval [0.0, 0.05] and a maximum in the interval [0.7, 0.75]. Around 12% of the points are negatively aligned for the Boussinesq constitutive relation, which is not negligible. No certain explanation has been found concerning this important non-physical behaviour. The CDF is comparable to the previous results for Υ, with 94% of the points for which the Boussinesq hypothesis is not verified. The QCR yields again better results in term of tensor alignment, but the improvement is not as important as for the inlet domain. A significant number of points still present an anti-alignment between the tensors. Only one peak is noticeable though, in the interval [0.9, 0.95]. The peak is inside the area where the alignment hypothesis is verified, and the CDF indicates 47% of the points are valid.

12.2.4 Tip-leakage vortex domain

The last domain is located on the suction side of the blade. It is the domain where the tip-leakage vortex develops downstream. The flow is three-dimensional and vortical, and probably more complex than in the previous domains. It is comparable to the outlet domain of the corner separation, except that in the present case, the vortical structures are bigger and more coherent. The number of points from this domain, weighted by the mass, represents 88% of the total mass-weighted number of points. The PDF and CDF of the tip-leakage vortex domain are given in figure 12.5. Surprisingly, the Boussinesq constitutive relation yields better results compared to the results on the simple boundary-layer at the inlet. A few negatively aligned points are present (around 5% for both constitutive relations). Concerning the QCR, almost no improvement is visible compared to the Boussinesq constitutive relation. The difference in term of alignment correction on the CDF is about 3%. In this complex, vortical region, the QCR behaviour, in term of tensor alignment, is much closer to the Boussinesq constitutive relation than in the boundary layer at the inlet. The CDF shows that the quantity of misaligned points is much smaller compared to the previous results

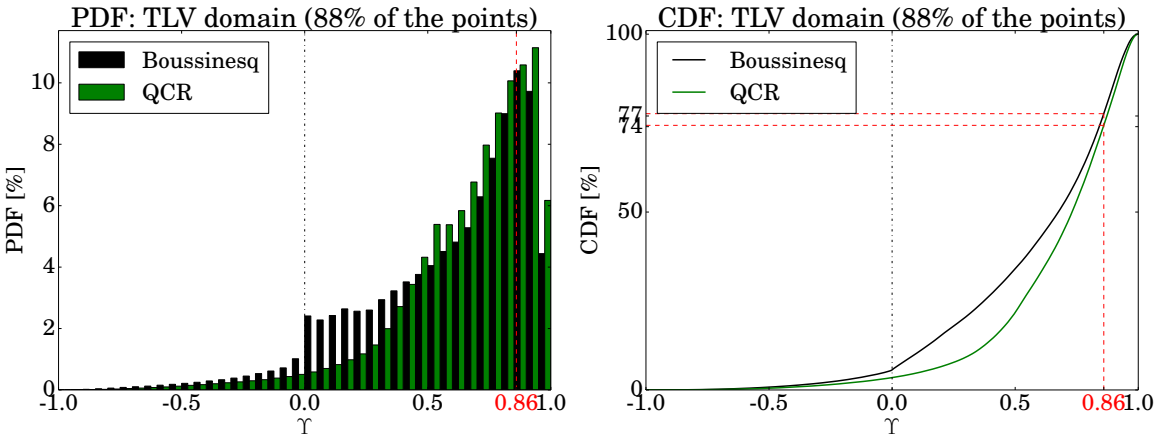

(a) PDF (b) CDF

Figure 12.5: PDF (a) and CDF (b) of the Υ and Υ^{QCR} criteria in the tip-leakage vortex domain.

for Υ (Boussinesq), with "only" 77%, but for Υ^{QCR} the number of points where the tensors are not aligned raises to 74%. As for the corner separation case, this result is counter-intuitive. Given that the formulation of the QCR explicitly contains a normalised rotation tensor, it was expected to be more effective in highly vortical areas. However, in both the corner separation case and the present tip-leakage case, the opposite occurs.

12.3 Eddy-viscosity comparisons

The eddy-viscosities, defined in equations (8.7−8.8), are plotted in figure 12.6. They are compared to the eddy-viscosities extracted from the three RANS simulations studied. They are plotted on the plane through the tip-leakage vortex, presented in figure 11.2b, and normalised by the dynamic viscosity $\mu = 1.81 \times 10^{-5}\text{kg.m}^{-1}.\text{s}^{-1}$.

It is remarkable that the three ZLES eddy-viscosities present a similar topology, and are comparable in term of intensity. $\mu_t^{(1)}$, defined as $< \overline{\rho} > [\widetilde{k}]/[\widetilde{\omega}]$, is a bit more intense (about three times) than $\mu_t^{(0)}$ or $\mu_t^{(0)QCR}$, computed as the ratio of two tensor norms. They remain of the same order of magnitude, which indicates the estimates of μ_t as $< \overline{\rho} > [\widetilde{k}]/[\widetilde{\omega}]$ is physically sound. However, the RANS simulations present smaller eddy-viscosities. This may be a consequence of the general behaviour of the RANS simulations to underestimate the turbulent quantities in this particular case. Given the similarity between the values of $\mu_t^{(0)}$ and $\mu_t^{(0)QCR}$, the QCR bears no significant modification on the norm of The constitutive relation tensor. As seen previously with the PDFs, the Boussinesq constitutive relation and the QCR have almost the same behaviour in the tip-leakage vortex domain. The conclusion is that the QCR has only a weak effect on the constitutive relation tensor, in the tip-leakage vortex. It realigns it slightly, with little effect on its norm. Its influence is essentially a rotation.

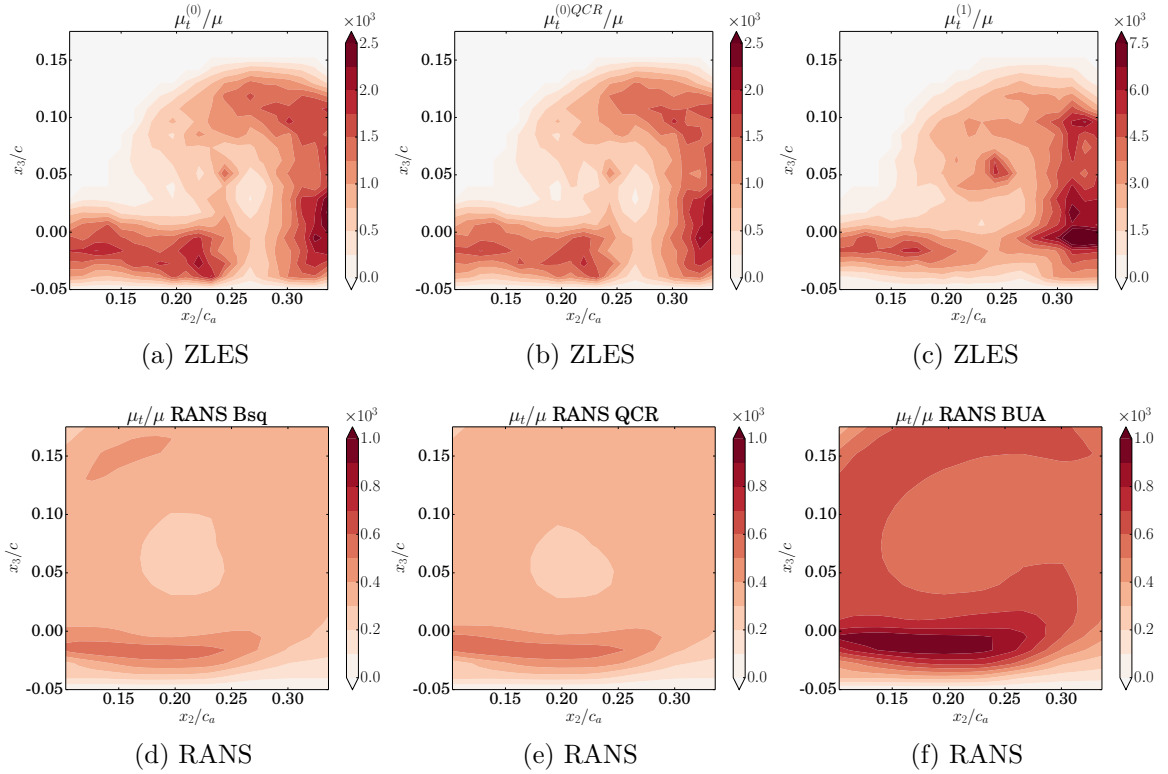

(a) ZLES (b) ZLES (c) ZLES

(d) RANS (e) RANS (f) RANS

Figure 12.6: Eddy-viscosity comparison in the tip-leakage vortex. For the sake of readability, the figures are scaled differently.

12.4 Partial conclusion

The two constitutive relation tested rely on a set of two hypotheses, an hypothesis of tensor alignment and an hypothesis on the manner to calculate the proportionality coefficient (turbulent viscosity). The first hypothesis has been tested with an alignment indicator, derived from the inner product of the two tensors. The hypothesis of alignment is rarely verified for the Boussinesq constitutive relation, with around 80% of the mass-weighted points where the misalignment is higher than an angle of $\pi/6$. The Boussinesq constitutive relation yields similar results in all the studied subdomains. The quadratic constitutive relation succeeds in realigning the constitutive relation tensor with the Reynolds stress tensor for around 11% of the mass-weighted points. The correction impacts very favourably the inlet, where a flat-plate boundary layer develops, with flow characteristics close to the ones used for the QCR calibration. The impact of the QCR decreases in the tip-clearance and in the tip-leakage vortex regions. In the tip-leakage vortex region, the QCR yields results very close to the Boussinesq constitutive relation. These results complete the observations and confirm the conclusions made on the corner separation case.

The second hypothesis has been tested by measuring the ratios of the tensor norms, and by comparing them to the ratio $< \overline{\rho} > [\widetilde{k}]/[\widetilde{\omega}]$ extracted from the ZLES, and to the eddy-viscosities calculated with the three RANS simulations. All the eddy-viscosities present similar amplitudes and topologies for the ZLES. The RANS eddy-viscosities are much smaller than the ZLES ones. This is due to the important underestimation of all the turbulent quantities in the RANS simulations, as presented in chapter 11.

Based on the ZLES, the choice of k and ω to compute the eddy-viscosity is legitimate. The viscosities computed as the ratios of the norms of the tensors are very similar, yielding that the QCR rotates the constitutive relation tensor without dilating it.

As for the corner separation case, the Boussinesq constitutive relation shows an important alignment default, but the calculation of the coefficient of proportionality (turbulent viscosity) from modelled statistics is legitimate. To correct the alignment, the path seems to add a rotation to the zero-trace mean strain-rate tensor in order to realign it with the Reynolds stress tensor. The QCR goes in that direction, but is not sufficient in the highly vortical part of the flow. The correction may be improved to be more accurate. A general approach, introduced by Pope (1975) and presented in the conclusion of chapter 8, could be investigated on the present flow cases.

Chapter 13

Tip-leakage TKE budget analysis

Sections

THE turbulent kinetic energy budget shows the physics of turbulence through the production, dissipation and transport. For the RANS simulations with a k equation, it shows the ability of the model to represent correctly the fine physics of turbulence. The TKE budget is extracted on the same two planes as the Reynolds stresses. They are presented in chapter 11 (*c.f.* Fig. 11.2). The TKE budget terms are normalised by $(\rho^2 u_e^4)/\mu$.

13.1 Statistical convergence

The numerical residual term, presented in figures 13.1a and 13.1c, is used to gauge the closure of the TKE budget. This term results from the numerical effects, such as artificial viscosity effects, numerical dissipation, or statistical convergence imperfection. In the ZLES case, the term can be positive or negative, and seems roughly opposed to the transport term (Figs. 13.5 and 13.9). The term is really intense, and no such effect was observed in the previous cases (flat-plate and corner separation). The residual seems to counter-part the spatial oscillations of the transport term. The transport term includes triple correlations, which necessitate many samples to be statistically

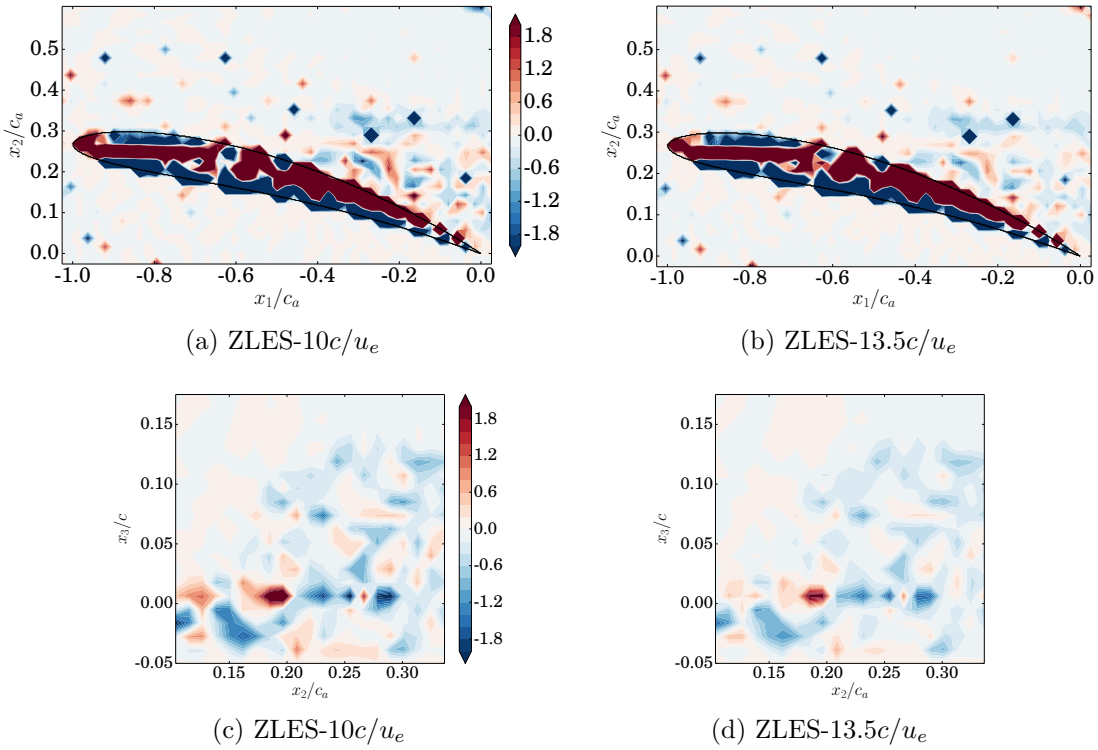

(a) ZLES-10c/u_e (b) ZLES-13.5c/u_e

(c) ZLES-10c/u_e (d) ZLES-13.5c/u_e

Figure 13.1: Comparison of the numerical residuals of the ZLES, with different sampling duration. (a), (c): statistics accumulated during 10 through flow periods. (b), (d): statistics accumulated during 13.5 through flow periods. (a), (b): through the tip-clearance. (c), (d): in the tip-leakage vortex.

converged. The statistics have been originally computed over ten through-flow periods ($10c/u_e = 28.57$ms). In order to test if the strong numerical residual is a consequence of a lack of statistical convergence, the computation have been run over three and a half more through-flow periods ($\approx$ 10ms). For computational cost reasons, only the acquisition of these three and a half more through-flow periods has been possible during this work. The results are presented in figures 13.1b and 13.1d.

The residual computed over 13.5 periods is slightly smaller everywhere, compared to the residual computed over 10 periods. However, the difference is far from being sufficient to consider that the statistics are converged. Besides, no difference is visible for the first and second order statistics (mean velocity and Reynolds stresses, not presented here). The conclusion is that the first and second order statistics are statistically converged, and the third order statistics (triple correlations) lack of statistical convergence. In the following sections, the ZLES TKE budget terms presented are computed using the statistics over the 13.5 through-flow periods. In order to analyse the physical terms of the budget (production, dissipation and transport) in the areas where they are meaningful, areas are greyed and ignored if they meet the two following conditions:

1. Locally, the term considered is bigger than five percent of the maximum of the production term: term $> 0.05 \times$ **max** (Production).

2. Locally, the term considered is smaller than twice the numerical residual: term $< 2.0 \times$ Numerical residual.

The first condition evaluates if the term is significant, while the second condition imposes a mask if the numerical residual is too important.

13.2 Through the tip-clearance

13.2.1 Numerical residual

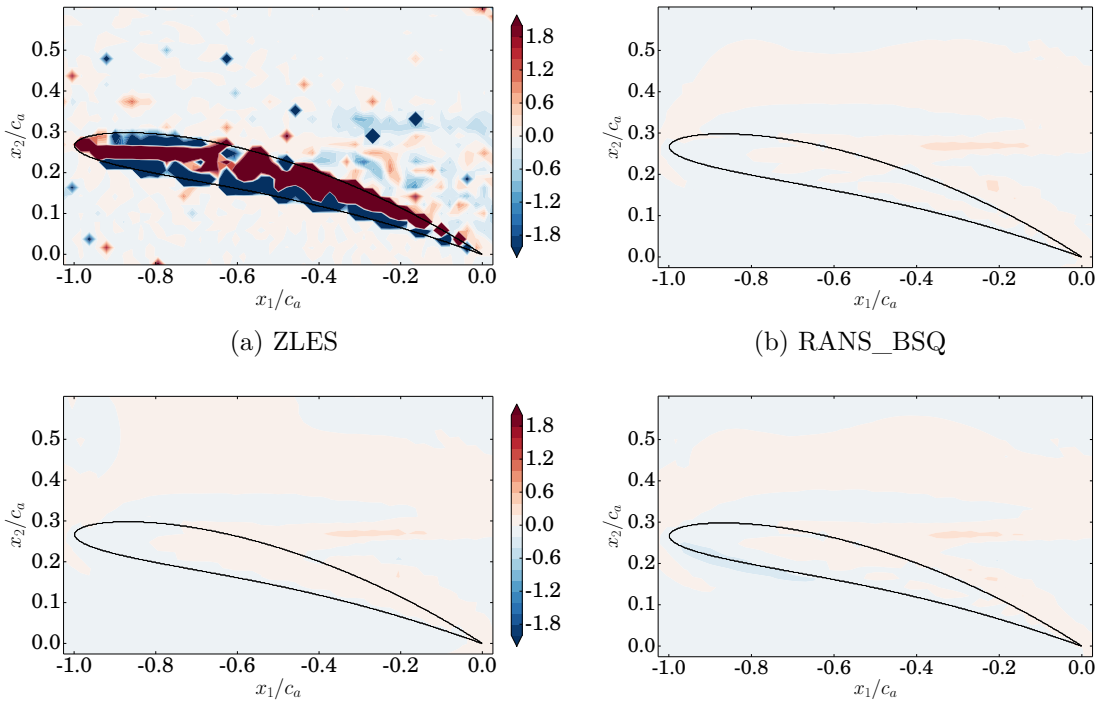

(a) ZLES (b) RANS_BSQ

(c) RANS_QCR (d) RANS_BUA

Figure 13.2: Numerical residual through the tip-clearance, normalised by $(\rho^2 u_e^4)/\mu$.

The numerical residual term is presented in figure 13.2. As said before, the ZLES term is quite intense. The suspected reason is a lack of statistical convergence. The RANS simulations show a small amount of numerical residual because the k-equation is directly solved.

13.2.2 Production

The production term of the TKE budget accounts for the turbulent kinetic energy creation. It is presented in figure 13.3. The main areas of production are located in the leakage jet, close to the suction side of the blade (Fig 13.3a (1)) and in the second area of maximal normal Reynolds stresses, further from the blade (Fig 13.3a (2)). Those areas correspond to the areas of high intensity for both the normal Reynolds stresses and the shear Reynolds stresses, as presented in chapter 11. In the area further from the blade, the production is due to the interaction between the leakage jet and the end-wall boundary-layer (Tan et al., 2015). The RANS simulations show the same topology as the ZLES for the production term, but with an intensity ten times smaller. This is directly related to the under-prediction of the Reynolds stresses. As

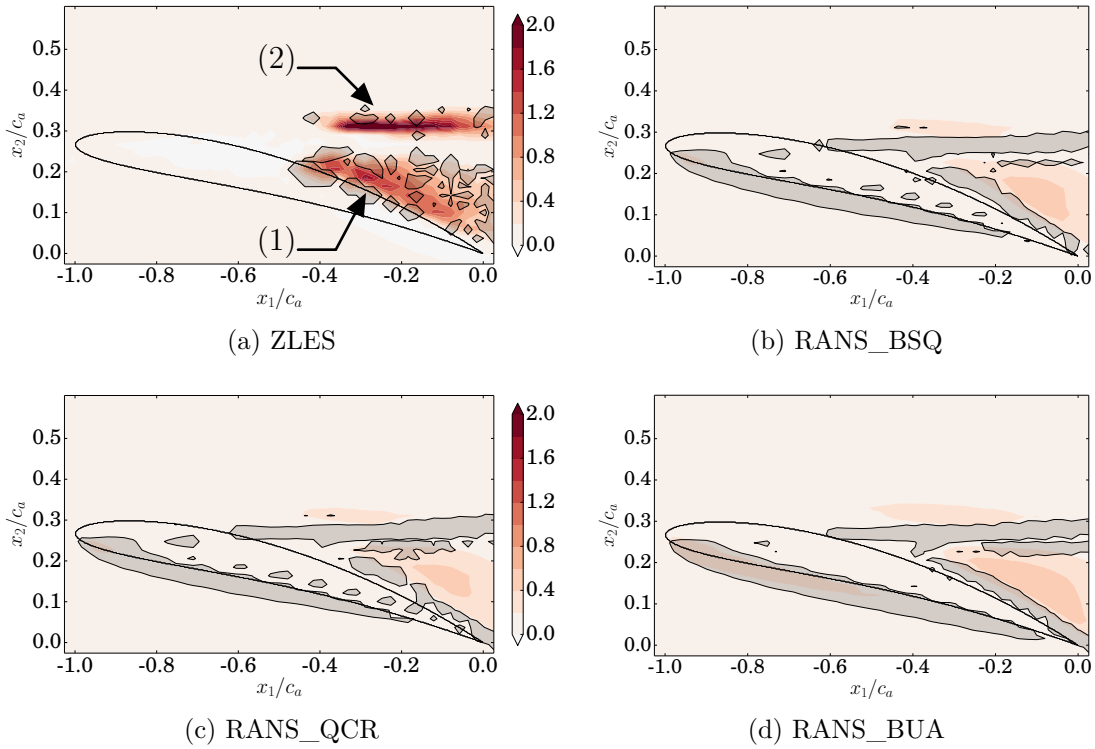

(a) ZLES (b) RANS_BSQ

(c) RANS_QCR (d) RANS_BUA

Figure 13.3: Production through the tip-clearance, normalised by $(\rho^2 u_e^4)/\mu$.

for the Reynolds stresses, neither the quadratic nor the modified Wilcox models yield significant effects compared to the original Wilcox model.

13.2.3 Dissipation

The dissipation term of the TKE budget accounts for the turbulent kinetic energy damping. It is presented in figure 13.4. In the ZLES, no significant area of dissipation can be found on the studied plane. All the areas of dissipation present an intensity too weak to pass the threshold on the numerical residual criterion. The dissipation is found to occur mainly close to the walls, but not significantly in the tip-leakage vortex. For the RANS simulations, dissipation occurs in the jet area, where the production is intense. This is a known behaviour of RANS models, to superimpose production and dissipation, with only a small amount of transport (Wilcox, 2006). Again, neither the quadratic nor the modified Wilcox models yield significant effects compared to the original Wilcox model.

13.2.4 Transport

The transport term of the TKE budget accounts for the turbulent kinetic energy displacement in the flow. It is presented in figure 13.5. As mentioned, the ZLES term oscillates within the clearance, with its value roughly opposed to the value of the numerical residual term. This is probably due to insufficient statistical convergence. On the suction side, two important areas of negative energy transportation are found superimposed with the areas of high production, with absolute values about twice the numerical residual. A significant part of the energy produced in these areas is transported elsewhere, and not locally dissipated, contrary to the behaviour of the

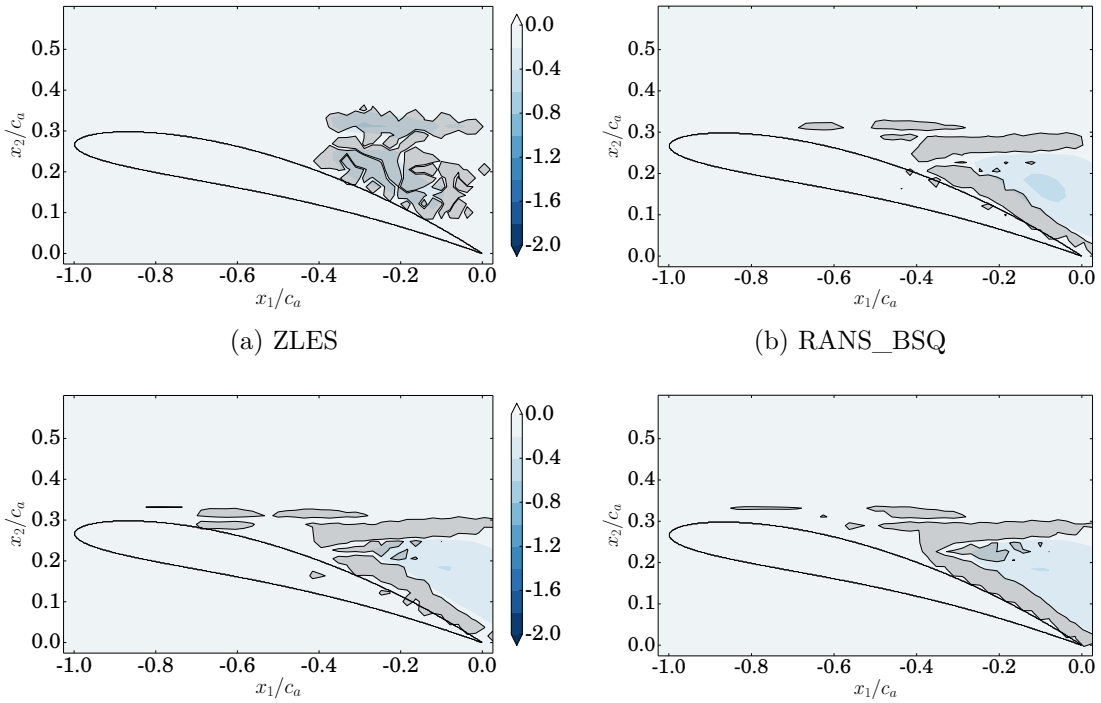

(a) ZLES (b) RANS_BSQ

(c) RANS_QCR (d) RANS_BUA

Figure 13.4: Dissipation through the tip-clearance, normalised by $(\rho^2 u_e^4)/\mu$.

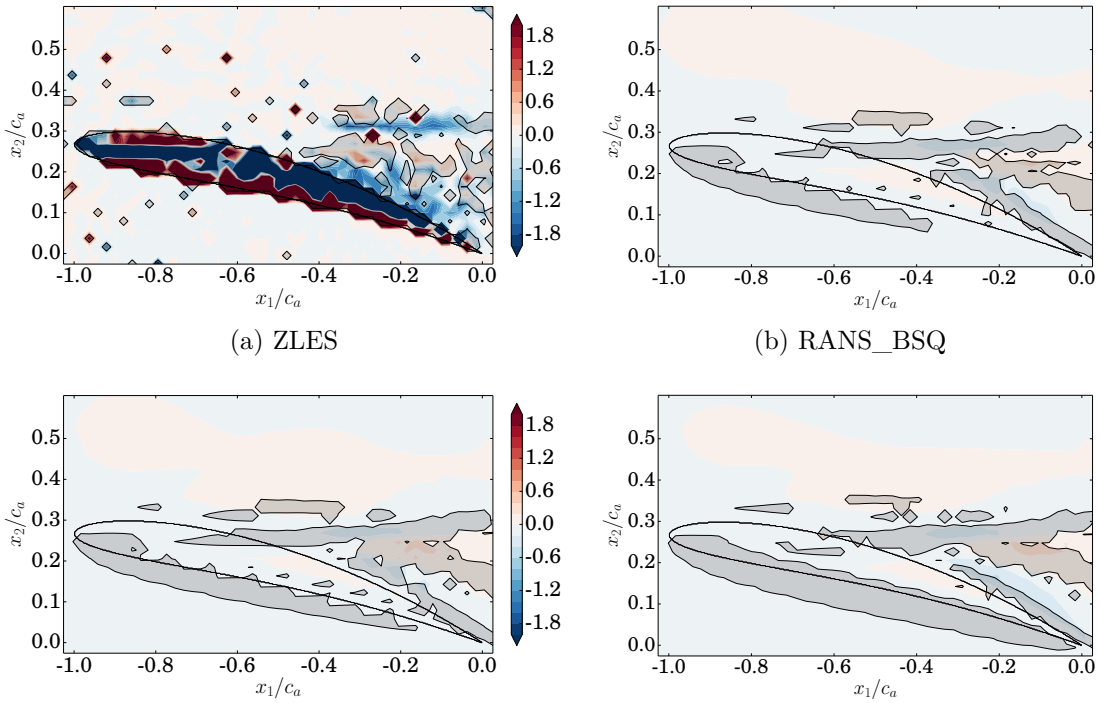

(a) ZLES (b) RANS_BSQ

(c) RANS_QCR (d) RANS_BUA

Figure 13.5: Transport through the tip-clearance, normalised by $(\rho^2 u_e^4)/\mu$.

RANS simulations. The RANS simulations show almost no transport. As previously mentioned, the turbulent kinetic energy is produced and dissipated locally, without

transport. Once again, no significant effects of the quadratic or modified Wilcox models can be seen.

13.3 In the tip-leakage vortex

13.3.1 Numerical residual

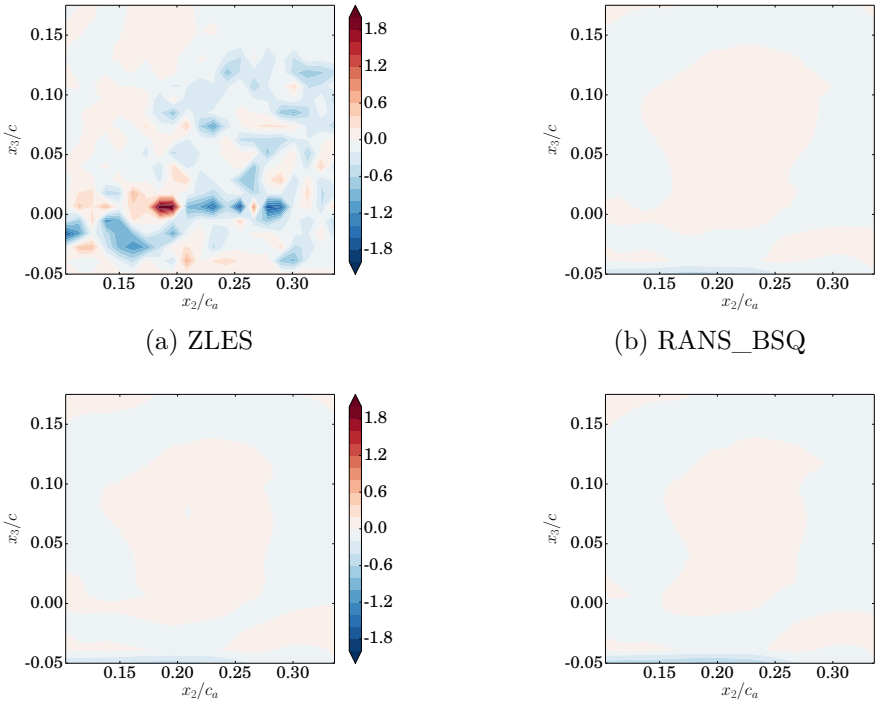

(a) ZLES (b) RANS_BSQ

(c) RANS_QCR (d) RANS_BUA

Figure 13.6: Numerical residual in the tip-leakage vortex, normalised by $(\rho^2 u_e^4)/\mu$.

The numerical residual term is presented in figure 13.6. As said before, the ZLES term is quite intense, and opposed to the transport term (Fig. 13.9). The RANS simulations show again a small amount of numerical residual because the k-equation is directly solved. Slightly more intense values are observed near the end-wall, where mesh expansion is stronger.

13.3.2 Production

The production term is presented in figure 13.7. The main areas of production for the ZLES simulation are the jet and at the bottom right-hand side corner of the figure (Fig. 13.7a (1) and (2)). Those areas correspond to regions of high intensity for both the normal Reynolds stresses and the shear Reynolds stresses, as presented in figures 11.18a to 11.23a. The important production area in the jet is impacted by the high residual, but not entirely, while the other area of important production is not significantly impacted by the high residual. The bottom right corner area corresponds to the area where the vortex interacts with the casing end-wall boundary-layer, as mentioned by Tan et al. (2015). This area seems to be the same area as that labelled (2) in the plane through the clearance (Fig. 13.3a). Interestingly, the third and fourth

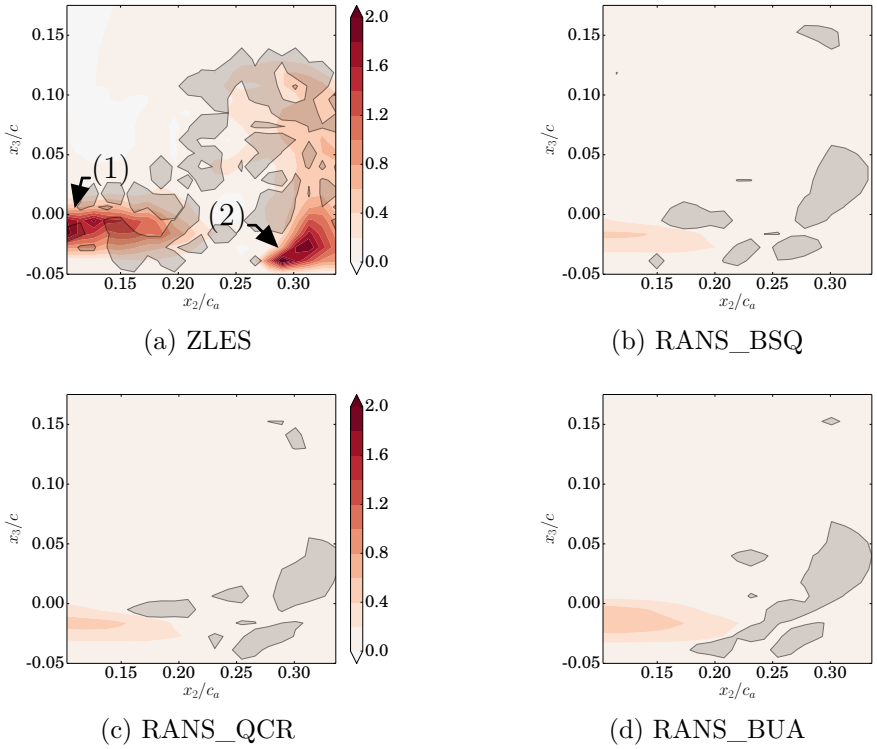

(a) ZLES (b) RANS_BSQ

(c) RANS_QCR (d) RANS_BUA

Figure 13.7: Production in the tip-leakage vortex, normalised by $(\rho^2 u_e^4)/\mu$.

areas of high Reynolds stresses (Figs. 11.18a to 11.23a, (3) and (4)) are not linked with areas of high turbulent kinetic energy production. This indicates shear is moderate in those regions and turbulence originates from upstream regions. Concerning the RANS simulations, the main area of production is in the jet, but with levels ten times smaller than for the ZLES. As could be expected, the global under-prediction of the Reynolds stresses is associated with an under-prediction of the turbulent kinetic energy production. The bottom right corner area is not visible at all, even though the second lobe of production is present in Figs. 13.3b, 13.3c, and 13.3d (label (1)), at upstream chord-wise positions, again very weak. As for the previous results, neither the quadratic nor the modified Wilcox models yield significant effects compared to the original Wilcox model.

13.3.3 Dissipation

The dissipation term is presented in figure 13.8. The main area of dissipation for the ZLES is close to the end-wall, at $x_3/c \leqslant -0.04$ (Fig. 13.8a), and particularly in the bottom right hand corner where the TLV interacts with the boundary-layer. No significant dissipation can be seen in the jet area, where production is intense. The area of important dissipation is not affected by the high numerical residual. For the RANS simulations, the dissipation occurs in the jet, where the production is intense. This is a classical issue in RANS, production and dissipation are superimposed, with a small amount of transport (Wilcox, 2006). This behaviour is not corrected by the use of the quadratic or the modified Wilcox models.

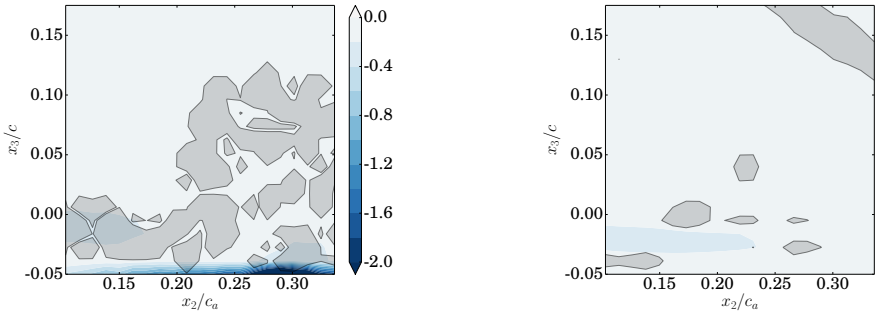

(a) ZLES (b) RANS_BSQ

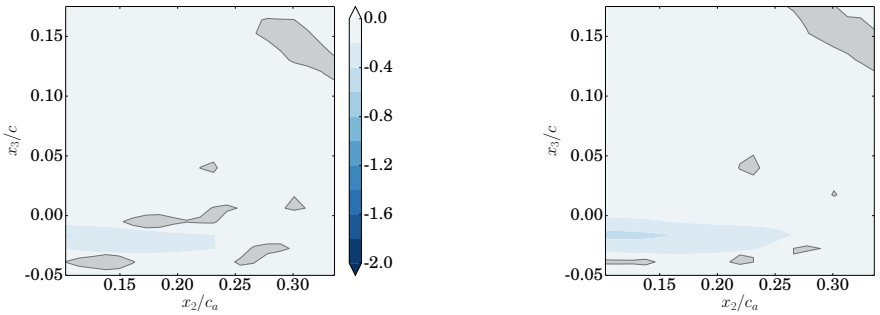

(c) RANS_QCR (d) RANS_BUA

Figure 13.8: Dissipation in the tip-leakage vortex, normalised by $(\rho^2 u_e^4)/\mu$.

13.3.4 Transport

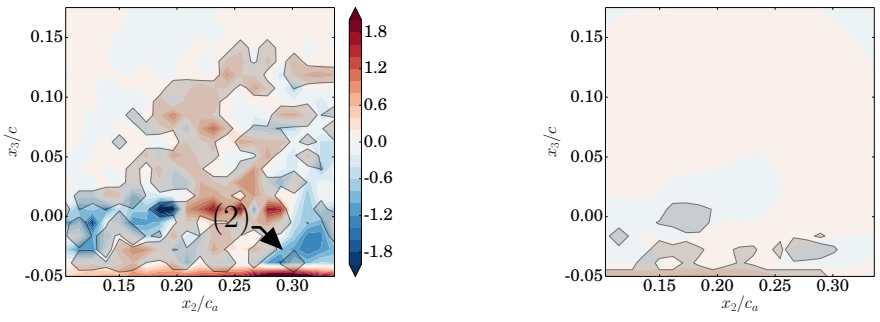

(a) ZLES (b) RANS_BSQ

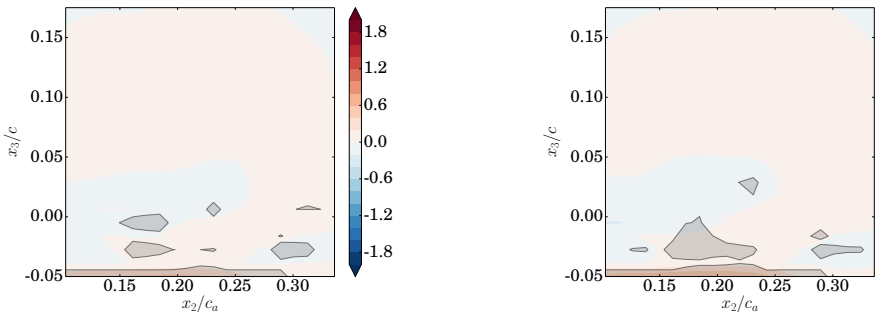

(c) RANS_QCR (d) RANS_BUA

Figure 13.9: Transport in the tip-leakage vortex, normalised by $(\rho^2 u_e^4)/\mu$.

The transport term is presented in figure 13.9. For the ZLES, as already pointed out, the transport term shows strong oscillations, in opposition with the numerical residual term. This seems to be due to an insufficient statistical convergence. However, the region in the bottom right corner of the figure (Fig. 13.9a (2), and $x_3/c \leqslant -0.04$) shows values sufficiently intense compared to the residual, and can be analysed. A significant positive energy transportation is found in the area of high dissipation, near the end-wall. Energy is taken from the vortex above (negative transport) and transferred to the end-wall (positive transport) where it is dissipated. The RANS simulations show very little transport, because production and dissipation are superimposed. Still, no significant effect of the quadratic or modified Wilcox models can be seen compared to the original Wilcox model.

13.4 Partial conclusion

The TKE budget extraction methodology used on this configuration allows a fine understanding of the turbulence physics through the tip-clearance and in the tip-leakage vortex. For the ZLES, in this configuration, the numerical residual is found to be intense and oscillating, and opposed to the transport term. This seems to be mainly due to a lack of statistical convergence of the triple correlations. However, some regions of the flow show significant intensities of the TKE budget terms in comparison to the residual. The production is mainly located in the jet-leakage and in the area where the vortex interacts with the end-wall boundary-layer. The dissipation is very weak inside the tip-leakage vortex, and occurs mainly close to the end-wall. The ZLES is used as a reference to evaluate the RANS turbulence models.

The RANS simulations present very weak budget terms (around 10% of the intensity of the ZLES budget terms). It is directly linked with the under-estimation of the Reynolds stresses. The spatial distribution of the terms is never correctly estimated. The leakage-jet area is present, but the area of interaction between the vortex and the end-wall boundary-layer is very weak. The modifications introduced in the quadratic Wilcox model and the modified Wilcox model yield no significant effect compared to the original Wilcox model.

Conclusion and further work

Conclusion

The main objective of the present work was to characterise the turbulence modelling in Reynolds-averaged Navier-Stokes simulations of vortical flows. The characterisation has been made through various aspects, from the analysis of the Reynolds stress tensor to the term-to-term comparison of the modelled turbulent kinetic energy equation, against large-eddy simulation results used as reference. The alignment hypotheses on which the constitutive relations rely were also analysed. The turbulence characterisation was made for three different turbulence models, the original Wilcox $k-\omega$ turbulence model with the Boussinesq constitutive relation, the Wilcox $k-\omega$ turbulence model with the quadratic constitutive relation, and a modified version of the Wilcox $k-\omega$ turbulence model with the Boussinesq constitutive relation. Two academic test-cases have been considered: a corner separation flow in a linear compressor cascade, and a tip-leakage flow from a single blade in the potential core of a jet. These flows, three-dimensional and highly vortical, are representative of what is encountered in actual turbomachines.

For both test cases, the three RANS models fail to represent accurately the Reynolds stresses, compared to the LES. Both the topology and intensity are wrongly estimated. The incorrect estimation of the Reynolds stresses can be a consequence of a defect of the constitutive relation, a defect of the modelled turbulence equations, or a coupling of the two.

The studied constitutive relations rely on two strong hypotheses: the alignment between the Reynolds stress tensor and a tensor computed from velocity gradients, and the possibility to use k and ω to compute the eddy-viscosity. These hypotheses have been tested using large-eddy simulation results, where all the quantities (*e.g.* Reynolds stress tensor, the zero-trace mean strain rate tensor, k, and ω) are known independently from each others. The analysis showed that the alignment hypothesis is generally not verified. The Boussinesq constitutive relation relies on an alignment that is not verified even on simple flows, such as a developing boundary layer. The quadratic constitutive relation, that bears a term explicitly taking into account the local vorticity of the flow, gives much better results on a developing boundary layer flow but has little effect on the highly vortical flows, the corner separation or the tip-leakage vortex. The use of k and ω to calculate the eddy-viscosity gives correct results.

The modelled turbulent kinetic energy budget presents, for the three turbulence models, on the two test-cases, almost the same behaviour. The production term is not accurately represented, which is directly linked with the erroneous representation of the Reynolds stresses, compared with LES results. The transport term is almost

non-existent in the RANS simulations, while it is not negligible in LES. Last, the dissipation term is locally opposed to the production term in the RANS simulations, while in LES the turbulent kinetic energy dissipation is not located in the same area as the production. This superimposition is typical of RANS turbulence models that rely implicitly on the strong hypothesis of equilibrium turbulence, *i.e.* a local equilibrium between production and dissipation with little transport.

LES has been successfully used to characterise turbulence modelling, given its capacity to represent accurately the physics compared to the RANS approach. However, the high computational cost of LES makes it unaffordable in nowadays industrial design process of compressors. In order to cumulate the precision of LES and the reduced computational cost of RANS, an hybrid RANS-LES approach has been proposed and tested on a channel flow and the corner separation case. The results are mitigated. The computations are quite robust and much less expensive than pure LES. The channel flow results are good. With the default hybrid parameters, the corner separation seems to be more similar, in terms of size and intensity, to the LES one, but a suction side separation is generated. When the RANS-LES transition is set further from the walls, the suction-side separation is not anymore present, but the prediction of the corner separation size and intensity is only slightly better than with pure RANS. These rather poor results may come from a maladapted mesh.

Further work

The results obtained in the present work raise three interrogations. Which physically more relevant constitutive relation can be used to replace the Boussinesq constitutive relation or the QCR? What would be the impact of a turbulence model that takes into account the non-equilibrium of turbulence, in realistic turbomachinery flows? Is it possible to modify the hybrid approach in order to improve the description of the corner separation?

The Boussinesq constitutive relation, that relies on one point statistics and a scalar eddy-viscosity, is too simplistic to take into account the reality of the physics. Among the possible approaches to find a more physical constitutive relation, an analysis and calibration of a more complex model, such as Pope (1975) constitutive relation, can be imagined. The calibration is complex, but given the various LES and DNS existing databases, a statistical calibration, based on a "big data" approach, can be attempted.

The second point, the non-equilibrium turbulence modelling, may lead to an improvement of the physical description of the flows. Indeed, the corner separation is a spectrally (Touil, 2002) and spatially (Shao, 1992) non-equilibrated turbulent flow. Various approaches exist in order to take into account the non-equilibrium of turbulence, and the interactions of the different length-scales of turbulence. The construction of a non-equilibrium turbulence model is in progress at the LMFA (Bos and Rubinstein, 2017).

Last, concerning the hybrid approach, the weak improvement of the corner separation prediction, compared to pure RANS, may be a consequence of a maladapted mesh. The influence of the mesh density in the prediction of the corner separation for the present hybrid formulation should be investigated by a mesh sensitivity analysis. Another point to be tested is the sensitivity of the hybrid approach to the RANS model used close to the walls.

Appendix

Appendix A

Reynolds stress budget equations

Sections

In the present appendix, the calculation to obtain the Reynolds stress budget equations and the turbulent kinetic energy (TKE) budget equation are presented. The calculation is the same as in Bogey and Bailly (2009).

A.1 Budget equations calculation

A.1.1 Preliminary steps

The calculation begins with the mass equation and the three momentum equations:

$$\frac{\partial \overline{\rho}}{\partial t} + \frac{\partial \overline{\rho}\widetilde{u_k}}{\partial x_k} = 0 \tag{A.1}$$

$$\forall i \in [\![\ 1\ ;\ 3\ ]\!],\ \frac{\partial \overline{\rho}\widetilde{u_i}}{\partial t} + \frac{\partial \overline{\rho}\widetilde{u_i}\widetilde{u_k}}{\partial x_k} = -\frac{\partial \overline{p}}{\partial x_i} + \frac{\partial \overline{\tau_{ik}}}{\partial x_k} + \frac{\partial \overline{\Pi_{ik}}}{\partial x_k} \tag{A.2}$$

Equation (A.2) can also be written as follows:

$$\forall i \in [\![\ 1\ ;\ 3\ ]\!],\ \widetilde{u_i}\frac{\partial \overline{\rho}}{\partial t} + \overline{\rho}\frac{\partial \widetilde{u_i}}{\partial t} + \widetilde{u_i}\frac{\partial \overline{\rho}\widetilde{u_k}}{\partial x_k} + \overline{\rho}\widetilde{u_k}\frac{\partial \widetilde{u_i}}{\partial x_k} = -\frac{\partial \overline{p}}{\partial x_i} + \frac{\partial \overline{\tau_{ik}}}{\partial x_k} + \frac{\partial \overline{\Pi_{ik}}}{\partial x_k} \tag{A.3}$$

By merging the equations (A.1) and (A.3), the momentum equation becomes:

$$\forall i \in [\![\ 1\ ;\ 3\ ]\!],\ \overline{\rho}\frac{\partial \widetilde{u_i}}{\partial t} + \overline{\rho}\widetilde{u_k}\frac{\partial \widetilde{u_i}}{\partial x_k} = -\frac{\partial \overline{p}}{\partial x_i} + \frac{\partial \overline{\tau_{ik}}}{\partial x_k} + \frac{\partial \overline{\Pi_{ik}}}{\partial x_k} \tag{A.4}$$

Then, for $(i,j) \in [\![1 ; 3]\!]^2$, equation (A.4) is multiplied by u_j'':

$$\overline{\rho} u_j'' \frac{\partial \widetilde{u_i}}{\partial t} + \overline{\rho} u_j'' \widetilde{u_k} \frac{\partial \widetilde{u_i}}{\partial x_k} = -u_j'' \frac{\partial \overline{p}}{\partial x_i} + u_j'' \frac{\partial \overline{\tau_{ik}}}{\partial x_k} + u_j'' \frac{\partial \overline{\Pi_{ik}}}{\partial x_k} \tag{A.5}$$

Given the symmetry on the indexes, equation (A.5) is straightforwardly re-written as follows:

$$\overline{\rho} u_i'' \frac{\partial \widetilde{u_j}}{\partial t} + \overline{\rho} u_i'' \widetilde{u_k} \frac{\partial \widetilde{u_j}}{\partial x_k} = -u_i'' \frac{\partial \overline{p}}{\partial x_j} + u_i'' \frac{\partial \overline{\tau_{jk}}}{\partial x_k} + u_i'' \frac{\partial \overline{\Pi_{jk}}}{\partial x_k} \tag{A.6}$$

Equations (A.5) and (A.6) are summed into the following equation:
$\forall (i,j) \in [\![1 ; 3]\!]^2$,

$$\begin{aligned} \underbrace{\overline{\rho} u_j'' \frac{\partial \widetilde{u_i}}{\partial t} + \overline{\rho} u_i'' \frac{\partial \widetilde{u_j}}{\partial t}}_{\text{(A)}} \underbrace{+\overline{\rho} u_j'' \widetilde{u_k} \frac{\partial \widetilde{u_i}}{\partial x_k} + \overline{\rho} u_i'' \widetilde{u_k} \frac{\partial \widetilde{u_j}}{\partial x_k}}_{\text{(B)}} &= \underbrace{-u_j'' \frac{\partial \overline{p}}{\partial x_i} - u_i'' \frac{\partial \overline{p}}{\partial x_j}}_{\text{(C)}} \\ &\underbrace{+u_j'' \frac{\partial \overline{\tau_{ik}}}{\partial x_k} + u_i'' \frac{\partial \overline{\tau_{jk}}}{\partial x_k}}_{\text{(D)}} \underbrace{+u_j'' \frac{\partial \overline{\Pi_{ik}}}{\partial x_k} + u_i'' \frac{\partial \overline{\Pi_{jk}}}{\partial x_k}}_{\text{(E)}} \end{aligned} \tag{A.7}$$

Each underlined term from equation (A.7) is to be developed and averaged in order to get the Reynolds stress equation.

A.1.2 Development and averaging

The development and averaging of the terms begins with the term (A):
$\forall (i,j) \in [\![1 ; 3]\!]^2$,

$$(\mathrm{A}) = \overline{\rho} u_j'' \frac{\partial \widetilde{u_i}}{\partial t} + \overline{\rho} u_i'' \frac{\partial \widetilde{u_j}}{\partial t} \tag{A.8}$$

$$(\mathrm{A}) = \overline{\rho} u_j'' \frac{\partial}{\partial t} \left([\widetilde{u_i}] + u_i'' \right) + \overline{\rho} u_i'' \frac{\partial}{\partial t} \left([\widetilde{u_j}] + u_j'' \right) \tag{A.9}$$

$$(\mathrm{A}) = \overline{\rho} u_j'' \frac{\partial [\widetilde{u_i}]}{\partial t} + \overline{\rho} u_i'' \frac{\partial [\widetilde{u_j}]}{\partial t} + \frac{\partial \overline{\rho} u_i'' u_j''}{\partial t} - u_i'' u_j'' \frac{\partial \overline{\rho}}{\partial t} \tag{A.10}$$

Finally, by applying the ensemble average to (A), and given that $\langle [\varphi] \rangle = [\varphi]$ and $\langle \overline{\rho} \varphi'' \rangle = 0$, and by switching the average and the time derivation, (A) becomes:

$$\langle (\mathrm{A}) \rangle = \frac{\partial \left\langle \overline{\rho} u_i'' u_j'' \right\rangle}{\partial t} + \left\langle u_i'' u_j'' \frac{\partial \overline{\rho} \widetilde{u_k}}{\partial x_k} \right\rangle \tag{A.11}$$

The same process is applied for the term (B):
$\forall (i,j) \in [\![1 ; 3]\!]^2$,

$$(\mathrm{B}) = \overline{\rho} u_j'' \widetilde{u_k} \frac{\partial \widetilde{u_i}}{\partial x_k} + \overline{\rho} u_i'' \widetilde{u_k} \frac{\partial \widetilde{u_j}}{\partial x_k} \tag{A.12}$$

$$(\mathrm{B}) = \overline{\rho} u_j'' \left([\widetilde{u_k}] + u_k'' \right) \frac{\partial \left([\widetilde{u_i}] + u_i'' \right)}{\partial x_k} + \overline{\rho} u_i'' \left([\widetilde{u_k}] + u_k'' \right) \frac{\partial \left([\widetilde{u_j}] + u_j'' \right)}{\partial x_k} \tag{A.13}$$

$$\begin{aligned}(\mathrm{B}) = {} & \overline{\rho} u_j'' [\widetilde{u_k}] \frac{\partial [\widetilde{u_i}]}{\partial x_k} + \overline{\rho} u_i'' [\widetilde{u_k}] \frac{\partial [\widetilde{u_j}]}{\partial x_k} + \overline{\rho} u_j'' u_k'' \frac{\partial [\widetilde{u_i}]}{\partial x_k} + \overline{\rho} u_i'' u_k'' \frac{\partial [\widetilde{u_j}]}{\partial x_k} \\ & + \frac{\partial}{\partial x_k} \left(\overline{\rho} u_i'' u_j'' [\widetilde{u_k}] \right) + \frac{\partial}{\partial x_k} \left(\overline{\rho} u_i'' u_j'' u_k'' \right) - u_i'' u_j'' \frac{\partial \overline{\rho} \widetilde{u_k}}{\partial x_k}\end{aligned} \tag{A.14}$$

As before, the ensemble averaging is applied:

$$\begin{aligned}\langle (\mathrm{B}) \rangle = {} & \left\langle \overline{\rho} u_j'' u_k'' \right\rangle \frac{\partial [\widetilde{u_i}]}{\partial x_k} + \left\langle \overline{\rho} u_i'' u_k'' \right\rangle \frac{\partial [\widetilde{u_j}]}{\partial x_k} + \frac{\partial}{\partial x_k} \left(\left\langle \overline{\rho} u_i'' u_j'' \right\rangle [\widetilde{u_k}] \right) \\ & + \frac{\partial}{\partial x_k} \left(\left\langle \overline{\rho} u_i'' u_j'' u_k'' \right\rangle \right) - \left\langle u_i'' u_j'' \frac{\partial \overline{\rho} \widetilde{u_k}}{\partial x_k} \right\rangle\end{aligned} \tag{A.15}$$

Again, for (C):
$\forall (i,j) \in [\![\ 1 \ ; \ 3 \ ]\!]^2$,

$$(\mathrm{C}) = -u_j'' \frac{\partial \overline{p}}{\partial x_i} - u_i'' \frac{\partial \overline{p}}{\partial x_j} \tag{A.16}$$

$$(\mathrm{C}) = -u_j'' \frac{\partial}{\partial x_i} \left(\langle \overline{p} \rangle + p' \right) - u_i'' \frac{\partial}{\partial x_j} \left(\langle \overline{p} \rangle + p' \right) \tag{A.17}$$

$$(\mathrm{C}) = -u_j'' \frac{\partial \langle \overline{p} \rangle}{\partial x_i} - u_i'' \frac{\partial \langle \overline{p} \rangle}{\partial x_j} - \frac{\partial u_j'' p'}{\partial x_i} - \frac{\partial u_i'' p'}{\partial x_j} + p' \frac{\partial u_j''}{\partial x_i} + p' \frac{\partial u_i''}{\partial x_j} \tag{A.18}$$

Again, the ensemble averaging is applied:

$$\begin{aligned}\langle (\mathrm{C}) \rangle = {} & - \left\langle u_j'' \right\rangle \frac{\partial \langle \overline{p} \rangle}{\partial x_i} - \langle u_i'' \rangle \frac{\partial \langle \overline{p} \rangle}{\partial x_j} - \frac{\partial \left\langle u_j'' p' \right\rangle}{\partial x_i} - \frac{\partial \langle u_i'' p' \rangle}{\partial x_j} \\ & + \left\langle p' \frac{\partial u_j''}{\partial x_i} \right\rangle + \left\langle p' \frac{\partial u_i''}{\partial x_j} \right\rangle\end{aligned} \tag{A.19}$$

Again, for (D):
$\forall (i,j) \in [\![\ 1 \ ; \ 3 \ ]\!]^2$,

$$(\mathrm{D}) = u_j'' \frac{\partial \overline{\tau_{ik}}}{\partial x_k} + u_i'' \frac{\partial \overline{\tau_{jk}}}{\partial x_k} \tag{A.20}$$

$$(\mathrm{D}) = \frac{\partial \overline{\tau_{ik}} u_j''}{\partial x_k} + \frac{\partial \overline{\tau_{jk}} u_i''}{\partial x_k} - \overline{\tau_{ik}} \frac{\partial u_j''}{\partial x_k} - \overline{\tau_{jk}} \frac{\partial u_i''}{\partial x_k} \tag{A.21}$$

Again, the ensemble averaging is applied:

$$\langle (\mathrm{D}) \rangle = \frac{\partial \left\langle \overline{\tau_{ik}} u_j'' \right\rangle}{\partial x_k} + \frac{\partial \left\langle \overline{\tau_{jk}} u_i'' \right\rangle}{\partial x_k} - \left\langle \overline{\tau_{ik}} \frac{\partial u_j''}{\partial x_k} \right\rangle - \left\langle \overline{\tau_{jk}} \frac{\partial u_i''}{\partial x_k} \right\rangle \tag{A.22}$$

Last, for (E):
$\forall (i,j) \in [\![1 ; 3]\!]^2$,

$$(\mathrm{E}) = u_j'' \frac{\partial \overline{\Pi_{ik}}}{\partial x_k} + u_i'' \frac{\partial \overline{\Pi_{jk}}}{\partial x_k} \tag{A.23}$$

$$(\mathrm{E}) = \frac{\partial \overline{\Pi_{ik}} u_j''}{\partial x_k} + \frac{\partial \overline{\Pi_{jk}} u_i''}{\partial x_k} - \overline{\Pi_{ik}} \frac{\partial u_j''}{\partial x_k} - \overline{\Pi_{jk}} \frac{\partial u_i''}{\partial x_k} \tag{A.24}$$

Again, the ensemble averaging is applied:

$$\langle (\mathrm{E}) \rangle = \frac{\partial \left\langle \overline{\Pi_{ik}} u_j'' \right\rangle}{\partial x_k} + \frac{\partial \left\langle \overline{\Pi_{jk}} u_i'' \right\rangle}{\partial x_k} - \left\langle \overline{\Pi_{ik}} \frac{\partial u_j''}{\partial x_k} \right\rangle - \left\langle \overline{\Pi_{jk}} \frac{\partial u_i''}{\partial x_k} \right\rangle \tag{A.25}$$

Finally, the five terms are summed ($\langle (\mathrm{A}) \rangle + \langle (\mathrm{B}) \rangle = \langle (\mathrm{C}) \rangle + \langle (\mathrm{D}) \rangle + \langle (\mathrm{E}) \rangle$) to obtain the Reynolds stress budget equations.

A.1.3 Reynolds stress equations

The Reynolds stress equations, already presented in chapter 2, are presented again here:
$\forall (i,j) \in [\![1 ; 3]\!]^2$,

$$\begin{aligned}
\frac{\partial \left\langle \overline{\rho} u_i'' u_j'' \right\rangle}{\partial t} = & \underbrace{-\frac{\partial}{\partial x_k} \left(\left\langle \overline{\rho} u_i'' u_j'' \right\rangle \left[\widetilde{u_k} \right] \right)}_{\text{Advection}} \underbrace{- \left\langle \overline{\rho} u_j'' u_k'' \right\rangle \frac{\partial \left[\widetilde{u_i} \right]}{\partial x_k} - \left\langle \overline{\rho} u_i'' u_k'' \right\rangle \frac{\partial \left[\widetilde{u_j} \right]}{\partial x_k}}_{\text{Production}} \\
& \underbrace{-\frac{\partial}{\partial x_k} \left(\left\langle \overline{\rho} u_i'' u_j'' u_k'' \right\rangle \right)}_{\text{Turbulent diffusion}} \underbrace{- \frac{\partial \left\langle u_j'' p' \right\rangle}{\partial x_i} - \frac{\partial \left\langle u_i'' p' \right\rangle}{\partial x_j}}_{\text{Pressure diffusion}} \underbrace{+ \left\langle p' \frac{\partial u_j''}{\partial x_i} \right\rangle + \left\langle p' \frac{\partial u_i''}{\partial x_j} \right\rangle}_{\text{Pressure dilatation}} \\
& - \left\langle u_j'' \right\rangle \frac{\partial \left\langle \overline{p} \right\rangle}{\partial x_i} - \left\langle u_i'' \right\rangle \frac{\partial \left\langle \overline{p} \right\rangle}{\partial x_j} \underbrace{+ \frac{\partial \left\langle \overline{\tau_{ik}} u_j'' \right\rangle}{\partial x_k} + \frac{\partial \left\langle \overline{\tau_{jk}} u_i'' \right\rangle}{\partial x_k}}_{\text{Viscous diffusion}} \underbrace{- \left\langle \overline{\tau_{ik}} \frac{\partial u_j''}{\partial x_k} \right\rangle - \left\langle \overline{\tau_{jk}} \frac{\partial u_i''}{\partial x_k} \right\rangle}_{\text{Viscous dissipation}} \\
& \underbrace{+ \frac{\partial \left\langle \overline{\Pi_{ik}} u_j'' \right\rangle}{\partial x_k} + \frac{\partial \left\langle \overline{\Pi_{jk}} u_i'' \right\rangle}{\partial x_k}}_{\text{SGS diffusion}} \underbrace{- \left\langle \overline{\Pi_{ik}} \frac{\partial u_j''}{\partial x_k} \right\rangle - \left\langle \overline{\Pi_{jk}} \frac{\partial u_i''}{\partial x_k} \right\rangle}_{\text{SGS dissipation}}
\end{aligned} \tag{A.26}$$

A.1.4 TKE budget equation

The TKE budget equation is derived from the Reynolds stress equations, with k defined as $k = 1/2 \; u_i'' u_i''$:

$$0 = \frac{\partial \langle \overline{\rho} k \rangle}{\partial t} = \underbrace{-\frac{\partial}{\partial x_k}\left(\langle \overline{\rho} k \rangle \left[\widetilde{u_k}\right]\right)}_{\text{Advection}} \underbrace{-\langle \overline{\rho} u_i'' u_k'' \rangle \frac{\partial \left[\widetilde{u_i}\right]}{\partial x_k}}_{\text{Production}} \underbrace{-\frac{\partial}{\partial x_k}\left(\langle \overline{\rho} k u_k'' \rangle\right)}_{\text{Turbulent diffusion}}$$
$$\underbrace{-\frac{\partial \langle u_i'' p' \rangle}{\partial x_i}}_{\text{Pressure Diffusion}} \underbrace{+\left\langle p' \frac{\partial u_i''}{\partial x_i} \right\rangle}_{\text{Pressure dilatation}} - \langle u_i'' \rangle \frac{\partial \langle \overline{p} \rangle}{\partial x_i}$$
$$\underbrace{+\frac{\partial \langle \overline{\tau_{ik}} u_i'' \rangle}{\partial x_k}}_{\text{Viscous diffusion}} \underbrace{-\left\langle \overline{\tau_{ik}} \frac{\partial u_i''}{\partial x_k} \right\rangle}_{\text{Viscous dissipation}} \underbrace{+\frac{\partial \left\langle \overline{\Pi_{ik}} u_i'' \right\rangle}{\partial x_k}}_{\text{SGS diffusion}} \underbrace{-\left\langle \overline{\Pi_{ik}} \frac{\partial u_i''}{\partial x_k} \right\rangle}_{\text{SGS dissipation}} \quad \text{(A.27)}$$

A.2 Required fields to extract the budgets

The budget extracted is directly the Reynolds stresses budget. In order to build these equations, 138 fields are averaged and stored, on the fly. The ensemble averaged is estimated as a time average, as presented in chapter 4. The list of the fields is given, with $(i, j, k) \in [\![1 ; 3]\!]^3$, as follows:

Quantity	Description	Number of fields
$\langle \overline{\rho} \rangle$	Density	1 field
$\langle \overline{\rho} \widetilde{u_i} \rangle$	Momentum	3 fields
$\langle \overline{p} \rangle$	Pressure	1 field
$\langle \widetilde{u_i} \rangle$	Velocity	3 fields
$\langle \overline{\rho} \widetilde{u_i} \widetilde{u_j} \rangle$	Reynolds stresses	6 fields
$\langle \overline{\rho} \widetilde{u_i} \widetilde{u_j} \widetilde{u_k} \rangle$	Triple correlations	10 fields
$\langle \widetilde{u_i} \overline{p} \rangle$	Pressure-velocity correlation	3 fields
$\langle \overline{p} \partial \widetilde{u_i} / \partial x_j \rangle$	Pressure-acceleration correlation	9 fields
$\langle \overline{\tau}_{ij} \rangle$	Viscous stresses	6 fields
$\langle \widetilde{u_i} \overline{\tau}_{jk} \rangle$	Velocity-viscous stresses correlation	18 fields
$\langle \partial \widetilde{u_i} / \partial x_k \overline{\tau}_{jk} \rangle$	Acceleration-viscous stresses correlation	27 fields
$\langle \overline{\Pi}_{ij} \rangle$	SGS stresses	6 fields
$\langle \widetilde{u_i} \overline{\Pi}_{jk} \rangle$	Velocity-SGS stresses correlation	18 fields
$\langle \partial \widetilde{u_i} / \partial x_k \overline{\Pi}_{jk} \rangle$	Acceleration-SGS stresses correlation	27 fields
	Total:	138 fields

Table A.1: Necessary fields for the Reynolds stress budget equations calculation.

The fluctuating quantities are calculated as presented in chapter 4, section 4.2. With these fields, any term of the Reynolds stress budget equations can be calculated.

Appendix B

List of publications

The work presented in this thesis lead to the following publications:

1. Monier, J.-F., Poujol, N., Laurent, M., Gao, F., Boudet, J., Aubert, S., and Shao, L. (2018). Investigation Of Boussinesq Constitutive Relation Validity In A Corner Separation Flow. *Final paper accepted for ASME TurboExpo 2018: Turbomachinery Technical Conference and Exposition, GT2018, June 11-15, 2018, Oslo, Norway*, pages 1-12, GT2018-75792. American Society of Mechanical Engineers.

2. Monier, J.-F., Boudet, J., Caro, J., and Shao, L. (2017). Turbulent energy budget in a tip leakage flow: a comparison between RANS and LES. *In Proceedings of ASME TurboExpo 2017: Turbomachinery Technical Conference and Exposition, GT2017, June 26-30, 2017, Charlotte, NC, USA*, pages 1-10. GT2017-63611. American Society of Mechanical Engineers.

3. Monier, J.-F., Boudet, J., Caro, J., and Shao, L. (2017). Budget analysis of turbulent kinetic energy in a tip-leakage flow of a single blade: RANS vs Zonal LES. *In Proceedings of 12th European Conference on Turbomachinery Fluid dynamics & Thermodynamics ETC12, April 3-7, 2017, Stockholm, Sweden*, ETC2017-113

4. Monier, J.-F., Gao, F., Boudet, J., Shao, L., and Lu, L. (2016). Budget analysis of turbulent kinetic energy in corner separation : RANS VS LES. *In Proceedings of the European Conference on Computational Fluid Dynamics, June 5-10, 2016*. European Community on Computational Methods in Applied Sciences (ECCOMAS).

5. Boudet, J., Monier, J. F., and Gao, F. (2015). Implementation of a roughness element to trip transition in large-eddy simulation. *Journal of Thermal Science*, 24(1):30–36.

Appendix C

Corner separation Reynolds stresses

Sections

In this appendix are presented the results not presented in the core of the manuscript. The interpretation for these results is similar with the one for the results on outlet plane 1, presented in chapter 7, section 7.2.4.

C.1 On outlet 0

C.1.1 Normal stresses

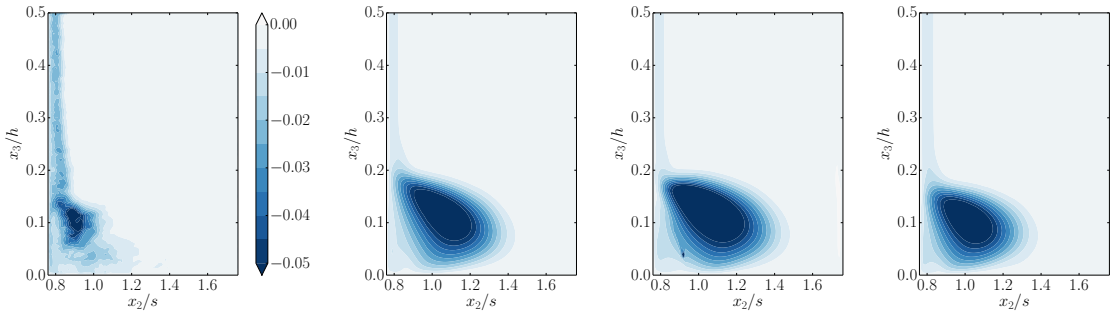

(a) LES (b) RANS_BSQ (c) RANS_QCR (d) RANS_BUA

Figure C.1: τ_{t11} on the plane outlet 0.

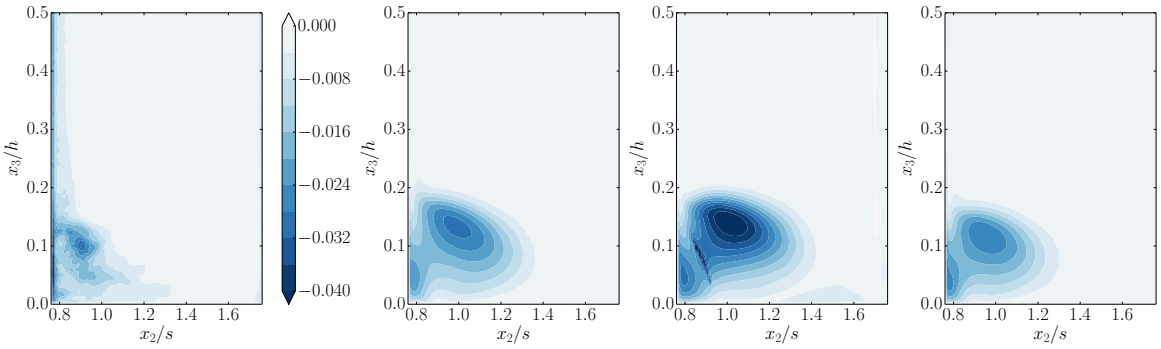

(a) LES (b) RANS_BSQ (c) RANS_QCR (d) RANS_BUA

Figure C.2: τ_{t22} on the plane outlet 0.

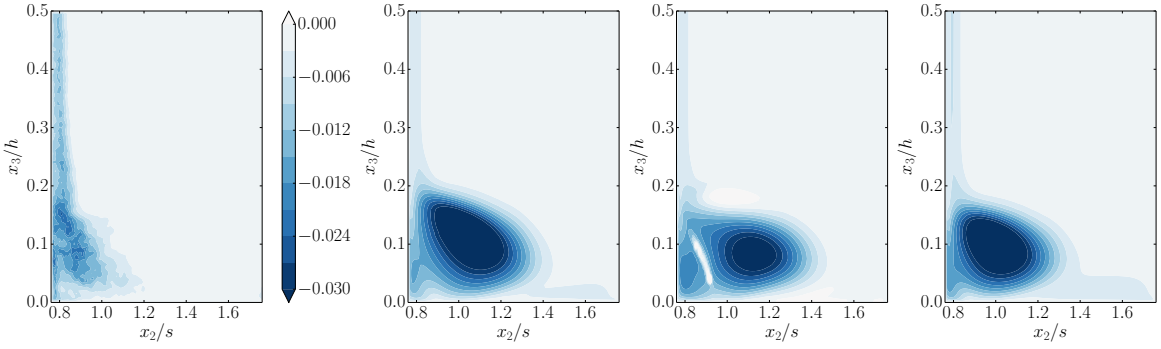

(a) LES (b) RANS_BSQ (c) RANS_QCR (d) RANS_BUA

Figure C.3: τ_{t33} on the plane outlet 0.

C.1.2 Shear stresses

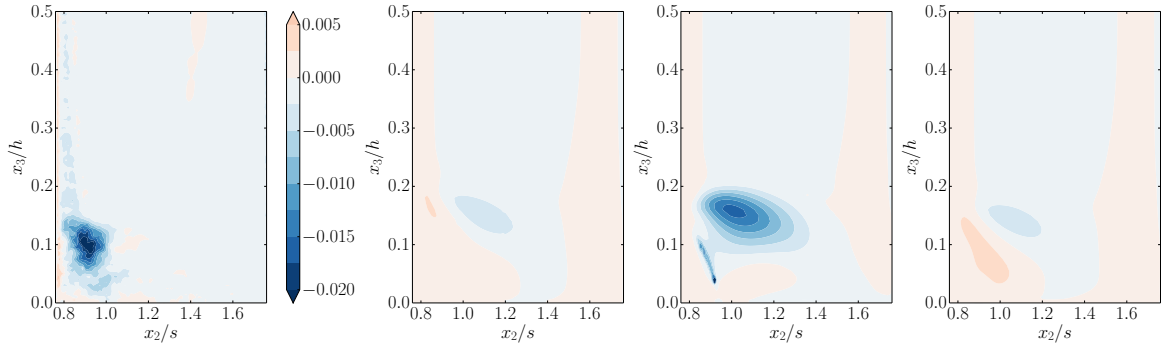

(a) LES (b) RANS_BSQ (c) RANS_QCR (d) RANS_BUA

Figure C.4: τ_{t12} on the plane outlet 0.

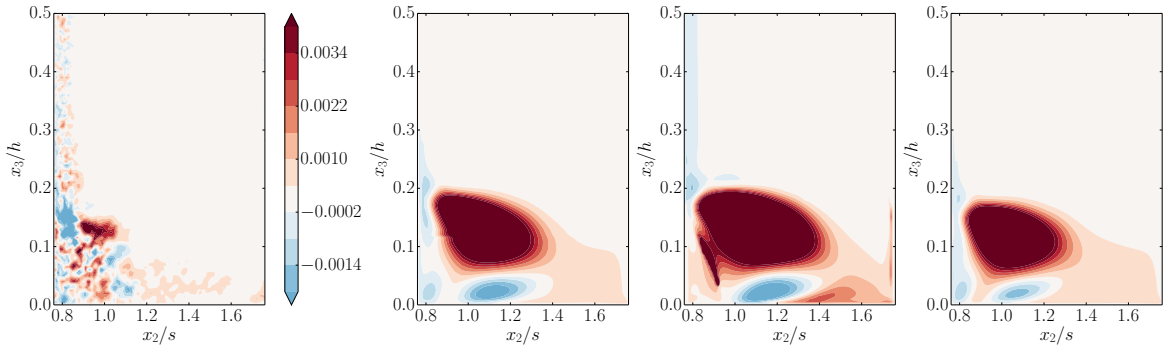

(a) LES (b) RANS_BSQ (c) RANS_QCR (d) RANS_BUA

Figure C.5: τ_{t13} on the plane outlet 0.

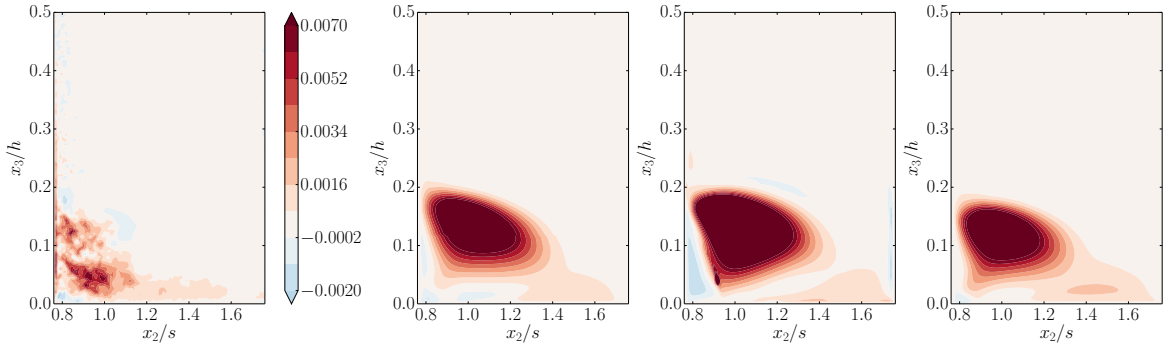

(a) LES (b) RANS_BSQ (c) RANS_QCR (d) RANS_BUA

Figure C.6: τ_{t23} on the plane outlet 0.

C.2 On outlet 2

C.2.1 Normal stresses

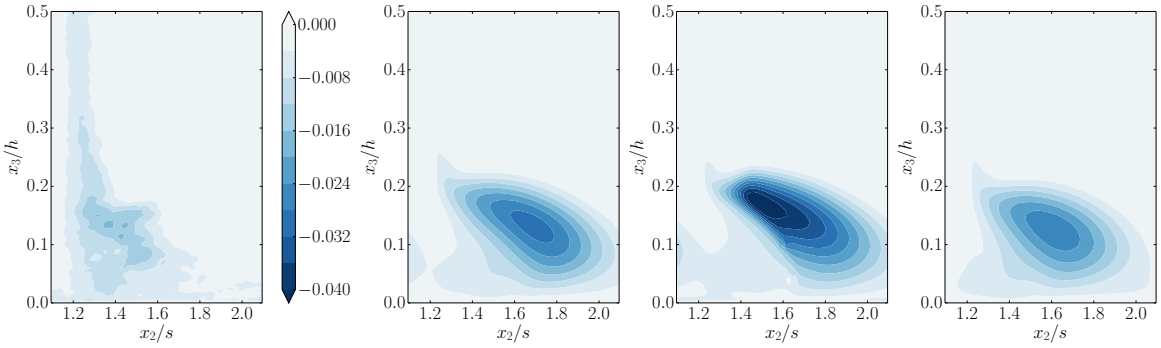

(a) LES (b) RANS_BSQ (c) RANS_QCR (d) RANS_BUA

Figure C.7: τ_{t11} on the plane outlet 2.

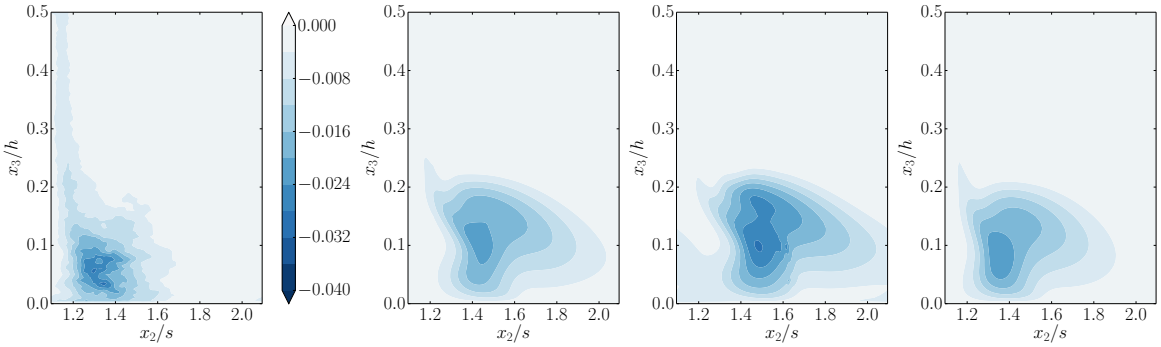

(a) LES (b) RANS_BSQ (c) RANS_QCR (d) RANS_BUA

Figure C.8: τ_{t22} on the plane outlet 2.

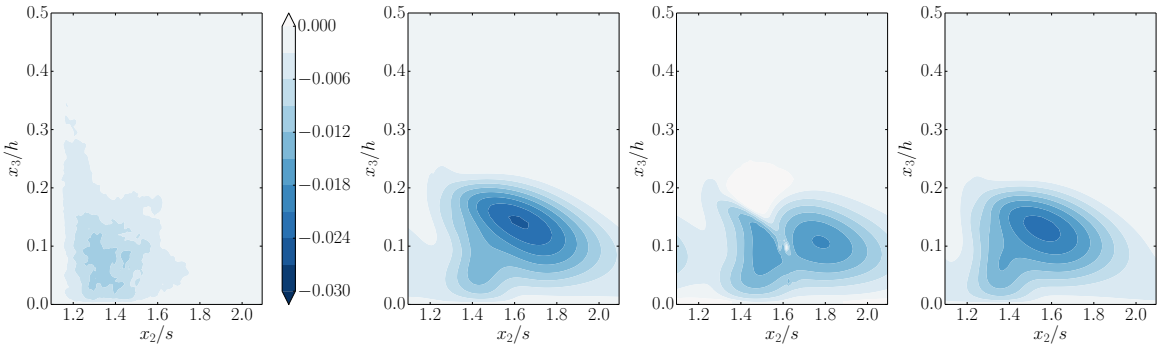

(a) LES (b) RANS_BSQ (c) RANS_QCR (d) RANS_BUA

Figure C.9: τ_{t33} on the plane outlet 2.

C.2.2 Shear stresses

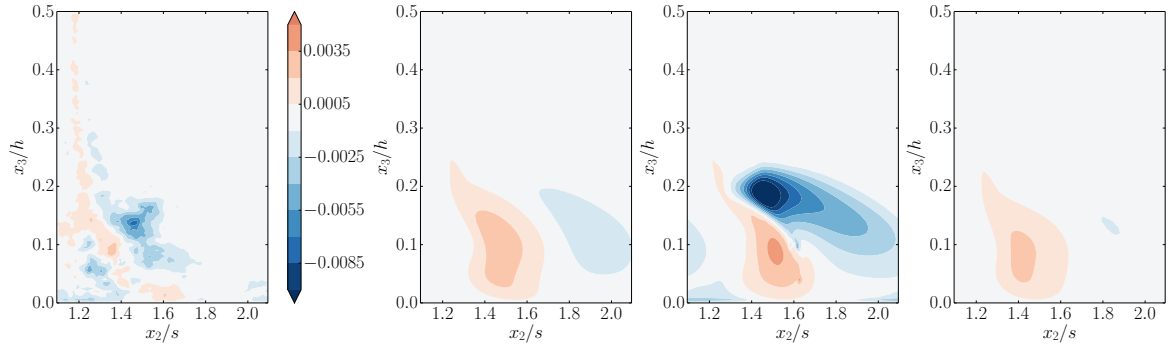

(a) LES (b) RANS_BSQ (c) RANS_QCR (d) RANS_BUA

Figure C.10: τ_{t12} on the plane outlet 2.

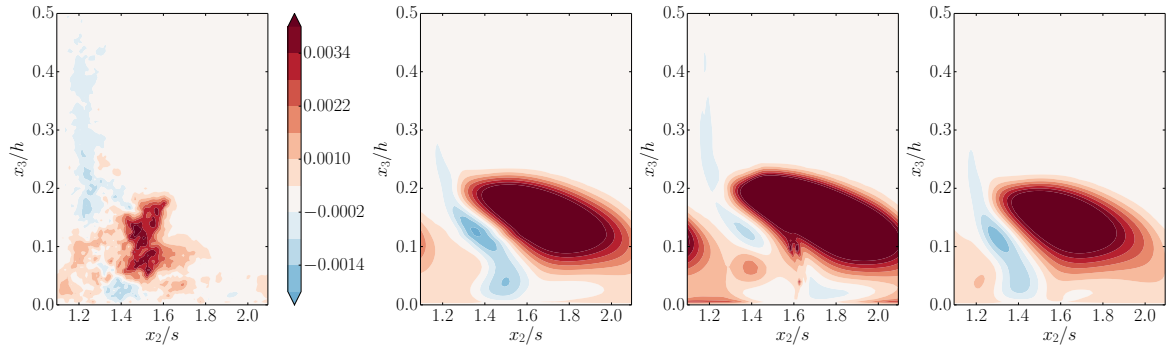

(a) LES (b) RANS_BSQ (c) RANS_QCR (d) RANS_BUA

Figure C.11: τ_{t13} on the plane outlet 2.

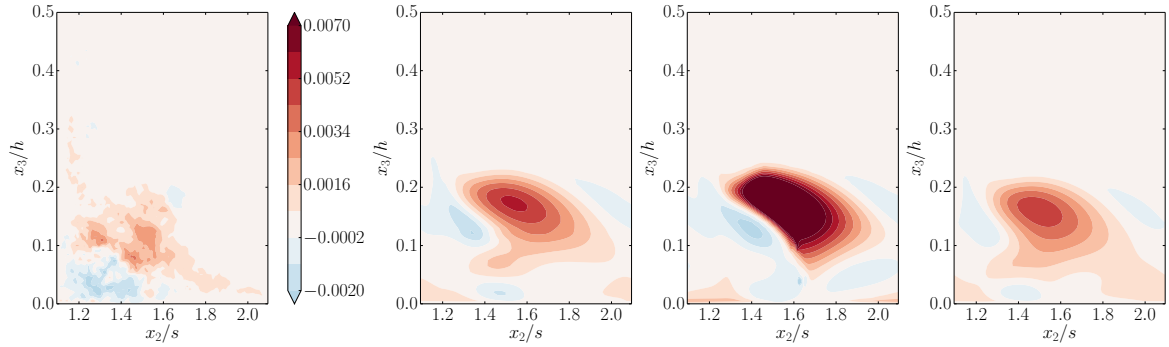

(a) LES (b) RANS_BSQ (c) RANS_QCR (d) RANS_BUA

Figure C.12: τ_{t23} on the plane outlet 2.

C.3 On outlet 3

C.3.1 Normal stresses

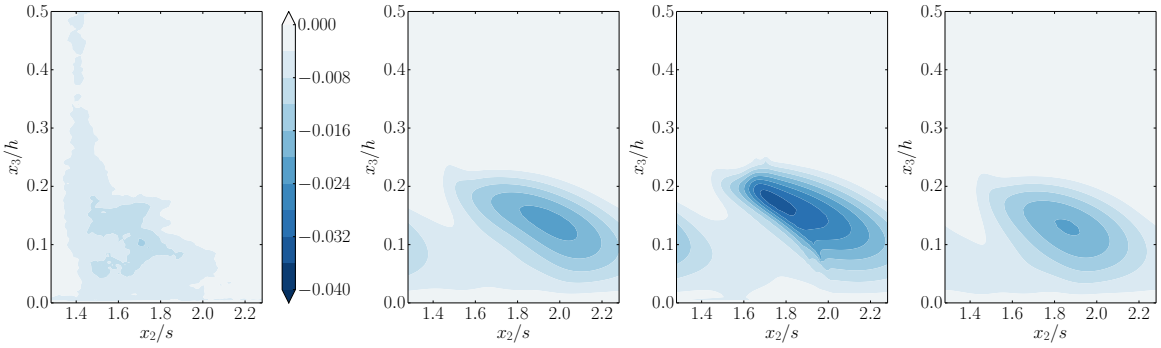

(a) LES (b) RANS_BSQ (c) RANS_QCR (d) RANS_BUA

Figure C.13: τ_{t11} on the plane outlet 3.

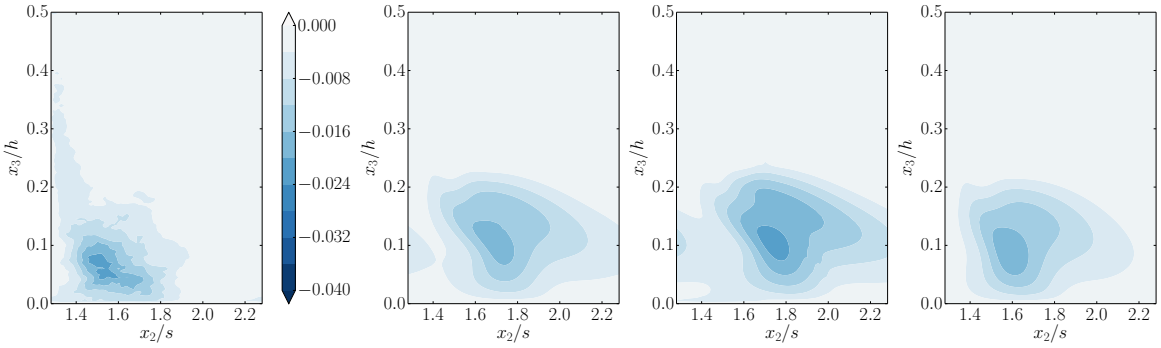

(a) LES (b) RANS_BSQ (c) RANS_QCR (d) RANS_BUA

Figure C.14: τ_{t22} on the plane outlet 3.

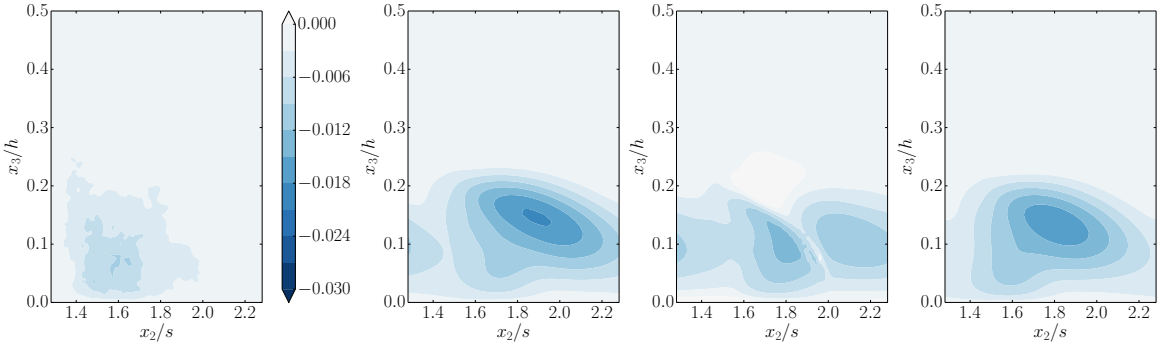

(a) LES (b) RANS_BSQ (c) RANS_QCR (d) RANS_BUA

Figure C.15: τ_{t33} on the plane outlet 3.

C.3.2 Shear stresses

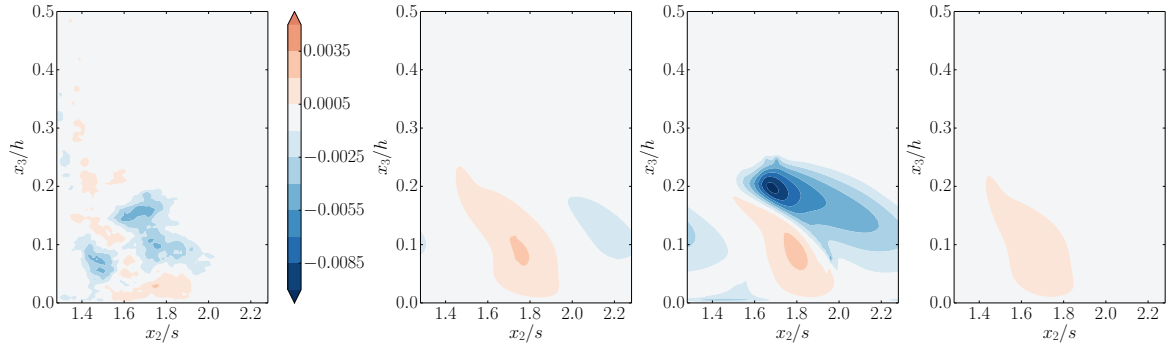

(a) LES (b) RANS_BSQ (c) RANS_QCR (d) RANS_BUA

Figure C.16: τ_{t12} on the plane outlet 3.

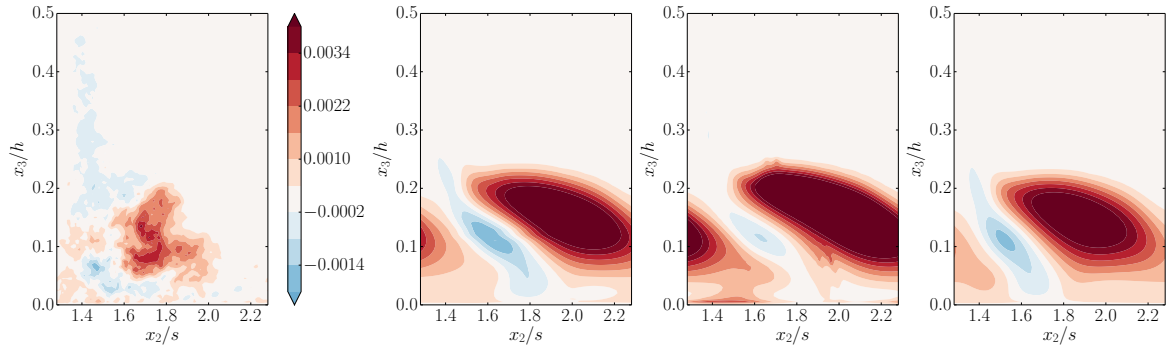

(a) LES (b) RANS_BSQ (c) RANS_QCR (d) RANS_BUA

Figure C.17: τ_{t13} on the plane outlet 3.

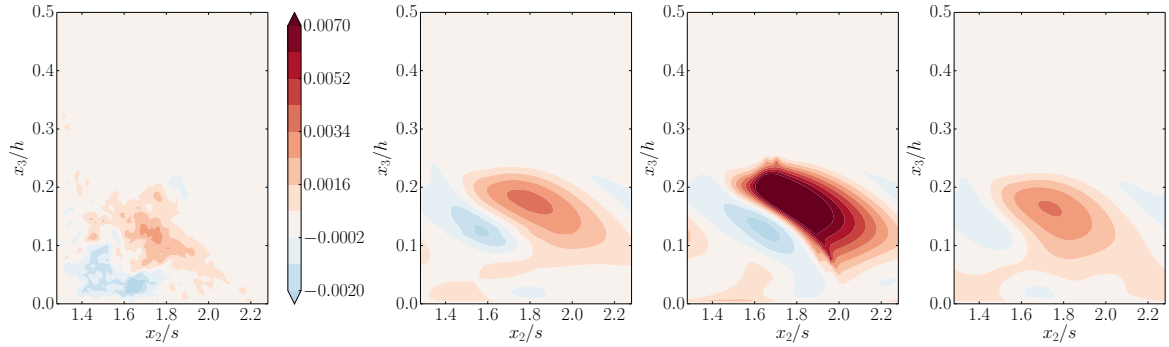

(a) LES (b) RANS_BSQ (c) RANS_QCR (d) RANS_BUA

Figure C.18: τ_{t23} on the plane outlet 3.

Appendix D

Corner separation turbulent kinetic energy budget

Sections

In this appendix are presented the results not presented in the core of the manuscript. The interpretation for these results is similar with the one for the results on outlet plane 1, presented in chapter 9, section 9.3.

D.1 On outlet 0

D.1.1 Numerical residual

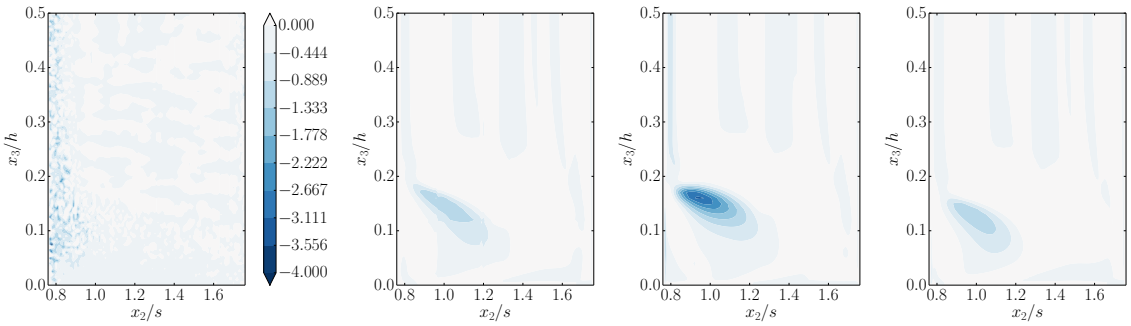

(a) LES (b) RANS_BSQ (c) RANS_QCR (d) RANS_BUA

Figure D.1: Numerical residual on the plane outlet 0, normalised by $(\rho^2 u_e^4)/\mu$.

D.1.2 Production

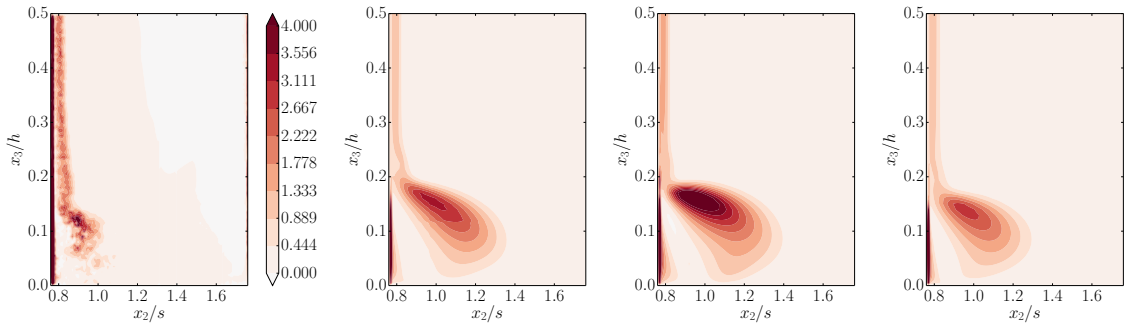

(a) LES (b) RANS_BSQ (c) RANS_QCR (d) RANS_BUA

Figure D.2: Production on the plane outlet 0, normalised by $(\rho^2 u_e^4)/\mu$.

D.1.3 Dissipation

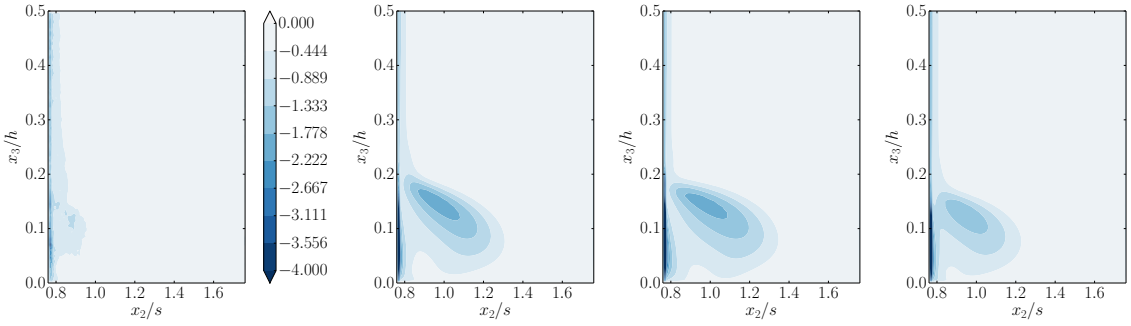

(a) LES (b) RANS_BSQ (c) RANS_QCR (d) RANS_BUA

Figure D.3: Dissipation on the plane outlet 0, normalised by $(\rho^2 u_e^4)/\mu$.

D.1.4 Transport

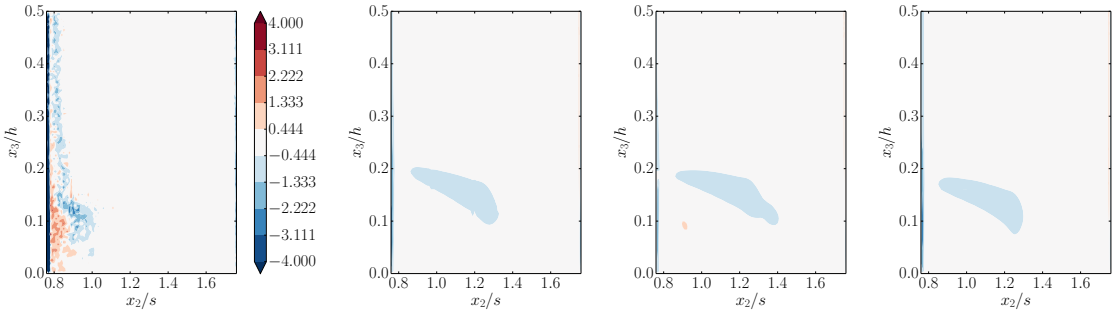

(a) LES (b) RANS_BSQ (c) RANS_QCR (d) RANS_BUA

Figure D.4: Transport on the plane outlet 0, normalised by $(\rho^2 u_e^4)/\mu$.

D.2 On outlet 2

D.2.1 Numerical residual

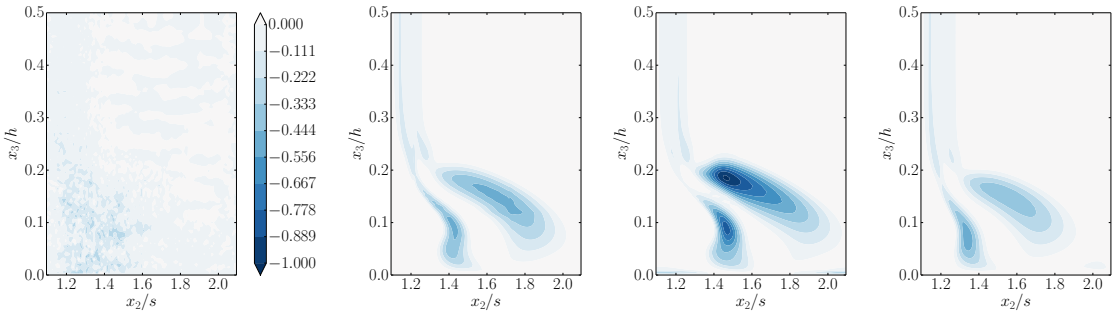

(a) LES (b) RANS_BSQ (c) RANS_QCR (d) RANS_BUA

Figure D.5: Numerical residual on the plane outlet 2, normalised by $(\rho^2 u_e^4)/\mu$.

D.2.2 Production

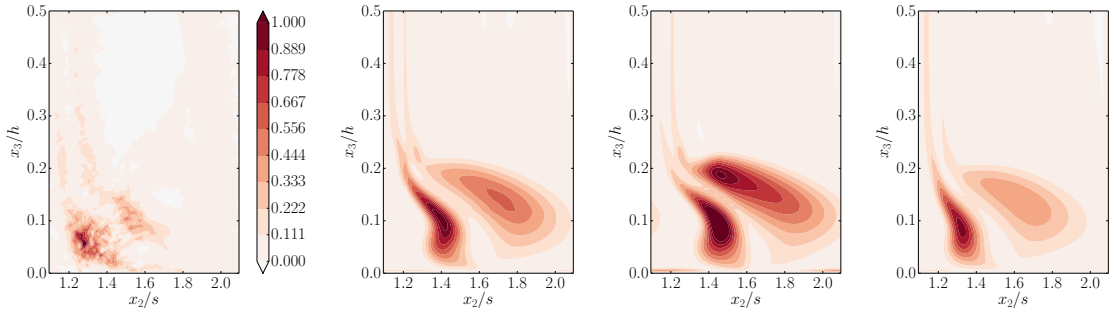

(a) LES (b) RANS_BSQ (c) RANS_QCR (d) RANS_BUA

Figure D.6: Production on the plane outlet 2, normalised by $(\rho^2 u_e^4)/\mu$.

D.2.3 Dissipation

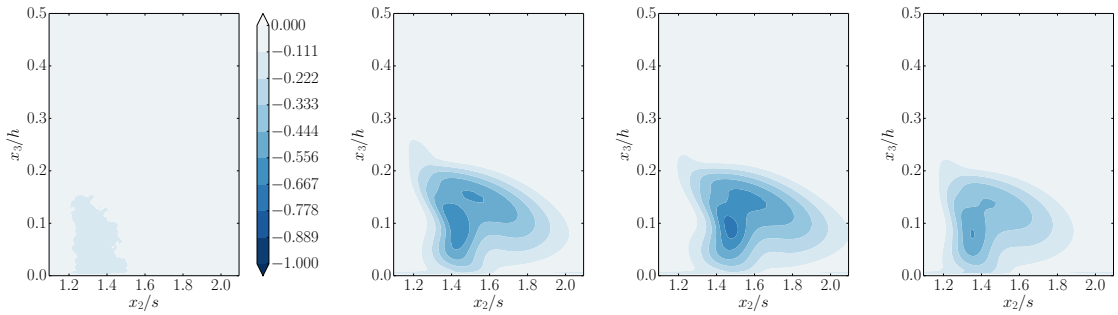

(a) LES (b) RANS_BSQ (c) RANS_QCR (d) RANS_BUA

Figure D.7: Dissipation on the plane outlet 2, normalised by $(\rho^2 u_e^4)/\mu$.

D.2.4 Transport

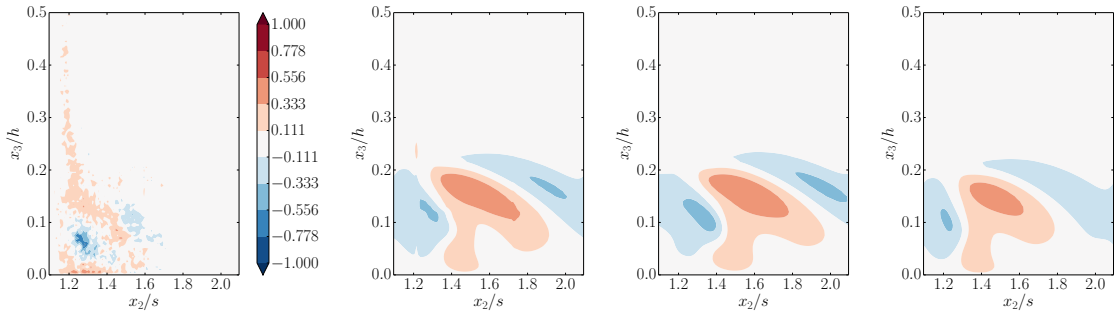

(a) LES (b) RANS_BSQ (c) RANS_QCR (d) RANS_BUA

Figure D.8: Transport on the plane outlet 2, normalised by $(\rho^2 u_e^4)/\mu$.

D.3 On outlet 3

D.3.1 Numerical residual

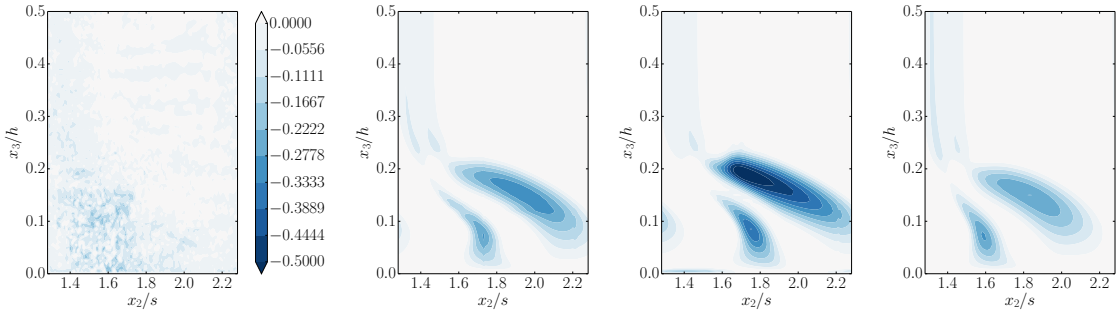

(a) LES (b) RANS_BSQ (c) RANS_QCR (d) RANS_BUA

Figure D.9: Numerical residual on the plane outlet 3, normalised by $(\rho^2 u_e^4)/\mu$.

D.3.2 Production

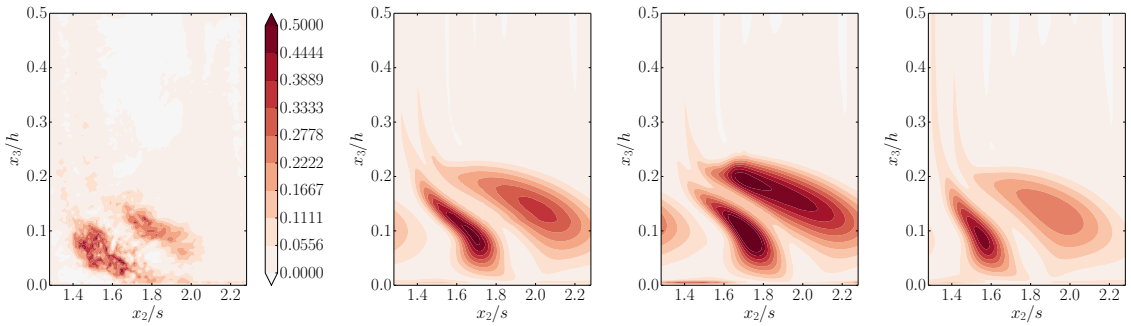

(a) LES (b) RANS_BSQ (c) RANS_QCR (d) RANS_BUA

Figure D.10: Production on the plane outlet 3, normalised by $(\rho^2 u_e^4)/\mu$.

D.3.3 Dissipation

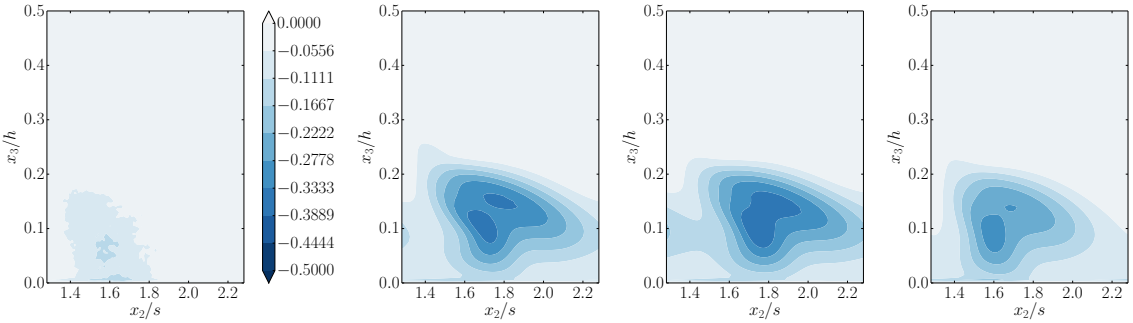

(a) LES (b) RANS_BSQ (c) RANS_QCR (d) RANS_BUA

Figure D.11: Dissipation on the plane outlet 3, normalised by $(\rho^2 u_e^4)/\mu$.

D.3.4 Transport

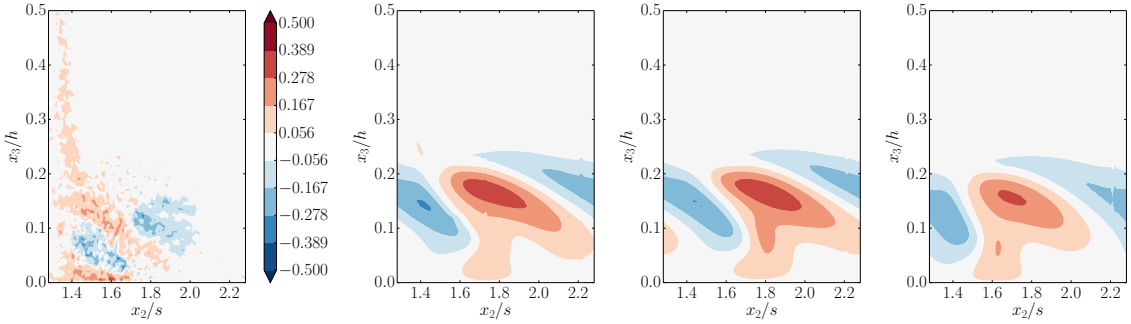

(a) LES (b) RANS_BSQ (c) RANS_QCR (d) RANS_BUA

Figure D.12: Transport on the plane outlet 3, normalised by $(\rho^2 u_e^4)/\mu$.

References

Aubert, S. (1993). *Etude des schémas à haute précision pour la simulation d'écoulements transsoniques instationnaires ou visqueux. Application aux turbomachines*. PhD Thesis, Ecole Centrale de Lyon, Ecully. [Cited on pages 29 and 51.]

Bailly, C. and Comte-Bellot, G. (2003). *Turbulence*. Science et techniques de l'ingénieur. CNRS Edition, Paris, cnrs éditions edition. [Cited on page 23.]

Baldwin, B. S. and Lomax, H. (1978). Thin layer approximation and algebraic model for separated turbulent flows. *American Institute of Aeronautics and Astronautics*, 257. [Cited on pages 16 and 33.]

Bogey, C. and Bailly, C. (2002). Three-dimensional non-reflective boundary conditions for acoustic simulations: far field formulation and validation test cases. *Acta Acustica united with Acustica*, 88(4):463–471. [Cited on page 86.]

Bogey, C. and Bailly, C. (2009). Turbulence and energy budget in a self-preserving round jet: direct evaluation using large eddy simulation. *Journal of Fluid Mechanics*, 627:129–160. [Cited on pages 28 and 187.]

Bordji, M., Gand, F., Deck, S., and Brunet, V. (2015). Investigation of a Nonlinear Reynolds-Averaged Navier–Stokes Closure for Corner Flows. *AIAA Journal*, pages 1–13. [Cited on pages 9, 33, and 44.]

Borello, D., Rispoli, F., and Hanjalic, K. (2006). Prediction of Tip-Leakage Flow in Axial Flow Compressor with Second Moment Closure. In *Proceedings of the ASME Turbo Expo 2006: Power for Land, Sea, and Air, Barcelona, Spain, May 8–11, 2006*, pages 271–281. American Society of Mechanical Engineers. [Cited on page 16.]

Boris, J. P., Grinstein, F. F., Oran, E. S., and Kolbe, R. L. (1992). New insights into large eddy simulation. *Fluid Dynamics Research*, 10(4-6):199–228. [Cited on page 45.]

Bos, W. J. T. and Rubinstein, R. (2017). Dissipation in unsteady turbulence. *Physical Review Fluids*, 2(2). [Cited on page 184.]

Boudet, J. (2003). *Approches numeriques pour la simulation du bruit a large bande en vue de l'application aux turbomachines*. PhD Thesis, Ecole Centrale de Lyon, Ecully. [Cited on page 25.]

Boudet, J. (2014). *Simulation des grandes échelles pour l'aérodynamique des turbomachines*. Habilitation à diriger les recherches, Ecole Centrale de Lyon, Écully. [Cited on pages xix and 10.]

Boudet, J., Cahuzac, A., Kausche, P., and Jacob, M. C. (2015a). Zonal Large-Eddy Simulation of a Fan Tip-Clearance Flow, With Evidence of Vortex Wandering. *Journal of Turbomachinery*, 137(6):061001. [Cited on pages xix, xxvii, xxviii, 17, and 45.]

Boudet, J., Caro, J., Li, B., Jondeau, E., and Jacob, M. C. (2016a). Zonal large-eddy simulation of a tip leakage flow. *International Journal of Aeroacoustics*, 15(6-7):646–661. [Cited on pages xix, xx, 16, 18, 19, 24, 26, 45, 67, 89, 91, 95, and 149.]

Boudet, J., Caro, J., Shao, L., and Lévêque, E. (2007). Numerical studies towards practical large-eddy simulation. *Journal of Thermal Science*, 16(4):328–336. [Cited on pages 24 and 71.]

Boudet, J., Grilliat, J., Caro, J., and Jacob, M. C. (2009). Combined experimental/-computational study of tip clearance flow and acoustics. In *8th European Turbomachinery Conference*, Graz, Austria. [Cited on page 154.]

Boudet, J., Monier, J. F., and Gao, F. (2015b). Implementation of a roughness element to trip transition in large-eddy simulation. *Journal of Thermal Science*, 24(1):30–36. [Cited on pages 46, 55, 58, 72, 88, 92, and 93.]

Boudet, J. C., Li, B., Caro, J., Jondeau, E., and Jacob, M. C. (2016b). Tip-Leakage Flow: a Detailed Simulation with a Zonal Approach. In *Proceedings of the 22nd AIAA/CEAS Aeroacoustics conference, Lyon, France, May 30 - June 1st, 2016*. American Institute of Aeronautics and Astronautics. [Cited on pages xix, 16, 18, 19, 45, 89, 91, and 95.]

Boussinesq, J. (1877). *Essai sur la théorie des eaux courantes*. Imprimerie nationale. [Cited on page 31.]

Cahuzac, A. (2012). *Aspects cinétiques et acoustiques en simulation numérique des grandes échelles, et application à l'étude du contrôle de l'écoulement de jeu en turbomachines*. PhD Thesis, Ecole Centrale de Lyon, Ecully. [Cited on pages 26 and 71.]

Cahuzac, A., Boudet, J., Borgnat, P., and Lévêque, E. (2010). Smoothing algorithms for mean-flow extraction in large-eddy simulation of complex turbulent flows. *Physics of Fluids*, 22(12):125104. [Cited on pages xxv, 27, and 58.]

Cahuzac, A., Boudet, J., Jacob, M., and Kausche, P. (2011). Large-Eddy Simulation of a rotor tip-clearance flow. In *Proceedings of the 17th AIAA/CEAS Aeroacoustics Conference (32nd AIAA Aeroacoustics Conference), Portland, Oregon, USA, June 05-08, 2011*. American Institute of Aeronautics and Astronautics. [Cited on page 26.]

Courtiade, N. (2012). *Experimental analysis of the unsteady flow and instabilities in a high-speed multistage compressor*. PhD Thesis, Ecole Centrale de Lyon, Ecully. [Cited on page 1.]

Cousteix, J. (1989). *Aérodynamique: Turbulence et Couche Limite*. Cepadues-éditions. [Cited on pages 59, 60, 70, and 138.]

Deck, S. (2005). Zonal-Detached-Eddy Simulation of the Flow Around a High-Lift Configuration. *AIAA Journal*. [Cited on page 42.]

Deck, S. (2012). Recent improvements in the Zonal Detached Eddy Simulation (ZDES) formulation. *Theoretical and Computational Fluid Dynamics*, 26(6):523–550. [Cited on pages xxv, xxvi, and 42.]

Denton, J. D. (2010). Some Limitations of Turbomachinery CFD. pages 735–745. ASME. [Cited on page 102.]

Devenport, W. J., Wittmer, K. S., Muthanna, C., and Wenger, C. W. (2004). Wake of a Compressor Cascade with Tip Gap, Part 3: Two Point Statistics. *AIAA Journal*, 42(11):2341–2346. [Cited on pages 14 and 15.]

Dring, R. P., Joslyn, H. D., and Hardin, L. W. (1982). An Investigation of Axial Compressor Rotor Aerodynamics. *Journal of Engineering for Gas Turbines and Power*, 104(1):84–96. [Cited on page 9.]

Favre, A. (1969). Problems of hydrodynamics and continuum mechanics. *Society for Industrial and Applied Mathematics, Philadelphia*, page 231. [Cited on page 29.]

Gao, F. (2014). *Advanced numerical simulation of corner separation in a linear compressor cascade*. PhD Thesis, Ecole Centrale de Lyon, Ecully. [Cited on pages xix, xx, 13, 14, 28, 84, 85, 87, and 89.]

Gao, F., Ma, W., Sun, J., Boudet, J., Ottavy, X., Liu, Y., Lu, L., and Shao, L. (2017). Parameter study on numerical simulation of corner separation in LMFA-NACA65 linear compressor cascade. *Chinese Journal of Aeronautics*, 30(1):15–30. [Cited on pages 84 and 89.]

Gao, F., Ma, W., Zambonini, G., Boudet, J., Ottavy, X., Lu, L., and Shao, L. (2015a). Large-eddy simulation of 3-D corner separation in a linear compressor cascade. *Physics of Fluids*, 27(8):085105. [Cited on pages 12, 24, 26, 84, and 89.]

Gao, F., Zambonini, G., Boudet, J., Ottavy, X., Lu, L., and Shao, L. (2015b). Unsteady behavior of corner separation in a compressor cascade: Large eddy simulation and experimental study. *Proceedings of the Institution of Mechanical Engineers, Part A: Journal of Power and Energy*, 229(5):508–519. [Cited on pages 12, 84, and 89.]

Garnier, E., Adams, N., and Sagaut, P. (2009). *Large Eddy Simulation for Compressible Flows*. Springer Science & Business Media. Google-Books-ID: _7zowRoPSnoC. [Cited on pages 22 and 24.]

Gbadebo, S. A., Cumpsty, N. A., and Hynes, T. P. (2005). Three-Dimensional Separations in Axial Compressors. *Journal of Turbomachinery*, 127(2):331. [Cited on page 35.]

Gbadebo, S. A., Cumpsty, N. A., and Hynes, T. P. (2007). Interaction of Tip Clearance Flow and Three-Dimensional Separations in Axial Compressors. *Journal of Turbomachinery*, 129(4):679. [Cited on page 35.]

Gbadebo, S. A., Hynes, T. P., and Cumpsty, N. A. (2004). Influence of Surface Roughness on Three-Dimensional Separation in Axial Compressors. pages 471–481. ASME. [Cited on page 35.]

Greschner, B., Grilliat, J., Jacob, M., and Thiele, F. (2010). Measurements and wall modeled LES simulation of trailing edge noise caused by a turbulent boundary layer. *International Journal of Aeroacoustics*, 9(3):329–356. [Cited on page 41.]

Greschner, B. and Thiele, F. (2011). Wall Modeled LES simulation of Rotor-Stator-Cascade Broadband Noise. American Institute of Aeronautics and Astronautics. [Cited on page 41.]

Gritskevich, M. S., Garbaruk, A. V., Schütze, J., and Menter, F. R. (2012). Development of DDES and IDDES Formulations for the k- Shear Stress Transport Model. *Flow, Turbulence and Combustion*, 88(3):431–449. [Cited on pages 40 and 42.]

Hah, C. and Loellbach, J. (1999). Development of hub corner stall and its influence on the performance of axial compressor blade rows. *Journal of turbomachinery*, 121(1):67–77. [Cited on pages xix, 10, and 11.]

Holmén, V. (2012). *Methods for Vortex Identification*. Master Thesis, Lund University, Lund. [Cited on pages 71 and 101.]

Jacob, M. C., Grilliat, J., Camussi, R., and Gennaro, G. C. (2010). Aeroacoustic Investigation of a Single Airfoil Tip Leakage Flow. *International Journal of Aeroacoustics*, 9(3):253–272. [Cited on page 89.]

Jacob, M. C., Jondeau, E., and Li, B. (2016a). Time-resolved PIV measurements of a tip leakage flow. *International Journal of Aeroacoustics*, 5(6-7):662–685. [Cited on pages xix, 16, 18, 89, 90, and 148.]

Jacob, M. C., Jondeau, E., Li, B., and Boudet, J. C. (2016b). Tip Leakage Flow: Advanced Measurements and Analysis. In *Proceedings of 22nd AIAA/CEAS Aeroacoustics Conference, May 30 - June 1st, 2016, Lyon, France*, pages AIAA–2016–2823. American Institute of Aeronautics and Astronautics. [Cited on pages 16, 18, 89, and 148.]

Jameson, A., Schmidt, W., Turkel, E., and others (1981). Numerical solutions of the Euler equations by finite volume methods using Runge-Kutta time-stepping schemes. *AIAA paper*, 1259:1981. [Cited on pages 88 and 93.]

Jiménez, J., Hoyas, S., Simens, M. P., and Mizuno, Y. (2010). Turbulent boundary layers and channels at moderate Reynolds numbers. *Journal of Fluid Mechanics*, 657:335–360. [Cited on pages 23, 28, 55, 59, and 61.]

Joslyn, H. D. and Dring, R. P. (1985). Axial Compressor Stator Aerodynamics. *Journal of Engineering for Gas Turbines and Power*, 107:485–493. [Cited on page 9.]

Kato, M. (1993). The modeling of turbulent flow around stationary and vibrating square cylinders. *Ninth Symposium on Turbulent Shear Flows, 1993*. [Cited on page 34.]

Kok, J., Dol, H., Oskam, B., and van der Ven, H. (2004). Extra-Large Eddy Simulation of Massively Separated Flows. American Institute of Aeronautics and Astronautics. [Cited on pages xxv, xxvi, and 39.]

Kok, J. C. (2000). Resolving the Dependence on Freestream Values for the k-w Turbulence Model. *AIAA Journal*, 38(7):1292 – 1295. [Cited on page 34.]

Kuban, L., Laval, J.-P., Elsner, W., Tyliszczak, A., and Marquillie, M. (2012). LES modeling of converging-diverging turbulent channel flow. *Journal of Turbulence*, 13:N11. [Cited on page 28.]

Lakshminarayana, B., Zaccaria, M., and Marathe, B. (1995). The Structure of Tip Clearance Flow in Axial Flow Compressors. *Journal of Turbomachinery*, 117(3):336. [Cited on page 13.]

Launder, B. and Sharma, B. (1974). Application of the energy-dissipation model of turbulence to the calculation of flow near a spinning disc. *Letters in Heat and Mass Transfer*, 1(2):131–137. [Cited on page 34.]

Lei, V.-M., Spakovszky, Z. S., and Greitzer, E. M. (2008). A Criterion for Axial Compressor Hub-Corner Stall. *Journal of Turbomachinery*, 130(3):031006–01–031006–10. [Cited on pages xix, xxvii, 12, and 13.]

Leichtfuß, S., Holzinger, F., Brandstetter, C., Wartzek, F., and Schiffer, H. P. (2013). Aeroelastic Investigation of a Transonic Research Compressor. In *Proceedings of ASME Turbo Expo 2013: Turbine Technical Conference and Exposition, GT2013, June 3-7, 2013, San Antonio, Texas, USA*, pages 1–11, San Antonio, Texas, USA. American Society of Mechanical Engineers. [Cited on page 17.]

Li, B. (2016). *Aerodynamic and acoustic analysis of the tip-leakage flow on a single airfoil*. PhD Thesis, Ecole Centrale de Lyon, Ecully. [Cited on page 92.]

Li, Y., Chen, H., and Katz, J. (2017). Measurements and Characterization of Turbulence in the Tip Region of an Axial Compressor Rotor. pages 1–13. American Society of Mechanical Engineers. [Cited on page 15.]

Li, Y., Ye, D., and Lu, B. (1992). Experimental investigation of the three-dimensional flow in an annular compressor cascade at large incidence. *Journal of Thermal Science*, 1(1):3–10. [Cited on page 10.]

Lieblein, S. (1959). Loss and Stall Analysis of Compressor Cascades. *Journal of Basic Engineering*, 81:387–400. [Cited on pages xxv and 12.]

Liu, Y., Yan, H., Fang, L., Lu, L., Li, Q., and Shao, L. (2016). Modified k- model using kinematic vorticity for corner separation in compressor cascades. *Science China Technological Sciences*. [Cited on pages xxvi and 35.]

Lu, L. and Chen, M. (2000). A theoretical model for Reynolds-stress and dissipation-rate budgets in near-wall region. *Science in China Series A: Mathematics*, 43(2):199–204. [Cited on page 28.]

Lévêque, E., Toschi, F., Shao, L., and Bertoglio, J.-P. (2007). Shear-improved Smagorinsky model for large-eddy simulation of wall-bounded turbulent flows. *Journal of Fluid Mechanics*, 570:491. [Cited on pages xxvii, 26, 46, 58, 73, 88, and 94.]

Ma, W. (2012). *Experimental investigation of corner stall in a linear compressor cascade*. PhD Thesis, Ecole Centrale de Lyon, Ecully. [Cited on page 84.]

Ma, W., Ottavy, X., Lu, L., and Leboeuf, F. (2013). Intermittent corner separation in a linear compressor cascade. *Experiments in Fluids*, 54(6):1–17. [Cited on pages xix, 11, 12, and 84.]

Ma, W., Ottavy, X., Lu, L., Leboeuf, F., and Gao, F. (2011). Experimental Study of Corner Stall in a Linear Compressor Cascade. *Chinese Journal of Aeronautics*, 24(3):235–242. [Cited on pages 11, 12, and 84.]

Mani, M., Babcock, D., Winkler, C., and Spalart, P. (2013). Predictions of a Supersonic Turbulent Flow in a Square Duct. In *51st AIAA Aerospace Sciences Meeting including the New Horizons Forum and Aerospace Exposition*, Aerospace Sciences Meetings. American Institute of Aeronautics and Astronautics. DOI: 10.2514/6.2013-860 DOI: 10.2514/6.2013-860. [Cited on page 33.]

Marquillie, M., Laval, J.-P., and Dolganov, R. (2008). Direct numerical simulation of a separated channel flow with a smooth profile. *Journal of Turbulence*, (9). [Cited on page 28.]

Menter, F. R. (1992). Improved two-equation k-omega turbulence models for aerodynamic flows. *NASA STI/Recon Technical Report N*, 93:22809. [Cited on page 34.]

Menter, F. R. (1994). Two-equation eddy-viscosity turbulence models for engineering applications. *AIAA Journal*, 32(8):1598–1605. [Cited on pages 34, 35, 39, 40, and 42.]

Menter, F. R., Kuntz, M., and Langtry, R. (2003). Ten years of industrial experience with the SST turbulence model. *Turbulence, heat and mass transfer*, 4(1). [Cited on pages 39, 40, 42, and 139.]

Merle, X. and Robinet, J. C. (2009). Schémas aux différences finies appliquésa l'analyse de stabilité globale en maillages curvilignes pour écoulements incompressibles. In *Proceedings of the 19eme Congrès Français de Mécanique, Marseille, France, 24-28 Août, 2015*, Marseille. [Cited on page 51.]

Monier, J.-F. (2014). *Etude de la dynamique turbulente en écoulement décollé à partir de résultats LES et expérimentaux. Recherche d'améliorations en modélisation RANS.* Master Thesis, Ecole Centrale de Lyon, Ecully. [Cited on pages 55 and 61.]

Moser, R. D., Kim, J., and Mansour, N. N. (1999). Direct numerical simulation of turbulent channel flow up to Re=590. *Physics of Fluids*, 11(4):943–945. [Cited on page 71.]

Muthanna, C. and Devenport, W. J. (2004). Wake of a Compressor Cascade with Tip Gap, Part 1: Mean Flow and Turbulence Structure. *AIAA Journal*, 42(11):2320–2331. [Cited on page 14.]

Möller, D., Jüngst, M., Holzinger, F., Brandstetter, C., Schiffer, H.-P., and Leichtfuß, S. (2016). Numerical Investigation of Tip Clearance Flow Induced Flutter in an Axial Research Compressor. In *Proceedings of ASME Turbo Expo 2016: Turbomachinery Technical Conference and Exposition, GT2016, June 13 – 17, 2016, Seoul, South Korea*, pages 1–12, Seoul, South Korea. American Society of Mechanical Engineers. [Cited on page 18.]

Nicoud, F. and Ducros, F. (1999). Subgrid-scale stress modelling based on the square of the velocity gradient tensor. *Flow, Turbulence and Combustion*, 62(3):183–200. [Cited on pages 12 and 26.]

Nicoud, F., Toda, H. B., Cabrit, O., Bose, S., and Lee, J. (2011). Using singular values to build a subgrid-scale model for large eddy simulations. *Physics of Fluids*, 23(8):085106–1–12. [Cited on page 12.]

Pope, S. B. (1975). A more general effective-viscosity hypothesis. *Journal of Fluid Mechanics*, 72(02):331–340. [Cited on pages 125, 172, and 184.]

Pope, S. B. (2000). *Turbulent Flows*. Cambridge university press. [Cited on page 23.]

Reynolds, O. (1895). On the Dynamical Theory of Incompressible Viscous Fluids and the Determination of the Criterion. *Philosophical Transactions of the Royal Society A: Mathematical, Physical and Engineering Sciences*, 186:123–164. [Cited on page 29.]

Riera, W. (2014). *Evaluation of the ZDES method on an axial compressor: analysis of the effects of upstream wake and throttle on the tip-leakage flow*. PhD Thesis, Ecole Centrale de Lyon, Écully. [Cited on page 145.]

Sagaut, P. (2006). *Large Eddy Simulation for Incompressible Flows: An Introduction*. Springer Science & Business Media. [Cited on page 24.]

Schiavo, L. A. C. A., Wolf, W. R., and Azevedo, J. L. F. (2017). Turbulent kinetic energy budgets in wall bounded flows with pressure gradients and separation. *Physics of Fluids*, 29(11):115108–1 – 115108–15. [Cited on page 63.]

Schlichting, H. and Gersten, K. (2000). *Boundary-layer theory*. Springer. [Cited on pages 59 and 60.]

Schmitt, F. G. (2007). About Boussinesq's turbulent viscosity hypothesis: historical remarks and a direct evaluation of its validity. *Comptes Rendus Mécanique*, 335(9-10):617–627. [Cited on pages xxviii, 32, 33, and 118.]

Schulz, H. D. and Gallus, H. D. (1988). Experimental investigation of the three-dimensional flow in an annular compressor cascade. *Journal of Turbomachinery*, 110(4):467–478. [Cited on page 10.]

Scillitoe, A. D., Tucker, P. G., and Adami, P. (2015). Evaluation of RANS and ZDES methods for the prediction of three-dimensional separation in axial flow compressors. *ASME Paper No. GT2015-43975*. [Cited on page 33.]

Scillitoe, A. D., Tucker, P. G., and Adami, P. (2017). Numerical Investigation of Three-Dimensional Separation in an Axial Flow Compressor: The Influence of Freestream Turbulence Intensity and Endwall Boundary Layer State. *Journal of Turbomachinery*, 139(2):021011–1–10. [Cited on page 12.]

Shao, L. (1992). *Etude d'une couche de mélange turbulente non cisaillée par simulation des grandes échelles*. PhD Thesis, Ecole Centrale de Lyon, Ecully. [Cited on page 184.]

Shih, T.-H., Zhu, J., and Lumley, J. L. (1996). CALCULATION OF WALL-BOUNDED COMPLEX FLOWS AND FREE SHEAR FLOWS. *International Journal for Numerical Methods in Fluids*, 23(11):1133–1144. [Cited on page 125.]

Shur, M. L., Spalart, P. R., Strelets, M. K., and Travin, A. K. (2008). A hybrid RANS-LES approach with delayed-DES and wall-modelled LES capabilities. *International Journal of Heat and Fluid Flow*, 29(6):1638–1649. [Cited on pages xxv, xxvi, xxvii, 40, and 41.]

Smagorinsky, J. (1963). General Circulation Experiments with the Primitive Equations: I. The Basic Experiment. *Monthly Weather Review*, 91(3):99 – 163. [Cited on pages xxv, 12, 26, and 39.]

Smati, L. (1997). *Contribution au développement d'une méthode numérique d'analyse des écoulements instationnaires. Applications aux turbomachines.* PhD Thesis, Ecole Centrale de Lyon, Ecully. [Cited on pages 29, 30, and 54.]

Smith, A. and Cebeci, T. (1967). Numerical Solution of the Turbulent-boundary-layer Equations. Technical report, DOUGLAS AIRCRAFT CO LONG BEACH CA AIRCRAFT DIV. [Cited on page 33.]

Spalart, P. and Allmaras, S. (1992). A one equation turbulence model for aerodinamic flows. *AIAA Journal*, 94-439. [Cited on page 38.]

Spalart, P. and Allmaras, S. R. (1994). A One-Equation Turbulence Model for Aerodynamic Flows. *La Recherche Aerospatiale*, (No. 1):5 – 21. [Cited on pages xxv, xxvi, xxvii, xxviii, xxix, 33, 38, and 45.]

Spalart, P. R. (2000). Strategies for turbulence modelling and simulations. *International Journal of Heat and Fluid Flow*, 21(3):252–263. [Cited on pages 33, 122, and 168.]

Spalart, P. R. (2009). Detached-Eddy Simulation. *Annual Review of Fluid Mechanics*, 41(1):181–202. [Cited on pages 38, 40, 42, and 44.]

Spalart, P. R., Deck, S., Shur, M. L., Squires, K. D., Strelets, M. K., and Travin, A. (2006). A New Version of Detached-eddy Simulation, Resistant to Ambiguous Grid Densities. *Theoretical and Computational Fluid Dynamics*, 20(3):181–195. [Cited on pages xxvi, xxvii, xxix, 39, 40, and 139.]

Spalart, P. R., Jou, W. H., Strelets, M., and Allmaras, S. R. (1997). Comments on the feasibility of LES for wings, and on a hybrid RANS/LES approach. *Advances in DNS/LES*, 1:4 – 8. [Cited on pages xxv, xxvii, and 38.]

Storer, J. A. and Cumpsty, N. A. (1991). Tip Leakage Flow in Axial Compressors. *Journal of Turbomachinery*, 113(2):252–259. [Cited on pages 13, 16, and 152.]

Strahle, W. C. (1985). Stagnation point flows with freestream turbulence - The matching condition. *AIAA Journal*, 23(11):1822–1824. [Cited on page 35.]

Tan, D., Li, Y., Wilkes, I., Miorini, R. L., and Katz, J. (2015). Visualization and Time-Resolved Particle Image Velocimetry Measurements of the Flow in the Tip Region of a Subsonic Compressor Rotor. *Journal of Turbomachinery*, 137(4):041007. [Cited on pages xix, 15, 175, and 178.]

Touil, H. (2002). *Modélisation spectrale de la turbulence inhomogène anisotrope*. PhD Thesis, Ecole Centrale de Lyon, Écully. [Cited on page 184.]

Travin, A., Shur, M., Strelets, M., and Spalart, P. R. (2004). Physical and Numerical Upgrades in the Detached-Eddy Simulation of Complex Turbulent Flows. In Friedrich, R. and Rodi, W., editors, *Advances in LES of Complex Flows*, volume 65, pages 239–254. Kluwer Academic Publishers, Dordrecht. [Cited on page 39.]

Travin, A. K., Shur, M. L., Spalart, P. R., and Strelets, M. K. (2006). Improvement of delayed detached-eddy simulation for LES with wall modelling. In *Proceedings of the European Conference on Computational Fluid Dynamics, Egmond aan Zee, The Netherlands, September 5-8, 2006*, Egmond aan Zee, The Netherlands. Delft University of Technology; European Community on Computational Methods in Applied Sciences (ECCOMAS). [Cited on page 41.]

Tucker, P. (2013). *Unsteady Computational Fluid Dynamics in Aeronautics*, volume 104. Springer Science & Business Media. [Cited on page 1.]

Tucker, P., Eastwood, S., Klostermeier, C., Jefferson-Loveday, R., Tyacke, J., and Liu, Y. (2012a). Hybrid LES Approach for Practical Turbomachinery Flows—Part I: Hierarchy and Example Simulations. *Journal of Turbomachinery*, 134(2):021023. [Cited on pages xix, xxvi, xxviii, 2, 45, 46, 67, and 69.]

Tucker, P., Eastwood, S., Klostermeier, C., Xia, H., Ray, P., Tyacke, J., and Dawes, W. (2012b). Hybrid LES Approach for Practical Turbomachinery Flows—Part II: Further Applications. *Journal of Turbomachinery*, 134(2):021024. [Cited on pages xix, 45, and 46.]

Wang, Y. and Devenport, W. J. (2004). Wake of a Compressor Cascade with Tip Gap, Part 2: Effects of Endwall Motion. *AIAA Journal*, 42(11):2332–2340. [Cited on pages 14 and 15.]

Wilcox, C., D. (1988). Reassessment of the scale-determining equation for advanced turbulence models. *AIAA Journal*, 26(11):1299 – 1310. [Cited on pages xxv, xxviii, 17, 18, 30, 34, 39, 46, and 73.]

Wilcox, D. C. (2006). *Turbulence Modeling for CFD*. D C W Industries, La Cãnada, Calif, 3rd edition edition. [Cited on pages 63, 135, 176, and 179.]

Wilcox, D. C. (2008). Formulation of the k-w Turbulence Model Revisited. *AIAA Journal*, 46(11):2823–2838. [Cited on page 34.]

Wisler, D. C. (1985). Loss reduction in axial-flow compressors through low-speed model testing. *Journal of Engineering for Gas Turbines and Power*, 107(2):354–363. [Cited on page 9.]

Yamada, K., Furukawa, M., Tamura, Y., Saito, S., Matsuoka, A., and Nakayama, K. (2016). Large-Scale DES Analysis of Stall Inception Process in a Multi-Stage Axial Flow Compressor. In *Proceedings of the ASME Turbo Expo 2016: Turbomachinery Technical Conference and Exposition, Seoul, South Korea, June 13–17, 2016*, pages 1–12. American Society of Mechanical Engineers. [Cited on page 11.]

Yocum, A. M. and O'Brien, W. F. (1993a). Separated Flow in a Low-Speed Two-Dimensional Cascade: Part I-Flow Visualization and Time-Mean Velocity Measurements. *Journal of Turbomachinery*, 115:409–420. [Cited on page 11.]

Yocum, A. M. and O'Brien, W. F. (1993b). Separated Flow in a Low-Speed Two-Dimensional Cascade: Part II-Cascade Performance. *Journal of Turbomachinery*, 115:421–434. [Cited on page 11.]

You, D., Wang, M., Moin, P., and Mittal, R. (2007a). Large-eddy simulation analysis of mechanisms for viscous losses in a turbomachinery tip-clearance flow. *Journal of Fluid Mechanics*, 586:177. [Cited on pages xix, 13, 14, and 17.]

You, D., Wang, M., Moin, P., and Mittal, R. (2007b). Vortex Dynamics and Low-Pressure Fluctuations in the Tip-Clearance Flow. *Journal of Fluids Engineering*, 129(8):1002. [Cited on page 17.]

Zambonini, G. (2016). *Unsteady dynamics of corner separation in a linear compressor cascade*. PhD Thesis, Ecole Centrale de Lyon, Ecully. [Cited on pages 11 and 84.]

Zambonini, G. and Ottavy, X. (2015). Unsteady Pressure Investigations of Corner Separated Flow in a Linear Compressor Cascade. In *Proceedings of the ASME Turbo Expo 2015: Turbine Technical Conference and Exposition, Montreal, Quebec, Canada, June 15–19, 2015*, pages 1–14. ASME. [Cited on pages 11 and 84.]

Zambonini, G., Ottavy, X., and Kriegseis, J. (2017). Corner Separation Dynamics in a Linear Compressor Cascade. *Journal of Fluids Engineering*, 139(6):061101. [Cited on pages 11, 84, 101, and 102.]

dernière page de la thèse

AUTORISATION DE SOUTENANCE

Vu les dispositions de l'arrêté du 25 mai 2016,

Vu la demande des directeurs de thèse

Messieurs L. SHAO et J. BOUDET

et les rapports de

M. E. LAMBALLAIS
Professeur - Faculté de Sciences Fondamentales et Appliquées - Université de Poitiers
Bâtiment B5 - 9 rue Charles-Claude Chenou - TSA 51 106 - 86073 Poitiers cedex 9

et de

M. G. BALARAC
Maître de Conférences HDR - Laboratoire LEGI (UMR 5519) - Bureau A116
Domaine Universitaire - CS 40700 - 38058 Grenoble cedex 9

Monsieur MONIER Jean-François

est autorisé à soutenir une thèse pour l'obtention du grade de **DOCTEUR**

Ecole doctorale MECANIQUE, ENERGETIQUE, GENIE CIVIL ET ACOUSTIQUE

Fait à Ecully, le 21 juin 2018

P/Le directeur de l'E.C.L.
La directrice des Etudes

ECOLE CENTRALE DE LYON
Service Scolarité
ECULLY

M-A. GALLAND